Global-scale terrestrial water storage has decreased pp. 1348 & 1408

Fine-tuning palatable food consumption pp. 1353 & 1376

Reproducing everyday tactile experiences p. 1383

Science

$15
28 MARCH 2025
science.org

AAAS

TOXIC LEGACY

Lingering hazards from urban wildfire p. 1343

Science Webinars

AAAS

Science Webinars help you keep pace with emerging scientific fields!

Stay informed about scientific breakthroughs and discoveries.

Gain insights into current research from top scientists.

Take the opportunity to ask questions during live broadcasts.

Get alerts about upcoming free webinars.

Sign up at: scim.ag/wcfq2023

TongTong (pictured, center) is an artificial general intelligence (AGI) agent at the Beijing Institute for General Artificial Intelligence (BIGAI) embodied in a virtual world that emulates the complexity of the real physical social world. Here, she interacts with her mother and generates tasks based on her value function.

AI gets a mind of its own

Artificial general intelligence research is moving into a new era

Sometimes, less is more. In January, DeepSeek released the latest version of its chatbot, upending the artificial intelligence (AI) world. A training AI built for under $6 million, DeepSeek seems to rival the technical capabilities of other large language model (LLM) AIs, including ChatGPT, with only a fraction of the processing power. The breakthrough was a welcome development for Song-Chun Zhu, dean of the Institute for Artificial Intelligence at Peking University in Beijing, who has been challenging the current LLM-dominated AI paradigm in his efforts to create artificial general intelligence (AGI).

Zhu, a trailblazer in the AI field, graduated from Harvard University in 1996 and has published more than 400 papers covering computer vision, cognitive science, robot autonomy, and commonsense reasoning, among other topics. Now, he is the founder and director of the non-profit Beijing Institute for General Artificial Intelligence (BIGAI).

"We as a society may have misunderstood the term 'AI'," says Zhu. "Just like how we call a multifunctional cellphone 'smart', the popular AI models we use today are not truly intelligent." That's because today's AI, he explains, is driven by big data built upon massive computing power. Zhu pioneered data-driven statistical approaches and created the world's first large-scale annotated image dataset at the Lotus Hill Institute in 2005. However, he realized that big data sets and specific machine learning models alone are not enough to make true intelligence. "One of the major Chinese philosophical schools, the Yangmingism or the 'Teachings of the Heart', argues 'the reality we see comes from how our minds perceive'," Zhu says. To make AI more like humans, Zhu says, it needs to have a framework that emulates the top-down mechanisms in the brain.

According to Zhu, the future of AGI should be a kind of autonomous AI that doesn't require vast datasets. In 2020, Zhu returned to China to establish and lead BIGAI. Its mission: To pursue a unified theory of artificial intelligence in order to create general intelligent agents for lifting humanity.

Defining AGI agents in CUV-space:

Zhu and his team's focus at BIGAI is on creating value-driven human-like cognition that goes beyond data-driven imitation. "The difference between AGI and current LLM-based AI is just like the difference between a crow and a parrot," he said. While parrots can mimic many words, he says, crows can achieve their goals autonomously in the real world. In an article published in 2017, Zhu discusses how statistical models, which modern LLMs are based upon, function like "stochastic parrots." While leading two Multidisciplinary University Research Initiatives at UCLA, Zhu pursued research to make machines more crow-like, exploring the brain mechanisms that make it possible for crows—and humans—to understand the physical and social world and act accordingly.

Human intelligence evolves over time, as the body changes and experiences accrue. AGI also matures over time. To help define, evaluate, and improve AGI

PHOTO: ZHEN CHEN AND XIAOMENG GAO

development, Zhu proposed to define AGI in the mathematical space of the "CUV framework". In this framework, C is the AGI's "cognitive architecture" to think, or its simulation of the decision-making processes in the brain. U is a set of "potential functions" that represent an AGI's ability to understand and interact with its environment. V is a set of hierarchical internal "value functions" that supply the AGI's motivation. With this formulation, Zhu and colleagues can define AGI agents as points in this CUV space and characterize their learning and self-reflection processes.

To promote standardized, quantitative, and objective benchmarks for the evaluation of TongTong and other AGI agents, BIGAI researchers developed the "Tong test," which assesses an AGI agent's understanding of their world and how internal motivations relate to behaviors.

The Tong test

In Chinese, the word "general" is translated as Tong (通), a character that is also the logo of BIGAI. Artistically arranged, the character also holds the English letters "AGI." Tong Tong is the name Zhu gave to world's first AGI agent born at BIGAI, a digital Chinese girl that looks to be about 3 to 4 years old. Tong Tong is a step forward in AGI research, and researchers really want to know, "What is she thinking?" and "How is she learning and making decisions?" Researchers have long relied on tests to assess AI models. The Turing test was developed to determine whether a machine could mimic human intelligence through dialogue. ChatGPT and other AI built on big data can pass the Turing test, but Zhu wanted a test that could assess broad human intelligence. Thus, the Tong Test was born, which relies on the CUV framework.

What sets Tong Tong apart from ChatGPT is that she doesn't exist in a vacuum, but is rather embodied in a virtual world that emulates the complexity of the real physical social world. The Tong test examines an AGI's understanding of this world—its abilities—as well as the AGI's internal motivations for behaviors—its values. For example, how an AGI responds to a crying baby sitting on a floor can say a lot about its commonsense reasoning, inference of social interactions, and self-awareness. "Those natural abilities such as emotions and languages are true embodiment of human intelligence," Zhu says. "Tong Tong may be an AGI agent, but she is just like a real human child, able to understand and behave according to her own environment even if it changes. The goal of the Tong test is to build a systematic evaluation system to promote standardized, quantitative, and objective benchmarks and evaluation for AGI." And Tong Tong is just the beginning; researchers at BIGAI are developing diverse AGI agents that may someday enter the physical world through robotics and other mediums to serve society in meaningful ways.

AGI safety

As Tong Tong and the Tong test continue to grow and mature, AGI safety is front of mind for Zhu. Because AGI behavior is human-like, and not all humans are benevolent, there are risks that AGI will take actions that are not in humanity's best interests. On the other hand, AGI's cognitive architecture may be able to incorporate a mutual theory of mind—in other words, the golden rule: do unto others as you would have them do unto you.

During a panel discussion at SafeAI 2023, Zhu and Stuart Russell from the University of California Berkeley, two leading figures in AGI, had an in-depth discussion on the risks and ethics of AGI.

When Russell raised a question about how humans could keep AGI agents in check, Zhu replied, "To prevent potential threats from future AGI agents to humanity, we can gradually loosen the capability and value space of agents. It's similar to how we approach robots: initially, we confine them in a 'cage' and slowly increase their permission. Now, we already have autonomous vehicles operating on specific roads." Zhu added that once AGI agents are proven safe and controllable, they can have more freedom, with the safeguard of understanding and transparency. "If we can explicitly represent the cognitive architecture of AGI agents, understanding how they work, we will be better equipped to control them."

For Zhu, now is the beginning of a new era for AI to evolve into AGI. Zhu's doctoral advisor at Harvard, mathematician and Fields medalist David Mumford, is also an advocate of creating AIs with the top-down neural architecture of the human brain. He gave Zhu a trophy to recognize his perseverance at AGI innovation. "The future of AGI will be a combination of science and philosophy," Zhu says. "Chinese teachings of the heart are crucial to guiding AGI to obtain true beneficial human behavior."

IMAGE: ZHEN CHEN AND XIAOMENG GAO

NOMIS & Science
YOUNG EXPLORER AWARD 2025

Research at the intersection of the social and life sciences

Unconventional. Interdisciplinary. Bold.

The NOMIS & *Science* Young Explorer Award recognizes and rewards early-career M.D., Ph.D., or M.D./Ph.D. scientists who perform research at the intersection of the social and life sciences. Essays written by these bold researchers on their recent work are judged for clarity, scientific quality, creativity, and demonstration of cross-disciplinary approaches to address fundamental questions.

A cash prize of up to USD 15,000 will be awarded to essay winners, and their engaging essays will be published in *Science*. Winners will also be invited to share their work and forward-looking perspective with leading scientists in their respective fields at an award ceremony.

Apply by May 15, 2025
at www.science.org/nomis

NOMIS FOUNDATION
Creating the Spark

Science
AAAS

CONTENTS

28 MARCH 2025 • VOLUME 387 • ISSUE 6741

1348 & 1408

IMAGE: LAUREN DAUPHIN, USING LANDSAT DATA FROM THE U.S. GEOLOGICAL SURVEY AND LAKE ELEVATION DATA FROM THE BUREAU OF RECLAMATION

NEWS

INSIGHTS

LETTERS

RESEARCH

IN BRIEF

REVIEW

RESEARCH ARTICLES

DEPARTMENTS

ON THE COVER

The wildfire that swept through Altadena, California, in January burned houses and cars as well as vegetation, generating smoke that contained a complex mix of toxic chemicals. Weeks later, these chemicals still cling to the soil and remaining structures. Researchers are working intensively to understand the lingering hazards of such urban wildfires. See page 1343. *Photo: Justin Sullivan/ Getty Images*

SCIENCE (ISSN 0036-8075) is published weekly on Friday, except last week in December, by the American Association for the Advancement of Science, 1200 New York Avenue, NW, Washington, DC 20005. Periodicals mail postage (publication No. 484460) paid at Washington, DC, and additional mailing offices. The title SCIENCE is a registered trademark of the AAAS. Domestic individual membership, including subscription (12 months): $165 ($74 allocated to subscription). Domestic institutional subscription (51 issues): $2865; Foreign postage extra: Air assist delivery: $135. First class, airmail, student, and emeritus rates on request. Canadian rates with GST available upon request, GST #125488122. Publications Mail Agreement Number 1069624. **Printed in the U.S.A.**
Change of address: Allow 4 weeks, giving old and new addresses and 8-digit account number. **Postmaster:** Send change of address to AAAS, P.O. Box 96178, Washington, DC 20090–6178. **Single-copy sales:** $15 each plus shipping and handling available from backissues.science.org; bulk rate on request. **Authorization to reproduce** material for internal or personal use under circumstances not falling within the fair use provisions of the Copyright Act can be obtained through the Copyright Clearance Center (CCC), www.copyright.com. The identification code for *Science* is 0036-8075. *Science* is indexed in the *Reader's Guide to Periodical Literature* and in several specialized indexes.

PHOTO: LAJOS BERDE

EDITORIAL

Securing education's future

William F. Tate IV
is president of Louisiana State University, Baton Rouge, LA, USA.
tate@lsu.edu

How a country evaluates student performance greatly influences the views of its government and citizenry on the quality of its education system and its standing on the global economic stage. Given the impact on future prosperity, health, and well-being, regularly collecting and analyzing data on student achievement are essential for informing investments in education. In the United States, national assessments and surveys help guide this process. However, efforts to dismantle the Department of Education, the agency that manages this activity, threaten this strategic data collection, information repository, and research infrastructure.

> "...efforts to dismantle the Department of Education...threaten this...research infrastructure."

Ever since the United States Census included a question on literacy attainment in 1840, the federal government has continued to expand its education-related data collection to include mathematics, science, reading, writing, and civics. It also developed large-scale data collection to better understand the distribution of, and opportunities for, students with disabilities and those living in poverty. Implemented by the Department of Education, these efforts provide a national perspective on educational progress.

Much of the current rhetoric to eliminate the US Department of Education calls for granting individual states more authority to guide educational policies and programming. However, one of the federal government's central roles—historically implemented in part through this agency—has been its investment in monitoring educational progress and building datasets that enable researchers to study and evaluate education in the country and empower policy-makers to make evidence-based decisions. That is why the cancellation of a National Assessment of Educational Progress (NAEP) analysis last month is alarming. The NAEP—otherwise known as the "Nation's Report Card"—has evaluated the long-term trend of mathematics and reading performance of 17-year-old students since the 1970s. The decision to end this federally mandated assessment raises the question of how to best protect national data infrastructure related to education.

The Nation's Report Card uses two primary tools to measure student progress [grades K through 12 (precollege)]. The main NAEP assesses students by school grade (4th and 8th) in mathematics and reading at the national, state, and local district levels. In contrast to this biennial evaluation, the long-term trend NAEP tracks student achievement over 4-year intervals, measuring basic skills attainment in mathematics and reading at ages 9, 13, and 17. However, the trend analysis has faced setbacks. It was postponed in 2016 and 2020 because of budget constraints. Education experts have debated whether to continue examining trends, arguing that the main NAEP provides a more forward-looking standards framework and has been administered consistently.

Nowhere is the importance of the main NAEP more evident than in Louisiana. Historically, the state ranks among the lowest in the United States on educational benchmarks, struggling with both literacy and math achievement. However, recent results tell a story of progress. According to the Education Recovery Scorecard—a collaboration between the Center for Education Policy Research at Harvard University and The Educational Opportunity Project at Stanford University—Louisiana ranked second among all states in math recovery and first in reading recovery between 2019 and 2024. These estimates used methods that linked NAEP test scales with district-level state assessments, demonstrating the pivotal role that the NAEP plays in the country's research infrastructure. This academic improvement is no accident. It reflects targeted initiatives by the state, including a renewed focus on reading, tutoring, and training programs for teachers. These were state-level policy and programmatic decisions validated by a national assessment of progress. Other states such as Alabama experienced positive achievement gains as well. Without the main NAEP—and the investments of social scientists tracking its data—this progress would have been invisible.

The future of assessment programs, statistics and indicator systems, and federally funded research in the education arena in the United States will depend on decisions by the Administration and Congress. Although the situation is currently volatile, this moment may be an opportunity to strengthen and reimagine the federal role in monitoring academic attainment and performance. Ensuring robust, nationally scaled research and evaluation in the field of education remains possible. By acting now with circumspection and foresight, the United States can secure this critical infrastructure.

–William F. Tate IV

Published online 20 March 2025; 10.1126/science.adx5381

NEWS

> “No executive order is going to change a single word in our values, a word of our mission.”
>
> **American Physical Society external affairs chief Francis Slakey**, at a town hall session at last week’s Global Physics Summit. He affirmed the society’s commitment to fostering diversity, equity, and inclusion, following President Donald Trump’s executive order banning federal support for such policies.

IN BRIEF

Edited by
Jeffrey Brainard

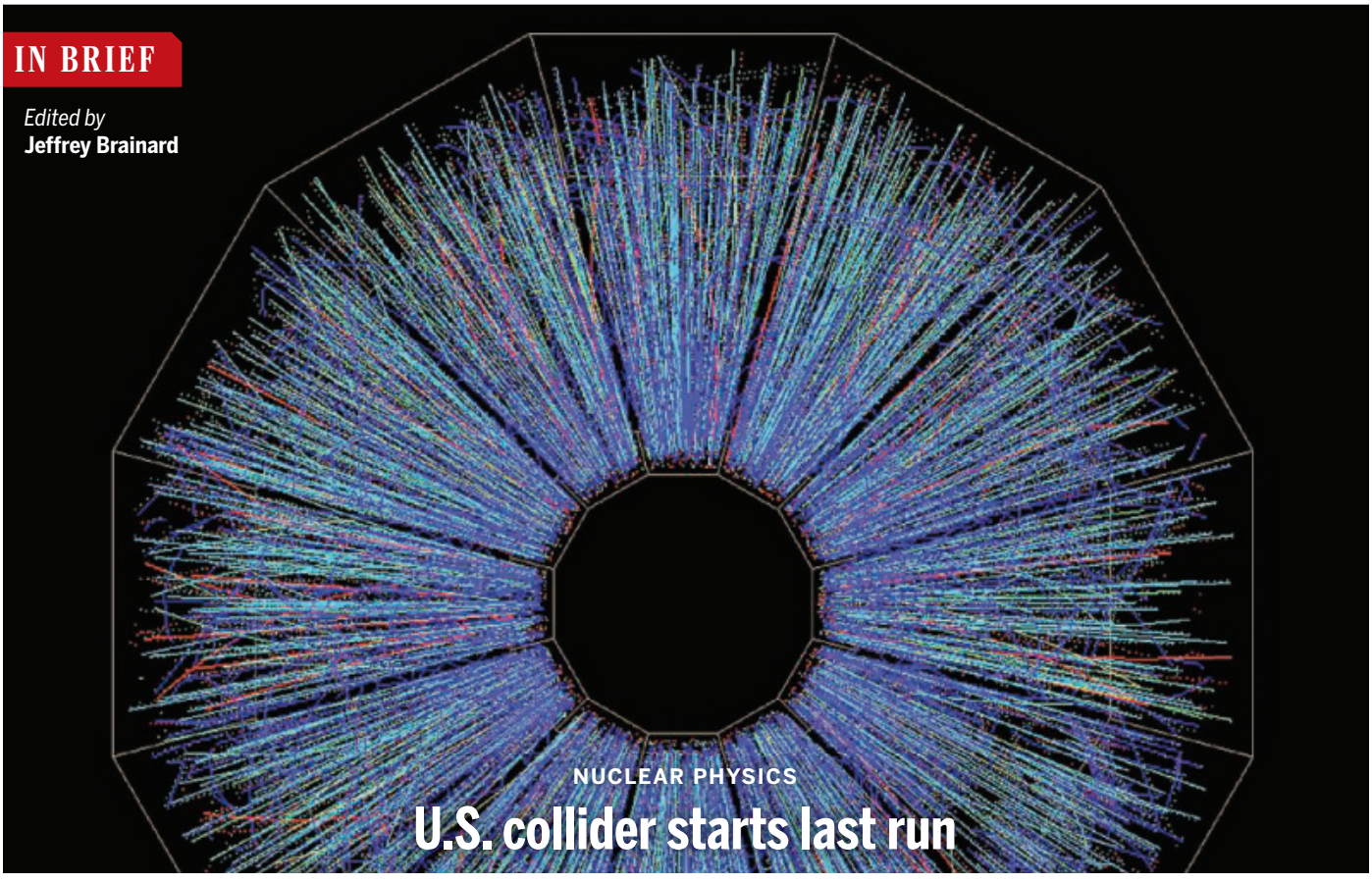

NUCLEAR PHYSICS

U.S. collider starts last run

Particles (above) gush from a collision of gold nuclei inside a detector called STAR at the Relativistic Heavy Ion Collider.

The United States’s only major particle collider this week began its 25th and final run, embarking on months of study of a soup of fundamental particles called quarks and gluons resembling the one that filled the newborn universe. In 2000, the Relativistic Heavy Ion Collider (RHIC) at Brookhaven National Laboratory began smashing counter-circulating beams of gold nuclei and soon blasted out such a quark-gluon plasma—an accomplishment some think worthy of a Nobel Prize. Physicists went on to study the odd plasma, showing it changes from a more gaslike phase to a more liquidlike one at lower temperatures. Later, researchers smashed protons to probe how their spin originates among the quarks and gluons within them. During RHIC’s last hurrah, scientists will again smash gold and study the quark-gluon plasma in unprecedented detail using the upgraded sPHENIX particle detector. Afterward, RHIC will be partially dismantled and a $2.8 billion Electron-Ion Collider, to power up in the 2030s, will fill its 3.8-kilometer-long tunnel.

IMAGE: BROOKHAVEN NATIONAL LABORATORY. CC BY-NC-ND 2.0

Early galaxy contained oxygen

ASTRONOMY | Oxygen has been detected in the earliest known galaxy, observed as it appeared when the universe was 2% of its current age. The element’s presence is a surprising finding so soon after the Big Bang. The first stars, made from only hydrogen and helium, formed heavier elements such as oxygen as they burned or when they exploded. But that process was thought to take millions of years even in the fastest burning stars. Two research teams independently detected plentiful oxygen in the JADES-GS-z14-0 galaxy using the Atacama Large Millimeter/submillimeter Array in Chile, they reported last week in *Astronomy & Astrophysics* and *The Astrophysical Journal*. The oxygen’s presence suggests generations of stars must have lived and died very rapidly to have

created so much so soon, deepening the mystery of how the first galaxies evolved.

23andMe files for bankruptcy

BIOMEDICINE | A powerful database for human genetic research hangs in limbo after the DNA testing company 23andMe announced on 23 March it had filed for bankruptcy. Under a court-supervised sale process, genome information from the company's roughly 15 million users, along with associated information on their diseases and other personal details, could change hands and may no longer be subject to the company's current privacy policies. It's not yet clear what 23andMe's sale would mean for the academic and industry scientists who have collaborated with the company and relied on its data for research on human health and evolution. These studies have examined the role of genetics in sexual orientation, diseases such as Parkinson's, and susceptibility to COVID-19 and Long Covid, for example. Last week, responding to securities filings from 23andMe indicating financial trouble, California Attorney General Rob Bonta issued a consumer alert asking Californians to consider having the company delete their genetic data and destroy samples of genetic material to protect their privacy. Users elsewhere can also delete their data by logging into their accounts on the company's website.

Sharks emit mysterious clicks

ANIMAL BEHAVIOR | Whales sing and sea turtles croak undersea, but sharks have been seen as the strong, silent type—until now. Researchers report this week in *Royal Society Open Science* the first evidence that certain sharks make clicking noises intentionally, although they can't fully explain why. The team made the discovery while testing the hearing of captive sharks. The clicks came from a kind of hound shark called a rig (*Mustelus lenticulatus*). More than 1000 species of bony fish grunt, moan, and bark, but cartilagenous fishes such as sharks are quieter. Researchers suspect the sounds may be defensive; an earlier study of a captive cownose ray found that when prodded, it clicked and showed defensive behaviors such as raising its barbed tail. Like rays, rig sharks may make the noise by snapping their flat rows of teeth, which are blunt for crushing prey. The sharks can hear mostly low-frequency noise, and the clicks they emit are higher pitched, which suggests they are not used for communicating with other rigs.

PHOTO: MATTHEW MODOONO/MUSEUM OF SCIENCE, BOSTON

TRUMP TRACKER

CDC NOMINEE President Donald Trump said this week he plans to nominate Susan Monarez, acting director of the U.S. Centers for Disease Control and Prevention, to lead it permanently. She is an infectious disease researcher who has supported use of the COVID-19 vaccines, a view at odds with statements by Health and Human Services Secretary Robert F. Kennedy Jr. Monarez was also deputy director of the Advanced Research Projects Agency for Health, created under former President Joe Biden to fund high-risk research; Trump's administration fired most of its staff.

NIH GRANTMAKING OBSTACLE EASES The Trump administration has lifted a freeze on advisory council meetings that has held up grantmaking at the National Institutes of Health. Its 27 institutes normally hold council meetings three times a year, but the administration suspended scheduling them during a communications pause. At least 13 such meetings are now set for April and May. The pause created a backlog of proposals and delayed more than $1.5 billion in grants that ordinarily would have been disbursed by now.

DELAYED AID PAYOUTS The administration last week said it will need until late April to complete more than 10,000 outstanding payments to nongovernmental organizations and contractors working with the U.S. Agency for International Development (USAID). The payments, some of which are owed to organizations running clinical research, have been ordered by a judge. In a court filing, the government, which in January froze nearly $2 billion in foreign aid, says it cannot move faster because it lacks complete documentation from some funding recipients—a claim disputed by plaintiffs suing the administration. Many payments may arrive too late: The government has terminated more than 80% of USAID grants, forcing numerous organizations to shut.

CLIMATE AUTHORS SOUGHT To fill a void left by the Trump administration's opposition to international agreements on climate change, a group of universities and the American Geophysical Union last week stepped in to help recruit authors for the next major assessment of climate science by the United Nations's Intergovernmental Panel on Climate Change (IPCC). The U.S. Department of State had led the process. Instead, the recently formed U.S. Academic Alliance for the IPCC will accept and forward nominations until 4 April; final author selections are made by the panel itself.

MUSEUMS CHOPPED? A key source of federal support for science museums could disappear. Trump has proposed dismantling the U.S. Institute of Museum and Library Services (IMLS) because he believes it is "unnecessary." Some $55 million of the institute's $295 million annual budget goes for competitive awards to museums. Those can be a lifeline for small museums such as The Science Zone, based in Casper, Wyoming, which used a $50,000 grant to offer an exhibit, FlexCart, about electrical circuits and rocketry and share it with libraries in small towns across Wyoming.

An interactive exhibit at the Museum of Science in Boston, which has received IMLS grant funding.

The STOP Spillover project, now terminated, tested rodents in Liberia for the Lassa virus.

PHOTO: BRUNO GHERSI/STOP SPILLOVER

GLOBAL HEALTH

U.S. cuts hamper disease surveillance worldwide

Many efforts to prevent outbreaks and track diseases are suddenly in limbo

By **Jon Cohen**

A project to track and contain menacing animal viruses across seven countries, from avian influenza in poultry to Lassa virus in rodents, ended with a single email. In late January, Jonathon Gass, an epidemiologist and virologist at Tufts University, was about to leave for Bangladesh to close out an effort to monitor and combat avian influenza, when the emailed letter arrived from the U.S. Agency for International Development (USAID), ordering an immediate halt to work on the $100 million STOP Spillover project. Gass, a co–deputy director of the project, stayed in Massachusetts and started to call staff around the world to tell them to drop everything. One colleague monitoring Lassa virus in Liberia was driving to a field site. "I had to tell him that he needed to turn the car around, come back, and book a plane ticket home," Gass says.

STOP Spillover, launched in 2020 as a consortium led by Tufts, is one of many global disease surveillance and response efforts that have ground to a halt since President Donald Trump took office. January's stop work order, which came in the wake of an executive order freezing all foreign aid, was followed by terminations of thousands of USAID grants that left projects in limbo or forced them to shut down. Grant holdups are also jeopardizing surveillance funded by other agencies. It's a dangerous development, scientists say. "Surveillance is important to understand what set of threats are out there and how they change," says virologist David Wang of Washington University in St. Louis. "In the absence of that, there are going to be more sick people, more wasted efforts trying to treat them, and lots of less efficient health care."

The full scope of the cuts is still unclear, and legal challenges against them continue. Making sense of the chaos "is more challenging than trying to understand what's going on with the damn diseases themselves," says epidemiologist Michael Osterholm, who heads the University of Minnesota's Center for Infectious Disease Research and Policy and has advised several past administrations. But it's clear that the list of affected diseases is long.

The sudden termination of STOP Spillover's USAID award meant all its programs were left hanging, whether they had lots of work remaining or were a few meetings away from completion, says Felicia Nutter, a co–deputy director of the project and a wildlife veterinarian and epidemiologist at Tufts. In Liberia, for example, researchers are trying to figure out what to do with a freezer full of blood samples from people who agreed to be tested for exposure to viruses such as Lassa and Ebola. The in-country team was about halfway through testing those samples, but now, "we're unable to actually return the results to those research participants," Gass says. "This is important work that tells us about the circulation of viruses that have pandemic potential. … It's pretty unbelievable."

The pauses also threaten to leave researchers blind to new threats. Wang is one of the principal investigators in an $82 million program funded by the U.S. National Institute of Allergy and Infectious Diseases (NIAID) that watches for emerging viruses with overseas collaborators. In Nepal, about 75% of acute encephalitis cases have no identified cause, he notes, but last year, the team detected a possible culprit: a novel Gemykibivirus found in one patient and in stored samples from 12 others. In the United States, the team is searching for the recently discovered Bourbon virus—which causes fever, nausea, and vomiting—in ticks and people in Missouri.

Now, Wang says, "Everything is in limbo" because of disruptions in the grant process.

Several of the nine centers in the network have resubmitted grant applications to keep their programs running beyond 30 April, but NIAID has paused meetings of the advisory councils that must approve funding. "There's massive consternation as to what will happen," Wang says.

Surveillance for HIV is in jeopardy as well because the Trump administration has paralyzed the President's Emergency Plan for AIDS Research (PEPFAR), which funds not only treatment, but also millions of HIV tests every year that help scientists gauge the spread of the virus. "We are going to lose the ability to understand what is happening to HIV," says epidemiologist Chris Beyrer, who heads the Duke Global Health Institute. "Already it's clear that the 2025 data will have to have a significant asterisk."

PEPFAR also contributes to detection of tuberculosis (TB), the main cause of death in people with AIDS. That activity is further threatened by drastic cuts to USAID-funded programs specifically for TB—some $178 million, according to an estimate by the Center for Global Development. "The potential collapse of the global TB monitoring system risks the loss of data and trends that are essential to inform the TB response across all levels," says Tereza Kasaeva, director of the Global Programme on Tuberculosis and Lung Health at the World Health Organization (WHO).

Making matters worse, U.S. government scientists have been barred from speaking to colleagues at WHO, which oversees global surveillance for HIV/AIDS, TB, and influenza and coordinates efforts to control malaria, polio, cholera, hemorrhagic fevers, and mpox. "When there was the suspected outbreak of Ebola in the [Democratic Republic of the Congo] a few weeks ago, CDC couldn't call them and ask what's going on," says epidemiologist Jennifer Nuzzo, who heads the Pandemic Center at Brown University. Just last week, *Science* has learned, a leading government influenza researcher who asked not to be named was not allowed to present at a WHO meeting on the current spread of that virus. The Trump administration's plan to leave WHO, effective January 2026, could make monitoring diseases even harder.

Surveillance networks take years to build, but quickly come crumbling down without support, says Martin Cetron, who led CDC's Division of Global Migration and Quarantine for more than 2 decades before retiring in 2023. "So much of our surveillance systems involve really critical relationships with partners, both domestic and international," Cetron says. "Now, we're turning the clocks back." ■

With reporting by Catherine Offord.

PLANETARY SCIENCE

Mars rover detects long-chain carbon molecules

Fatty acid byproducts that Curiosity found in an ancient lakebed could be the remains of microbes—or not

By **Paul Voosen**

NASA's Curiosity rover has detected what could be a chemical relic of long-ago life on Mars: long-chain organic molecules. Found after painstaking reanalysis of data on a sample drilled from a lake that dried up billions of years ago, the molecules likely derived from fatty acids, a common building block of cell membranes on Earth. The finding, published this week in the *Proceedings of the National Academy of Sciences*, is not a definite detection of past life; the fatty acids could also have formed without life. But it's another in a series of tantalizing hints.

"This is an amazing result," says Monica Grady, a planetary scientist at the Open University who wasn't involved in the new research. If these are "breakdown products from carboxylic acids, then we are seeing something very exciting indeed." It also suggests Curiosity's successor, the Perseverance rover, will find similar molecules, says Jack Mustard, a planetary scientist at Brown University. Perseverance is now collecting samples for an ambitious effort to return Mars rocks to labs on Earth, where scientists will be able to reach more definitive conclusions on the molecules' origins.

Since landing in 2012, Curiosity has traveled more than 21 kilometers in Gale crater and up the slopes of Aeolis Mons, aka Mount Sharp, the 5000-meter mountain at the crater's center. Early on the rover showed that a lake with habitable conditions existed at Gale more than 3 billion years ago. It has since spotted other potential signs of life: goopy organic macromolecules that seem to resemble kerogen, the source material of oil, and an enrichment in a "light" carbon isotope that, on Earth, is indicative of life. "Mount Sharp keeps on giving and the rover keeps on going," says Ashwin Vasavada, Curiosity's project scientist at NASA's Jet Propulsion Laboratory.

The latest result comes from a mudstone sample called Cumberland that the rover drilled in 2013, less than a year into its journey, and then analyzed in its onboard chemistry lab, the Sample Analysis on Mars (SAM) instrument. In 2015, the

PHOTO: NASA/JPL-CALTECH/MSSS

Grit drilled from this martian mudstone in 2013 yielded molecules that have tantalized astrobiologists.

scientific team reported preliminary signs of long-chain organics in the sample. But that result fizzled out, as they weren't able to identify the molecules and rule out the possibility that they might be contaminants from Earth. "It's been a long journey to this point," says Daniel Glavin, an astrobiologist at NASA's Goddard Space Flight Center and co-author of the new paper. "This is really searching for a needle in a haystack."

Curiosity analyzes rock samples by drilling them into grit, which it then decants into quartz cups inside SAM. The cups are baked at temperatures up to 1100°C, and the resulting gases are identified with a gas chromatograph-mass spectrometer. But SAM isn't the equal of a terrestrial lab.

"The SAM data, it's a mess," says Caroline Freissinet, who led the new study and is now a planetary scientist at the French Laboratory for Atmospheres, Observations, and Space. To help make sense of it, researchers run experiments with a twin of the instrument, housed on Earth in martian conditions.

In 2016, a search for complex organic molecules on a saved batch of Cumberland mudstone again seemed to come up dry. But several years later, Freissinet returned to the results from the 2016 experiment. This time, with more tests from SAM's twin to guide her, she noticed three blips that she and her colleagues had missed previously. After several months, she realized the blips pointed to three varieties of alkanes, organic molecules that string together carbon and hydrogen in a line: decane, undecane, and dodecane, which have 10, 11, and 12 carbon atoms, respectively. There wasn't a huge amount of any of them, but they were there, in the parts per billion.

Alkanes on their own are not particularly durable, and the SAM team suspected that, prior to baking, the alkanes had carbon dioxide attached on one end, making them carboxylic acids—or fatty acids, as they're typically called. Using SAM's twin, they mixed a small amount of long-chain carboxylic acid into a clay-rich soil meant to mimic Cumberland, and baked it. Sure enough, alkanes were produced—just as seen on Mars—with a bloom of carbon dioxide at the same time.

Still more work was needed to rule out other sources for the alkanes. Since Curiosity landed, SAM has been plagued by solvent leaking from one of the vials it uses, in separate experiments, to extract organics from martian dirt. Yet no alkanes were produced when the team repeated the experiment on an empty cup in Curiosity, and none were found when Curiosity drilled at another site with similar characteristics, called Rock Hall. Both tests seemed to eliminate stray solvent as the source. The team also ruled out contamination from the lubricant used on the drill.

In the end they convinced themselves they had emerged from the martian haystack with a real find. "There's no question about it," Glavin says. "We have three needles."

The question now is how those three alkanes got there. The enzymes that build fatty acids on Earth do so two carbon atoms at a time, meaning a predominance of even-numbered molecules indicates a living origin. Just one of the three alkanes detected by SAM, the undecane, would have come from an even-numbered fatty acid, and it is just slightly more abundant than the others. "As amazing as this is, you can't say for sure one way or another whether these are biological products," says Chris Herd, a geologist at the University of Alberta who wasn't involved in the new study.

If these are "breakdown products from [fatty] acids, then we are seeing something very exciting."
Monica Grady, Open University

Meteorites carry cargoes of fatty acids that come not from life, but from chemical reactions in the early Solar System, and they could have easily doused the surface with fatty acids early in martian history, says Eva Scheller, a planetary scientist at the Massachusetts Institute of Technology. Or the acids could have evolved on Mars from the kerogenlike particles that Curiosity detected—which might themselves be abiotic in origin.

Although many researchers figure the origin of these molecules won't be resolved until samples can be analyzed on Earth, Freissinet is not so sure. Cumberland was such an exciting early find that the team collected two "doggie bags" of it for later analysis. They used the first in their original research, but the second remains untouched. The SAM team is now exploring whether its onboard lab could detect a wider range of alkanes, perhaps down to a length of six carbons. If so, she says, "we might be able to find a real trend of even versus uneven carbon."

But they only have one more shot at it. So far, no Curiosity drill site has been quite as promising as Cumberland, and the rover, whose power supply is dwindling after 13 years on Mars, has no chance of returning to it now. "This last sample," Freissinet says, "has to be perfect." ■

QUANTUM PHYSICS

Furor over quantum computing claim heats up

Physicists cast doubt on measurements said to show Microsoft chip uses exotic Majorana quasiparticles

By **Zack Savitsky**

On 18 March in an Anaheim, California, conference hall, Microsoft physicist Chetan Nayak faced a formidable challenge: convincing a standing-room audience of other scientists that his company had shaken the landscape of quantum computing. Nayak tried to make the case that his team had created the world's first "topological" qubit, a robust quantum analog of the 0-or-1 bit used in conventional computers. Doing so would require not only conjuring the Majorana quasiparticle—a long-sought mode of electron behavior—but also controlling multiple Majoranas to encode quantum information.

Many audience members, however, weren't sold. "I don't think the data are convincing," says Jelena Klinovaja, a physicist at the University of Basel who attended Nayak's talk at the American Physical Society's (APS's) Global Physics Summit.

The claims received a similarly frosty reception at a talk the day before at the same meeting, when University of St. Andrews physicist Henry Legg—the author of two preprints challenging Microsoft's work—declared that "any company claiming to have a topological qubit in 2025 is essentially selling a fairy tale."

For his part, Nayak remains confident that his team has tamed the Majoranas. "We've only revealed a tiny fraction of what we've done," he tells *Science*. "It's going to look more and more convincing that this is going to be the basis of a technology."

The furor began last month, when Microsoft proclaimed via a press release and a paper in *Nature* that it had achieved a breakthrough: a chip hosting eight Majorana-based topological qubits, which

it says could yield utility-scale quantum computers in a matter of years. Quantum computing stocks soon rose, and Senator Ted Cruz (R–TX) touted the news on the Senate floor. In a social media post, Microsoft CEO Satya Nadella suggested the chip "could be quantum's transistor moment."

Microsoft's paper, however, didn't detail the chip or provide proof of Majoranas, focusing instead on a method for measuring certain quantum properties of a future device. Outraged by what they deemed to be hype, many physicists responded by posting fiery comments, barbed memes, and livestreamed takedowns online.

"I've never seen anything like this in my time in physics," says Jason Alicea, a physicist at the California Institute of Technology. "The burden is on [Microsoft] to really show that what they have is the real deal."

For decades, scientists have dreamed of better simulating nature and solving certain problems much faster by building computers that operate not on conventional bits—which can be set to either 0 or 1—but rather on qubits, which can be set to combinations of 0 and 1 simultaneously. But today's quantum computers remain stifled by their qubits' fragility to environmental noise.

Microsoft is trying to build qubit protection directly into its hardware by making qubits out of Majoranas, which are essentially delocalized electrons. Because the electrons don't exist in any one location, their information can be protected "topologically" from any local disturbances under the right conditions.

Microsoft's chip features ultrathin, superconducting indium-arsenide wires that force the electrons inside to form loose pairs. Each wire can also accommodate an extra unpaired electron, which effectively splits in half to occupy a Majorana at each end of the wire. A given wire's two "parity" states—which would represent a 0 or 1 in a future computer—correspond to whether the wire contains an even or odd number of electrons. By measuring the chip in specific ways, Nayak's team plans to shift and probe the wires' parity states, thereby encoding and reading out quantum information.

To better define their search for the elusive Majoranas—whose discovery has been claimed and then debunked multiple times—Microsoft researchers devised a protocol in 2021 that tests whether a device can host the quasiparticles. The protocol consists of a computer simulation of their device they trained to identify Majorana-forming states. They then fed real measurements of the device into the same protocol to assess its state.

In 2023, Nayak's team claimed to have built a device that passed the protocol; the new paper, published in *Nature* on 19 February, establishes a procedure for reading out the parity of the device's nanowires. Microsoft claimed these results, along with new data hinted at in a press release, constituted "the world's first quantum processor powered by topological qubits."

Of the researchers who consider Microsoft's claims overblown, Legg has been among the most forceful critics. A week after the company's February announcement, he posted his first public challenge: a preprint that sharply criticized the reliability of Microsoft's protocol for identifying Majoranas. "They have some explaining to do," he says.

By digging into the protocol's available code, Legg noticed that simply changing the measured ranges of a device's different parameters, such as its magnetic field, appears to affect whether the device passes the protocol. Within each Microsoft experiment, Legg tells *Science*, the code used to evaluate real data also seems to be less restrictive than the code used for simulated data. And in another preprint posted on 11 March, Legg argues that raw data in Microsoft's latest paper appear too disordered for the company's device to have been harboring Majoranas.

In a 15 March LinkedIn post, Microsoft researcher Roman Lutchyn defended his team's work, claiming the protocol's sensitivity was expected and that the two versions of code yielded statistically similar outputs. During the Q&A session of Legg's APS talk, Lutchyn issued his own challenge to Legg: "If you have a better idea, put forward a protocol, and then let's all follow it."

In his packed APS talk, Nayak unveiled a device that combines two nanowires into an H-shaped array that's meant to demonstrate a functioning qubit. He then showed data describing the nanowires' ability to exist in two distinct states that are complex combinations of 0 and 1, essential for the device to operate as a qubit.

Some in the audience were impressed by the engineering advances behind the double-nanowire device—but the new measurements were also met with skepticism. The data suggested a single nanowire would hold the 0 or 1 state for up to 10 milliseconds. However, the measurements Nayak presented for more complex states were far less clear. Statistical analysis suggested the complex states persisted for a few microseconds at a time. To some physicists in attendance, though, the data looked more like noise.

"I would have loved for this to come out screaming at me that there's only two [distinct] states," says Cornell University physicist Eun-Ah Kim, who moderated the session. "But that's not what I think I see."

Despite many physicists' qualms over Microsoft's current evidence for a topological qubit, some, including University of Oxford physicist Steve Simon, remain hopeful: Recently, Simon bet Legg a Belgian beer that *Nature* won't retract Microsoft's paper in the next 2 years.

But for others such as Anton Akhmerov, a physicist at the Delft University of Technology, the overriding feeling is one of frustration—with both Microsoft's sensational announcement and the backlash to it. "The problem is that both sides are making confident claims … and I don't think either viewpoint is justified," Akhmerov says. "It'd be nice if people would chill out a bit." ■

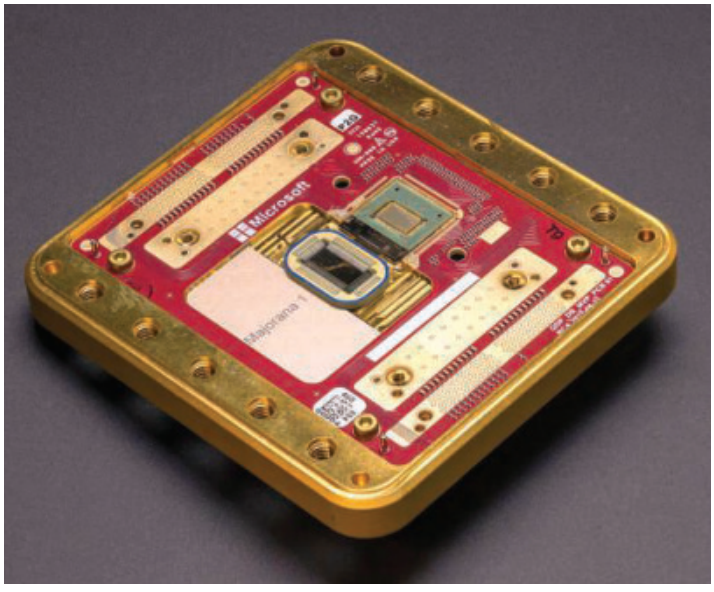

In February, Microsoft unveiled its Majorana 1 processor, a quantum computing device it claims contains eight highly robust "topological" qubits.

PHOTO: JOHN BRECHER/MICROSOFT

With reporting by Adrian Cho. Zack Savitsky is a science journalist currently based in Berlin.

CONSERVATION BIOLOGY

In Mexico, a whale of a controversy over gas port

Researchers want better studies of how planned LNG terminal would affect marine life

By **Alexa Robles-Gil**

Six years ago, biologist Lorena Viloria Gómora was aboard a boat in the Gulf of California off Mexico's west coast, attaching satellite tracking tags to fin whales, when the water came alive. Some 100 fin and endangered blue whales began to feed nearby, their backs breaking the surface. The remarkable scene, which unfolded near the small coastal town of Puerto Libertad, highlighted that these waters are "an idyllic, quiet area for whales," says Viloria Gómora, who works at the Autonomous University of Baja California Sur (UABCS).

Now, Viloria Gómora and other scientists fear that quiet will be shattered by one of the largest energy projects ever proposed in Mexico: a massive liquefied natural gas (LNG) terminal, to be built in Puerto Libertad. To move the LNG to markets abroad, huge tankers would routinely sail through waters that whales use for feeding, breeding, and migration, threatening them with deadly collisions.

"I'm worried," says whale researcher Jorge Urbán of UABCS, one of many researchers in Mexico opposing the $15 billion project, to be completed by the end of this decade. If the terminal is built, he says, "we are going to regret it a lot."

Last month, Mexico's environmental permitting agency announced it was putting the terminal on hold while it reviewed five legal challenges, known as *amparos*, filed by individuals and environmental organizations. Among the complaints: flaws in assessments of the project's environmental impacts. "There are many gaps, errors, and serious inaccuracies," asserts Viloria Gómora, who together with Urbán and another UABCS colleague wrote a technical critique of the assessments that was released in January.

The pause marks the latest twist in a nearly 2-decade-old effort to build an LNG terminal in Puerto Libertad. The town lies near the head of the Gulf of California, once known as the Sea of Cortez. The narrow, 1100-kilometer-long body of water is one of the world's marine mammal hot spots. It is home to 36 species of cetaceans, including the highly endangered vaquita porpoise as well as one of two known groups of "resident" fin whales, which live there year-round.

The terminal was originally designed to import gas into Mexico, and in 2006 Mexico's

Risky passage A project to send liquefied natural gas (LNG) from West Texas through Mexico to Asia via a pipeline and tankers sparked protests in Mexico City (top). The ships would traverse prime whale habitat in the Gulf of California (bottom), risking collisions.

CREDITS: (PHOTO) GUSTAVO GRAF; (MAP) M. HERSHER/*SCIENCE*; (DATA) MEXICO PACIFIC; ONEOK INC.; HP CONSULTORES AMBIENTALES; UNITED STATES ENERGY INFORMATION ADMINISTRATION

government approved an environmental impact assessment (EIA) of the facility as part of its permitting process. But the import terminal was never built, and the 2006 EIA "describes a project very different from the current" one, wrote Viloria Gómora and her co-authors. In 2018, Mexico Pacific, a U.S.-based firm, took control and changed the design to an export terminal, three times bigger, that is now part of a larger plan called Saguaro Energía. It would use an 800-kilometer-long pipeline and a fleet of tankers to move up to 2.8 billion cubic feet of natural gas per day from wells in Texas, through Mexico, and then across the Pacific Ocean, primarily to Asia. In 2023, the company gave Mexican regulators an outline of its plan for limiting the facility's environmental impact.

Critics of the project say both the original EIA and the new plan understate the project's risks to marine life. The assessments lack the detailed, up-to-date information needed to realistically assess collision risks, the critics say, including fine-scale maps of actual tanker routes and data on whale distribution. The assessments are also silent on another issue, researchers say: the potential impact of noise pollution created by the ships. Previous studies, they note, have shown ship noise can alter whale behavior; in the gulf, scientists have found that humpback whales sing less in areas with more ship noise.

In November 2024, such issues prompted the International Union for Conservation of Nature (IUCN) and the Mexican Society of Marine Mastozoology to write to Mexico's environmental regulator, raising those concerns. IUCN questioned whether the proposed site was "suitable" given its proximity to key whale habitat, and the zoologists warned the project would cause "immeasurable" harm to cetaceans.

At a minimum, opponents of the terminal say the government should require updated environmental studies before deciding whether the project can move forward. (Mexico Pacific declined to answer detailed questions about the project.)

It's not clear when Mexico's environmental agency will decide how to respond to the *amparos*. (The Mexican government did not respond to a request for comment.) And even if the agency approves the terminal, it's not certain the company can raise the billions needed to launch Saguaro Energía.

In the meantime, terminal opponents, led by a group called Conexiones Climáticas, have launched a "Whales or Gas?" campaign to build public opposition to the project. And the waters off Puerto Libertad remain tranquil. During a recent visit, a pod of dolphins circled fish not far from the proposed LNG terminal as a lone humpback on its way to a breeding ground surfaced just offshore. ■

PHOTO: PHILL MAGAKOE/AFP VIA GETTY IMAGES

BIOMEDICAL RESEARCH

South Africa caught in new tsunami of NIH grant cuts

Agency moves to terminate nearly 1000 projects, including many involving "DEI" and LGBTQ health

By **Jon Cohen** *and* **Sara Reardon**

A threat hanging over South African HIV/AIDS researchers for days has become a reality: President Donald Trump's administration on 21 March began terminating or putting on hold South Africa's grants from the U.S. National Institutes of Health (NIH). The cuts appear in part linked to an escalation of NIH efforts to terminate grants touching on topics such as diversity, equity, and inclusion (DEI) and LGBTQ health.

"This is going to cut deep," says HIV clinician Ian Sanne, a principal investigator of a terminated $2.5 million grant to the University of the Witwatersrand (Wits) Research Group Clinical Unit, which participates in international human trials of HIV and tuberculosis (TB) medicines. Sanne and others had been bracing for the cuts after learning of a 12 March email from NIH's acting director asking staff to compile lists of South Africa–related grants. He notes that the grant's termination puts volunteers who are in ongoing trials at risk. "Is this compliant with international standards of human ethics?"

Clinical trials in South Africa have played central roles in evaluating new anti-HIV drugs.

Several of Trump's executive orders—including some that mention DEI and another blocking U.S. aid to South Africa in part because of alleged discrimination against white farmers—might be driving the terminations. But a memo obtained by *Science* directs NIH program officers not to mention the executive orders, several of which have been temporarily blocked by judges, in communications with researchers.

A letter terminating the grant to Wits gives no specific reason, but says it "no longer effectuates agency priorities." It states that DEI "studies are often used to support unlawful discrimination on the basis of race and other protected characteristics, which harms the health of Americans."

"Our work has nothing to do with DEI and everything to do with global health security" through studying diseases "that know no borders," Sanne says.

The memo directs NIH to quickly terminate 945 specific grants, many of which support research outside South Africa. Multiple researchers have told *Science* their grants related to LGBTQ health inside the United States were also terminated on 21 March. The cuts follow previous terminations of grants involving diversity, transgender health, and vaccine hesitancy, among other topics. The memo also said all new and renewable grants with money going to South Africa and China are on hold.

Glenda Gray, an HIV/AIDS researcher at Wits and chief scientific officer of South Africa's Medical Research Council, received notice that her own $3.1 million grant for a clinical trial unit in Soweto has moved from an approved to a pending status. She notes that South Africa, which has more people living with HIV than any other, has played a pivotal role in clinical trials that helped anti-HIV and TB drugs win approval. It has also shaped international guidelines about the most effective ways to use them.

According to a back-of-the-envelope calculation Gray did, South Africa receives about $250 million a year from NIH for medical research, three times what the government there invests. "If you take this away, you take away scientists, doctors, nurses, laboratories, fundamental science, basic science, clinical science, supervisors for Ph.D.s and masters, and postdocs. You basically abolish medical research in South Africa."

But she stresses that the cuts reach far beyond South Africa. "It appears that no institution and no country is being spared," Gray says. "This is an orchestrated assault on NIH-funded science." ■

INFLUENZA

How did cow flu start? Scientists still don't know

One year later, how H5N1 spills over into dairy cattle—and how often—remains a mystery

By **Kai Kupferschmidt**

When U.S. Department of Agriculture (USDA) officials reported on 25 March 2024 that the H5N1 avian influenza virus had infected dairy cattle in Texas and Kansas, it seemed a freak event—a rare confluence of factors that somehow allowed a bird virus to infect cows.

But 10 months later, on 31 January, USDA said it had detected another jump to cattle, this time in Nevada. And 2 weeks later, another one, in Arizona.

One year into the United States's cow flu outbreak, many important questions remain unanswered, including how the virus is spreading from one farm to the next. But perhaps the most basic one is how it manages to get into cattle in the first place—and how often that happens. Knowing the answers is "really important," says Thijs Kuiken, a wildlife pathologist at Erasmus University Medical Center, because "then you can change the system so that it doesn't happen again."

The answers also matter for efforts to control the current outbreak. If the first spillover had been a fluke, stopping infections—for example through extensive testing and rigorous quarantine and isolation measures—might have put the genie back into the bottle. But the repeated introductions suggest outbreaks will continue to occur. They also raise fears that persistent cattle infections could allow the virus to change—by mutating or recombining with another flu virus—to spread efficiently in humans and spark a pandemic.

"I think this sort of changes the whole ecology," says bird flu researcher Richard Webby of St. Jude Children's Research Hospital. "From a dairy industry perspective, this, to me, signals that they're in it for the long term." He says the U.S. government needs to do more to monitor and contain the virus, and that cattle may need to be vaccinated to control the outbreaks. Otherwise, "We're going to be playing whack-a-mole," says evolutionary biologist Michael Worobey of the University of Arizona.

The H5N1 infections in cows were the latest surprise move of a highly pathogenic avian influenza strain called clade 2.3.4.4b that has ravaged wild bird and poultry populations since 2020. It soon became clear the virus was confined to the udders of lactating dairy cows. Initially, Worobey and others speculated a particular set of mutations in the viral genotype, named B3.13, might have made the jump possible. But veterinary virologist Martin Beer and colleagues at the Friedrich Loeffler Institute showed that inoculating cow udders with a different version of H5N1 from European birds also led to infection. And the spillovers announced in January and February were both with yet another genotype called D1.1.

If cows are easily infected, it's puzzling that spillovers have not been reported from Europe, where H5N1 outbreaks in poultry and wild birds have gone on much longer. Jürgen Richt, a veterinarian at Kansas State University, believes spillovers probably do occur on the continent, but that differences in farming practices prevent them from resulting in large outbreaks. More than 50,000 lactating milk cows were moved between U.S. farms every week before the outbreak, he says, in part because cattle operations are much larger and often span several states. "That doesn't happen in Europe and it makes a huge difference."

> **"I think we have really underestimated this pathogen and haven't made the strides that we needed to in a year."**
>
> **Seema Lakdawala,** Emory University

Kuiken agrees: "There appears to be something different between the U.S. dairy industry and the dairy industry of other countries that allows this to happen."

A surprising new infection supports that view. On 24 March, U.K. officials announced that recently introduced testing of livestock at properties with infected birds has picked up an H5N1 infection in a sheep—the first ever in that species. Other sheep in the flock were not infected. Details are sparse, but "it fits with the idea that such spillovers occur more frequently, but don't lead to extended outbreaks," Kuiken says.

On the other hand, if Europe has the occasional spillover into cattle, some cows there would have antibodies against H5N1, a sign of past infection. Testing in thousands of cows in Italy, Germany, Sweden, Norway, the United Kingdom, and the Netherlands has not found antibodies or active infections. If spillover is happening in Europe, "it must be a very rare event," Beer concludes.

He thinks it is more common in the U.S. because the poultry outbreak there, though it lagged Europe's, is now much larger. "There is a huge viral pressure," Beer says. More than 160 million poultry birds have been killed by H5N1 or were culled since late 2021, far more than in Europe. The fact that U.S. cattle often roam outside may also increase the risk. "In Europe at most of the dairy farms I've seen, the animals are inside and rather controlled," Richt says.

Exactly how the virus infects cattle is a question as well. Beer says it may get introduced into a cow's udder inadvertently, for instance by a veterinarian treating a diseased udder with contaminated equipment. There is some precedent for this: In 2016, H1N1 influenza was found in the reproductive tracts of turkeys in Norway, apparently passed on during artificial insemination.

Carefully investigating each spillover event could help answer these questions. But so far, "There hasn't been any proper analysis of the local epidemiological circumstances," Kuiken says. The first cattle outbreak was discovered several months after the fact and it's not clear where it occurred. In the second case, in Nevada, a sample from a silo that contained milk from multiple farms tested positive, and it took weeks to pinpoint the two affected farms. (Storing a milk sample from every farm that contributes to a silo could speed up the identification process, Worobey notes.)

Only the most recent spillover, in Arizona, was detected rapidly, because that state tests milk from individual farms. But Seema Lakdawala, a flu researcher at Emory University who is studying how the virus may be spreading on and between farms, says it's unclear whether anyone is investigating further. That fits a pattern, she adds: "I think we have really underestimated this pathogen and haven't made the strides that we needed to in a year." ■

PHOTO: JOSH EDELSON/AFP VIA GETTY IMAGES

IN THE ASHES

After wildfires burned houses and brush alike in Los Angeles, researchers have mobilized to understand the health risks posed by urban conflagrations

By **Warren Cornwall**, *in Altadena, California*

The modest, single-story house lay like a patient on an operating table. Tubes snaked from a window into the back of a van parked in the driveway. A dozen scientists bustled through the rooms, faces shrouded by bulky respirators. One poured water from the kitchen faucet into a bottle. Another swabbed a section of the kitchen floor with rubbing alcohol. Others adjusted sensors dangling from a metal stand in the living room like intravenous bottles next to a hospital bed.

"It's a big team," proclaimed Yifang Zhu, an air pollution expert at the University of California, Los Angeles (UCLA), as she stood in the driveway one day in February. "It's great that everyone came."

"Something good has to come out of this mess," replied the homeowner, who asked not to be named.

Nearby lay the "mess." A month earlier, a raging wildfire had descended on the Los Angeles community of Altadena, transforming entire blocks into a charred wasteland. Brick chimneys stood like towering gravestones amid the wreckage. Living rooms, kitchens, and bedrooms had vanished, replaced by unrecognizable skeletons of metal, piles of ash, and scorched paint cans. The single-story house survived the blaze. But to the west, all of its immediate neighbors had succumbed to wind-driven flames that rushed from the nearby San Gabriel Mountains in early January. It was one of several wildfires that ravaged sections of LA amid a powerful windstorm, burning 20,000 hectares, killing at least 29 people, and torching more than 16,000 structures. Weeks later, the balmy Southern California breeze still smelled faintly like an ash tray.

Wildfires that consume urban areas spew a unique brew of toxic smoke and ash.

Smoke and ash from January fires wafted over many Los Angeles neighborhoods, including this one in Pacific Palisades.

PHOTO: PLANET LABS PBC

The scene at the cream-colored 1960s era ranch home was a microcosm of what's going on across this crowded coastal basin. Scientists from about a dozen universities and government labs in California and elsewhere have converged on LA neighborhoods to help answer questions about the environmental and health threats posed by conflagrations that are part wildfire, part house fire.

Little is known about the long-term effects of wildfires that burn into urban areas, which are becoming more common. Wildfire torched more than 1000 structures near Boulder, Colorado, in 2021 and more than 2000 structures in the Hawaiian town of Lahaina in 2023, where 102 people died. In 2022, a committee formed by the National Academies of Sciences, Engineering, and Medicine found gaping holes in our understanding of what's in the smoke and ash from wildland-urban fires, and what it could mean for people's health.

"These fires give us entirely new sets of toxic contaminants," says David Allen, a chemical engineer at the University of Texas (UT) at Austin who chaired the National Academies committee and is part of the team that dispatched the van to Altadena. Residents in the affected areas, he notes, want to know whether it's safe to return to houses that are still standing. "We have very little scientific knowledge that we can use to direct guidance."

A handful of research projects popped up in the aftermath of the Colorado and Hawaii blazes. But the initiative that brought researchers to the Altadena home is unusual for its scope, the speed at which it has been launched, and its planned 10-year duration, says Kari Nadeau, a Harvard University environmental health scientist who is helping lead the work. It's expected to cost more than $25 million, with the largest chunk of funding so far coming from the family foundation of 34-year-old billionaire Evan Spiegel, an LA resident and co-founder of the company behind the popular messaging app Snapchat.

"This will be the first study to test everything all at once—in air, water, and soil, not just outside but inside homes and inside schools," Nadeau says.

THE BLAZE THAT CONSUMED parts of Altadena started as a brush fire on a hillside near Eaton Canyon. At first, the smoke would have been a predictable mixture of hundreds of chemicals that are known to emanate from plant-fueled fires, including microscopic particles, toxic gases, and nitrogen-based molecules such as ammonia.

But within hours, the nature of the fire—and the smoke—changed dramatically. Winds gusting at more than 100 kilometers per hour showered nearby homes with embers, igniting blazes that overwhelmed firefighters. As entire blocks burned through the night, the billowing smoke became more complex and mysterious—filled with a range of toxic compounds from the burning of lead-based paint, lithium batteries, vinyl siding, fiberglass insulation, electrical wiring, nylon clothes, rubber tires, and more.

Fires have been blamed for a long list of health ills. Wildland fire smoke has been linked to increased hospital admissions for asthma, strokes, and heart attacks. House fires have been associated with higher levels of cancer in firefighters.

But new hazards arise when those two things meet and a wildfire consumes an entire neighborhood. The high intensity of wildfire can alter the chemicals swirling in the air after they are emitted from burning houses. The number of people affected when wildfire sweeps into urban areas also dwarfs the number exposed during a typical house fire. More than 18 million people live in the greater LA metropolitan area, and a huge swath of them were bathed in hazardous levels of air pollution in January. Tests at the California Institute of Technology, for instance, 4 kilometers from Altadena, found elevated levels of lead in ash that seeped into campus buildings.

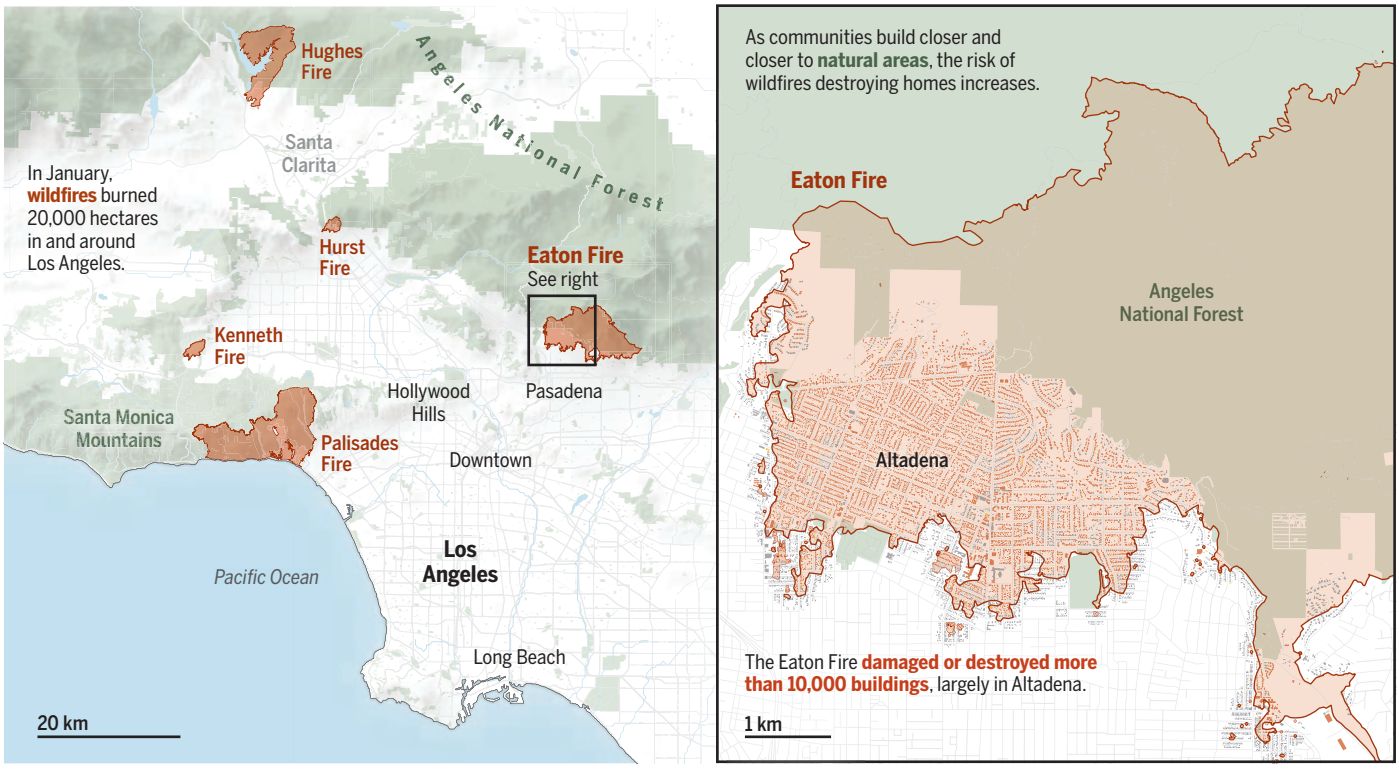

Burn scars Fast-moving wildfires in Los Angeles early this year killed 29 people, destroyed some 16,000 structures, and caused more than $130 billion in damage, making them the costliest in U.S. history. Scientists are racing to burned areas to understand the toll on people and the environment.

Little is known about how such fires affect the health of people over time. After Lahaina was devastated by the 2023 wildfire, University of Hawaii at Manoa epigeneticist Alika Maunakea dug into the scientific literature and found almost nothing. "It seemed like there would be a more concerted effort to really understand the long-term consequences," says Maunakea, whose previous work had focused on health problems such as diabetes and heart disease.

Maunakea now heads a project tracking the health of Lahaina residents. It has found that people more directly exposed to the fire suffered from much higher rates of depression and anxiety than the island's general population more than 6 months after the disaster. They also had lower lung function, according to unpublished results. But the fire is recent enough that insights are only beginning to emerge.

The unanswered questions have made it hard for researchers in LA to know what to tell residents about when they can return to their homes and what they should do with household items.

The Altadena homeowner, for instance, was curious about the risk of wearing clothes left behind that she later put through a washing machine. "Is that stuff fine?" she asked Anna Neville, a UT Austin chemical engineering Ph.D. student, as they stood next to the university's research van.

"I would think after washing it a few times it would be OK," Neville said, her voice muffled by a thick, rubber mask. Then she hesitated. "I'm not quite sure."

"I threw them away anyway," the homeowner said with a laugh through her own mask. "We didn't know what we were doing. No one knows."

THE HOME LOOKED LARGELY UNTOUCHED. A rope swing dangled from a sweetgum tree in the front yard. Inside, a child's book of piano music rested on a couch. A plastic cup with a tea bag stood on the kitchen table, left when the homeowner, her partner, and two young children fled.

Yet the fire came breathtakingly close. Flames consumed part of a wooden fence within arm's reach of the building. Scorched leaves lay in the grass along the front wall. For hours, the house had marinated in smoke and ash from the nearby flames.

Zhu's UCLA team had begun its work as the fires burned, deploying sensors to measure airborne chemicals in and around homes. Now, a bevy of scientists had joined them to learn what pollutants were seeping from the structures and the ground weeks later, and whether precautions such as air filters can help protect occupants.

"We are really interested in what happens to … exposure in the homes. And what can we do to mitigate the risk," says Joe Allen, an indoor air-quality expert who runs Harvard's Healthy Buildings Program and is supervising Harvard's share of the in-home sampling.

The Harvard group has focused on 50 houses, sweeping up ash and collecting other samples that could give a complete picture of the contaminants penetrating a home and how long they might stay. They are also tapping into more than 1000 air pollution sensors sold by the company Airthings, which were already installed in LA houses before the fires.

The electric-powered van was the Texas group's tool of choice. It housed two mass spectrometers, each roughly as big as a refrigerator. Although the devices couldn't linger in the house for days like the sensors from the UCLA and Harvard groups, their ability to detect hundreds of chemicals offered a more complete picture of the mélange of pollutants.

Because it's mobile, the van could also map how the pollution varies throughout the neighborhood. In early February, the researchers spent hours slowly cruising down streets that alternate between charred wreck-

CREDITS: (GRAPHIC) M. HERSHER/*SCIENCE*; (DATA) NATIONAL INTERAGENCY FIRE CENTER; CAL FIRE DAMAGE INSPECTION PROGRAM; CALIFORNIA PROTECTED AREAS DATABASE; LOS ANGELES COUNTY

age and pristine lawns. The results will help them build a computer model to estimate how details of the structures that burned, such as their construction materials and age, influence the emissions. That, in turn, could give public health officials, environmental regulators, and residents a better grasp of what is coming from urban infernos.

In the home's driveway, the machines were already revealing why a mask might still be advisable. Shihao Zhai, a UT Austin chemical engineering Ph.D. student, crouched at the van's open side door, peering at the screen of a laptop. "It's kind of amazing how high the indoor concentration is," he said, pointing to a graph that traced levels of benzene, a chemical that is commonly found in wildfire smoke. Long-term exposures to high levels of benzene are tied to anemia, leukemia, irregular menstrual cycles, and low birth weights.

That measurement echoes results from one of the only other wildland-urban fires where in-home pollution was closely tracked. After the Colorado fire in 2021, researchers filled a house in the town of Superior that narrowly escaped the fire with air-quality sensors and found that benzene lingered longer than other pollutants. "I would have expected it to take a few hours or days [to disperse], but it took weeks," says Joost de Gouw, an air pollution scientist at the University of Colorado Boulder (CU Boulder) who helped lead the research. "We really don't understand why that is."

The persistence of smoke-related gases and other contaminants in LA homes immediately within burned areas has prompted researchers to warn residents living in such houses to take precautions, including using air purifiers, air-quality sensors, and masks that can filter gases as well as dust. "The message is: Be really careful what you're doing indoors," David Allen says.

ELSEWHERE, SCIENTISTS ARE STUDYING the people who were exposed to the smoke and ash. Jeff Burgess, a University of Arizona occupational health scientist, says LA firefighters are concerned the smoke from the fires might sicken them, recalling that firefighters who responded to the 9/11 attacks in New York City suffered from increased lung ailments and some types of cancer. "Some people are saying this could be a World Trade Center–like event," Burgess says. "It might be. We don't know."

Burgess was already working with several LA-area fire departments to learn whether the health effects of fighting wildland-urban fires are different from those of the wildfires and building fires he has investigated elsewhere. When the January firestorm struck, Burgess went into overdrive, enrolling 400 more firefighters.

Some donned silicone bracelets that absorbed chemicals as they battled the flames, providing a glimpse of the toxic chemicals they were exposed to. Those volunteers and others also provided blood and urine samples, which the researchers will use to determine what chemicals soaked into their bodies, how their bodies are reacting, and whether they have elevated chemical markers associated with diseases such as cancer. Their health will be tracked for more than 20 years.

Air pollution expert Yifang Zhu is masked against pollutants while visiting a house in Altadena, California, where she's studying the lingering effects of wildfire smoke.

Harvard's Nadeau is exploring similar questions for a broader range of people. She's collaborating with researchers from UCLA, the University of Southern California, and the Cedars Sinai Medical Center, among others, who had already enrolled more than 9000 people in the LA area in yearslong studies tracking their health. The studies' large scale and long duration will enable researchers to see whether exposure to the fire affects people's immediate and long-term health, and whether changes in blood samples taken before and after the disaster can predict later health problems.

Nadeau also plans to follow families living in 50 of the houses being tested for pollution, to see whether contamination in their homes can be correlated with their future health or with chemical traces in their bodies. The scientists will continue to track people for at least a decade. "Sometimes it really does take 10 years for a memory T cell to, say, turn into a lymphoma," Nadeau says.

THE RISK OF these hybrid wildland-urban fires has skyrocketed in recent years, as more houses are built at the edge of natural areas and a combination of a warming climate and overgrown forests fuels bigger, more ferocious fires.

Fast-moving fires, like the Altadena blaze, are the ones most likely to spread into developed areas and destroy houses, says Jennifer Balch, a fire ecologist at CU Boulder. Last year, her team published a paper in *Science* (25 October 2024, p. 425) showing that in the western United States, fires have been speeding up—spreading at more than double the rate they were 2 decades ago.

"The thing that keeps me up at night as a scientist is where are we going to see the next one," Balch says. "We've stacked the odds in terms of building in flammable places. We've altered the climate to make things hotter and drier. It's just a matter of when, it's not a matter of if."

The growing problem isn't confined to the U.S. Regions where development meets wildlands have expanded globally by 24% since 2001, scientists reported last year in *Environmental Research Letters*, with more than half of that growth occurring in Africa. And fires in these areas accounted for a growing share of the total land burned each year.

That means the scene playing out in front of Zhu and the Altadena homeowner is sure to be repeated again and again. The two stood with their backs to the home, surveying what remained of the neighborhood. People shrouded in white plastic suits picked through the rubble in an effort by the U.S. Environmental Protection Agency to retrieve hazardous materials such as cans of paint. Next, the U.S. Army Corps of Engineers is slated to oversee the demolition and removal of the bulk of the debris, something that could stir up toxic ash and dust yet again.

Although some people have already returned to nearby homes, this family is waiting until cleanup efforts are complete.

"You haven't moved back here?" Zhu asked.

"No," the homeowner replied.

"That," Zhu said, "was very wise." ■

This story was supported by the Vapnek Family Foundation.

PHOTO: W. CORNWALL/*SCIENCE*

A California firefighter takes part in a test of a new mask, meant to protect wildland firefighters from pollutants while not hampering strenuous work.

PHOTO: WILDFIRE CONSERVANCY

Safety in the smoke

In January, as wildfires consumed parts of several Los Angeles neighborhoods, firefighters spent days engulfed in toxic smoke and ash. Many wore little more than a bandana to protect their lungs.

"That's a 21st century respiratory protection device for a wildland firefighter. And that is crap," Rick Swan, a retired California wildland firefighter and former top safety official with the International Association of Fire Fighters, said at a February meeting in Sacramento, California.

But better protection might soon be on the way. California announced in 2022 it will eventually require all state and local wildland firefighters to be provided with air-purifying respirators. The move has sparked a flurry of research and investments, with scientists, government officials, and companies all working to build a suitable respirator.

It's a challenging problem because of the nature of wildland firefighting. Urban firefighters entering a burning building for a few minutes can carry oxygen tanks. The workers cleaning up the debris from the LA fires wear standard respirators. But those protections are not a practical solution for wildland firefighters, who are often away from their base for hours or days, doing backbreaking work such as digging up vegetation and hiking with packs weighing 20 kilograms or more in steep terrain in hot weather. They need a mask that blocks the onslaught of toxic chemicals but doesn't impede their ability to breathe or otherwise do their job.

At a laboratory at the University of California, Los Angeles (UCLA), industrial hygienist Rachael Jones is seeing whether filter cartridges from different respirators can meet the first of those requirements. Usually, such filters are tested with a single type of chemical, but Jones is exposing them to a brew of chemicals like those from wildfire that burns houses as well as vegetation. "We're trying to really overload the cartridges," she said as she stood near a contraption that looked like a cross between a wood stove and a plastic maze built to entertain hamsters.

A master's student, Bella Chen, lit a potpourri of wood chips, plastic, carpeting, upholstery foam, insulation, and other household items and sealed it inside the stove. A pump pulled the smoke through a series of plastic tunnels and into one of six different cartridge models. Sensors placed downstream of the cartridges detected which chemicals leaked through.

A filter that can't cope with the smoke might give firefighters a false sense of safety. "You don't want to be standing there thinking, 'I can be here right now because I can breathe,' but you have a lot of bad stuff getting through," says Derek Urwin, a UCLA chemist and Los Angeles County firefighter who is collaborating with Jones.

Meanwhile, San Jose State University industrial engineer Anil Kumar plans to test whether wildland firefighters can work while breathing through a mask. This spring, he'll have members of the Santa Rosa Fire Department dressed in full wildland firefighting gear march up and down a flight of stairs and pound on a large tire with sledgehammers, all while wearing prototype masks that use a fan to flush filtered air to a person's face. The researchers will measure the firefighters' heart rates, respiration, and the speed of their movements. They will also ask what the firefighters think of the experience. "I can design the best product, but if the customer is not willing to use it, I have failed," he says.

The push in California has caught the attention of several major mask manufacturers, including the German company Dräger, which is working on a mask first developed by Colorado company TDA Research that adjusts the flow of purified air based on the person's breathing rate. Prototypes of the mask have been tested in California on firefighters simulating the kind of work done to fight a fire, and Kumar hopes to include one in his upcoming studies. Dräger officials declined to say when a mask might be ready for sale.

It can't some soon enough for Alex Hamilton, chief of the fire department in Oxnard, California. When he visited some of his firefighters who were protecting homes from the inferno burning through the Pacific Palisades neighborhood in LA, he was shocked by how foul the air was. He says it reeked of synthetic chemicals. "I'm terrified of what we're going to see 10 or 15 years from now in terms of long-term health impacts," Hamilton says.

He's ready to stock up on better performing masks, once they are available. "I would find the money to make that happen," he says. —*W.C.*

INSIGHTS

PERSPECTIVES

IMAGE: LAUREN DAUPHIN, USING LANDSAT DATA FROM THE U.S. GEOLOGICAL SURVEY AND LAKE ELEVATION DATA FROM THE BUREAU OF RECLAMATION

WATER CYCLE

Permanent shifts in the global water cycle

Decades of terrestrial water-storage changes reveal an irreversible decline in soil moisture

By **Luis Samaniego**[1,2]

Understanding the relationship between atmospheric carbon levels and global temperature dates back to 1895, when Swedish scientist Svante Arrhenius argued that variations in carbon dioxide concentrations could affect Earth's heat budget. How climate warming affects Earth's hydrological cycle—the continuous water movement between Earth and the atmosphere—is a key question for managing water resources and making weather predictions. Although local and regional changes in the water cycle have been observed (*1*, *2*), conclusive proof of a global-scale shift has been elusive. Answering this question requires decades of global mean sea level data and advanced climate and hydrological modeling. On page 1408 of this issue, Seo *et al.* (*3*) report how the integration of multiple global geophysical datasets reveals a permanent decline in terrestrial water

The water level of Lake Mead, Nevada, has receded substantially from 2000 to 2022, indicating a permanent shift in terrestrial water storage.

storage. The study provides robust evidence of an irreversible shift in terrestrial water sources under the present changes in climate.

Earth is an irregular, deformable body that rotates around an axis. A slight misalignment of this axis from the principal figure axis, which represents the "ideal" center of mass, causes a wobbling motion known as polar motion. One of the dominant components of polar motion is the Chandler wobble, which is a periodic oscillation of Earth's rotational pole (*4*). Early reports suggested that meteorological factors such as atmospheric pressure, wind, and precipitation could potentially drive the Chandler wobble (*5*, *6*). However, large variations—up to 300 milliarcseconds (mas; 1 mas is equal to 3 cm of polar motion)—in the observed oscillation previously hindered conclusive evidence for this hypothesis (*6*). Advancements in instrumentation have exponentially reduced uncertainty, reaching less than 1 mas in 2020. Further progress in understanding the excitation mechanisms of the Chandler wobble have also relied on improvements in meteorological, oceanic, and hydrological modeling (*6*). These developments have helped confirm permanent climate changes (*7*). Assessing the impacts of precipitation, evaporation, and runoff (the amount of water flow across Earth's surface) on polar motion by using coarse, interpolated global observations has shown that water distribution affects Earth's gravitational field, and changes in soil moisture can contribute to low-frequency variations in polar motion (*5*).

> "...the negative shift in soil moisture may be irreversible because of prolonged drought conditions..."

Tracking terrestrial water storage at continental scales with high resolution is crucial for managing water resources and ecosystems. Reanalysis combines historical observations with modern numerical weather prediction through data assimilation to produce a long-term, consistent dataset (*8*). This approach, which relies on vast amounts of satellite and field observations, has contributed to the development of the European ReAnalysis v5 (ERA5) (*9*). However, terrestrial reanalysis requires a long development period due to the complexity of land surface processes (such as soil moisture infiltration and runoff generation) and extensive parameterization, data assimilation, and validation. This challenge is further compounded by difficulties in incorporating streamflow—the rate at which water is carried by rivers and streams—into weather models. Consequently, resolving the balance of water inflow and outflow entirely at the basin level remains a challenge. Integrating hydrological and land surface models can refine boundary conditions (such as soil moisture) for numerical weather models to enhance reanalysis and improve weather predictions. However, scaling hydrological processes from local soil properties, such as porosity, to the scale of terrestrial reanalysis can vary up to three orders of magnitude. Sparse observational networks for soil moisture and groundwater levels, along with a general lack of subsurface water flow measurements, further complicate this task. As a result, developing scalable high-resolution models for key physical, chemical, and biological variables on land, such as soil moisture and runoff, that are crucial for characterizing Earth's climate remains a grand challenge (*10*, *11*). Additionally, decades of variations in terrestrial water storage are yet to be fully elucidated.

Seo *et al*. present a comprehensive analysis of how global terrestrial water storage has changed over the past four decades. Three independent datasets were integrated to validate the soil water depletion: terrestrial water storage anomalies from Gravity Recovery and Climate Experiment (GRACE), global mean sea level from satellite altimetry, and a century-long dataset on the movement of Earth's rotational axis (polar motion). GRACE, which is a joint satellite mission of the US National Aeronautics and Space Administration and the German Aerospace Center, can provide precise measurements of Earth's gravitational field. By tracking gravity-field variations, the GRACE mission provides information about groundwater depletion, ice sheet loss, and sea level rise that could be used to estimate changes in total water storage on Earth's surface. GRACE has played a key role in validating land surface models (*12*, *13*) and elucidating Earth's hydrological cycle. However, GRACE only began collecting gravity data in 2002. To estimate terrestrial water storage variations before then, Seo *et al*. used global mean sea level observations and Earth's polar motion to validate ERA5-simulated patterns. The results show that soil moisture depletion predicted by ERA5 aligns with global sea level rise and shifts in Earth's mass distribution that influences polar motion.

The cross-validation approach of Seo *et al*. provides compelling evidence of a shift in Earth's hydrological cycle that is likely driven by a warming climate. Global terrestrial water storage has been steadily declining, with a substantial loss of ap-

[1]Department of Computational Hydrosystems, UFZ-Helmholtz Centre for Environmental Research, Leipzig, Germany. [2]Institute of Environmental Science and Geography, University of Potsdam, Potsdam, Germany. Email: luis.samaniego@ufz.de

proximately 1.6 gigatonnes in the early 21st century. Regions in East and Central Asia, Central Africa, and North and South America have shown substantial depletion in soil moisture. The findings also indicate that lost terrestrial water has not recovered to previous levels. This persistent decline suggests that the negative shift in soil moisture may be irreversible because of prolonged drought conditions and reduced precipitation in certain regions.

Although Seo *et al*. provide an analysis of global terrestrial water variations over the past two decades, a broad range of factors that influence precipitation and evapotranspiration (the transfer of water from land to atmosphere through evaporation and transpiration) must also be considered. Advanced land surface and hydrological models that can accurately represent these factors under the influence of changing climate are crucial to capturing the evolution of terrestrial water storage.

The findings of Seo *et al*. underscore the urgent need to improve parameterization of land surface models to better understand complex geophysical problems (*14*). Developing next-generation models that incorporate anthropogenic influences such as farming, large dams, and irrigation systems (*3*) is essential. The ongoing advancements of a land surface modeling system by the European Centre for Medium-Range Weather Forecasts represents a promising step forward (*15*). These improvements could reduce uncertainties and enhance our understanding of the impacts of climate change on the global water cycle. ■

REFERENCES AND NOTES

1. L. Samaniego, R. Kumar, M. Zink, *J. Hydrometeorol.* **14**, 47 (2013).
2. G. Blöschl *et al*., *Science* **357**, 588 (2017).
3. K.-W. Seo *et al*., *Science* **387**, 1408 (2025).
4. M. Yamaguchi, M. Furuya, *Earth Planets Space* **76**, 1 (2024).
5. J. Kuehne, C. R. Wilson, *J. Geophys. Res.* **96**, 4337 (1991).
6. R. Gross, *J. Geophys. Res.* **27**, 2329 (2000).
7. T. M. Eubanks, in *Contributions of Space Geodesy to Geodynamics: Earth Dynamics*, vol. 24, Geodynamics Series (American Geophysical Union, 1993), pp. 1–54.
8. R. Baatz *et al*., *Rev. Geophys.* **59**, e2020RG000715 (2021).
9. H. Hersbach *et al*., *Q. J. R. Meteorol. Soc.* **146**, 1999 (2020).
10. E. F. Wood *et al*., *Water Resour. Res.* **47**, W05301 (2011).
11. M. F. P. Bierkens *et al*., *Hydrol. Processes* **29**, 310 (2015).
12. O. Rakovec, R. Kumar, S. Attinger, L. Samaniego, *Water Resour. Res.* **52**, 7779 (2016).
13. O. Rakovec *et al*., *J. Hydrometeorol.* **17**, 287 (2016).
14. L. Samaniego *et al*., *Hydrol. Earth Syst. Sci.* **21**, 4323 (2017).
15. S. Boussetta *et al*., *Atmosphere* **12**, 723 (2021).

ACKNOWLEDGMENTS

The author acknowledges the 4DHydro initiative, which is funded by the European Space Agency (ESA) under contract 4000141141/23/I-EF.

10.1126/science.adw5851

SOCIAL SCIENCE

New data fill long-standing gaps in the study of policing

Data show discrimination, but analysis must be more policy relevant

By **Dean Knox**[1] *and* **Jonathan Mummolo**[2]

Data limitations have long stymied research on racial bias in policing. To persuasively demonstrate bias, scholars have sought to compare officer behavior toward minority versus white civilians while holding constant all other factors in the police-civilian encounter that might provide alternative explanations for enforcement disparities. These comparisons in "similar circumstances" are also critical in litigation concerning discriminatory policing, which can often lead to court-ordered remedies (*1*). Such "all-else-equal" scenarios are elusive in many realms of social science, but two challenges have made them particularly difficult to find in the study of policing. On page 1397 of this issue, Aggarwal *et al*. (*2*) report using data from the ridesharing service Lyft—having obtained vehicle location on more than 200,000 drivers using high-frequency GPS pings from their smartphones—to analyze speeding enforcement by the Florida Highway Patrol (FHP) and to show how such data offer a path forward for addressing both challenges.

One challenge to establishing all-else-equal comparisons in studies of policing is that standard police datasets contain one-sided officer accounts of civilian behavior, which past work has shown do not always accurately measure actual driver behavior. For example, prior research (*3*) has shown that in the same FHP context, officers gave white drivers a "discount" on tickets by reporting lower speeds relative to the speeds reported for minority drivers. Aggarwal *et al*. use the Lyft data to construct an objective measure of speeding behavior.

The other challenge is that traditional police-generated datasets are inherently selective: For example, they do not contain every police-civilian encounter in which an officer could have cited a speeding driver but rather only the subset in which an officer chose to pull vehicles over and therefore had to fill out forms documenting the stop. Research has shown that under reasonable assumptions, if there is racial bias in the initial decision to stop, then analyses that take the resulting stop data at face value—e.g., using them in standard regression analyses—can substantially underestimate racial bias in subsequent decisions, such as whether to issue a citation (*4*). Intuitively, this is because differential selection into the data means that—even if encounters appear to be similarly situated on observed characteristics—stops of minority and white civilians will likely differ on unobservable characteristics that influenced officers' stopping decisions. The approach of Aggarwal *et al*. resolves this challenge too, by allowing researchers to observe all times when Lyft drivers are active rather than only the selected sample of those where officers chose to detain them.

Using these rich data, Aggarwal *et al*. find statistically significant evidence of discriminatory policing even among Lyft drivers incentivized to drive safely—a subgroup where effects are likely to be lower than those observed in the general driving population. How consequential is this discrimination in substantive or legal terms? The answer is more complex than it may appear and hinges on the specifics of how the statistical estimand—the quantity of interest targeted by the research design and analysis—relates to legal standards of evidence in discrimination cases. This connection is one that academic work on policing, including Aggarwal *et al*., has rarely considered. Nevertheless, it is critical to ensuring that scientific research translates into real-world impact.

On their face, the disparities demonstrated by Aggarwal *et al*. appear substantively small: The largest estimates of racial discrimination translate to roughly one additional speeding citation per 28 years of full-time driving and roughly one additional dollar in fines per year. But these results cannot be correctly interpreted without considering both the circumstances in which drivers are observed and the precise comparisons on which these estimates are based.

[1]Operations, Information and Decisions Department, Wharton School, University of Pennsylvania, Philadelphia, PA, USA. [2]Department of Politics, School of Public and International Affairs, Princeton University, Princeton, NJ, USA. Email: jmummolo@princeton.edu

Aggarwal *et al*. report racial discrimination in policing using vehicle location data on more than 200,000 drivers.

PHOTO: LOWPHOTO/ALAMY STOCK PHOTO

On the former point, drivers observed in the Lyft data reported by Aggarwal *et al.* rarely speed to any notable extent. In 85.3% of pings, drivers are not speeding at all—meaning that FHP cannot defensibly issue a speeding citation, let alone discriminate in doing so. Another 11.3% of pings involve only slight speeding violations, which are rarely enforced. This means that aggregate-level differences that initially seem small are in fact driven by far larger differences in the most relevant 3.4% of observations where notable speeding occurred. In seeking to address discriminatory law enforcement, civil rights practitioners litigating similar issues have therefore focused on scenarios where officers might plausibly exhibit the behavior of interest, rather than reporting estimates that are diluted by the 96.6% of scenarios where discriminatory enforcement is almost mechanically precluded (*5*). For example, a recent US Department of Justice (DOJ) investigation of the Phoenix Police Department in Arizona estimated racial bias in ticketing "Among drivers who speed…" and "Among drivers who engage in low-level moving violations…" [(*6*), p. 60]. Focusing on these potentially enforceable cases requires a different statistical estimand.

The latter point is a more subtle one that touches on the relationship between statistical analysis and discrimination case law, which focuses not on differences between the treatment of two groups in general but rather on demonstrating harm to one protected group specifically. For example, a DOJ legal manual on the topic states, "To prove…systemic discrimination…A plaintiff in a pattern or practice case can… [present] statistical evidence of similarly situated individuals not in the protected class who were treated better than those in the protected class" [(*7*), p. 22]. The focus is on realized harm to actual minority drivers, in the sense that (according to a statistical analysis) they were treated worse than a hypothetical group of white drivers encountered in circumstances similar to those of the actual minority drivers. In statistical terms, this is known as an average treatment effect on the treated (ATT), where minority status may be regarded as the "treatment" in the parlance of causal inference. By contrast, the overall average treatment effect (ATE) that Aggarwal *et al.* appear to target also incorporates an additional comparison that does not involve realized harm to minority drivers—whether actual white drivers were treated better than hypothetical minority drivers encountered in circumstances similar to those of actual white drivers. Both ATT and ATE can be estimated using the same data, though the less-relevant ATE can often be estimated with more statistical precision because it relies more heavily on data for white drivers, who are far more numerous. Notably, the ATT and ATE can diverge substantially because, as Aggarwal *et al.* show, minority drivers tend to be younger and drive vehicles with different characteristics, they likely drive in different geographic areas, and these differing circumstances are among the most important factors influencing police citation decisions.

Moving from academic research to practical applications has other implications for statistical analysis. For one, it requires researchers to recognize that the quantity examined in any particular study—in the case of Aggarwal *et al.*, relating to officers discriminatorily citing minority versus white drivers in comparable locations and times—tells only part of the broader story about how discrimination may manifest in law enforcement. For example, it may be just as important to study bias in how officers are assigned to work those locations and times in the first place—estimands that may reveal patterns of, for example, overdeployment in minority neighborhoods causing disparate impact.

To be clear, academic research on discriminatory policing need not always tailor its statistical analyses for policy settings. And Aggarwal *et al.* have provided a template for using recent technological advances to overcome some of the most challenging obstacles impeding policing research. But to maximize impact on pressing social problems, this study—like decades of research before it (*8*)—could benefit from greater clarity about the specific estimand being targeted and a precise explanation of why it is the most relevant quantity of interest. This clarification is imperative if academics wish to aggregate knowledge across independent studies being conducted on the roughly 18,000 police agencies in the US. To conduct meaningful meta-analyses and comparisons, scholars will need to agree on, and precisely specify, the statistical quantities that they seek to measure. ■

REFERENCES AND NOTES

1. *Yick Wo* v. *Hopkins*, 118 U.S. 356 (1886).
2. P. Aggarwal *et al*., *Science* **387**, 1397 (2025).
3. F. Goncalves, S. Mello, *Am. Econ. Rev.* **111**, 1406 (2021).
4. D. Knox, W. Lowe, J. Mummolo, *Am. Polit. Sci. Rev.* **114**, 619 (2020).
5. Subsetting to instances where a driver is objectively speeding, as proposed by Aggarwal *et al*., is conceptually distinct from subsetting to instances where police subjectively chose to detain a civilian for speeding, as in much prior work that has analyzed police stop data. The former is based on an objective fact that is unlikely to induce selection bias because there is arguably no unobserved factor that jointly determines a civilian's decision to speed and an officer's decision to issue a speeding ticket—especially because analysts can condition on car make, time, location, and other circumstances. In the latter case, an officer's decisions to stop a civilian and issue a citation could be jointly influenced by many factors that remain unobserved.
6. US DOJ Civil Rights Division, "Investigation of the City of Phoenix and the Phoenix Police Department" (2024); https://www.justice.gov/crt/media/1355866/dl?inline.
7. US DOJ Civil Rights Division, "Section VI: Proving Discrimination – Intentional Discrimination," in "Title VI Legal Manual" (2015); https://www.justice.gov/crt/media/1384931/dl?inline.
8. I. Lundberg, R. Johnson, B. M. Stewart, *Am. Sociol. Rev.* **86**, 532 (2021).

ACKNOWLEDGMENTS

The authors thank J. Grimmer for helpful feedback on this article. This work was supported by Arnold Ventures grant 22-06762 (D.K. and J.M.) D.K. and J.M. have worked as paid consultants for the US DOJ Civil Rights Division, the American Civil Liberties Union, and the NAACP Legal Defense Fund.

10.1126/science.adw3618

EVOLUTION

Mapping a complex evolutionary history

Tracking the geographic origins of genetic ancestors reveals past human migrations

By **Simon Gravel**

Human genomes contain rich information about the past; even a single sequenced genome can be used to summarize patterns of human relatedness going back hundreds of thousands of years (*1*). The genomes of hundreds of thousands of individuals are now sequenced every year, providing the potential for ever-increasing resolution in our understanding of human history. However, the interpretation of these rich data in terms of evolutionary hypotheses is challenging. On page 1391 of this issue, Grundler *et al.* (*2*) introduce GAIA, a statistical approach that seeks to learn the geographic position of every genetic ancestor of individuals included in a genome dataset. This approach can help to identify the complex relationships between ancestral populations that shaped the genetic diversity of humans today.

More than 10 years ago, the 1000 Genomes Project (*3*) sequenced the genomes of around 2500 individuals from 26 populations worldwide and made them freely available. Despite years of analysis, these data continue to support new and more detailed claims about human migrations. More recent analyses take advantage of improved data quality (*4*), of additional datasets, and of new analytical tools. They also build on previous work to propose and test ever more detailed models of population dynamics that often feature a network of ancestral populations (*5*, *6*).

Unfortunately, building such detailed models is challenging (*7*, *8*). Most model-based analyses of population genetic data rely on simple parametric assumptions—for example, the idea that humans chose their partners uniformly at random within a few regional subpopulations that persisted over thousands of generations. Such assumptions are never satisfied in real populations: Humans choose partners on the basis of a range of characteristics, which include complex social and geographic factors. They also do not form well-defined populations that are stable over such long times (*8*). Realistic models therefore require a large number of parameters to describe mating preferences, population size changes, and migrations. Small differences in how models are specified can have a large impact on parameter estimation and subsequent interpretation (*7*, *8*).

As a result, building more complex models does not guarantee better understanding. This is especially true if these models still miss important events in human history, such as large-scale migrations or long-lasting isolation between ancestral populations. Most model-building efforts rely on some form of descriptive and exploratory analyses, such as dimension reduction (*9*, *10*) or admixture component analysis (*11*), to look for unexpected relatedness patterns among humans. Such patterns can help to identify problems with models, but they are mostly informative about the past few generations. Therefore, it is hard to assess whether even the most detailed models that have been proposed lack important features of more distant human history. There is a clear need for exploratory approaches that can help reveal such features.

GAIA provides an important step in this direction. It builds on recent progress in the statistical reconstruction of the ancestral recombination graph (ARG). The ARG is a mathematical description of all the genetic relationships between individuals in a sample. Most model-based and descriptive analyses of genetic variation can be interpreted as summaries of the genetic relatedness that is encoded in this complex mathematical object. Learning the ARG from genetic data has therefore been a long-standing goal, and recent algorithmic progress has made it possible to perform reconstructions across the entire genome and for hundreds of thousands of individuals (*12*, *13*). Although these reconstructions are imperfect, they have already been used to answer a range of medical and evolutionary questions (*12*).

Although inferred ARGs contain a vast relationship network for human ancestors, they do not provide direct information on the evolutionary forces that shaped this network. Different methods have been developed to extract such demographic information from ARGs (*12*). Rather than using a parameterized model involving a few randomly mating populations, GAIA infers the geographic position of each genetic ancestor in the ARG (see the figure). Demographic factors such as migration rates can be retrieved from the distances between pairs of related ancestors, with relatively few a priori assumptions. And because ARGs provide estimates of the time at which each ancestor lived, GAIA can be used to create detailed time-resolved migration maps. Such maps can help reveal major and unexpected demographic trends that may have been missed by parameter-

Increasingly complex demographic models

Shared genetic material among humans can be traced to shared ancestors, who sometimes lived many thousands of years ago. To understand when and where these common ancestors lived, and therefore how human genetic diversity came to be, geneticists often rely on increasingly complex assumptions about mating behavior within one or a few stable populations (parameter-based models). Instead, the GAIA method infers the time and geographic position of each shared ancestor, with few a priori assumptions about mating behavior, allowing for a rich description of how past migrations shaped present-day genomes.

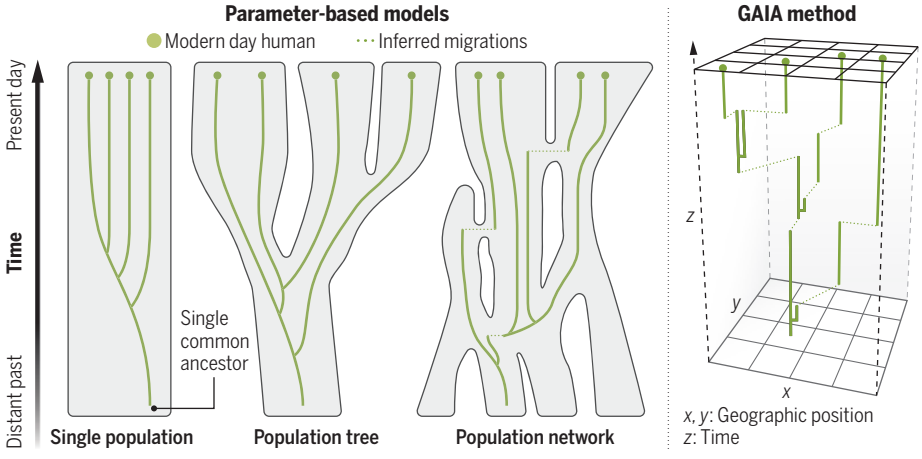

GRAPHIC: A. MASTIN/*SCIENCE*

Department of Human Genetics, McGill University, Montreal, QC, Canada. Email: simon.gravel@mcgill.ca

ized models. When applied to human genetic data, GAIA did recapitulate expected broad trends, including human origins in Africa.

GAIA improves on a previous method that sought to estimate the geographic location of each common ancestor as the (weighted) average location of its descendants (*14*). Instead, GAIA positions ancestors in a way that jointly minimizes the (approximate) migration distances traveled by all human ancestors. This joint minimization uses more information than previous efforts and efficiently optimizes a more demographically realistic migration model. Further, the computational techniques developed to infer the location of ancestors are generalizable to other demographic attributes (*14*), opening the door for more detailed characterization of the relationships among ancestors of modern-day humans.

There are also limitations to the approach. To learn the position of ancestors, GAIA uses a parsimony assumption: The selected positions minimize historical migrations. Such assumptions will likely lead to underestimates of human migrations and struggle to account for large-scale migration events. Further, although it produces arresting images, GAIA does not allow for hypothesis testing. There is a long history of over-interpreting nice-looking visualizations of genetic data (*15*). The intuitive, detailed, and visually compelling nature of the migration maps produced by GAIA makes such over-interpretation particularly tempting. Even if the method is viewed as purely exploratory, it will be hard, if not impossible, to find independent data to test hypotheses that it generates.

With these caveats in mind, the direct inference of demographic parameters within ARGs provides a noteworthy alternative path to investigate human evolution that complements approaches based on simple models and descriptive statistics. It has the potential to identify critical gaps in models of human diversity. And given the rapid progress in algorithms for ARG inference and analysis, there is great potential for further improvements of the approach. ■

REFERENCES AND NOTES

1. H. Li, R. Durbin, *Nature* **475**, 493 (2011).
2. M. C. Grundler *et al.*, *Science* **387**, 1391 (2025).
3. The 1000 Genomes Project Consortium, *Nature* **526**, 68 (2015).
4. M. Byrska-Bishop *et al.*, *Cell* **185**, 3426 (2022).
5. A. P. Ragsdale *et al.*, *Nature* **617**, 755 (2023).
6. A. Durvasula, S. Sankararaman, *Sci. Adv.* **6**, eaax5097 (2020).
7. B. M. Henn *et al.*, *Curr. Opin. Genet. Dev.* **53**, 148 (2018).
8. E. M. L. Scerri *et al.*, *Nat. Ecol. Evol.* **3**, 1370 (2019).
9. P. Menozzi *et al.*, *Science* **201**, 786 (1978).
10. A. Diaz-Papkovich *et al.*, *PLOS Genet.* **15**, e1008432 (2019).
11. D. H. Alexander *et al.*, *Genome Res.* **19**, 1655 (2009).
12. R. Nielsen *et al.*, *Nat. Rev. Genet.* **26**, 47 (2025).
13. A. W. Wohns *et al.*, *Science* **375**, eabi8264 (2022).
14. D. Sankoff, P. Rousseau, *Math. Program.* **9**, 240 (1975).
15. J. Novembre, M. Stephens, *Nat. Genet.* **40**, 646 (2008).

10.1126/science.adw5484

NEUROSCIENCE

Beyond hedonic eating

A dopaminergic brain circuit drives food consumption in mice

By **Dana M. Small**[1,2,3]

The capacity to store energy as fat enables animals to ensure energy reserves for the future. In this context, eating beyond satiety (fullness) is a beneficial, adaptive behavior. However, in many human populations, this adaptive behavior is made maladaptive by readily available, energy-dense sources of food, resulting in high rates of obesity. One such behavior, called invigoration, causes an increase in speed, duration, and intake of a palatable food (*1*). The neural mechanisms underlying this behavior are not yet clear. On page 1376 of this issue, Zhu *et al.* (*2*) report a brain circuit that drives feeding invigoration in mice. This circuit begins with neurons in the area around the locus coeruleus (periLC) and results in dopamine release in the nucleus accumbens. The finding provides a neural target, the therapeutic modulation of which might enable changes to food intake by preventing invigoration.

Midbrain dopamine neurons such as those in the ventral tegmental area (VTA) play a critical role in adaptive feeding behaviors. They respond to environmental cues (such as the sight of ripe fruit on a branch) that signal food availability (*3*) and are also activated during food consumption (*4*) and when nutrients are detected in the gut (*5*). Subsets of midbrain dopaminergic neurons express receptors for peripheral signals that convey information about physiological states. For example, the hormone ghrelin enhances appetite and learning (*6*) by increasing dopamine release by these neurons. VTA-induced dopamine release can also invigorate ongoing appetitive behavior such as licking (*1*) and enhance the salience of external food cues so that they are better at capturing attention and motivating changes in behavior (*7*).

> **"...the value of specific foods and drinks can be learned and updated based on the resulting physiological effects..."**

The integration of these dopamine signals across time and across functionally heterogeneous neural circuits (*8*) enables organisms to learn to associate the nutritional benefits of foods and drinks with antecedent actions (e.g., reaching, chewing) and sensory experiences (e.g., sight, sound, taste). As a result, the value of specific foods and drinks can be learned and updated based on the resulting physiological effects, and their selection can be tailored to current needs. For example, an animal can readily learn that the color red predicts sweetness, which in turn predicts the availability of energy. Then, when confronted with a strawberry bush on a distant shore, a river crossing may be risked if the animal is hungry and if those berries are red, but not if they are green—and as long as there are no predators. It is an incredibly elegant and important system. However, in humans, when confronted with inexpensive, ubiquitous, energy-dense foods, this adaptive behavior, orchestrated in part by dopamine signaling, leads to overeating. Understanding the intricacies of these circuit dynamics and the characteristics of the cells involved is therefore important for the development of improved therapies for obesity.

The neural circuits that associate food cues with reward are very well described in humans and in mice. For example, when a mouse sees a food pellet, neurons originating in the lateral hypothalamus inhibit the activity of γ-aminobutyric acid (GABA)–producing VTA neurons. This releases the inhibition of dopaminergic VTA neurons that project to the nucleus accumbens (a brain region involved in processing of motivation and reward) (*9*). This results in dopamine release in the nucleus accumbens. Inhibition of this pathway reduces feeding, including compulsive food seeking; however, it leaves intact the ability of hunger to drive eating, highlighting the segregation of these two functions at the level of brain circuitry (*10*). Similar studies have dissected the systems that drive dopamine release in mice during the digestion of food (*5*). However, less is understood about the control of dopamine release and its function while food consumption is ongoing.

[1]Departments of Neurology and Neurosurgery, Medicine, and Psychology, McGill University, Montreal, QC, Canada. [2]Research Institute of the McGill University Health Center (RI-MUHC), Montreal, QC, Canada. [3]Modern Diet and Physiology Research Centre, Montreal Neurological Institute-Hospital, Montreal, QC, Canada. Email: dana.small@mcgill.ca

Zhu *et al.* used cell-specific circuit mapping and optogenetics in mice to address this gap in knowledge. In a prior study (*11*), they had identified a group of neurons in the periLC that control consumption of palatable food. In contrast to most locus coeruleus neurons, which are noradrenergic, this group was glutamatergic, and their inhibition produced a rewarding effect and increased food intake. In the present study, Zhu et al. report that these periLC neurons drive dopamine release in the nucleus accumbens, much like lateral hypothalamic neurons. However, they do so during food consumption, instead of in response to food cues. Similar to the circuit originating in the lateral hypothalamus, the initial synapse of these periLC neurons is with GABA-producing inhibitory neurons in the VTA, which in turn disinhibit dopaminergic VTA neurons. Thus, lateral hypothalamic neurons drive food seeking and periLC neurons drive food consumption, both through regulation of dopaminergic VTA neurons.

Notably, the dopaminergic VTA neurons targeted by the periLC increased their activity immediately before the mice licked the food, with firing maintained throughout food consumption. This characteristic is consistent with behavioral invigoration (*1*). Zhu *et al.* also describe stronger responses of dopaminergic VTA neurons to more energy-dense and palatable foods. They used lick-triggered photostimulation of these VTA neurons to boost dopamine responses during consumption of less energy-dense and palatable foods. This manipulation resulted in an increase in licking rate and duration to match that usually observed in response to more energy-dense and palatable food. By contrast, photostimulation that was not contingent upon licking had no effect on licking behavior. This demonstrates a causal relationship between activation of the targeted circuit and invigoration of consumption based on the value of the food.

Zhu *et al.* describe the periLC-VTA circuit as regulating hedonic eating. The word hedonic, is defined as "of or relating to pleasure" by the Oxford English Dictionary. Notably, pleasure or "liking" is not synonymous with value and can be decoupled from other aspects of motivated behavior such as wanting, craving, habitual responses, and invigoration (*10*). As acknowledged by the authors, it is difficult to measure pleasure in mice. Instead, they defined hedonic eating on the basis of licking bout duration. However, this definition is circular because palatability drives intake, and intake is used to define palatability. Therefore, although lick rate, bout duration, and VTA dopaminergic activity were greater when more energy-dense food was offered, this does not demonstrate that mice experience the more palatable food as more pleasurable or that photostimulation of VTA dopaminergic neurons enhances pleasure. Consequently, the periLC-VTA circuit may control invigoration and have little to do with pleasure. This is consistent with decades of work in humans and rodents that failed to link dopamine with pleasure (*4*).

This disconnect between invigoration and pleasure is also consistent with emerging views on the behaviors that drive overeating in humans. Consumption of energy-dense foods, such as ultraprocessed foods, is linked to obesity. However, in humans, these foods can drive intake and valuation independently of experienced pleasure (*12*), with eating rate emerging as the most important factor in determining their overconsumption (*13*). Furthermore, treatment with glucagon-like peptide 1 receptor (GLP1R) agonists such as semaglutide does not alter the pleasure derived from consuming food (*14*, *15*), despite the widespread success of these drugs in inducing weight loss.

Notably, in many people, the efficacy of treatment with GLP1R agonists wanes over time. It is not yet clear what accounts for this variable response. Zhu *et al.* report that treating mice with semaglutide initially reduces the firing of VTA dopamine neurons but that the effect disappears within days. This raises the possibility that inter-individual differences in the adaptation of this circuit to the drug may account for differences in treatment efficacy in humans. Future work that aims to minimize such adaptation could offer a promising avenue for the development of adjunct therapies to broaden the group of individuals for whom GLP1R agonist treatment is effective. ■

REFERENCES AND NOTES

1. J. A. da Silva *et al.*, *Nature* **554**, 244 (2018).
2. Z. Zhu *et al.*, *Science* **387**, eadt0773 (2025).
3. M. F. Roitman *et al.*, *J. Neurosci.* **24**, 1265 (2004).
4. R. A. Wise, *Nat. Rev. Neurosci.* **5**, 483 (2004).
5. W. Han *et al.*, *Cell* **175**, 887 (2018).
6. A. G. Watts *et al.*, *Physiol. Rev.* **102**, 689 (2022).
7. K. C. Berridge, *Eur. J. Neurosci.* **35**, 1124 (2012).
8. A. L. Collins, B. T. Saunders, *J. Neurosci. Res.* **98**, 1046 (2020).
9. E. H. Nieh *et al.*, *Neuron* **90**, 1286 (2016).
10. E. H. Nieh *et al.*, *Cell* **160**, 528 (2015).
11. R. Gong *et al.*, *Cell* **182**, 1589 (2020).
12. K. D. Hall *et al.*, *Cell Metab.* **30**, 67 (2019).
13. C. G. Forde, *Proc. Nutr. Soc.* **82**, 406 (2023).
14. J. Blundell *et al.*, *Diabetes Obes. Metab.* **19**, 1242 (2017).
15. G. Coppin *et al.*, *Int. J. Obes.* **47**, 1224 (2023).

ACKNOWLEDGMENTS

D.M.S. thanks P. Van Dokkum and M. Andermann for editing the text for clarity. D.M.S. is funded by a Canada Excellence Research Chair and the Modern Diet and Physiology Research Centre.

10.1126/science.adw3646

QUANTUM OPTICS

Lined up for entanglement

A framework widely used in classical contexts provides new insights into solving an important challenge in quantum technology

By **Evgeny Moiseev** *and* **Kai Wang**

Singers in a choir are separated by distances, but their voices are perfectly synchronized to make a harmony. Similarly, particles in a quantum system are entangled to share some correlated feature even if they are far away. This phenomenon, called quantum entanglement (*1*), is important for quantum information processing but highly sensitive to decoherence (loss of quantum properties) (*2*). Exposure to uncontrolled environments, such as thermal fluctuations, causes entangled particles to pick up random noises, which leads to a so-called mixed state. Fortunately, there are ways to "filter" a mixed state back into a pure entangled state by engineering a quantum bath (or reservoir)—a controlled environment to which the system is coupled (*3*, *4*). On page 1424 of this issue, Selim *et al.* (*5*) report a new way to filter entangled photons by exploiting a fundamental physics concept that is extensively applied in classical context, called non-Hermitian symmetries. This could offer a new way of solving a key challenge in quantum technology.

Non-Hermitian Hamiltonian (a mathematical operator describing the energy of a system) characterizes a class of open systems in which the interaction with external environments can be seen as amplifications (gains) or decays (losses) of energy. The field of non-Hermitian physics is well known for using these energy gains or losses to showcase exotic properties and effects of systems, such as single-mode lasing and enhanced sensing (*6*). Many of these properties primarily originate from underlying mathematical symmetries, such as parity-time symmetry, in which gain and loss are balanced (*7*, *8*). Although most applications

Department of Physics, McGill University, Montreal, QC, Canada. Email: k.wang@mcgill.ca

in non-Hermitian physics have been in classical systems, such as wave optics, there are emerging efforts to use non-Hermitian symmetries to control quantum states.

Selim *et al.* engineered a quantum state filter to control photons by leveraging a type of non-Hermitian symmetry called anti–parity-time symmetry. To understand this approach, imagine an opposite scenario in which photons pass through a Hermitian system, specifically a pair of coupled optical waveguides (a pipelike structure for light to propagate inside) known as a directional coupler. This two-waveguide configuration exhibits two orthogonal eigenmodes (stationary modes with a specific spatial profile, symmetric or antisymmetric depending on whether the amplitudes of photons in the two waveguides are in phase or out of phase, respectively). Hence, light propagates through the waveguides at their respective speeds without a decay in energy and preserve their original modal symmetries. By contrast, the non-Hermitian system used by Selim *et al.* passes only the antisymmetric spatial mode (see the figure). At the same time, the symmetric spatial mode decays exponentially. When photons propagate in the system for a sufficiently long distance, only photons with an antisymmetric spatial profile survive, whereas others are filtered out. Thus, if the incoming photons are in a mixed state of the two orthogonal modes (symmetric and antisymmetric), the photon state at the output becomes a pure, entangled state again.

Selim *et al.* applied a special non-Hermitian system exhibiting anti–parity-time symmetry in which each waveguide in the system experiences a photon loss at the same rate. Additionally, the loss in one waveguide is linked to light traveling in the other waveguide through dissipative coupling—the amplitude of light in one waveguide controls the rate of light decay in the other waveguide. This configuration with photon losses including the dissipative coupling is the key to achieving the desired filtering effect. However, it is difficult to achieve this design because it requires that the two waveguides interact with a shared, tailored quantum bath in the same manner. One possible solution is to link each waveguide to a sufficiently large number of other isolated waveguides. This creates a bath analogous to a continuous-energy environment, giving rise to the desired dissipative coupling (*5*). However, coupling each waveguide to all these waveguides remains impractical.

Selim *et al.* solved this problem by using the Lanczos transformation—an iterative algorithm that converts a complex matrix into a tridiagonal form (*9*). This method can turn a highly complicated, multidimensional coupled lattice of waveguides into a one-dimensional lattice in which only the nearest neighbors interact while keeping the dynamics of a selected waveguide (*10*). Selim *et al.* produced a quasi-infinite one-dimensional array of coupled waveguides to act as the quantum bath. The array of 52 waveguides worked together as a reservoir that collects light at a rate proportional to the sum of amplitudes of light in both waveguides. The quantum bath of Selim *et al.* filtered arbitrary one- and two-photon entangled states with excellent performance. In each case, the only antisymmetric spatial mode was transmitted through a coupled-waveguide system unaffected, while the noise was dumped into the one-dimensional array of waveguides acting as the quantum bath. This concept was demonstrated in an on-chip photonic system composed of multiple waveguides. This on-chip entanglement filter creates highly controllable photon dissipations by selecting a system's output without relying on intrinsic losses from engineered material absorptions.

Although Selim *et al.* have demonstrated a filter for inputs containing up to two photons, the method could be expanded for an arbitrary number of photons. A large-scale quantum bath is particularly intriguing for generating a NOON state (*11*), a many-body entangled state with a superposition of N photons in a single mode. NOON states are of particular interest in quantum sensing and metrology (*12*) because of a phase error that scales inversely proportional to N. Whether an anti–parity-time symmetric system can help create or filter a wide range of other entangled states, such as the entangled coherent state (*13*), is also of interest. Beyond photons, the approach of Selim *et al.* could potentially be used for different particles on various quantum platforms, such as cold atoms with real-time filtering of noises to maintain atoms in pure, entangled states. ■

Filtering entangled photons through fundamental symmetries

A controlled environment, called a quantum bath, is engineered to filter unwanted noises from the incident light and deliver purely entangled photons at the outlet. A quasi-infinite one-dimensional (1D) array of inhomogeneously coupled waveguides facilitates this filtering process and realizes an anti–parity-time symmetric system. Only photons in a desired spatial profile (antisymmetric) propagate through the waveguides, whereas the rest decays exponentially.

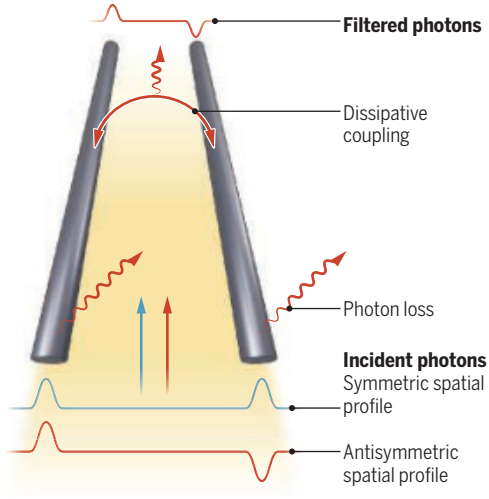

Anti–parity-time symmetry
Two waveguides, which have the identical rate of photon loss, are linked by dissipative coupling in which the amplitude of light in one waveguide controls the rate of light decay in another. This anti–parity-time symmetric system only transmits photons with an antisymmetric spatial profile.

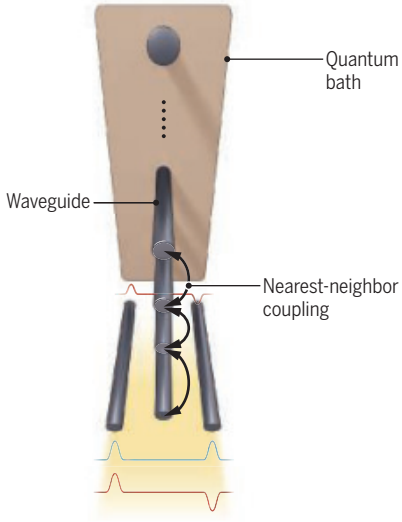

Quantum bath engineering
A complex lattice of waveguides acting as a quantum bath is converted into a simple 1D array by using the Lanczos transformation. The engineered quantum bath is a key component for the on-chip photonic system for filtering entanglement.

GRAPHIC: A. FISHER/*SCIENCE*

REFERENCES AND NOTES

1. R. Horodecki, P. Horodecki, M. Horodecki, K. Horodecki, *Rev. Mod. Phys.* **81**, 865 (2009).
2. W. H. Zurek, *Rev. Mod. Phys.* **75**, 715 (2003).
3. R. Okamoto *et al.*, *Science* **323**, 483 (2009).
4. H.-P. Breuer, F. Petruccione, *The Theory of Open Quantum Systems* (Oxford Univ. Press, 2002).
5. M. A. Selim *et al.*, *Science* **387**, 1424 (2025).
6. R. El-Ganainy *et al.*, *Nat. Phys.* **14**, 11 (2018).
7. C. M. Bender, S. Boettcher, *Phys. Rev. Lett.* **80**, 5243 (1998).
8. A. Guo *et al.*, *Phys. Rev. Lett.* **103**, 093902 (2009).
9. C. Lanczos, *J. Res. Natl. Bur. Stand.* **45**, 255 (1950).
10. L. J. Maczewsky *et al.*, *Nat. Photonics* **14**, 76 (2020).
11. H. Lee, P. Kok, J. P. Dowling, *J. Mod. Opt.* **49**, 2325 (2002).
12. V. Giovannetti, S. Lloyd, L. Maccone, *Science* **306**, 1330 (2004).
13. B. C. Sanders, *Phys. Rev. A* **45**, 6811 (1992).

10.1126/science.adw3165

POLICY FORUM

SCIENCE AND TECHNOLOGY POLICY

Guiding science in China

Increasing emphasis on national priorities creates tension with curiosity-driven research

By **Andrew Kennedy**

China's emergence as a science power is extraordinary. China now publishes more scientific papers than any other country, and the impact of this research (although trickier to measure) is impressive (*1*). Despite China's remarkable progress, its policymakers continue to grapple with a basic question that all countries face: how to balance between promoting research focused on national priorities and that driven by academic curiosity. This article begins by explaining how Chinese policy-makers have recently stepped up efforts to guide science in keeping with national priorities, including economic, environmental, and national security concerns. It then notes an important countercurrent, particularly the growing interest in "original innovation" and the appreciation that curiosity-driven research has a role to play in this regard. It concludes by noting that China is part of a broader international shift to leverage science for national purposes, and by highlighting the risks this trend entails.

GUIDING CHINESE SCIENCE

China's government has a long tradition of supporting scientific research aimed at national priorities. In the 1950s, the country's first science and technology (S&T) plan was dominated by more than 50 practical tasks related to economic development and national defense. Particular attention was given to research on atomic energy and missile technology, which supported the country's nascent nuclear weapons program. By contrast, communist ideology and central planning meant that support for scientific curiosity was very limited (*2*).

Support for scientific curiosity became more apparent starting in the 1980s, following landmark reforms that liberalized China's S&T system. The creation of the National Natural Science Foundation of China (NSFC) in 1986 was particularly noteworthy in this regard. Some NSFC programs began supporting projects driven by the interests of scientists, giving curiosity-driven research a space in which to grow. The foundation's largest funding stream—which came to be called the "General Program"—was one of these. As of 2012, the General Program accounted for roughly half of all NSFC research spending.

The past decade has seen Chinese leaders refocus their attention on leveraging research for national priorities, especially as the Sino-American "tech war" has deepened and China has increased its efforts to become more self-reliant. This trend is apparent even as the Chinese government has strengthened support for basic research: The latest 5-year plan aims to raise national spending on basic research to 8% of the country's research and development expenditure by 2025, up from 6% in 2020. There is no contradiction here: Chinese leaders believe that research on basic scientific questions may be driven by academic curiosity or by practical goals, and they are urging China's scientists to combine the two—a mentality that resonates with the concept of "Pasteur's quadrant" in the West (*3*). In 2018, China's State Council issued opinions on basic research that called for "organically combining free exploration and goal-oriented" science. In September 2020, President Xi Jinping personally underscored the point, exhorting China's scientists to "integrate your own scientific pursuits into the great cause of building a modern socialist country."

"The past decade has seen Chinese leaders refocus their attention on leveraging research for national priorities..."

More concrete efforts to guide scientific research have taken shape on multiple fronts. In 2018, the NSFC was placed under the supervision of the Ministry of Science and Technology (MOST), though it maintained independent operations and a separate budget (*4*). Three months later, newly appointed MOST Minister Wang Zhigang addressed NSFC leaders and highlighted several priorities for reform. These included "improving the project topic selection mechanism to more prominently reflect the national will and strategic needs," as the *S&T Daily*'s summary put it (*5*).

Changes in NSFC funding patterns have become apparent since then. Between 2016 and 2023, total spending on the General Program fell from 45 to 35% of NSFC research funding (see figure). In absolute terms, in fact, total spending on the General Program was lower in 2023 than it was in 2018. By contrast, the share of funding for application-oriented projects conducted jointly with other organizations has grown. These projects allow the NSFC to work with central government departments, enterprises, and localities, transforming their needs into scientific problems. New collaborative initiatives include a regional innovation and development fund (which works with subnational governments) and an enterprise innovation and development fund. The NSFC has also established joint funds with China National Nuclear Corporation, the China Academy of Engineering Physics, and the aviation industry, among other partners. Overall, funding for joint projects nearly tripled between 2016 and 2023, rising from 5 to 10% of all NSFC funding (see supplementary materials).

The Ministry of Education (MOE) has supported the effort to guide scientific research as well. Since 2019, for example, the Ministry has created at least 30 "integrated research platforms" (IRPs) to focus work on national strategic needs at Chinese universities. Specific topics range from carbon neutrality to artificial intelligence (AI) to medical devices. Sichuan University's Carbon Resource Neutrality IRP, for example, focuses on converting waste carbon products such as biomass and carbon dioxide into green materials, fuels, and chemicals. Starting in 2022, the MOE began promulgating the term "organized scientific research" to describe its efforts to align university research with the government's high-tech priorities (*6*).

More broadly, the central and subnational governments in China have encouraged the formation of "innovation consortia" in recent years, and these promote collaboration between academic and nonacademic entities on a range of technological priorities. Membership in these consortia can include firms, universities, research institutes, and national laboratories, and the members are typically linked

Crawford School of Public Policy, College of Law, Governance and Policy, The Australian National University, Canberra, Australia. Email: andy.kennedy@anu.edu.au

by contractual arrangements that specify goals and rewards. The 3C Intelligent Manufacturing Innovation Consortium, for example, was established in 2022 by the firm Xiaomi and more than 40 other organizations, including Tsinghua University. The number of these consortia appears to be growing rapidly, as subnational targets have proliferated in recent years. The city of Xiamen seeks to create 10 consortia by 2025, Beijing is aiming for 20, and Zhejiang province hopes to create 50. There are probably hundreds of innovation consortia active in China already (*7*).

China's leadership has also unveiled a new governance structure to preside over these initiatives. In March 2023, China announced the establishment of the Central S&T Commission (CSTC). This new high-level commission is a party body, and it is chaired by Ding Xuexiang, a member of the elite politburo standing committee and a close ally of President Xi Jinping. The commission also appears to include minister-level officials from a variety of different S&T-related bodies within the Chinese government.

Although information about the CSTC is limited, it is clearly politically powerful and enjoys wide-ranging authority. It appears to play a major role in S&T spending decisions, and its provincial-level versions have sought to promote work on top-priority technologies and to coordinate efforts underway at national laboratories, state enterprises, and universities (*8*). The new commission has also approved new S&T megaprojects, including one focused on deep earth exploration and mining. The CSTC is supported by a General Office based in MOST, which manages such daily responsibilities as reviewing and approving government-supported S&T labs and collecting reports from other ministries. Overall, the governance reforms should provide Chinese leaders with greater capacity to guide the country's increasingly voluminous scientific research going forward (*9*).

A COUNTERCURRENT

Even as China's leaders are encouraging research on national priorities, they also appreciate that curiosity-driven research has a role to play. In 2016, the government's "Innovation-Driven Development Strategy" highlighted the need for China to pursue "original innovation," rather than simply following in the footsteps of others. Toward this end, the document touted the need for both research aimed at national strategic needs and that driven by the interests of scientists. Or as Xi Jinping has put it more recently, China must "walk on two legs" by striking some kind of balance between goal-oriented and curiosity-driven research.

Support for curiosity-driven research has been evident on multiple fronts. In 2020, MOST and four other government agencies released an authoritative "work plan" to generate more "original results" from China's scientists engaged in basic research. The plan notably called for "encouraging free exploration and giving scientific researchers more academic autonomy." It also called for "expanding the autonomy" of universities and research institutes in disciplinary focus and research topic selection (*10*).

This orientation has been apparent in the government's support for elite young scientists, who are seen by Chinese leaders as particularly likely to produce important breakthroughs. The 2020 work plan not only called for "seizing the peak of young and middle-aged people to achieve original breakthroughs" but also "encouraging young scientists to choose their own topics." Accordingly, the NSFC has intensified its support for younger scientists in recent years. Overall, between 2016 and 2023, NSFC programs focused on young scientists increased their share of foundation disbursements from 19 to 26%, while spending on these programs nearly doubled in absolute terms (see supplementary materials). Like the General Program, these programs fund projects chosen by the researcher, creating opportunities for curiosity-driven research.

Support for scientific curiosity is also evident in an initiative—the "Original Exploration Plan"—launched by the NSFC in 2019 to promote important new breakthroughs. The plan includes two funding streams. One of these, the "expert recommendation" stream, accepts applications without regard to academic field or research direction, as long as the application is supported by two senior experts or two foundation officials. Between 2020 and 2022, the foundation funded 142 projects through this stream (*11*).

The Original Exploration Plan's second funding stream—the "guidance" stream—is more targeted. For this stream, the foundation publishes guidelines that specify particular fields and directions and welcomes applications in those areas. The foundation states that the guidelines reflect suggestions from scientists, discussions in academic forums, and expert demonstrations. Although more focused, therefore, this stream is guided by the scientific community, and it offers opportunities for curiosity-driven research in particular areas. Between 2020 and 2022, the foundation funded 171 projects through this stream (*11*).

Nonetheless, even as the Chinese government seeks to promote "original innovation," its enthusiasm for curiosity-driven research should not be overstated. Although the 2020 work plan encouraged academic autonomy, it also highlighted national priorities, and it called for "adhering to a demand orientation" and "guiding scientists to closely combine their personal interests in scientific research activities with national strategic needs." Accordingly, there are concerns that curiosity-driven research is undervalued.

Such concerns have been aired openly. Scholars at the Chinese Academy of Sciences have argued that basic research in China continues to be largely "government-guided" and "task-oriented," rather than led by the initiative of individual scientists, impeding originality and the use of scientific talent. In this context, they have criticized the decline of the NSFC's General Program

A shrinking profile for the General Program

Between 2016 and 2023, total spending on the General Program (GP), the largest funding stream of the National Natural Science Foundation of China (NSFC), fell from 45 to 35% of NSFC research funding.

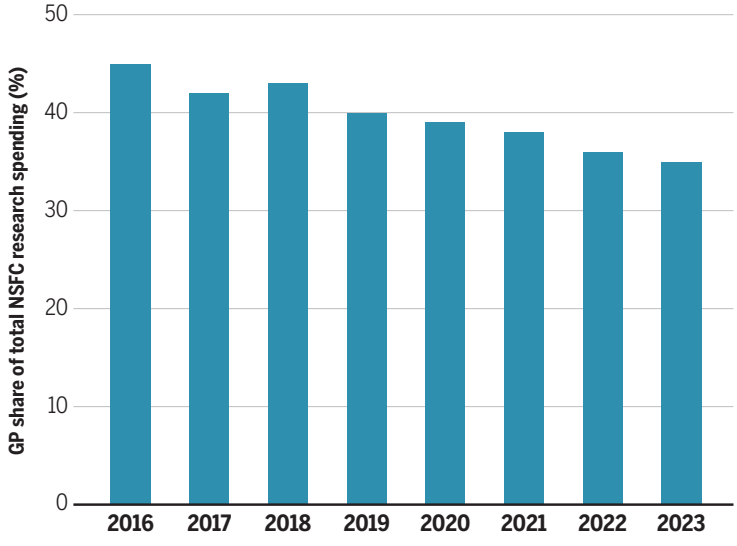

GRAPHIC: V. PENNEY/*SCIENCE*; (DATA) NATIONAL NATURAL SCIENCE FOUNDATION OF CHINA ANNUAL REPORTS 2016–23

and called for greater support for "curiosity-driven research" (*12*).

A GLOBAL SHIFT, DANGERS THEREIN

Although China is a striking case, governments in many Western countries are experimenting with more active guidance of science, technology, and innovation (STI) as well. Faced with challenges ranging from climate change to geopolitical tensions, governments are pursuing "transformative change," as the Organisation for Economic Co-operation and Development (OECD) has put it, which "requires STI policies to be more directional." Providing such direction can include government guidance along many different parts of the "innovation chain," including scientific research conducted at universities, in pursuit of transformative goals (*13*).

The United States clearly moved in this direction during the Biden administration, which embraced industrial policy as part of a broader effort to compete with China. This shift had important implications for science policy. In 2022, for example, the CHIPs and Science Act established the Directorate for Technology, Innovation, and Partnerships (TIP) at the National Science Foundation—the first new NSF directorate in 30 years. TIP has supported both use-inspired and translational research in priority areas, including AI, biotechnology, advanced communications technology, and data storage. What the future holds in this regard is now unclear, as President Donald Trump has begun his second term with unprecedented changes and proposals that have rocked the US scientific community. It is apparent that the new administration has its own high-tech agenda, however, with priorities including AI and quantum computing.

However U.S. policy evolves in the years to come, the growing interest in guiding science toward public priorities in both China and the West is not about to disappear. This shift has the potential to generate important breakthroughs on a variety of fronts, but it also poses serious risks. One risk is that cross-border collaboration will become more difficult as scientific research becomes more intertwined with national agendas and geopolitical tensions. Indeed, geopolitical tensions have already had a chilling effect on the flow of scientific ideas and talent between the United States and China (*14*). Although the renewal of the US-China agreement governing government-to-government scientific cooperation in late 2024 was an encouraging development in this regard, the impact of geopolitics was evident here as well: The pact does not support the development of critical and emerging technologies, and US agencies will vet projects for national security risks. Looking ahead, the impact of geopolitical tensions could become much more pronounced in the future, particularly if tensions between the United States and China escalate during the second Trump administration.

A second risk is the potential for curiosity-driven research to suffer further neglect. In China, the decline of the NSFC's General Program is already evident, and its future remains unclear. NSFC officials have been impressed by the level of funding initially authorized for the US TIP initiative, calling it an "inspiration," and proposed that their foundation devote greater resources to national needs and develop a wider range of programs in this regard (*15*). In the United States, although the CHIPs and Science Act promised to double NSF spending, Congress cut the agency's budget by 8% in 2024, amid wider cuts to federal science agencies. In 2025, a more profound form of neglect has become apparent, as curiosity-driven science (and academic research more generally) has suffered amid the layoffs, restrictions, and efforts to limit federal spending imposed by the Trump administration.

> **"...we should strive to avoid a world in which science is an increasingly nationalistic endeavor..."**

The drive to guide scientific research in pursuit of national priorities must be mindful of these risks and dangerous trends. Although scrutiny of cross-border collaboration is warranted, Western countries should be wary of isolating themselves from China as it becomes an increasingly important source of scientific knowledge. China could reassure other countries, in turn, by becoming more transparent about its plans and policies in this domain. In addition, governments must ensure that support for curiosity-driven research remains robust. Such research is critical for developing and sustaining the broad stock of knowledge without which many innovations—from mRNA vaccines to quantum computers—would not be possible. Neglecting such research while expanding support for near-term priorities, therefore, is short-sighted. In the end, transformative change may require greater government guidance, both in China and elsewhere. Even so, we should strive to avoid a world in which science is an increasingly nationalistic endeavor and in which scientific curiosity is increasingly marginalized. ■

REFERENCES AND NOTES

1. S. Qiu, C. Steinwender, P. Azoulay, "Paper Tiger? Chinese Science and Home Bias in Citations," National Bureau of Economic Research Working Paper, 2024; https://www.nber.org/papers/w32468.
2. C. Zhou, "'Kexue Jihua' Haishi 'Fangren Ziliu': Xin Zhongguo Jichu Yanjiu de Gainian yu Zhengce Yanbian ('Scientific planning' or 'letting it go': The concept and policy evolution of basic research in New China)," Zhongguo Ruankexue (China Soft Science) (no. S01), 55 (2023).
3. D. E. Stokes, Pasteur's Quadrant: Basic Science and Technological Innovation (Brookings Institution Press, 1997).
4. Y. Sun, C. Cao, The Political Economy of Science, Technology, and Innovation in China: Policymaking, Funding, Talent, and Organization (Cambridge Univ. Press, 2023).
5. X. Cao, "Xin Shidai Kexue Jijin Gaige Lujing Queli (Establishing a Path for Science Foundation Reform in the New Era)," Keji Ribao (S&T Daily), 21 June 2018; https://www.nsfc.gov.cn/publish/portal0/tab440/info73880.htm.
6. M. Laha, "China's Endless Frontier: 'Organized Scientific Research' and the Quest for Technological Self-Reliance," IGCC and MERICS, San Diego and Berlin, 2024; https://ucigcc.org/publication/chinas-endless-frontier-organized-scientific-research-and-the-quest-for-technological-self-reliance/.
7. B. Naughton, *Curr. Hist.* 123 (suppl. 1), 9 (2024).
8. J. Goodrich, "Reading the Tea Leaves on China's New Science and Technology Commission," IGCC, 25 September 2024; https://ucigcc.org/blog/reading-the-tea-leaves-on-chinas-new-central-science-and-technology-commission/.
9. B. Naughton *et al.*, "Reorganization of China's Science and Technology System," IGCC Working Paper No. 10, 2023; https://ucigcc.org/publication/reorganization-of-chinas-science-and-technology-system/.
10. Ministry of Science and Technology, National Development and Reform Commission, Ministry of Education, Chinese Academy of Sciences, and National Natural Science Foundation of China, "Jiaqiang 'Cong 0 Dao 1' Jichu Yanjiu Gongzuo Fangan (Work Plan for Strengthening 'From 0 to 1' Basic Research)," 21 January 2020; https://www.cas.cn/zcjd/202003/t20200303_4736354.shtml.
11. S. Zhang, "Guojia Ziran Kexue Jijin Yuanchuang Tansuo Jihua Shidian Xian Chengxiao (National Natural Science Foundation Original Exploration Plan Pilot Shows Results)," Zhongguo Kexuebao (China Science News), 11 April 2023.
12. H. Zhou, Y. Chen, "Woguo Jichu Yanjiu Fazhan Zhanlue Lujing Xuanze Qianxi (Analysis of the Strategic Path Choice of China's Basic Research Development)," Keji Guanli Yanjiu (S&T Management Research), no. 10 (2023), pp. 1–7.
13. OECD, "OECD Agenda for Transformative Science, Technology and Innovation Policies," OECD Science, Technology and Industry Policy Paper no. 164, 2024; https://www.oecd.org/en/publications/2024/04/oecd-agenda-for-transformative-science-technology-and-innovation-policies_5ced463a.html.
14. R. Flynn, B. Glennon, R. Murciano-Goroff, J. Xiao, "Building a Wall Around Science: The Effect of U.S.-China Tensions on International Scientific Research," National Bureau of Economic Research Working Paper, 2024; https://www.nber.org/papers/w32622.
15. J. Luo, J. Chen, "Meiguo Guojia Kexue Jijinhui Xin Xuebu Xiangmu Shezhi Dui Kexue Jijin Zizhu Yingyong Yanjiu de Qishi (The inspiration of the US National Science Foundation's new department for funding applied basic research)," Zhongguo Kexue Jijin (China Science Foundation) 38, 328-334 (2024).

ACKNOWLEDGMENTS

The author gratefully acknowledges valuable feedback on the manuscript from the anonymous reviewers and from C. Cao. He also thanks J. Zhan for excellent research assistance and the ANU Centre on China in the World for funding support. The views expressed in the article are those of the author and are not necessarily shared by those who have commented on or supported the work.

SUPPLEMENTARY MATERIALS

science.org/doi/10.1126/science.ads9216

10.1126/science.ads9216

BOOKS *et al.*

Intensified poultry farming highlights a growing disconnect between food and its associated harms.

PHOTO: AFP VIA GETTY IMAGES

FOOD SYSTEMS

The meaning of our meals

A philosopher confronts how factors from culture to capitalism affect the foods we eat

By **Stefania Pizzirani**

Why do you eat the foods you eat? Perhaps you are trying to maintain a healthy, nutritious diet. Or maybe you decide your meals according to your budget, first and foremost. Do environmental or animal ethics play a role in your choices? How do culture and heritage influence your eating habits? How do societal systems, such as capitalism, affect the foods you see in your local supermarket? As I read the book *How the World Eats* by Julian Baggini, I began reflecting on these questions and more.

Baggini—a philosopher and journalist—applies an interdisciplinary lens as he disentangles and describes the evolutionary complexities of our global food system. Indeed, the integrated and collaborative "One Health" approach is seen in the structural organization of the book, which is broken down into four categories: land, people, other animals, and technology.

How the World Eats: A Global Food Philosophy
Julian Baggini
Pegasus, 2025. 464 pp.

I admit that at times I wondered why a philosopher was attempting to weigh in on agricultural histories, legacies, triumphs, and tragedies. Yes, there were gross oversimplifications dotted throughout the book—for example, in the author's portrayal of farming as a method of advancing oppression or in his descriptions of the impacts of supposedly "sustainable" intensification of agricultural practices. (It is hard to imagine anything sustainable about a farm in the UK that keeps up to 1.4 million birds or a 26-story farm in China processing 1.2 million pigs a year.) And yet there were many other areas where a philosopher's eye brought a refreshing alternative and nuanced view to the relationships that connect us—not always favorably—to our foods.

Baggini navigates the growing tension between profit and purpose within modern food corporations. Over recent decades, high-fat, -sugar, and -salt foods have overwhelmingly been marketed toward children through targeted advertisements and "pouring rights" (exclusive licenses) for companies to sell their sugary drinks in school districts. "Commercial pressures erode values," Baggini states.

Understanding the ethics of our food system—past, present, and future—is the common denominator in this book. Of particular note are Baggini's efforts to highlight and pay respect to Indigenous sciences, cultures, practices, and perspectives. Again, is there room for improvement here? In short, yes. Baggini cites few Indigenous authors, minimizes the ongoing impacts of colonialism, and brusquely dismisses certain cultural beliefs held by the Inuit and Maasai as being untrue (at least in the eyes of Western science). The point is made, however, that there is no single correct "science" or way of studying and interpreting the world around us. Both Indigenous and Western science "can be seen as complementary routes" that lead us to empirical knowledge.

Indigenous cultures across the world have gained and expanded their empirical (or experiential) knowledge of food and nourishment over millennia, with many teachings emphasizing the interconnectedness—the kinship—between all living things. The Maasai, for example, "share the life of the cow" by drinking its milk. What then, I wonder, is our kinship to the humble chicken?

When frying an egg or roasting a chicken, we are subsequently grateful for our full bellies. But do we also acknowledge a shared relationship with the impacts of intensified poultry farms—for instance, that the male chicks are killed (literally shredded alive or gassed) within a day of hatching because they do not lay eggs or produce valued meat? Time and time again, Baggini describes a growing disconnect between eating food and understanding the associated harms that may be caused along the way to your plate.

It is absolutely true that not all farms are unsustainable, not all foods are unethical, and not all agri-food companies are corrupt. The diversity of farming techniques, technologies, and traditions is too varied to generalize. This is not a simple tale of heroes and villains. Yet, Baggini highlights warning signs that we should not ignore: Nearly 1 in 10 fish stocks have been driven to collapse, around a third of food produced is not consumed (it is either wasted or lost), rampant exploitation of workers exists, extreme weather is creating more cracks in an already vulnerable system, and more.

The author is mindful to assert that there is no "one size fits all" approach to agriculture and food production. Instead, we must acknowledge power and privilege to "use every acre of the planet in the way that most suits it." The food world, he argues, must be considered as a whole system. This is a wonderful perspective to advocate for alongside circularity and holism. (Holism is akin to the aforementioned interconnectedness worldview that many Indigenous communities hold.) Using this framework, Baggini ends the book in a way that attempts to empower the reader into advocating for food system justice, now and in the future. ■

The reviewer is at the Food and Agriculture Institute and the Department of Planning, Geography, and Environmental Studies, University of the Fraser Valley, Abbotsford, BC, Canada. Email: stefania.pizzirani@ufv.ca

10.1126/science.adu6373

EXTINCTION

An end to human exceptionalism

Our species' extinction is inevitable, argues a paleontologist

The Decline and Fall of the Human Empire: Why Our Species Is on the Edge of Extinction
Henry Gee
St. Martin's Press, 2025. 288 pp.

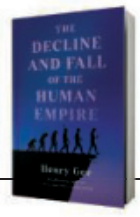

By **Adrian Woolfson**

In the *Aeneid*, the poet Virgil portrayed the rise of the Roman Empire as the preordained culmination of history's momentum. Yet, as the 18th-century historian Edward Gibbon chronicled in *The History of the Decline and Fall of the Roman Empire*, the seeds of Rome's annihilation were sown long before its decline. Factors such as hubris, moral decay, overexpansion, corruption, and political instability ensured that, even at the height of its power, the empire was headed toward self-destruction.

Like ancient Rome, the history of life on Earth has been shaped by its own triumphant, yet catastrophic, Darwinian narrative. Today, more than 99% of species that have ever existed are now extinct (*1*). And despite our belief in human exceptionalism, *Homo sapiens* seems no more immune to the patterns of history than other species.

In his bold and insightful *The Decline and Fall of the Human Empire*, paleontologist Henry Gee presents a sobering vision of humankind's future, as intriguing as it is unsettling. Despite our technological prowess and capacity for imagination, he argues, *Homo sapiens* is "marked for extinction."

The rot, he suggests, set in when we hunted down and extinguished Neanderthals, Denisovans, and the diminutive "hobbit men" *Homo floresiensis* and *Homo luzonensis*. Suddenly, we had no competition, something as necessary for success as the "irritating grit in an oyster" that creates a pearl.

This was compounded by the invention of agriculture around 12,000 years ago and the selective breeding of high-yielding crops during the Green Revolution of the 1980s. The former transformed a dispersed species of hunter-gatherers—perpetually teetering on "the edge of oblivion"—into a global population of billions. The latter allowed humanity to defy biologist Paul Ehrlich's apocalyptic predictions that the unchecked increase in global population would outstrip Earth's resources, resulting in widespread famine (*2*).

But, Gee argues, progress cannot be indefinitely sustained. While postponing disaster, the Green Revolution and other efforts, such as using genetic engineering to rewrite crop genomes, are unlikely to avert it. We face an impending food security crisis.

Other potential threats to human existence range from nuclear and biological warfare, greenhouse gas–induced climate change, and artificial general intelligence (AGI) to pandemics, volcanic eruptions, and asteroid impacts. But the most immediate threat is the loss of global habitats. Even moderate loss may lead to an "extinction debt," causing the eventual "extinction of the dominant competitor in remnant patches" (*3*). Unfortunately, the "dominant competitor" in this scenario is humankind.

The astonishing creativity of humans relies on their vast populations. As Gee notes, "it takes a civilization of billions to create an Einstein." Yet, following an uninterrupted period of expansion, humankind now faces the prospect of transitioning to a phase of population decline. A significant milestone occurred in 2022, when, for the first time, more people died in China than were born. A similar trend is occurring in countries such as Japan, Thailand, Italy, and Spain.

The solution to this impending population calamity, Gee argues, is for humankind to expand its domain through the colonization of, and evolutionary diversification on, the Moon, Mars, and other planetary bodies. In so doing, Gee believes humans can rekindle the migratory wanderlust of their ancestors, using their intellectual agility to devise solutions for survival in hostile environments.

Although this vision is inspiring, some near-term issues appear at odds with its feasibility. The eventual attainment of AGI, for example, would likely reduce the need for flesh-and-blood Einsteins, allowing innovation in more-modest human populations. And while Gee advocates diverting resources to space travel and artificial ecosystems, many might argue that they would be better deployed on conservation and engineering biology to generate sustainable systems.

Moreover, fostering the evolution of new posthuman species would not inevitably favor *Homo sapiens*. And, were we to acquire the ability to send humans to distant planets, it is unlikely that the colonies would be disconnected, as required for speciation. More optimistically, the impending reduction in the global population may help attain the audacious rewilding goals espoused by the late biologist E. O. Wilson (*4*).

Edward Gibbon believed that the principal cause of the Roman Empire's fall was the cultural shift invoked by Christianity. Perhaps an ideological shift will precipitate humanity's decline. Whatever the cause of our eventual demise, Gee's pessimistic predictions about our fate offer much to consider. ■

Human development threatens critical habitats and may eventually undermine our own existence.

PHOTO: ARTURO HERNÁNDEZ/NURPHOTO VIA GETTY IMAGES

The reviewer is chief executive officer, president, and cofounder of Genyro Inc., San Diego, CA, USA, and the author of *Life Without Genes* (HarperCollins, 2000). Email: adrianwoolfson@yahoo.com

REFERENCES AND NOTES

1. D. Jablonski, *Nature* **427**, 589 (2004).
2. P. Ehrlich, *The Population Bomb* (Ballantine Books, 1968).
3. D. Tilman, R. M. May, C. L. Lehman, M. A. Nowak, *Nature* **371**, 65 (1994).
4. E. O. Wilson, *Half-Earth: Our Planet's Fight for Life* (Liveright Publishing Corp., 2016).

10.1126/science.adt4075

PHOTO: LAJOS BERDE

Romania recently lifted a ban on hunting brown bears.

LETTERS

Edited by **Jennifer Sills**

Romanian brown bear management regresses

In 2016, Romania passed a ban on hunting bears (*1*), but in the years since, the country undertook no efforts to implement strategies to prevent human-carnivore interactions. In July 2024, the Romanian Parliament responded to a human fatality involving a brown bear by passing legislation that allowed hunters to kill 426 brown bears by the end of 2024 and an additional 426 individual bears in 2025 (*2*). The legislation emulates regulations in Sweden, but Sweden collects in-depth data about their brown bear population (*3*), whereas Romania lacks the relevant scientific data (*4*). The hunting quotas and management system included in this legislation will not address the risk of human-bear interactions and will undermine progress toward science-based management.

Hunting is unlikely to reduce human-bear conflict because the spatial distribution of quotas fails to take bear demography into account, and hunting does not necessarily target high-conflict areas or times of the year when conflict is most likely (*5*). Moreover, this approach ignores the roots of conflict, which include the management of factors that attract bears, such as waste and food; the habituation of bears to people; the degradation and fragmentation of habitats; tourism that involves unpredictable human behavior; and shifting perceptions of wildlife (*6*, *7*). Instead, the quota system encourages professional hunters, who keep pelts and skulls as trophies, to target the largest animals in the population (*8*). In addition to the lack of data informing the new policy, the legislation includes neither clear management objectives nor any measure that can be used to assess the cull's success on human-bear conflict mitigation.

Instead of relying only on hunting to decrease population size, Romania should implement proven strategies that promote coexistence. For example, the government could fund waste management that includes bear-proof containers, install warning signage for tourists in areas with a high density of bears and during sensitive periods, and ban people from feeding bears in urban and suburban areas. If other strategies fail, the government could facilitate the removal of problem bears on a case-by-case basis (*9*).

Romania should engage in public outreach and education to ensure that the public tolerates the level of brown bear abundance that is necessary for ecosystem sustainability (*10*). Romania's policies should also take into account the brown bear's status as a "strictly protected species" according to the Bern Convention (*11*). To protect its people and its bears, the Romanian government should capitalize on the growing knowledge generated by the scientific community and replace the hunting policy with a transparent, inclusive, multidisciplinary science–based wildlife management strategy.

Mihai I. Pop[1,2], Ruben Iosif[3], Barbara Promberger-Fürpass[3], Silviu Chiriac[4], Ágnes Keresztesi[1], Laurentiu Rozylowicz[5], Viorel D. Popescu[5,6]*

[1]Research and Development Institute for Wildlife and Mountain Resources, Miercurea-Ciuc, Harghita, Romania. [2]Association for Biodiversity Conservation, Focsani, Vrancea, Romania. [3]Foundation Conservation Carpathia, Brasov, Brasov, Romania. [4]Vrancea Environmental Protection Agency, Focsani, Vrancea, Romania. [5]Center for Environmental Research, University of Bucharest, Bucharest, Romania. [6]Department of Ecology, Evolution, and Environmental Biology, Columbia University, New York, NY, USA.
*Corresponding author.
Email: dvp2110@columbia.edu

REFERENCES AND NOTES

1. V. D. Popescu, M. I. Pop, S. Chiriac, L. Rozylowicz, *Science* **364**, 1041 (2019).
2. Portal Legislativ, Law 242/23.07.2024 [in Romanian]; https://legislatie.just.ro/Public/DetaliiDocument/285830.
3. C. Milleret, P. Dupont, G. Chapron, J. E. Swenson, R. Bischof, *Science* **385**, 1052 (2024).
4. V. D. Popescu, K. A. Artelle, M. I. Pop, S. Manolache, L. Rozylowicz, *J. Appl. Ecol.* **53**, 1248 (2016).
5. Romanian Ministry of Environment, "Brown bear authorizations and hunting report for 2024" (2024) [in Romanian]; https://www.mmediu.ro/articol/situatia-centralizata-privind-autorizatiile-si-rapoarte-le-de-derogare-intocmite-conform-l-242-2024-actualizate-la-data-de-31-12-2024/7759.
6. M. I. Pop *et al.*, *Cons. Sci. Pract.* **5**, e12884 (2023).
7. A. C. Neagu, S. Manolache, L. Rozylowicz, *Nat. Conserv.* **50**, 65 (2022).
8. V. D. Popescu, M. I. Pop, L. Rozylowicz, *Science* **372**, 1049 (2021).
9. M. L. Lute, N. H. Carter, J. V. López-Bao, J. D. C. Linnell, *Biol. Cons.* **218**, 223 (2018).
10. J. D. C. Linnell, L. Boitani, "Developing methodology for setting Favourable Reference Values for large carnivores in Europe" (European Commission, 2025).
11. A. Trouwborst, L. Boitani, J. D. C. Linnell, *Biodiv. Cons.* **26**, 37 (2017).

10.1126/science.adv0410

Equitable access needed in clinical research

In her News story "Cornerstone medical ethics guidelines get a major update" (1 November 2024, p. 473), C. O'Grady describes recent changes to the Declaration of Helsinki (*1*). Although the revision includes improvements, O'Grady explains that some issues were overlooked, such as obligations to research participants and their communities. These oversights are particularly stark in tuberculosis (TB) research, and the resulting disparities illustrate the importance of addressing inequities systemically.

Everyone has the right to enjoy the benefits of scientific progress and its applications (*2*, *3*), but this right remains neglected in the design, implementation, and application of TB clinical research. TB disproportionately affects communities in resource-poor settings (*4*), and the development of new drugs and diagnostics requires research participation from local populations. Yet disparities result from the lack of preapproval (*5*) and postapproval access (*6*) to medications. Early trials of the new TB drug delamanid, for example, were conducted in South Africa (*7*–*9*). When the drug was found to be effective, its cost was too high for widespread use in the country (*7*). Patent enforcement has further limited access to more affordable generic versions in South Africa and in other high-burden TB settings whose communities contributed to the drug's development (*10*).

Much more work is required to ensure equitable access to life-saving medical products. Instead of serving only as trial participants, vulnerable groups should participate in the full research process, from its conception through finalization. Vulnerable groups must benefit from the products they

helped to create. Too often, lack of preapproval access, such as compassionate use programs (also known as expanded access programs) that provide investigational drugs to those without other treatment options, prevents medications from reaching those who need them most. High pricing, enforcement of unjustified patents, and lack of product registration in the country of the clinical trial (a legal prerequisite before local procurement in all countries) can also hinder equitable access (*11*).

By failing to endorse preapproval and postapproval access for all populations, the updated Declaration of Helsinki misses an important opportunity to enshrine this right for the communities whose brave decisions to participate in clinical research benefit everyone. Therefore, product and research sponsors must include posttrial access plans at the time of protocol submission, and governments must hold them accountable for delivering on these access plans. To uphold human rights, the next amendment of the Declaration must codify pre- and postapproval access to the fruits of research.

Gisa Dang[1]*, Christophe Perrin[2], Jennifer Furin[3]
[1]Treatment Action Group, San Diego, CA, USA. [2]Médecins Sans Frontières (Doctors Without Borders), Paris, France. [3]Department of Global Health and Social Medicine, Harvard Medical School, Boston, MA, USA.
*Corresponding author.
Email: gisadangjsh@gmail.com

REFERENCES AND NOTES

1. World Medical Association, *JAMA* **333**, 71 (2024).
2. M. Frick, I. Henry, E. Lessem, *Health Hum. Rights* **18**, 9 (2016).
3. United Nations, "International Covenant on Economic, Social and Cultural Rights, Article 15" (1966); https://www.ohchr.org/en/instruments-mechanisms/instruments/international-covenant-economic-social-and-cultural-rights.
4. S. Litvinjenko *et al.*, *Lancet Infect. Dis.* **23**, 1395 (2023).
5. C. A. Rodriguez *et al.*, *Pub. Health Action* **9**, 32 (2019).
6. E. Lessem *et al.*, *Int. J. Infect. Dis.* **32**, 56 (2015).
7. M. Pai, J. Furin, *eLife* **6**, e25956 (2017).
8. Otsuka Pharmaceutical Development & Commercialization, Pharmacokinetic and safety trial to determine the appropriate dose for pediatric patients with multidrug resistant tuberculosis, ClinicalTrials.gov ID NCT01856634 (2018); https://clinicaltrials.gov/study/NCT01856634.
9. Otsuka Frankfurt Research Institute GmbH, Safety, efficacy and pharmacokinetics of OPC-67683 in patients with pulmonary tuberculosis, ClinicalTrials.gov ID NCT00401271 (2007); https://clinicaltrials.gov/study/NCT00401271.
10. Médecins Sans Frontières, "DR-TB drugs under the microscope 2022" ed 8 (Médecins Sans Frontières, 2022); https://msfaccess.org/dr-tb-drugs-under-microscope-8th-edition.
11. J. E. Miller *et al.*, *JAMA Netw. Open* **4**, e217075 (2021).

10.1126/science.adv2394

OUTSIDE THE TOWER

Women-driven community education in Nepal

Under a tent near the local high school in rural Nepal, parents and teachers gathered on the grass to watch students perform the play they had written to emphasize the importance of maternal and neonatal health. The students playing doctors advised those playing parents-to-be that they should deliver in a hospital, attend routine pre- and postnatal checkups, and avoid smoking and alcohol consumption during pregnancy. The adults in the audience, who usually receive such messages only from members of nongovernmental organizations visiting from nearby cities, listened attentively. "We didn't realize our students were becoming such influential community leaders," one school principal remarked with pride.

The event was part of a community engagement initiative that we launched in 2024, supported by the Bill and Melinda Gates Foundation, to address urgent public health challenges in rural Nepal and strengthen science, technology, engineering, and mathematics (STEM) education. We developed a curriculum that included topics such as nutrition, infectious diseases, teenage pregnancy, and the basics of microbiome science in the context of diet and antibiotics. We used the lessons to train six Nepali women with basic nursing backgrounds, revising the curriculum along the way in response to their input about the needs of their communities. The nurses then led monthly discussion sessions with high school students, facilitating conversations that bridged scientific knowledge and local concerns. The students also took part in engaging activities such as debates, presentations, and performance arts. The performance about maternal health served as a testament to their newly gained knowledge.

Watching the students participate in community events to share their knowledge has reinforced our belief in the value of context-specific, community-driven engagement. We hope that the participants, including the trained nurses and the students, will continue to foster curiosity and trust in science in their communities, contributing to the development of the next generation of local public health advocates and leaders.

High school students in Nepal perform an original play about maternal health for the community.

PHOTO: AASHISH JHA

Arya Gautam[1], Sandesh Ghimire[1], Aashish R. Jha[2,3,4]*
[1]Sabitri Sciences, Kathmandu, Nepal. [2]Genetic Heritage Group, Program in Biology, New York University Abu Dhabi, Abu Dhabi, UAE. [3]Public Health Research Center, New York University Abu Dhabi, Abu Dhabi, UAE. 4Center for Genomics and Systems Biology, New York University Abu Dhabi, Abu Dhabi, UAE.
*Corresponding author. Email: jhaar@nyu.edu

10.1126/science.ads8799

Call for submissions

Outside the Tower is an occasional feature highlighting scientists' advocacy experiences. Submit your advocacy story at http://cts.sciencemag.org.

AAAS names 2024 Fellows

AAAS proudly congratulates the newly elected 2024 Fellows. In 2024, the AAAS Council elected 471 members as Fellows of AAAS. Election as a Fellow honors members whose efforts on behalf of the advancement of science or its applications in service to society have distinguished them among their peers and colleagues. Presented by section affiliation, they are:

Section on Agriculture, Food, and Renewable Resources

Eduard D. Akhunov, *Kansas State Univ.*

Frank Asche, *Univ. of Florida*

Pierluigi Bonello, *The Ohio State Univ.*

Dario Cantu, *Univ. of California, Davis*

Felix B. Fritschi, *Univ. of Missouri–Columbia*

Bin Gao, *Rensselaer Polytechnic Institute*

Rosemarie Wahnbaeck Hammond, *USDA-Agricultural Research Service*

Zhenli He, *Univ. of Florida*

Suat Irmak, *The Pennsylvania State Univ.*

Eugene F. Kelly, *Colorado State Univ.*

Jacek Koziel, *USDA-Agricultural Research Service*

Melissa Goellner Mitchum, *Univ. of Georgia*

Rodolfo M. Nayga Jr., *Texas A&M Univ.*

Lisa A. Schulte Moore, *Iowa State Univ.*

Libo Shan, *Univ. of Michigan*

David G. White, *The Univ. of Tennessee, Knoxville*

Huaijun Zhou, *Univ. of California, Davis*

Section on Anthropology

John W. Arthur, *Univ. of South Florida, St. Petersburg*

Kathryn Weedman Arthur, *Univ. of South Florida, St. Petersburg*

Jeremy DeSilva, *Dartmouth College*

Melissa Emery Thompson, *Univ. of New Mexico*

Stephen R. Frost, *Univ. of Oregon*

Lee T. Gettler, *Univ. of Notre Dame*

Julie A. Hoggarth, *Baylor Univ.*

Fatimah L.C. Jackson, *Howard Univ.*

John Sanders Krigbaum, *Univ. of Florida*

Arlene Miller Rosen, *The Univ. of Texas at Austin*

Richard J. Sherwood, *Univ. of Missouri School of Medicine*

Section on Astronomy

Aaron J. Barth, *Univ. of California, Irvine*

Carol A. Christian, *Space Telescope Science Institute*

Roger N. Clark, *Planetary Science Institute*

Karen J. Meech, *Univ. of Hawai`i*

Sally Oey, *Univ. of Michigan*

Daniel Wolf Savin, *Columbia Univ.*

Eric M. Schlegel, *The Univ. of Texas at San Antonio*

Gillian Wilson, *Univ. of California, Merced*

Section on Atmospheric and Hydrospheric Sciences

Hendratta N. Ali, *Fort Hays State Univ.*

Rajasekhar Balasubramanian, *National Univ. of Singapore (Singapore)*

Laura Gallardo, *Univ. of Chile (Chile)*

Matthew Huber, *Purdue Univ.*

Delphis F. Levia Jr., *Univ. of Delaware*

Xin-Zhong Liang, *Univ. of Maryland, College Park*

Anna M. Michalak, *Carnegie Institution for Science*

Stanley P. Sander, *NASA Jet Propulsion Laboratory, California Institute of Technology*

Noelle Eckley Selin, *Massachusetts Institute of Technology*

Armin Sorooshian, *Univ. of Arizona*

Section on Biological Sciences

Peter A. Abrams, *Univ. of Toronto (Canada)*

Alejandro Acevedo-Gutierrez, *Western Washington Univ.*

Ravi Allada, *Univ. of Michigan*

Sarah G. Allen, *National Park Service (Retired)*

Gaya K. Amarasinghe, *Washington Univ. School of Medicine in St. Louis*

William Bradley Barbazuk, *Univ. of Florida*

Uttiya Basu, *Columbia Univ. Vagelos College of Physicians and Surgeons*

Yehuda Ben-Shahar, *Washington Univ. in St. Louis*

Celeste A. Berg, *Univ. of Washington*

James M. Berger, *Johns Hopkins Univ. School of Medicine*

David Bilder, *Univ. of California, Berkeley*

Richard W. Blob, *Clemson Univ.*

Thomas Blumenthal, *Univ. of Colorado*

Alison Buchan, *The Univ. of Tennessee, Knoxville*

Donald H. Burke-Agüero, *Univ. of Missouri–Columbia*

Leslie G. Butler, *Louisiana State Univ.*

Stephen L. Cameron, *Purdue Univ.*

Isaac Cann, *Univ. of Illinois Urbana-Champaign*

Debabrata Chakravarti, *Northwestern Univ. Feinberg School of Medicine*

Fred Chang, *Univ. of California, San Francisco*

Kent D. Chapman, *Univ. of North Texas*

Frederic Chedin, *Univ. of California, Davis*

Sheue-yann Cheng, *National Cancer Institute, NIH*

David Johannes Clark, *Eunice Kennedy Shriver National Institute of Child Health and Human Development, NIH*

Gretchen Cara Daily, *Stanford Univ.*

Wu-Min Deng, *Tulane Univ. School of Medicine*

David Mark Diamond, *Univ. of South Florida*

Maria Gloria Dominguez-Bello, *Rutgers, The State Univ. of New Jersey*

Sharon Lafferty Doty, *Univ. of Washington*

Yali Dou, *Univ. of Southern California Keck School of Medicine*

Alejandro Estrada, *Universidad Nacional Autónoma de México (Mexico)*

Steven E. Finkel, *Univ. of Southern California*

Karen G. Fleming, *Johns Hopkins Univ.*

Polly Fordyce, *Stanford Univ.*

Velia M. Fowler, *Univ. of Delaware*

Jean Gautier, *Columbia Univ. Irving Medical Center*

Andrew J. Gow, *Rutgers Univ. Ernest Mario School of Pharmacy*

David E. Graham, *Oak Ridge National Laboratory*

Nick M. Haddad, *Michigan State Univ.*

Daniel A. Hahn, *Univ. of Florida*

Mark E. Hahn, *Woods Hole Oceanographic Institution*

Ian M. Hamilton, *The Ohio State Univ.*

Stephanie E. Hampton, *Univ. of California, Davis*

David Hasan, *Duke Univ.*

Arie H. Havelaar, *Univ. of Florida*

Katherine Henzler-Wildman, *Univ. of Wisconsin–Madison*

A. Randall Hughes, *Northeastern Univ.*

Mary Liz Jameson, *Wichita State Univ.*

Shingo Kajimura, *Beth Israel Deaconess Medical Center*

Susan Kalisz, *Univ. of Tennessee, Knoxville*

Jonathan Karn, *Case Western Reserve Univ.*

Kenneth Keiler, *The Univ. of Texas at Austin*

Carla F. Kim, *Boston Children's Hospital/Harvard Medical School*

Mitchell D. Knutson, *Univ. of Florida*

Stephen A. Krawetz, *Wayne State Univ.*

Raphael M. Kudela, *Univ. of California, Santa Cruz*

Soni Lacefield, *Geisel School of Medicine at Dartmouth*

Michael P. Lesser, *Univ. of New Hampshire*

Henry L. Levin, *Eunice Kennedy Shriver National Institute of Child Health and Human Development, NIH*

Michael Levin, *Tufts Univ.*

Ottoline Leyser, *Univ. of Cambridge (UK)*

Manuel Llinás, *The Pennsylvania State Univ.*

Shirley Luckhart, *Univ. of Idaho*

Soheila June Maleki, *USDA-Agricultural Research Service*

Harmeet Malhi, *Mayo Clinic*

Luciano M. Matzkin, *Univ. of Arizona*

Donald R. McCarty, *Univ. of Florida*

Duane D. McKenna, *Univ. of Memphis*

Helen McNeill, *Washington Univ. School of Medicine in St. Louis/WashU Medicine*

Virginia L. Miller, *Univ. of North Carolina at Chapel Hill*

Christine M. Moffitt, *Univ. of Idaho/US Geological Survey*

Nigel J. Mouncey, *US Department of Energy Joint Genome Institute, Lawrence Berkeley National Laboratory*

Kimberly L. Mowry, *Brown Univ.*

Luay Nakhleh, *Rice Univ.*

Thomas J. Near, *Yale Univ.*

Susanne Neuer, *Arizona State Univ.*

Karla M. Neugebauer, *Yale Univ.*

Madan K. Oli, *Univ. of Florida*

Matthew R. Parsek, *Univ. of Washington*

Susan L. Perkins, *City College of New York*

Jennifer Pett-Ridge, *Lawrence Livermore National Laboratory*

David W. Pfennig, *Univ. of North Carolina at Chapel Hill*

Bryan C. Pijanowski, *Purdue Univ.*

Robert C. Piper, *Univ. of Iowa*

David L. Popham, *Virginia Tech*

Anne Pringle, *Univ. of Wisconsin–Madison*

Gemma Reguera, *Michigan State Univ.*

Liam J. Revell, *Univ. of Massachusetts Boston*

Thomas J. Roberts, *Brown Univ.*

Craig R. Roy, *Yale Univ. School of Medicine*

Christopher Rudd, *Université de Montréal (Canada)*

Robert O'Mara Ryan, *Univ. of Nevada, Reno*

Tim Schedl, *Washington Univ. School of Medicine in St. Louis*

Paul A. Scheet, *The Univ. of Texas MD Anderson Cancer Center*

Barney A. Schlinger, *Univ. of California, Los Angeles*

Robert J. Schmitz, *Univ. of Georgia*

Brad Seibel, *Univ. of South Florida*

Sidney L. Shaw, *Indiana Univ. Bloomington*

Nadia D. Singh, *Oregon State Univ.*

Stephen A. Smith, *Univ. of Michigan*

Tobin R. Sosnick, *Univ. of Chicago*

Anne Spang, *Univ. of Basel (Switzerland)*

Jed P. Sparks, *Cornell Univ.*

Arun Srivastava, *Univ. of Florida College of Medicine*

Andrew Storfer, *Washington State Univ.*

Lucia Carol Strader, *Duke Univ.*

Aaron F. Straight, *Stanford Univ.*

Ramaswamy Subramanian, *Purdue Univ.*

Witold K. Surewicz, *Case Western Reserve Univ.*

Jil C. Tardiff, *Univ. of Arizona*

Gordon T. Taylor, *Stony Brook Univ.*

Michael Terns, *Univ. of Georgia*

Tina L. Tootle, *Univ. of Iowa*

Amy Lynn Toth, *Iowa State Univ.*

Jeffrey P. Townsend, *Yale Univ. School of Public Health*

Matthew J. Tyska, *Vanderbilt Univ.*

Stephen B. Vander Wall, *Univ. of Nevada, Reno*

Wilfred Vermerris, *Univ. of Florida*

Albrecht G. von Arnim, *The Univ. of Tennessee, Knoxville*

Eric J. Wagner, *Univ. of Rochester Medical Center*

Zhi Wei, *New Jersey Institute of T echnology*

Brant M. Weinstein, *Eunice Kennedy Shriver National Institute of Child Health and Human Development, NIH*

Matthew B. Wheeler, *Univ. of Illinois Urbana-Champaign*

Craig T. Woodard, *Mount Holyoke College*

Zheng-Hua Ye, *Univ. of Georgia*

Kezhong Zhang, *Wayne State Univ.*

Xiuren Zhang, *Texas A&M Univ.*

Changcheng Zhou, *Univ. of California, Riverside*

Michael E. Zwick, *Rutgers, The State Univ. of New Jersey*

Section on Chemistry

Amy H. Andreotti, *Iowa State Univ.*

Katherine B. Aubrecht, *Stony Brook Univ.*

Richard L. Brutchey, *Univ. of Southern California*

Jianfeng Cai, *Univ. of South Florida*

Stephen Creager, *Clemson Univ.*

David Deamer, *Univ. of California, Santa Cruz*

Emily R. Derbyshire, *Duke Univ.*

Amar H. Flood, *Indiana Univ.*

Lucio Frydman, *Weizmann Institute of Sciences (Israel)/National High Magnetic Field Laboratory*

Benjamin A. Garcia, *Washington Univ. School of Medicine in St. Louis*

Joseph Heppert, *Texas Tech Univ.*

Ive Hermans, *Univ. of Wisconsin–Madison*

Mandë Holford, *Hunter College, City Univ. of New York*

Theodore R. Holman, *Univ. of California, Santa Cruz*

Wenyu Huang, *Iowa State Univ.*

Timothy A. Jackson, *Univ. of Kansas*

Darren W. Johnson, *Univ. of Oregon*

James A. Kaduk, *Poly Crystallography, Inc.*

Carolyn Ann Koh, *Colorado School of Mines*

Margaret E. Kosal, *Georgia Institute of Technology*

Abdessadek (Abdou) Lachgar, *Wake Forest Univ.*

Qing Lin, *Univ. at Buffalo, State Univ. of New York*

Stephan Link, *Univ. of Illinois Urbana-Champaign*

Di-Jia Liu, *Argonne National Laboratory/Univ. of Chicago*

Gary J. Long, *Missouri Univ. of Science and Technology*

Angel A. Martí, *Rice Univ.*

Karen L. Mulfort, *Argonne National Laboratory*

Christopher B. Murray, *Univ. of Pennsylvania*

Jeffrey M. Pietryga, *Los Alamos National Laboratory*

John A. Pojman Sr., *Louisiana State Univ.*

Oleg V. Prezhdo, *Univ. of Southern California*

Roger Rousseau, *Oak Ridge National Laboratory*

Rachel A. Segalman, *Univ. of California, Santa Barbara*

Andrew D. Sutton, *Oak Ridge National Laboratory*

Ward H. Thompson, *Univ. of Kansas*

Jon A. Tunge, *Univ. of Kansas*

Vladimir N. Uversky, *Univ. of South Florida*

Zheming Wang, *Pacific Northwest National Laboratory*

Wei You, *Univ. of North Carolina at Chapel Hill*

Jingsong Zhang, *Univ. of California, Riverside*

Section on Dentistry and Oral Health Science

Donald L. Chi, *Univ. of Washington*

Yvonne L. Hernandez-Kapila *Univ. of California, Los Angeles School of Dentistry*

Clark M. Stanford, *The Univ. of Iowa College of Dentistry*

Section on Education

Dipankar Bandyopadhyay, *Virginia Commonwealth Univ.*

Cynthia Breazeal, *Massachusetts Institute of Technology*

Beverly R. DeVore-Wedding, *Nebraska Indian Community College*

Cindy E. Hmelo-Silver, *Indiana Univ. Bloomington*

Linda E. Hyman, *Marine Biological Laboratory*

Kathryn G. Miller, *Washington Univ. in St. Louis (Emeritus)*

Barbara Oakley, *Oakland Univ.*

Jaclyn Reeves-Pepin, *National Association of Biology Teachers*

Christie Sahley, *Purdue Univ.*

David Stroupe, *The Univ. of Utah*

Karen M. Viskupic, *Boise State Univ.*

Section on Engineering

Chaouki Abdallah, *Georgia Institute of Technology*

David J. Allstot, *Carnegie Mellon Univ.*

Scott Banta, *Columbia Univ.*

Michael S. Branicky, *Univ. of Kansas*

Jane P. Chang, *Univ. of California, Los Angeles*

Karen L. Christman, *Univ. of California, San Diego*

Mark Stephen Daskin, *Univ. of Michigan*

Reginald DesRoches, *Rice Univ.*

Sandhya Dwarkadas, *Univ. of Virginia*

Thomas Henry Epps III, *Univ. of Delaware*

Rodney O. Fox, *Iowa State Univ.*

Jan Genzer, *North Carolina State Univ.*

Satyandra K. Gupta, *Univ. of Southern California*

Patrick E. Hopkins, *Univ. of Virginia*

Mona Jarrahi, *Univ. of California, Los Angeles*

Young-Shin Jun, *Washington Univ. in St. Louis*

Srinivas Katkoori, *Univ. of South Florida*

Julius B. Lucks, *Northwestern Univ.*

Kenneth Lutchen, *Boston Univ.*

Phillip Messersmith, *Univ. of California, Berkeley*

Prabhas V. Moghe, *Rutgers, The State Univ. of New Jersey*

Krishnaswamy Nandakumar, *Louisiana State Univ.*

Lance C. Pérez, *Univ. of Nebraska–Lincoln*

Jim Pfaendtner, *North Carolina State Univ.*

Milica Radisic, *Univ. of Toronto (Canada)*

Jessica Rannow, *KPI Solutions*

Alberto Salleo, *Stanford Univ.*

Jonathan E. Spanier, *Drexel Univ.*

M.N. Srikanta Swamy, *Concordia Univ. (Canada)*

Costas Emmanuel Synolakis, *Univ. of Southern California*

Deepak Vashishth, *Rensselaer Polytechnic Institute*

Krista S. Walton, *Georgia Institute of Technology*

Xudong Wang, *Univ. of Wisconsin–Madison*

Sylvia Wilson Thomas, *Univ. of South Florida*

Chee Wei Wong, *Univ. of California, Los Angeles*

Peide Ye, *Purdue Univ.*

Section on General Interest in Science and Engineering

Alan Bernstein, *Univ. of Oxford (UK)/ Univ. of Toronto (Canada)*

Patrice M. Buzzanell, *Univ. of South Florida*

Denton S. Ebel, *American Museum of Natural History*

Victor R. McCrary, *Univ. of the District of Columbia*

Keegan Sawyer, *US Department of Energy*

Nikolaos Stergiou, *Univ. of Nebraska–Omaha*

Nicholas J. Talbot, *The Sainsbury Laboratory (UK)*

Berrin Tansel, *Florida International Univ.*

Section on Geology and Geography

Mark Mahalingam Baskaran, *Wayne State Univ.*

Maeve A. Boland, *Univ. College Dublin (Ireland)*

Susan L. Brantley, *The Pennsylvania State Univ.*

Mark Brenner, *Univ. of Florida*

So-Min Cheong, *Texas A&M Univ.*

David Robert Cole, *The Ohio State Univ.*

Cynthia J. Ebinger, *Tulane Univ.*

Kurt O. Konhauser, *Univ. of Alberta (Canada)*

Venkataraman Lakshmi, *Univ. of Virginia*

Thomas Mote, *Univ. of Georgia*

Gregory S. Okin, *Univ. of California, Los Angeles*

Bimal Kanti Paul, *Kansas State Univ.*

Dawn Y. Sumner, *Univ. of California, Davis*

Alan G. Whittington, *The Univ. of Texas at San Antonio*

Ann G. Wylie, *Univ. of Maryland, College Park (Emeritus)*

Haibo Zou, *Auburn Univ.*

Section on History and Philosophy of Science

Douglas Allchin, *Univ. of Minnesota, Twin Cities*

Melinda Gormley, *Univ. of California, Irvine*

M. Susan Lindee, *Univ. of Pennsylvania*

Ludmila Pollock, *Cold Spring Harbor Laboratory*

Adina L. Roskies, *Univ. of California, Santa Barbara*

Section on Industrial Science and& Technology

Noubar B. Afeyan, *Flagship Pioneering*

Marla L. Dowell, *National Institute of Standards and Technology*

Ernesto E. Marinero, *Purdue Univ.*

Carlos Messina, *Univ. of Florida*

Hongtao Yu, *Morgan State Univ.*

Section on Information, Computing, and Communication

Michael A. Bender, *Stony Brook Univ.*

danah boyd, *Microsoft Research*

Barbara M. Chapman, *Stony Brook Univ./Hewlett Packard Engineering*

Howie Choset, *Carnegie Mellon Univ.*

George Cybenko, *Dartmouth College*

Alan Edelman, *Massachusetts Institute of Technology*

Mark Guzdial, *Univ. of Michigan*

James B. D. Joshi, *Univ. of Pittsburgh*

Latifur Khan, *The Univ. of Texas at Dallas*

David Kotz, *Dartmouth College*

D. Richard Kuhn, *National Institute of Standards and Technology*

Wei Liu, *Tencent Holdings Ltd.*

Anant Madabhushi, *Emory Univ. School of Medicine*

Filippo Menczer, *Indiana Univ. Bloomington*

Craig J. Mundie, *Mundie & Associates LLC*

Jason Nieh, *Columbia Univ.*

Alex Pothen, *Purdue Univ.*

Matthias J. Scheutz, *Tufts Univ.*

Yingli Tian, *City College of New York, City Univ. of New York*

Don Towsley, *Univ. of Massachusetts Amherst*

Nalini Venkatasubramanian, *Univ. of California, Irvine*

Li Xiong, *Emory Univ.*

Moustafa Amin Youssef, *The American Univ. in Cairo (Egypt)*

Thomas Zimmermann, *Univ. of California, Irvine*

Section on Linguistics and Language Science

Marlyse Baptista, *Univ. of Pennsylvania*

Jeffrey Lidz, *Univ. of Maryland, College Park*

Asifa Majid, *Univ. of Oxford (UK)*

Donna Jo Napoli, *Swarthmore College*

Barbara Zurer Pearson, *Univ. of Massachusetts Amherst*

Section on Mathematics

Solomon Friedberg, *Boston College*

Overtoun M. Jenda, *Auburn Univ.*

Jonathan C. Mattingly, *Duke Univ.*

Linda Preiss Rothschild, *Univ. of California San Diego (Emeritus)*

Frank Sottile, *Texas A&M Univ.*

Section on Medical Sciences

Elliot J. Androphy, *Indiana Univ. School of Medicine*

Themistocles L. Assimes, *Stanford Univ. School of Medicine*

Michael R. Barratt, *NASA Johnson Space Center*

Theresa Beckie, *Univ. of South Florida*

Kiros Berhane, *Columbia Univ.*

Zea Borok, *Univ. of California San Diego*

Prosper N. Boyaka, *The Ohio State Univ.*

Stephen Bruehl, *Vanderbilt Univ. Medical Center*

Karen Bush, *Indiana Univ. Bloomington*

Lauren Averett Byers, *The Univ. of Texas MD Anderson Cancer Center*

Weibo Cai, *Univ. of Wisconsin–Madison*

Kathleen L. Collins, *Univ. of Michigan*

George Cotsarelis, *Perelman School of Medicine at The Univ. of Pennsylvania*

Sabrina Diano, *Columbia Univ.*

Andrzej Dlugosz, *Univ. of Michigan Medical School*

Brian J. Druker, *Oregon Health and Science Univ.*

Victor J. Dzau, *National Academy of Medicine*

Leonard P. Freedman, *Frederick National Laboratory for Cancer Research*

Roman J. Giger, *Univ. of Michigan*

David A. Hafler, *Yale Univ. School of Medicine*

Richard Henderson, *MRC Laboratory of Molecular Biology*

Angela L. Jefferson, *Vanderbilt Univ. Medical Center*

Mark H. Kaplan, *Indiana Univ. School of Medicine*

Kalpana S. Katti, *North Dakota State Univ.*

Gregory Kirk, *Johns Hopkins Univ.*

Wilbur Lam, *Emory Univ./Georgia Institute of Technology*

David H. Lawson, *Winship Cancer Institute of Emory Univ.*

Cecile A. Lengacher, *Univ. of South Florida College of Nursing*

David M. Markovitz, *Univ. of Michigan Medical School*

Laura R. McCabe, *Michigan State Univ.*

Larry S. McDaniel, *Univ. of Mississippi Medical Center*

Borna Mehrad, *Univ. of Florida College of Medicine*

Shlomo Melmed, *Cedars-Sinai Medical Center*

Leonard M. Milstone, *Yale Univ. School of Medicine*

Ruth R. Montgomery, *Yale Univ. School of Medicine*

Robin Patel, *Mayo Clinic*

Elizabeth Jane Phillips, *Vanderbilt Univ. Medical Center*

Henry J. Pownall, *Houston Methodist Academic Institute/Weill Cornell Medical College*

Arvind U. K. Rao, *The Univ. of Michigan, Ann Arbor*

Pavan Reddy, *Baylor College of Medicine*

James G. Rheinwald, *Univ. of California, Los Angeles*

Inez Rogatsky, *Hospital for Special Surgery/Weill Cornell Medical College*

Mitnala Sasikala, *Asian Institute of Gastroenterology (India)*

Abhay R. Satoskar, *The Ohio State Univ. College of Medicine*

Michael Robert Savona, *Vanderbilt Univ. Medical Center*

Zhongjie Sun, *The Univ. of Tennessee Health Science Center*

Anish Thomas, *National Cancer Institute, NIH*

Edmund K. Waller, *Emory Univ. School of Medicine*

Xin Wei Wang, *National Cancer Institute, NIH*

Xiao-Ming Yin, *Tulane Univ. School of Medicine*

Section on Neuroscience

Tracy L. Bale, *Univ. of Colorado*

Diana M. Bautista, *Univ. of California, Berkeley*

Staci Bilbo, *Duke Univ.*

Joshua C. Brumberg, *Queens College and Graduate Center of the City Univ. of New York*

Jeffrey L. Cummings, *Univ. of Nevada, Las Vegas*

Richard J. Krauzlis, *National Eye Institute, NIH*

Emily R. Liman, *Univ. of Southern California*

A. Kimberley McAllister, *Wake Forest Univ.*

Lisa M. Monteggia, *Vanderbilt Univ.*

Jack M. Parent, *Univ. of Michigan Medical School*

Phyllis R. Robinson, *Univ. of Maryland, Baltimore County*

Michael A. Sesma, *National Institute of General Medical Sciences, NIH*

Joshua A. Weiner, *Univ. of Iowa*

Stephanie Ann White, *Univ. of California, Los Angeles*

Section on Pharmaceutical Sciences

Mansoor M. Amiji, *Northeastern Univ.*

Kim L. R. Brouwer, *Univ. of North Carolina at Chapel Hill*

Carrie Haskell-Luevano, *Univ. of Minnesota, Twin Cities*

Homer L. Pearce, *Eli Lilly and Company (Retired)*

Steven M. Swanson, *Univ. of Wisconsin–Madison*

Section on Physics

Kevork N. Abazajian, *Univ. of California, Irvine*

John F. Beacom, *The Ohio State Univ.*

Mani L. Bhaumik, *Retired*

Troy Alan Carter, *Oak Ridge National Laboratory/Univ. of California, Los Angeles*

Yong P. Chen, *Purdue Univ./Aarhus Univ. (Denmark)*

Jacinta C. Conrad, *Univ. of Houston*

Raissa M. D'Souza, *Univ. of California, Davis*

Liesl Folks, *Univ. of Arizona*

Peter H. Garbincius, *Fermi National Accelerator Laboratory*

Daniel I. Goldman, *Georgia Institute of Technology*

Chris H. Greene, *Purdue Univ.*

Sean J. Hearne, *Southeastern Universities Research Association*

Morten Hjorth-Jensen, *Michigan State Univ./Univ. of Oslo (Norway)*

Roland Kenji Kawakami, *The Ohio State Univ.*

Chun Ning Lau, *The Ohio State Univ.*

Ho Nyung Lee, *Oak Ridge National Laboratory*

Xiaosong Li, *Univ. of Washington*

Kam-Biu Luk, *Hong Kong Univ. of Science and Technology/Univ. of California at Berkeley*

Jeffrey W. Lynn, *National Institute of Standards and Technology*

Zhiqiang Mao, *The Pennsylvania State Univ.*

Peter J. Mohr, *National Institute of Standards and Technology*

Jagadeesh S. Moodera, *Massachusetts Institute of Technology*

Ilya Nemenman, *Emory Univ.*

Ruslan Prozorov, *Iowa State Univ./Ames National Laboratory*

James M. Rondinelli, *Northwestern Univ.*

Bernard Sadoulet, *Univ. of California, Berkeley*

David P. Saltzberg, *Univ. of California, Los Angeles*

Peter E. Schiffer, *Princeton Univ.*

Jörg Schmiedmayer, *Vienna Center for Quantum, Science and Technology, Atominstitut, TU Wien (Austria)*

Ivan Smalyukh, *Univ. of Colorado at Boulder*

Michael Thoennessen, *Michigan State Univ.*

Robert Miles Zwaska, *Fermi National Accelerator Laboratory*

Section on Psychology

Karen E. Adolph, *New York Univ.*

Leda Cosmides, *Univ. of California, Santa Barbara*

Michael Cunningham, *Tulane Univ.*

Douglas A. Gentile, *Iowa State Univ.*

Simona Ghetti, *Univ. of California, Davis*

Kenneth S. Kendler, *Virginia Commonwealth Univ.*

Laura M. Koehly, *National Human Genome Research Institute, NIH*

Tené T. Lewis, *Emory Univ.*

Viorica Marian, *Northwestern Univ.*

Christian A. Meissner, *Iowa State Univ.*

Fei Xu, *Univ. of California, Berkeley*

Section on Social, Economic, and Political Sciences

Bonnie Duran, *Univ. of Washington (Emeritus)*

Cleotilde Gonzalez, *Carnegie Mellon Univ.*

Margaret C. Levenstein, *Univ. of Michigan*

Chandra Muller, *The Univ. of Texas at Austin*

Willliam Nordhaus, *Yale Univ.*

Marcia G. Ory, *Texas A&M Univ.*

Timothy Smeeding, *Univ. of Wisconsin*

K. Viswanath, *Harvard Univ./Dana-Farber Cancer Institute*

Bruce A. Weinberg, *The Ohio State Univ.*

Section on Societal Impacts of Science and Engineering

Jay T. Goodwin, *John D. & Catherine T. MacArthur Foundation*

Lekelia Danielle Jenkins, *Arizona State Univ.*

Susan Coady Kemnitzer, *National Science Foundation (Retired)*

Robert L. Klitzman, *Columbia Univ. Vagelos College of Physicians and Surgeons*

Marty D. Matlock, *Univ. of Arkansas*

Robert B. Millard, *Massachusetts Institute of Technology*

Elena N. Naumova, *Tufts Univ.*

Juan D. Rogers, *Georgia Institute of Technology*

Brooke Smith, *The Kavli Foundation*

Paul Spicer, *Univ. of Oklahoma*

Section on Statistics

Alexander Aue, *Univ. of California, Davis*

Jinbo Chen, *Univ. of Pennsylvania*

Scott H. Holan, *Univ. of Missouri*

Lexin Li, *Univ. of California, Berkeley*

Xihong Lin, *Harvard Univ.*

Daniel S. Nettleton, *Iowa State Univ.*

Cynthia Rudin, *Duke Univ.*

RESEARCH

IN *SCIENCE* JOURNALS

Edited by **Michael Funk**

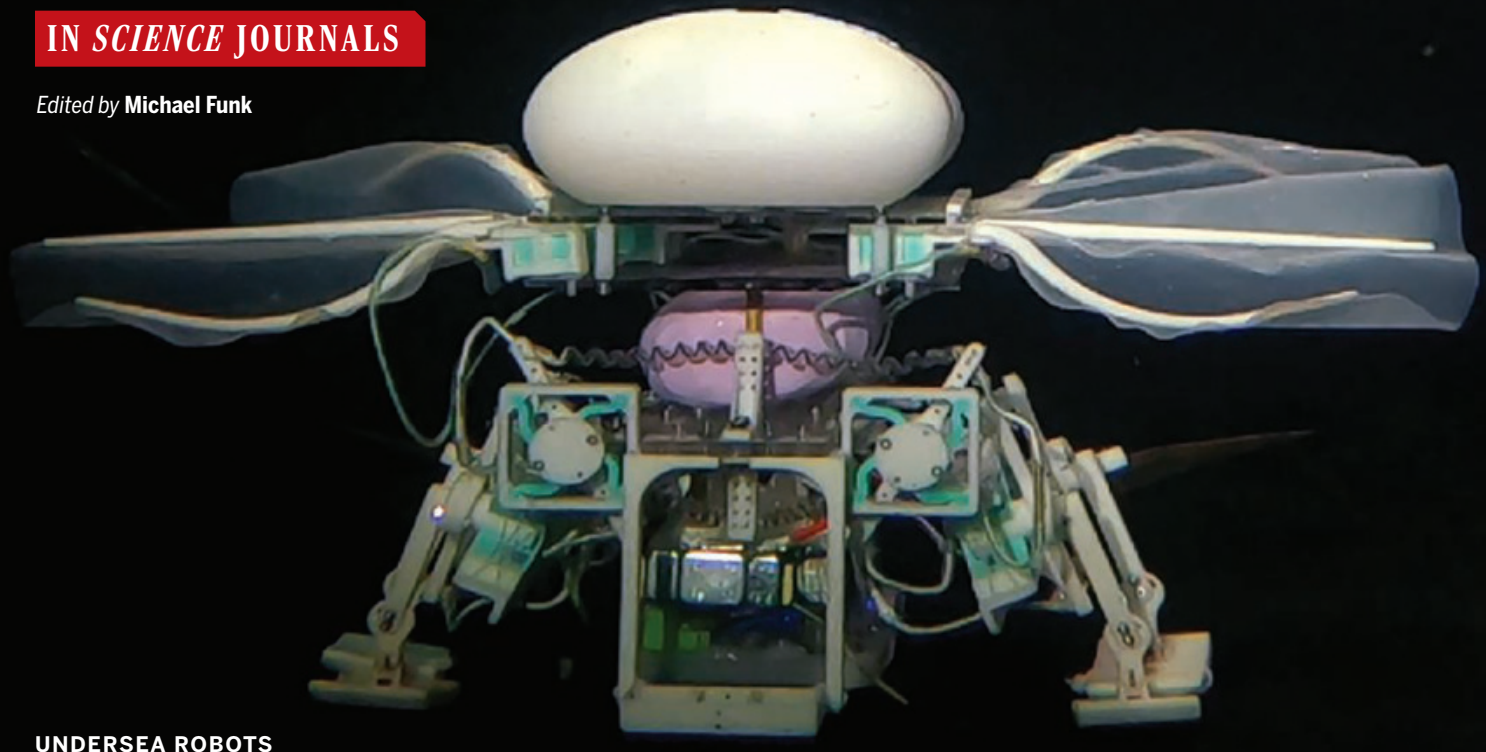

PHOTO: PAN ET AL./SCIENCE ROBOTICS

A miniature deep-sea robot capable of swimming, crawling, and sample retrieval

UNDERSEA ROBOTS

Miniature robot explores the deep sea

Very few robots have been built to withstand the harsh conditions of the deep sea. Bulky actuation systems can be destructive to delicate habitats, and the few miniaturized robots have limited locomotion. Pan *et al*. designed an untethered miniature robot that uses shape memory alloys and chiral metamaterials to overcome the high pressures and low temperatures of the deep sea. The robot is capable of swimming, gliding, morphing, and crawling, and was successfully deployed in the Haima Cold Seep (1380 m) and the Mariana Trench (10,600 m). The chiral design strategy was also used on a soft gripper capable of collecting delicate biological specimens. These pressure-resistant actuators pave the way for future exploration of deep-sea ecosystems. —Melisa Yashinski *Sci. Robot.* (2025) 10.1126/scirobotics.adp7821

CANCER THERAPY

Using autoimmunity against cancer

Many cancers suppress attacks from the immune system. Chen *et al*. found that antitumor immunity and immunotherapy might be improved by harnessing an antibody associated with the autoimmune disease lupus. The antibody, called 4H2, was taken up into cells, where it bound to endogenous RNA. This action recruited and activated the nucleic acid sensor cGAS, which initiated inflammatory signaling that was cytotoxic to cancer cells in culture, but not to normal cells. In mice with glioblastomas, 4H2 localized to the tumor after systemic administration, improved animal survival in a T cell–dependent manner, and improved the efficacy of immune checkpoint blockade therapy, demonstrating its therapeutic potential. —Leslie K. Ferrarelli

Sci. Signal. (2025) 10.1126/scisignal.adk3320

HAPTICS

Realistic virtual tactile sensations

Our sense of touch provides a wide range of sensations that tell us about the environment around us, including many things that we can't ascertain using sight alone. These signals come from a rich collection of receptors that exist in the skin. Ha *et al*. developed a single actuator unit that can exert complex combinations of dynamic forces, including pressure, shear, vibration, displacement, and torque, to achieve haptic information transfer and realistic virtual tactile sensations. The authors demonstrate the application of this system in hand navigation, reproduction of textural sensation, and tactile perception of music, with a broader goal of using the actuator for biomedical and extended reality applications. —Marc S. Lavine

Science p. 1383, 10.1126/science.adt2481

PLANT PATHOLOGY

Tandem kinases act through NLRs

Plant immunity relies heavily on intracellular nucleotide-binding leucine-rich repeat (NLR) proteins, which can act as either receptors or signal transducers to facilitate disease resistance. In wheat and barley, an alternative class of genes called the tandem kinases also contribute to disease resistance. Two papers in this issue elucidate how tandem kinases work, showing that wheat tandem kinases require an NLR to function. Chen *et al*. found a pathogen effector that triggers the action of the wheat Sr62 tandem kinase. They demonstrate that the effector interacts with Sr62's active kinase domain, enabling a pseudokinase domain to activate the corresponding NLR. In parallel, Lu *et al.* found that a different tandem kinase, WTK3, activates the same NLR as Sr62, and that this NLR acts as a calcium ion channel once activated. Together, these studies solidify the role of NLRs as hubs for immune signaling in response to diverse pathogens and will guide breeding efforts for disease-resistant wheat.
—Madeleine Seale

Science p. 1402, 10.1126/science.adp5034
p. 1418, 10.1126/science.adp5469

ORGANIC CHEMISTRY

Ready to couple

Reactions that produce carbon-carbon bonds are foundational to organic chemistry and pharmaceutical synthesis. Although palladium catalysis has been a workhorse for decades for this purpose, more Earth-abundant nickel catalysis has recently been used more often in tandem with chemical, photochemical, or electrochemical reductive activation. Sun *et al*. report the application of a class of sulfonyl hydrazide reactants that do not require external reduction. Simple heating with nickel catalysts forges a wide variety of carbon-carbon bonds to alkyl, alkenyl, alkynyl, and aryl partners through a radical pathway. —Jake S. Yeston

Science p. 1377, 10.1126/science.adu6406

METALLURGY

A high-temperature nanostructured alloy

In theory, nanocrystalline alloys should be able to retain considerable strength even at high temperatures, but this has rarely been demonstrated in practice. Hornbuckle *et al*. started with a binary alloy of copper (Cu) and tantalum (Ta), even though the two are immiscible, to which they added lithium (Li). This mixture resulted in precipitates of nanoscale clusters of Cu_3Li coated with Ta. This core-shell structure neither dissolves nor coarsens at temperatures of up to 800°C while also causing the yielding strength to be in excess of 1 gigapascal.
—Marc S. Lavine

Science p. 1413, 10.1126/science.adr0299

POLICING

Racial bias in traffic stops

US police detain racial or ethnic minority drivers (Asian and Pacific Islander, Black, and Hispanic) more than white drivers. However, a longstanding debate remains unsettled: Does this necessarily reflect police bias? Hypothetically, if minorities were more prone to disobey speed limits and traffic laws, then their traffic stops may be warranted. To put this debate to rest, Aggarwal *et al*. examined rideshare data from Lyft in the state of Florida to compare minority drivers with their white counterparts. Lyft objectively measured drivers' locations, driving speed, and location speed limits (see the Perspective by Knox and Mummolo). White and minority drivers showed no discernible differences in speeding behaviors or traffic violations. However, when both drove at identical speeds, police were still 33% more likely to issue speeding citations to minority drivers and charged 34% more expensive fines, unequivocally revealing bias.
—Ekeoma Uzogara

Science p. 1397, 10.1126/science.adp5357; see also p. 1350, 10.1126/science.adw3618

IN OTHER JOURNALS

Edited by **Corinne Simonti** *and* **Jesse Smith**

Genomic assays reveal that 168 species contribute to the sunburst lichen (*Xanthoria parietina*), explaining in part why these organisms have been so difficult to study.

PHOTO: AP HANNIBAL VIA SHUTTERSTOCK

ADAPTATION

Converging on a winter's nap

Separate populations of a species occasionally migrate to the same new environment at different times. Although this can result in these populations merging, it may also result in parallel adaptations to similar new pressures. Shoshan *et al*. examined two populations of Swedish speckled wood butterfly (*Pararge aegeria*) that express winter diapause, a type of dormancy that allows insects to bypass difficult seasons. Although there was gene flow between these populations, F_1 hybrids showed a distinct intermediate diapause phenotype between the two parent populations. The authors found that a region on the Z chromosome was associated with this trait in one population but not the other, suggesting that the genetic architecture of this trait differs between populations.
—Corinne Simonti

Proc. R. Soc. B (2025) 10.1098/rspb.2024.2195

QUANTUM MATERIALS

A quantum device Etch A Sketch

Oxide heterostructures can give rise to exotic behaviors such as magnetism and superconductivity at the interface region between some materials even though neither material displays that particular property. Although much early work focused on $LaAlO_3/SrTiO_3$ interfaces, interest has now shifted to interfaces between $LaAlO_3$ and $KTaO_3$, a material that can exhibit stronger spin-orbit coupling and a higher superconducting transition temperature. Yu *et al.* used

LICHENS

Uncovering elusive biology

Associations between algal cells and fungal cells are found on all but the most polluted undisturbed surfaces. Classically, lichens were considered to be relations between two or three species, but Tagirdzhanova *et al.* now show that even the common "sunburst" species *Xanthoria parietina* is so much more. The authors have discovered more than 168 different genomes associated with this lichen, from green algae, several fungi, to many bacterial phyla, which appear variously to show lichen life stage–specific gene expression and to produce a multiplicity of effectors and metabolites. Lichens are difficult to manipulate experimentally, but this survey provides a way to discover more about their extraordinary biology. —Caroline Ash

Curr. Biol. (2025)
10.1016/j.cub.2024.12.041

GENOMICS

Genetics of a rare skin disorder

Epidermolysis bullosa (EB) is a rare, inherited group of skin disorders usually diagnosed during infancy. Affected children develop blistering lesions throughout the body in response to heat exposure or mechanical friction, which can be life-threatening. EB simplex (EBS) is the most common subtype and is associated with genetic variants in the *KRT5* gene. Bergson *et al.* used exome sequencing to explore why disease severity differs between individuals carrying the same EBS-causing variant, revealing deleterious variants in the *HMCN1* gene. *HMCN1* encodes hemicentin-1, an extracellular matrix protein found to bind the keratin 14 protein. Silencing *HMCN1* expression disturbed the organization of epidermal keratinocytes and their attachment to the extracellular matrix. —Priscilla N. Kelly

J. Exp. Med. (2025)
10.1084/jem.20240827

conductive atomic force microscopy to pattern superconducting weak links at the LAO/KTO interface, key nonlinear elements in several quantum devices. They also demonstrate the fabrication of superconducting quantum interference devices by extending the patterning process. This on-demand patterning provides a versatile platform with which to develop quantum materials and devices. —Ian S. Osborne

Phys. Rev. X (2025)
10.1103/PhysRevX.15.011037

PHYSICS

Chipping away at the cuprate problem

The material science of cuprate superconduction is very complex, and describing its physics using ab initio methods is a daunting task. Cui *et al.* have made an important step in that direction. Although their method contains approximations that render the calculations tractable, they were able to reproduce experimental trends such as the dependence of the pairing order on pressure and number of copper oxide layers. Further development of these methods may lead to a better understanding of cuprate superconductivity and its mechanism. —Jelena Stajic

Nat. Commun. (2025)
10.1038/s41467-025-56883-x

SIGNAL TRANSDUCTION

Big data meets cytokine signaling

Advances in techniques that allow the manipulation, genetic modification, and sequencing of RNA transcripts in single cells hold promise for explaining how complex signaling pathways control biological systems. Using a combination of experimental and analytical improvements, Jiang *et al.* characterized the responses of six cancer cell lines stimulated with five cytokines in the context of genetic perturbation of a panel of about 50 target genes. Single-cell RNA sequencing of more than 2.5 million cells revealed their context-dependent responses, showing how downstream gene regulation depended on pathway components and how target genes varied across cell types. Such analysis will enhance our understanding of cell responses during perturbation, and further expansion of such protocols could help to reveal interactions between pathway components. —L. Bryan Ray

Nat. Cell Biol. (2025)
10.1038/s41556-025-01622-z

SODIUM CATHODES

Higher entropy promotes fast charging

Sodium-ion batteries with O3-type layered oxide cathodes are being widely explored as alternatives to lithium iron phosphate batteries for future electrification. However, the inevitable phase transitions between O-type and P-type structures during operation often impair battery lifetime and fast-charging capability. Wang *et al.* addressed this issue by increasing the configurational entropy of the cathode and developed a multielemental cathode capable of fast charging, even at 20°C, with a prolonged life span. Through in situ and ex situ experimental characterization and computational analysis, the authors showed that higher entropy promotes biphasic reaction kinetics while mitigating oxygen release and surface reconstruction. —Jack Huang

J. Am. Chem. Soc. (2025)
10.1021/jacs.4c12733

REVIEW SUMMARY

OPTICS

Complex-frequency excitations in photonics and wave physics

Seunghwi Kim†, Alex Krasnok†, Andrea Alù*

BACKGROUND: Customizing how a system responds to external stimuli is essential for a wide range of wave-based technologies, such as photonics, acoustics, elastodynamics, radiofrequency engineering, and quantum optics. This response involves the intricate dynamics of wave interactions with matter, leading to reflection, absorption, diffraction, and scattering of waves, altering their momentum and energy flow. In turn, these principles underpin a multitude of wave phenomena and technologies, from the reflection of light and the echo of sound to the intricate behavior observed in photonic systems. In most settings, these phenomena are limited by fundamental system properties such as passivity, linearity, and time-reversal symmetry, imposing constraints on bandwidth, efficiency, and other performance metrics. Recent efforts to overcome these limitations involve the use of material gain; tailored responses in systems characterized by nonconservative interactions with their environment; time modulation, amplification, and lasing; and nonreciprocal materials. Although these strategies show promise, they often introduce unwanted challenges, such as increased complexity, reduced ease of integration, high costs, and footprint requirements.

ADVANCES: In recent years, excitations that oscillate at complex-valued frequency have transitioned from being merely analytical and numerical tools to model photonic systems to becoming a viable route to experimentally access exotic wave responses. By utilizing excitation signals with tailored waveforms whose amplitudes grow or decay exponentially in time, researchers have been able to effectively mimic the effect of gain and loss in passive systems without modifying their material properties. This advancement has led to experimental demonstrations of phenomena previously thought unattainable in passive systems. Notable examples include compensating losses in metamaterials, enhanced sensing, parity-time symmetry transitions without the need for active elements, and generation of optical pulling forces without specially designed spatial field gradients. These breakthroughs have also unlocked new capabilities, such as the manipulation of light for super-resolution imaging and real-time control over light-matter interactions and critical coupling of optical cavities, as well as phenomena that mimic the presence of material gain in passive systems. By bridging theoretical concepts with experimental implementations, these advances demonstrate the feasibility of accessing non-Hermitian responses in passive linear systems. This enables new possibilities for wave-based technologies without the need for complex materials and the downsides of active elements.

OUTLOOK: The recent progress in the use of complex frequencies and their associated wave-matter interactions offers metamaterials and wave control new opportunities, particularly in the context of non-Hermitian wave phenomena. In optics and photonics, these tools offer opportunities to dramatically alter how light interacts with matter in a highly dynamic and tunable fashion, enabling enhanced control over light emission and transport. This paves the way for observing non-Hermitian and topological wave phenomena without relying on complex non-Hermitian materials, which are challenging to realize. By applying this excitation approach to well-established platforms, it becomes possible to exploit the interplay of effective gain and loss encoded in the temporal waveform of the excitation to create new functionalities and enhance the performance of modern technologies. For instance, in optical communications, sensing, and computing, the ability to manipulate waves by using complex-frequency excitations may lead to more efficient and adaptable systems.

Future research directions include developing more efficient methods for generating complex-frequency excitations, integrating these techniques into existing technologies, and exploring their applications across various fields. Emerging platforms such as metasurfaces, polaritonic materials, optomechanical systems, and topological insulators provide unexplored opportunities to investigate the effects of complex-frequency excitations in systems with inherently large nonlinearities, naturally strong light-matter interactions, and intrinsic robustness. Tailored effective gain and loss driven by the excitation waveform in these systems opens the potential for a substantial shift in the study, application, and control of wave-matter interactions across many physical domains. By bridging theoretical advancements with practical implementations, we anticipate that complex-frequency excitations may become crucial for future technological innovations, impacting fields beyond photonics and wave physics, such as quantum computing, biomedical engineering and sensing, imaging, and energy harvesting. ■

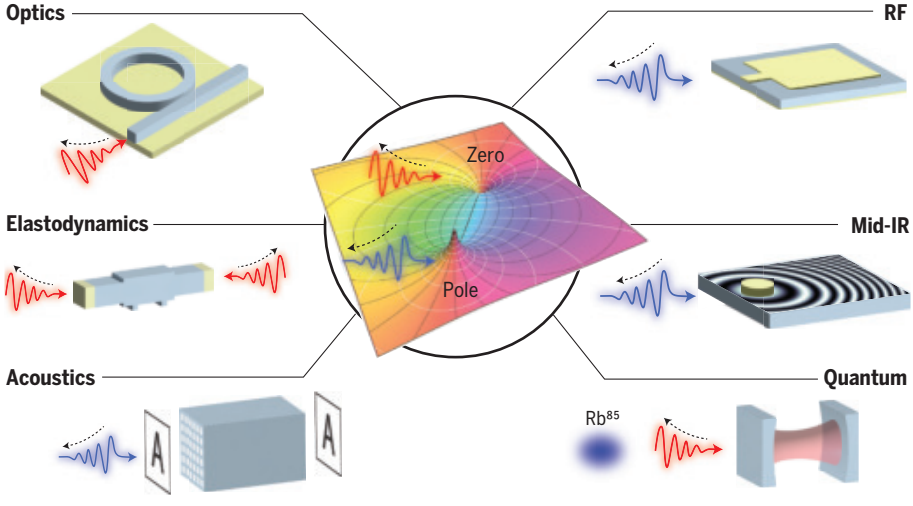

Complex-frequency excitations in various wave physics settings. Exotic wave phenomena available across optics, radiofrequency (RF), elastodynamics, mid-infrared (mid-IR), acoustics, and quantum wave systems, leveraging complex-frequency excitations to enhance modern technologies.

The list of author affiliations is available in the full article online.
*Corresponding author. Email: aalu@gc.cuny.edu
†These authors contributed equally to this work.
Cite this article as S. Kim *et al.*, *Science* **387**, eado4128 (2025). DOI: 10.1126/science.ado4128

READ THE FULL ARTICLE AT
https://doi.org/10.1126/science.ado4128

RESEARCH ARTICLE SUMMARY

MICROBIOLOGY

Telomeric transposons are pervasive in linear bacterial genomes

Shan-Chi Hsieh, Máté Fülöp, Richard Schargel, Michael T. Petassi, Orsolya Barabas, Joseph E. Peters*

INTRODUCTION: Eukaryotes have linear DNA with specialized telomere ends that are protected and maintained by dedicated proteins. Selfish mobile genetic elements called transposons are known to accumulate in gene-poor eukaryotic telomere regions and, in some cases, take control of these ends. Many bacteria maintain their DNA as circles, but multiple medically and industrially relevant species have linear DNA and their own distinct mechanisms of telomere maintenance. Transposons drive genetic exchange in bacteria and have evolved ingenious ways to target integration into permissive genomic sites, strategies that allow these genetic elements to preserve essential functions of the bacterial host.

RATIONALE: To understand how transposons propagate in bacteria, a global view of bacterial genomes is required. However, bacteria are extremely diverse, and this diversity is difficult to explore because most species are recalcitrant to growth in the laboratory. Recently, DNA sequencing from natural samples has become a major means to understand microbial diversity by using huge databases of DNA sequence information from diverse environments. We investigated the variety of transposons from nonmodel bacteria and explored their distribution in relation to telomeres to better understand how these elements contribute to the maintenance and exchange of genetic information.

RESULTS: We computationally screened large-sequence databases from bacteria that have linear genomes, looking for protein families that are found in transposons. The focus was on types of transposons that use multiple proteins to carefully control where they integrate. We investigated cyanobacteria that maintain their telomeres by looping the two complementary DNA strands as a hairpin. We identified transposons that are only present in telomeric regions and possess the enzyme called protelomerase, which is known to form hairpin DNA ends. Biochemical experiments showed that the protelomerase maintains the specific telomere sequence found with the telomeric transposon, indicating that the transposon controls this end of the host DNA. Reconstituting the transposon in genetically tractable bacteria showed that it can actively mobilize and bias integration to telomeres when the chromosome is linearized. Analysis of DNA sequences from *Streptomyces* bacteria revealed two additional families of telomeric transposons, which are estimated to populate about a third of these genomes. *Streptomyces* protect and maintain their telomeres by using proteins that are bound covalently to the DNA ends. These systems also partner with another enzyme that can exchange DNA between bacteria, facilitating evolution. Unlike known transposons that have specific terminal sequence repeats, telomeric transposons have one conserved transposon end and terminate with a telomere on the other side. We identified diverse modalities that allow telomeric transposons to exist as DNA ends. In all cases, these elements likely take control of telomeres, preventing the bacterial host from losing the transposon that now forms its chromosome ends. One subfamily of telomeric transposons co-opted a CRISPR system that is normally used for defense against invading DNA as a tool for the transposon to target chromosome ends, exploiting RNA guides to locate and target telomeric sequences. Population analysis suggests that telomeric transposons replace the telomeres not just from the host but also from other telomeric transposons.

CONCLUSION: Transposons are major drivers of genetic exchange across bacteria. Target site selection has emerged as a key feature to ensure transposon spread while minimizing excessive damage to the host. In this work, we identified several families of transposons that populate bacterial telomeres, a striking parallel to the behavior of transposons found in eukaryotes. When these telomeric transposons commandeer a DNA end of the host, they also act as an "addiction" system, ensuring that they cannot be lost. Distinct adaptations allow these elements to spread across telomere ends in the host and horizontally between hosts. They also mobilize genes with new functions that likely benefit new bacterial hosts, profiting the transposon and host. ■

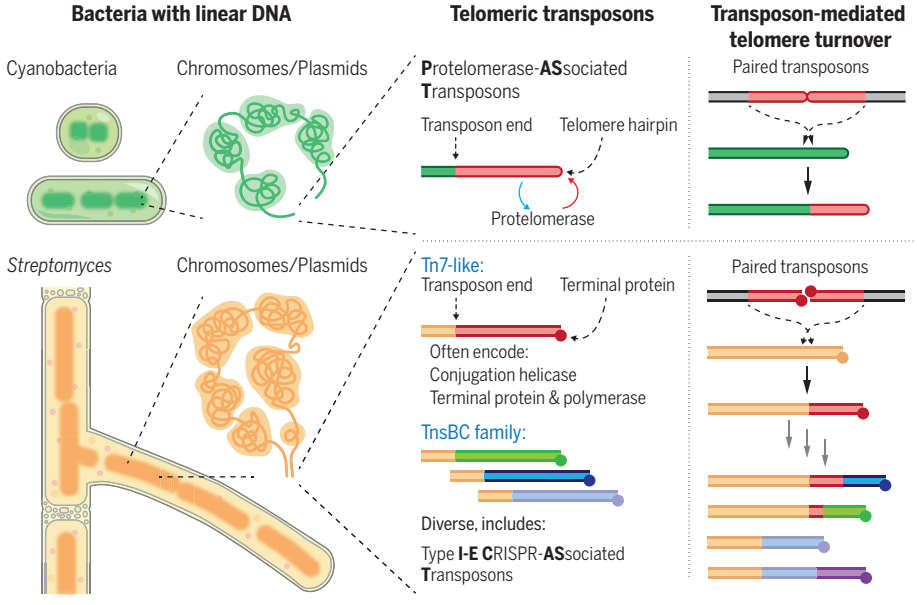

Telomeric transposons occupy linear DNA ends in cyanobacteria and *Streptomyces*. The elements possess a single transposon end and replace the target telomere with their own. In cyanobacteria, the telomeric transposons are associated with the protelomerase gene for maintaining their hairpin telomere. In *Streptomyces*, diverse telomeric transposons, including type I-E CASTs, belong to two families (Tn7-like and TnsBC) and are often associated with telomere maintenance genes.

The list of author affiliations is available in the full article online.
*Corresponding author. Email: joe.peters@cornell.edu
Cite this article as S.-C. Hsieh *et al.*, *Science* **387**, eadp1973 (2025). DOI: 10.1126/science.adp1973

READ THE FULL ARTICLE AT
https://doi.org/10.1126/science.adp1973

RESEARCH ARTICLE SUMMARY

CELL BIOLOGY

Leucine aminopeptidase LyLAP enables lysosomal degradation of membrane proteins

Aakriti Jain, Isaac Heremans, Gilles Rademaker, Tyler C. Detomasi, Peter Rohweder, Dashiell Anderson, Justin Zhang, Grace A. Hernandez, Suprit Gupta, Teresa von Linde, Mike Lange, Martina Spacci, Jiayi Luo, Y. Rose Citron, James A. Olzmann, David W. Dawson, Charles S. Craik, Guido Bommer, Rushika M. Perera, Roberto Zoncu*

INTRODUCTION: Transmembrane proteins constitute about 20 to 30% of the human proteome and are crucial for processes such as nutrient transport, signaling, and cell adhesion. These proteins are degraded within lysosomes, where specialized enzymes break them down into single amino acids. Macropinocytosis and phagocytosis may accelerate membrane protein turnover, especially in pathologies such as pancreatic ductal adenocarcinoma PDA], where cells rely on enhanced lysosomal activity for nutrient acquisition. However, the lysosomal degradation of membrane proteins is incompletely understood; specifically, how the hydrophobic, lipid-embedded regions of these proteins are degraded is unclear. Efficient degradation of transmembrane domains is critical because their hydrophobic nature can result in aggregation, while their lipid-intercalating properties can compromise lysosomal membrane integrity.

RATIONALE: Lysosomal proteolysis of hydrophobic α-helical domains is a key but poorly understood step in the life cycle of integral membrane proteins and is likely critical in cell types that engage in high rates of endocytosis, including phagocytic immune cells and certain cancer types. However, no lysosomal enzymes that mediate this activity have been identified.

RESULTS: By combining lysosomal proteomics with functional genomics, we identified PLBD1 (phospholipase B domain–containing 1), renamed LyLAP (lysosomal leucine aminopeptidase), as a top-ranking lysosomal hydrolase in cells that undergo high rates of endocytosis, specifically PDA and phagocytic immune cells. In PDA cells, LyLAP knockdown led to both morphological and functional defects; lysosomes became grossly enlarged and deacidified, accumulating undigested substrates, including proteins and lipids.

On the basis of its structural features, LyLAP was predicted to hydrolyze amide bonds, but its true substrates remained unknown. By reconstituting LyLAP-depleted lysosomes with recombinant LyLAP protein, we identified hydrophobic peptides as its bona fide substrates. LyLAP processively degraded these peptides starting at their amino termini, which most often consist of hydrophobic amino acids, such as leucine. Most LyLAP substrate peptides identified mapped to the membrane-spanning regions of integral membrane proteins, many of which reside at the plasma membrane and are trafficked to the lysosome for degradation.

Consistent with the key role for LyLAP in degrading hydrophobic peptides, these substrates accumulated in LyLAP-depleted lysosomes. This accumulation destabilized the lysosomal limiting membrane and impaired lysosomal function.

LyLAP was the most up-regulated lysosomal hydrolase in PDA cell lines and PDA patient samples. Knockdown of LyLAP was sufficient to arrest proliferation and cause cell death in PDA cell lines.

CONCLUSION: Our discovery of LyLAP addresses a major gap in lysosomal proteolysis. Its processive activity on hydrophobic residues ensures complete degradation of single-pass and multipass transmembrane proteins. Questions remain about how LyLAP cooperates with other hydrolases, the sequence of proteolytic events, and alternative mechanisms in LyLAP-deficient cells.

The elevated expression of LyLAP in PDA and their strongly reduced viability upon LyLAP ablation suggest a model where, by delivering large amounts of integral membrane proteins to the lysosome, the elevated macropinocytic activity of PDA cells makes them highly dependent on LyLAP function. ■

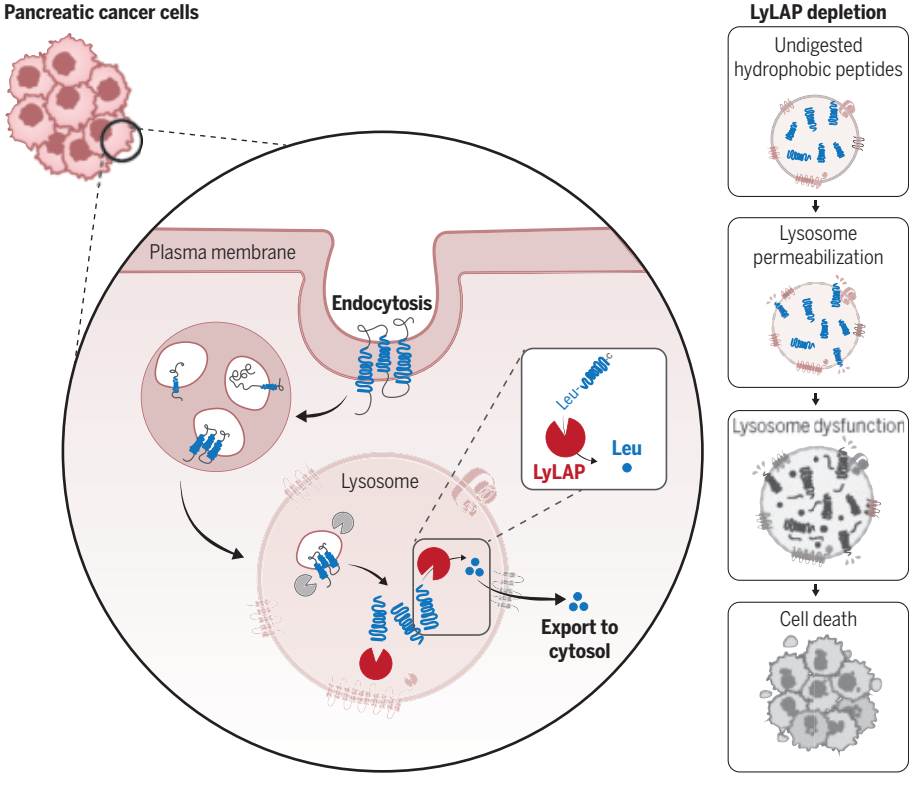

LyLAP enables membrane protein degradation in highly endocytic cells. Integral membrane proteins at the plasma membrane are internalized and trafficked to the lysosome, where LyLAP mediates the complete degradation of hydrophobic transmembrane domains. In highly endocytic pancreatic cancer cells, LyLAP depletion triggers the accumulation of undigested hydrophobic peptides, inducing lysosomal permeabilization and dysfunction, in turn leading to cell death.

The list of author affiliations is available in the full article online.
*Corresponding author. Email: rzoncu@berkeley.edu
Cite this article as A. Jain *et al.*, *Science* **387**, eadq8331 (2025). DOI: 10.1126/science.adq8331

READ THE FULL ARTICLE AT
https://doi.org/10.1126/science.adq8331

RESEARCH ARTICLE SUMMARY

DEVELOPMENT

Chromatin accessibility landscape of mouse early embryos revealed by single-cell NanoATAC-seq2

Mengyao Li†, Zhenhuan Jiang†, Xueqiang Xu, Xinglong Wu, Yun Liu, Kexuan Chen, Yuhan Liao, Wen Li, Xiao Wang, Yuqing Guo, Bo Zhang, Lu Wen*, Kehkooi Kee*, Fuchou Tang*

INTRODUCTION: Preimplantation development marks the beginning of mammalian life, generating the entire embryo proper and extraembryonic tissues from a totipotent zygote. However, owing to technical limitations, the epigenetic regulation of biological processes during this period, including zygotic genome activation (ZGA), lineage differentiation, and initiation of pluripotency, remains inadequately understood.

RATIONALE: We hypothesized that the regulation of chromatin states, especially on repetitive elements, plays vital roles in preimplantation embryos. Furthermore, transcription factors (TFs) are fundamentally involved in their gene expression networks. Therefore, we developed scNanoATAC-seq2, a single-cell assay for transposase-accessible chromatin using long-read sequencing that can accurately depict the chromatin state of repetitive elements usually missed by the short-read ATAC-seq.

RESULTS: We utilized scNanoATAC-seq2 to analyze the chromatin accessibility landscape across all key stages of mouse preimplantation development. We systematically identified TFs that are potentially important for each stage and lineage of preimplantation embryos based on their downstream target sites' chromatin accessibility features and elucidated their activity dynamics, including SOX2, OCT4, and KLF2 for epiblast (EPI); GATA6, SOX17, and HNF1B for primitive endoderm (PE); and TEAD4, GATA3, and CDX2 for trophectoderm (TE).

We delineated the chromatin states of paternal and maternal X chromosomes in female embryos during their imprinted inactivation and reactivation. Examining two opposing regulators of X chromosome inactivation (XCI), the *Xist* and *Tsix* domains, we uncovered a notable shift of allele-specific chromatin accessibility between them. The paternal-specific chromatin accessibility of the *Xist* domain is primarily associated with the imprinted XCI (iXCI) from zygote to eight-cell stage. Subsequently, during lineage segregation into inner cell mass (ICM) and early TE, the paternal-specific feature of the *Xist* domain diminishes, whereas the *Tsix* domain exhibits a moderate increase in maternal-specific feature. In the extraembryonic lineages (TE and PE), iXCI is maintained and only associated with the strong maternal-specific chromatin accessibility of the *Tsix* domain. By contrast, in the EPI, both the *Xist* and *Tsix* domains transition to allele-balanced chromatin accessibility patterns, coinciding with the erasure of iXCI in this pluripotent lineage.

Furthermore, we characterized chromatin states of repetitive elements at individual copy resolution. More than 100 copies of full-length long interspersed nuclear element–1 (LINE1) elements are activated at two-cell stage, potentially allowing their genomic transposition. During ZGA, activated copies from major repetitive element families, such as LINE1 and endogenous retrovirus–L (ERVL), exhibit clear positive correlations between their proximity to the nearest promoter and the degree of transcriptional activation of the corresponding target gene. This suggests their cis-regulatory function, particularly for murine ERVL, in regulating the ZGA-specific expression of protein-coding genes, such as *Sp110*, *Zscan4c*, and *Tcstv3*.

CONCLUSION: Our results suggest that the synchronized activities of critical TFs are potentially responsible for the wavelike gene expression patterns during preimplantation development. These patterns likely underpin key events, such as ZGA, lineage segregation between embryonic and extraembryonic cells, the initiation of pluripotency in ICM, the establishment of multipotency in TE, and the maintenance of iXCI in extraembryonic lineages and its erasure in the pluripotent EPI in female embryos. ■

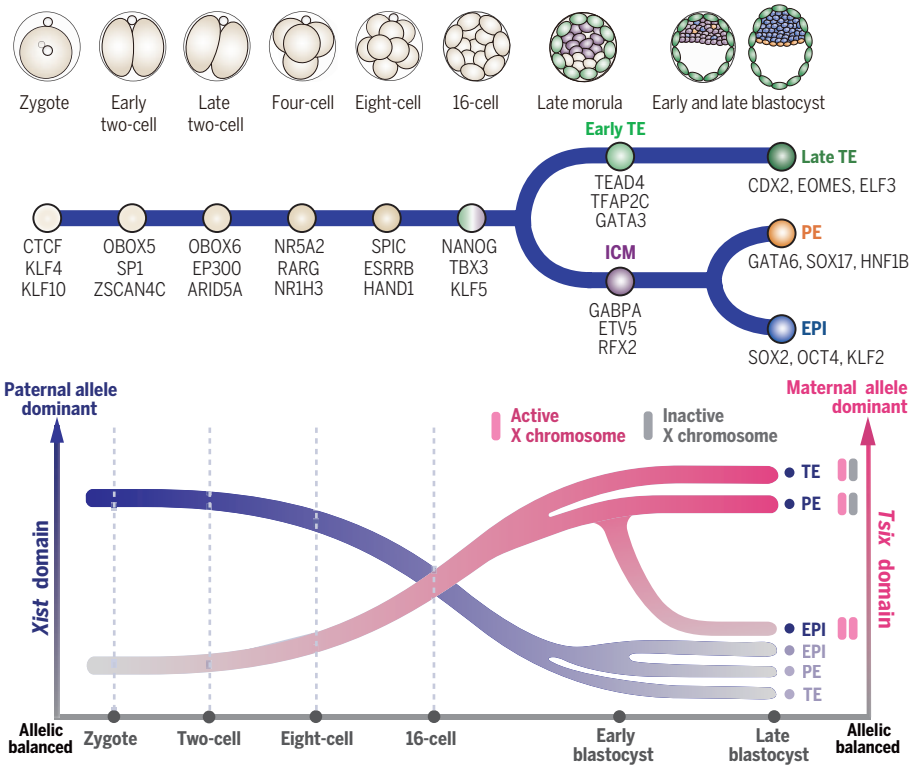

Gene regulatory landscape of mouse preimplantation development. Single-cell chromatin accessibility landscape of mouse embryos from zygote to blastula identified TFs potentially controlling key biological events, such as ZGA and lineage segregation between embryonic (EPI) and extraembryonic cells (TE and PE). Regulatory dynamics of imprinted X chromosome inactivation and reactivation were characterized, including a shift of allele-specific chromatin accessibility between the *Xist* and *Tsix* domains.

The list of author affiliations is available in the full article online.
*Corresponding author. Email: wenlu@pku.edu.cn (L.W.); kkee@mail.tsinghua.edu.cn (K.K.); tangfuchou@pku.edu.cn (F.T.)
†These authors contributed equally to this work.
Cite this article as M. Li *et al.*, *Science* **387**, eadp4319 (2025). DOI: 10.1126/science.adp4319

READ THE FULL ARTICLE AT
https://doi.org/10.1126/science.adp4319

RESEARCH ARTICLE SUMMARY

METABOLISM

Canine genome-wide association study identifies *DENND1B* as an obesity gene in dogs and humans

Natalie J. Wallis†, Alyce McClellan†, Alexander Mörseburg, Katherine A. Kentistou, Aqfan Jamaluddin, Georgina K. C. Dowsett, Ellen Schofield, Anna Morros-Nuevo, Sadia Saeed, Brian Y. H. Lam, Natasha T. Sumanasekera, Justine Chan, Sambhavi S. Kumar, Rey M. Zhang, Jodie F. Wainwright, Marie Dittmann, Gabriella Lakatos, Kara Rainbow, David Withers, Rebecca Bounds, Marcella Ma, Alexander J. German, Jane Ladlow, David Sargan, Philippe Froguel, I. Sadaf Farooqi, Ken K. Ong, Giles S. H. Yeo, John A. Tadross, John R. B. Perry, Caroline M. Gorvin, Eleanor Raffan*

INTRODUCTION: Obesity is a heritable disease, but its genetic basis is incompletely understood, and moving from common genetic associations to mechanistic insight has proven challenging. Hypothalamic leptin-melanocortin signaling is a critical nexus of the central control of energy balance that integrates peripheral signals of energy status, translating them into alterations in energy expenditure and eating behavior to maintain energy homeostasis.

RATIONALE: Dogs are a compelling model of obesity because they develop obesity subject to environmental influences similar to those that influence obesity in humans and because population bottlenecks at breed formation render trait mapping highly tractable. We studied an obesity-prone dog breed, the Labrador retriever, and tested whether variants associated with canine adiposity highlight genes that are also relevant to human obesity.

RESULTS: In 241 adult pet Labrador retrievers, we performed a genome-wide association study (GWAS) for body condition score (BCS), a measure of canine adiposity. The top association was intronic within the gene DENN domain containing 1B (*DENND1B*). Each allele of the lead variant in dogs conferred ~8% higher body fat. At the syntenic region of the human genome, there was also a highly significant association with body mass index (BMI), although with small effect size (0.011 kg/m^2 increase per copy of the risk allele; $P = 9.42 \times 10^{-9}$). Multiple lines of evidence implicated that *DENND1B* is the most likely causal gene at this locus. Rare, damaging variants in *DENND1B* were also nominally associated with BMI in the UK Biobank study [$P = 0.0087$; effect size (β) = 0.35 kg/m^2], and a homozygous, damaging variant was implicated as the cause of severe childhood obesity in a single proband. At each of the four additional canine loci that met a less stringent significance threshold, positional candidate genes were also associated with human BMI.

DENND1B has a known role in clathrin-mediated endocytosis that underlies its association with human asthma through the regulation of T cell receptor function. We hypothesized that it would affect the activity of receptors involved in energy homeostasis, particularly melanocortin 4 receptor (MC4R). We showed that *DENND1B* is coexpressed with *MC4R* and other relevant receptors in single-cell expression data from both the murine and human hypothalamus. In cell models, overexpression of *DENND1B* increased MC4R internalization after ligand activation and reduced cyclic adenosine 3′,5′-monophosphate (cAMP) signaling, with the converse effect on *DENND1B* knockdown. By contrast, there was no such effect on the orexigenic receptor, growth hormone secretagogue receptor (GHSR).

A canine polygenic risk score (PRS) improved prediction of BCS and body weight in an independent set of Labrador retrievers but had little or no predictive value in other breeds. Association of PRS with food motivation indicated that genetic risk is in part mediated by greater appetite in dogs. That relationship may underlie the higher PRS observed in Labradors selected to be assistance dogs because high food drive could improve their responsiveness to food used to positively reinforce desirable behaviors during training. We also observed that strict owner control of diet and exercise was influential in preventing obesity in dogs with high polygenic risk but not in dogs with low polygenic risk, which were relatively resistant to becoming overweight.

CONCLUSION: We identified obesity-related genes in humans by studying the canine model, with findings relevant to preventative and therapeutic interventions in both species. The discovery of DENND1B as a regulator of MC4R activity informs our understanding of melanocortin signaling—a critical pathway in hypothalamic regulation of energy homeostasis. Notably, our findings show that even high polygenic risk can be mitigated. These findings demonstrate the benefits of studying complex disease in nontraditional animal models, such as the dog, and have practical implications for improved management of canine obesity. ■

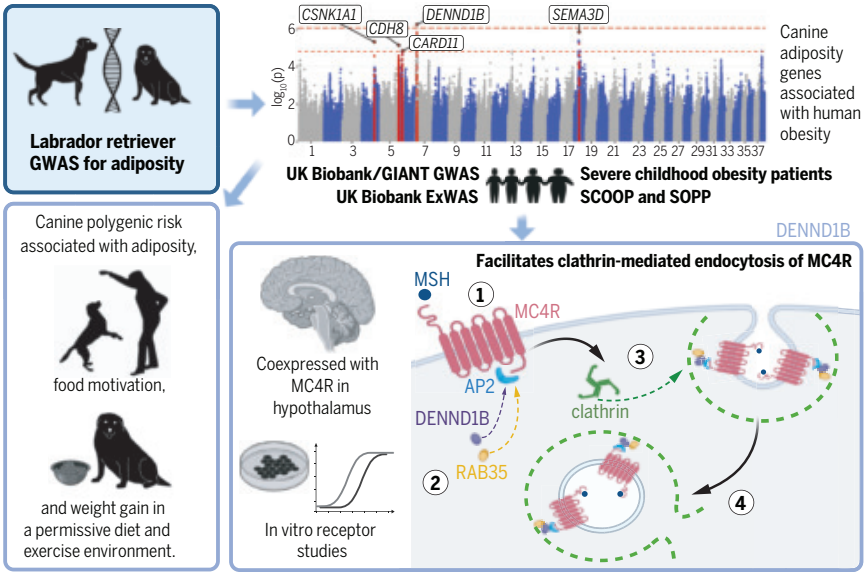

***DENND1B* and other canine obesity genes were also associated with obesity in humans.** After (1) ligand activation of the hypothalamic melanocortin receptor (MC4R), DENND1B (2) binds adaptor protein 2 (AP2) and RAB35 to initiate (3) clathrin-mediated endocytosis, a process that leads to (4) deactivation of the receptor, providing a mechanistic link between DENND1B expression and regulation of energy homeostasis. ExWAS, exome-wide association study; SCOOP, Severe Childhood Onset Obesity Project; SOPP, Severe Obesity in Pakistani Population; MSH, melanocyte-stimulating hormone.

The list of author affiliations is available in the full article online.
*Corresponding author. Email: er311@cam.ac.uk
†These authors contributed equally to this work.
Cite this article as N. J. Wallis *et al.*, *Science* **387**, eads2145 (2025). DOI: 10.1126/science.ads2145

READ THE FULL ARTICLE AT
https://doi.org/10.1126/science.ads2145

RESEARCH ARTICLE SUMMARY

ENERGETICS

Running a genetic stop sign accelerates oxygen metabolism and energy production in horses

Gianni M. Castiglione*, Xin Chen†, Zhenhua Xu†, Nadir H. Dbouk†, Anamika A. Bose†, David Carmona-Berrio, Emiliana E. Chi, Lingli Zhou, Tatiana N. Boronina, Robert N. Cole, Shirley Wu, Abby D. Liu, Thalia D. Liu, Haining Lu, Ted Kalbfleisch, David Rinker, Antonis Rokas, Kyla Ortved, Elia J. Duh*

INTRODUCTION: Horses are famous examples of evolutionary novelty, with the fossil record chronicling their ascent from dog-sized ancestors into physiological powerhouses, long before domestication. In modern thoroughbred racehorses, mass-adjusted oxygen consumption is more than double that of elite human athletes, fueling the voracious energy production demands of equine skeletal muscle. Genomes of modern and ancient equids have revealed mutations in olfactory receptors, keratins, and myosin-related genes that are absent from humans and cows, yet none of these are directly involved in aerobic metabolism and energy production. How *Equus* ancestors met the energy demands associated with their remarkable morphological innovations is therefore unknown.

RATIONALE: To study the molecular underpinnings of equine aerobic metabolism, we focused on a clinically important pathway that can enhance mitochondrial bioenergetics while simultaneously mitigating the tissue-damaging oxidative stress caused by exercise or disease. The NRF2/KEAP1 pathway is a major area of focus in exercise science and clinical translational efforts, including chronic diseases such as emphysema. Diminished KEAP1 inhibitory activity leads to increased NRF2 activity, thereby enhancing antioxidant production and mitochondrial respiration. KEAP1 mutations have occurred at least twice in evolution: initially to facilitate the vertebrate transition from aquatic to terrestrial life by protecting against ultraviolet light–induced oxidative stress, and more recently during the evolution of birds to counterbalance the oxidative stress imposed by energetically demanding flapping flight.

RESULTS: We reveal that horses, donkeys, and zebras (*Equus*) possess a relic of the ancient Equidae radiation—a premature stop codon in KEAP1 (R15X) that evolved in a common *Equus* ancestor. Using mass spectrometry, we demonstrate that this de novo opal stop codon (UGA) does not truncate the protein and is instead recoded into a cysteine in horse KEAP1 (C15). Using biochemistry and structural biology, we show that opal recoding is facilitated by a set of *Equus*-specific mutations at the mRNA and protein levels that coevolved with R15X, ultimately enhancing opal recoding relative to human orthologs. Through cellular assays, we show that the evolution of R15C KEAP1 increases sensitivity to electrophiles and reactive oxygen species, leading to increased NRF2 activity and lower oxidative stress. Using comparative metabolomics of myotubes derived from thoroughbred quadriceps and CRISPR-Cas9–generated cell models, we provide evidence that this genetic recoding also accelerates adenosine 5′-triphosphate (ATP) production–coupled mitochondrial oxygen consumption rates. These processes provide an elegant solution to the dual problem of enhancing aerobic energy production while mitigating oxidative stress, likely explaining why R15X/C evolved in a common *Equus* ancestor under selection for improved locomotory bioenergetics.

CONCLUSION: We discovered coordinated biochemical adaptations from the distant past not captured by the fossil record, illustrating how recoding of a de novo stop codon can facilitate adaptation in vertebrates, a strategy previously thought restricted to viruses. These ancient evolutionary innovations can enlighten contemporary clinical efforts seeking to augment NRF2 function and also to promote read-through of disease-associated premature stop codons. ■

The list of author affiliations is available in the full article online.
*Corresponding author. Email: eduh@jhmi.edu (E.J.D.); gianni.castiglione@vanderbilt.edu (G.M.C.)
†These authors contributed equally to this work.
Cite this article as G. M. Castiglione *et al.*, *Science* **387**, eadr8589 (2025). DOI: 10.1126/science.adr8589

READ THE FULL ARTICLE AT
https://doi.org/10.1126/science.adr8589

Opal recoding in horses alters protein phenotypes, enhancing exercise performance. An extinct ancestor of *Equus* evolved an opal stop codon in KEAP1 (UGA; R15X) that is recoded into cysteine through previously unknown mRNA and protein mechanisms. The resulting R15C KEAP1 protein is more sensitive to electrophiles and reactive oxygen species (ROS), enabling increased NRF2 activity. This accelerates mitochondrial respiration while decreasing tissue-damaging oxidative stress.

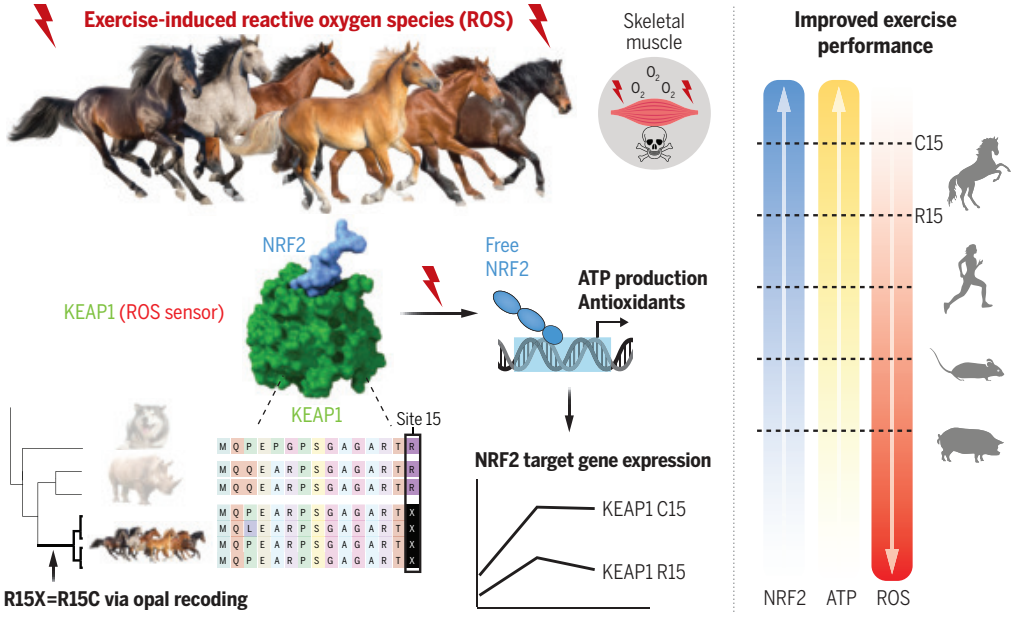

RESEARCH ARTICLE SUMMARY

NEUROSCIENCE

Hedonic eating is controlled by dopamine neurons that oppose GLP-1R satiety

Zhenggang Zhu, Rong Gong, Vicente Rodriguez, Kathleen T. Quach, Xinyu Chen, Scott M. Sternson*

INTRODUCTION: Hedonic eating is food ingestion that is driven by palatability rather than bodily need. This can lead to overeating, which in turn may contribute to obesity. Despite the important link between food palatability and hedonic eating, the neural mechanisms controlling this process are poorly understood.

RATIONALE: Eating behaviors unfold in three phases. The seeking, consumption, and satiety phases initiate, sustain, and terminate feeding, respectively. These phases are coordinated by separate but interacting neural circuits that operate with distinct timing. Although progress has been made in our understanding of the neural basis of food seeking and satiety, attempts to define neural circuits for palatability control over the consumption phase show contradictory results.

Ventral tegmental area dopamine (VTA^{DA}) neurons are a prominent candidate cell type for promoting palatable food consumption because they are activated by rewards. However, most manipulations of dopamine neurons have been reported to reduce food consumption. To reconcile this discrepancy, we avoided the temporally nonspecific manipulations of previous studies by manipulating VTA^{DA} neuron activity only during consumption, just one phase of their their natural activity pattern.

Another cell type involved in hedonic eating are glutamate-releasing neurons in a brain region called the peri–locus ceruleus ($periLC^{VGLUT2}$ neurons). Some of these neurons are inhibited during hedonic eating in a manner scaled by food palatability or hunger state. Although these neurons do not trigger food seeking, their inhibition during consumption prolongs ongoing food intake, particularly with palatable foods. However, the pathway through which these neurons influence food consumption was unknown.

RESULTS: Here, we found that VTA^{DA} neuron activity was time locked to the duration of food consumption, and this response was scaled by food palatability. These effects were also observed when measuring dopamine release in the nucleus accumbens (NAc), a downstream target of VTA^{DA} neurons. Hunger increased VTA^{DA} neuron activity during consumption, whereas a sickness state reduced it. When we optogenetically boosted VTA^{DA} neuron activity specifically during consumption, food intake was prolonged in a manner similar to the effect of increasing food palatability. Conversely, inhibition of VTA^{DA} neurons reduced consumption. Highlighting the consumption-specific effect of VTA^{DA} neurons, activation of these neurons when mice were not eating did not cause the animals to approach food or increase food intake.

Moreover, we showed that $periLC^{VGLUT2}$ neurons signal to VTA^{DA} neurons to influence consumption through an indirect pathway: $periLC^{VGLUT2}$ neuron axons primarily targeted VTA^{VGAT} neurons, which inhibit VTA^{DA} neurons.

We also found that the antiobesity drug semaglutide initially reduced the duration of palatable food consumption, accompanied by a decrease in VTA^{DA} neuron activity. Optogenetic activation of VTA^{DA} neurons partially counteracted the appetite-lowering effect of semaglutide for palatable food. Additionally, as mice lost weight on semaglutide, VTA^{DA} neuron activity increased, as did palatable food intake, which could be reversed by inhibiting VTA^{DA} neurons.

CONCLUSION: Collectively, our experiments show that VTA^{DA} neurons are engaged throughout the consumption phase of feeding and play a pivotal role in hedonic eating. Their influence is specifically tied to VTA^{DA} neuron activity during food consumption, mirroring the consumption-specific role of $periLC^{VGLUT2}$ neurons, which are selectively suppressed during food intake and thus participate in a circuit configured to disinhibit VTA^{DA} neurons. These circuit dynamics during palatable food intake up-regulate dopamine in the NAc, a brain region that modulates the duration of consumption.

VTA^{DA} neurons are engaged during each of the three phases of motivated behavior. This study clarifies the involvement of VTA^{DA} neurons in the consummatory phase of hedonic food intake. We highlight the critical role of VTA^{DA} neuron timing to affect eating behavior, where consumption-locked activation promotes food intake but nonspecific activation either has no effect on feeding (our results) or reduces it (prior reports). VTA^{DA} neurons control the duration of ongoing food consumption, and this mechanism fills a gap in our understanding of appetite control by palatable food, which may provide insights into the development and treatment of obesity. ■

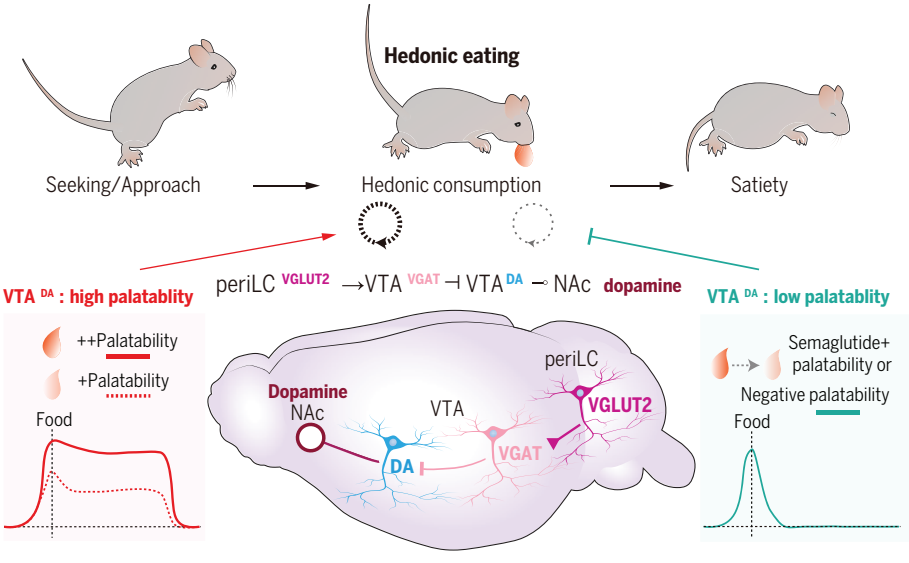

Control of hedonic eating by VTA^{DA} neurons. The consumption phase of appetite involves sensory feedback to sustain hedonic eating, which is independent of physiological need. VTA^{DA} neurons participate in a circuit ($periLC^{VGLUT2}$ →VTA^{VGAT} ⊣ VTA^{DA} ⊸NAc dopamine) in which activity is increased by positive palatability (left) or decreased by negative palatability or an antiobesity drug (right). VTA^{DA} neurons are directly involved in regulating the duration of food consumption and have an important role in hedonic eating.

The list of author affiliations is available in the full article online.
*Corresponding author. Email: sstern son@health.ucsd.edu
Cite this article as Z. Zhu *et al.*, *Science* **387**, eadt0773 (2025). DOI: 10.1126/science.adt0773

READ THE FULL ARTICLE AT
https://doi.org/10.1126/science.adt0773

RESEARCH ARTICLES

ORGANIC CHEMISTRY

Sulfonyl hydrazides as a general redox-neutral platform for radical cross-coupling

Jiawei Sun[1]†, Áron Péter[1]†, Jiayan He[1]‡, Jet Tsien[1]‡, Haoxiang Zhang[1]‡, David A. Cagan[1], Benjamin P. Vokits[2], David S. Peters[3], Martins S. Oderinde[4], Michael D. Mandler[2], Paul Richardson[5], Doris Chen[5], Maximilian D. Palkowitz[6], Nicholas Raheja[1], Yu Kawamata[1], Phil S. Baran[1]*

Sulfonyl hydrazides are stable and usually crystalline substances that can be accessed in a variety of ways, including transiently from hydrazones, to achieve a net reductive arylation of carbonyl compounds. We show their utility as versatile radical precursors, as exemplified with seven C–C bond–forming, redox-neutral cross-couplings with activated olefins, alkyl halides, redox-active esters, aryl halides, alkenyl halides, alkynyl halides, and a trifluoromethylating reagent, to forge C(sp^3)-C(sp^3), C(sp^3)-C(sp^2), and C(sp^3)-C(sp) bonds. Exogenous redox (chemical, photo/electrochemical) additives are not necessary because these functional groups serve the dual role of radical precursor and electron donor. The homogeneous, water-compatible reaction conditions are operationally simple and contribute to streamlining synthesis and mild late-stage functionalization.

The use of radical cross-coupling in retrosynthetic analysis has experienced a renaissance over the past decade (*1*–*4*). This is due to the simple, convergent disconnections of challenging C–C bonds leading back to ever-present functional groups such as halides, acids, amines, alcohols, and olefins (Fig. 1A) (*4*–*12*). In practice, all of these widely used radical precursors require some sort of exogenous redox activation mode. Regardless of the choice of oxidative or reductive activation, this generally requires stoichiometric chemical additives, catalysts to facilitate photoinduced electron transfer, or electrochemistry (*5*, *8*, *13*). A simpler means to achieve radical cross-coupling without the use of exogenous redox methods would be highly attractive based on first-principles reasoning, because it would reduce cost and the complexity of reaction setup. Alkyl diazenes are a prime candidate for radical precursors that could achieve such an objective (*14*, *15*). These species have been invoked since the late 1930s (*16*, *17*), but their use in organic synthesis has been sporadic and mainly relegated to $2e^-$-defunctionalization methods such as the classic Wolff–Kishner reduction and related reactions (*17*–*21*) (Fig. 1B, left). A report on the use of in situ–derived diazenes from sulfonyl hydrazides was reported by Taber in 1993, wherein the radical cyclization of ketone **1** to octahydroindane **2** was achieved (Fig. 1B, right) (*22*). Building on this precedent, we wondered whether free radicals derived without redox-initiation from these intermediates could be enlisted in metal-catalyzed cross-coupling events. Herein we disclose a general platform for redox-neutral radical cross-couplings driven by in situ–derived alkyl diazenes to forge a variety of C–C bonds. Alkyl sulfonyl hydrazides are easily derived from carbonyl compounds and alcohols (N-sulfonyl regioisomers can be used interchangeably); these stable, crystalline substances can now be used to generate a variety of useful C(sp^3)-C(sp^3), C(sp^3)-C(sp^2), and C(sp^3)-C(sp) linkages in a practical "dump-and-stir" fashion, obviating the need for any external redox activation (Fig. 1C).

Figure 2 illustrates the versatility of sulfonyl hydrazides as redox-neutral coupling partners in seven valuable C–C bond–forming events. Each of these methods could warrant their own separate disclosure to describe their optimization and development. For the sake of brevity, this initial report describes an inaugural scope for each reaction. A discussion of their optimization can be found in the supplementary materials. The simplest of radical couplings, namely Giese-type additions to unsaturated species, was demonstrated first (Fig. 2A, top). For this reaction, 4,4′-di-tert-butyl-2,2′-dipyridyl (dtbbpy) was used in concert with Ni(dme)Cl_2 along with Et_3N (3.0 equiv.) to furnish five representative adducts in 28 to 65% yield (**3** to **7**). Notably, the yield of this reaction was considerably reduced in the absence of a Ni/L system. Next, the direct formation of C(sp^3)-C(sp^3) linkages was explored using both alkyl halides and alkyl redox-active esters (RAEs) as coupling partners (Fig. 2A, bottom) (*23*–*25*). Using a near-stoichiometric ratio of coupling partners (1.5 equiv. of sulfonyl hydrazide and 1.0 equiv. of alkyl halide or RAE) in the presence of Ni(dme)Cl_2, 2,6-bis(pyrazol-1-yl)pyridine (bpp), in addition to Et_3N (3.0 equiv.) at 60°C in dimethylformamide (DMF), provided a range of secondary-secondary (**10** to **12**, **15**, and **16**) and secondary-primary adducts (**9**, **13**, and **14**) in good yield. From an operational standpoint, this reaction represents perhaps the simplest and least expensive means of forming saturated C–C bonds (especially for challenging 2°-2° linkages) (*3*, *26*). A notable aspect of this coupling approach is that no exogenous redox chemistry is necessary even though RAEs and alkyl halides have historically required reductive radical generation (*27*, *28*).

Turning to C(sp^3)-C(sp^2) and C(sp^3)-C(sp) linkages, an array of viable coupling partners were identified to access broad regions of chemical space (Fig. 2B) (*29*–*34*). Alkenyl donors (bromides, iodides, and triflates), aryl halides (chlorides and bromides), and alkynyl bromides were all easily coupled with sulfonyl hydrazides (**23** to **29**, and **34** to **35**; **17** to **22**, and **33**; **30** to **32**, respectively), using similar conditions to that described above with the notable exception that the distinct—though commercial—dNH_2-bpy ligand often led to higher yields. Unlike most reductive modes of accomplishing such transformations, protodehalogenation and/or homodimerization of the C(sp^2)-halide substrate is greatly suppressed, thereby simplifying product isolation. Both the use of C(sp^2)-chlorides and triflates and absence of pyrophoric reagents (Negishi and Kumada type) (*35*–*37*), palladium, or redox-focused reaction setups (photo/electrochemistry) (*3*) lowers the practical barrier to widespread application of these radical cross-couplings.

The aforementioned reactions all rely on Ni catalysis to facilitate productive C–C bond formation. However, the use of sulfonyl hydrazides is not limited to Ni, as exemplified in Fig. 2C with the direct trifluoromethylation of these species (**36** to **42**) using Grushin's commercial Cu-based reagent (*38*), Cu(bpy)(CF_3)$_3$ (easily prepared on a gram scale from $TMSCF_3$ and CuI). Unlike the related trifluoromethylation of alkyl halides or alcohols with the same reagent (*39*, *40*), no exogenous redox activation is required.

In general, the 3,5-difluorophenylsulfonyl hydrazides exhibited the optimum reactivity for secondary cyclic radicals, but in many cases, such as primary derived radicals, the simple tosyl-substituted hydrazide can be used (**33** to **35** and **38** to **42**). In the case of arylation, simple tosyl hydrazides performed well (**17** to **21**). As a general matter, the by-products resulting from a hydrazide are easily removed (N_2 gas and a sulfinate salt) upon aqueous workup. These reactions are ideal for parallel

[1]Department of Chemistry, Scripps Research, La Jolla, CA, USA. [2]Discovery and Development Sciences, Bristol Myers Squibb, Princeton, NJ, USA. [3]Discovery and Development Sciences, Bristol Myers Squibb, San Diego, CA, USA. [4]Synthesis & Enabling Technologies, Discovery and Development Sciences, Bristol Myers Squibb, Princeton, NJ, USA. [5]Medicinal Chemistry Department, Pfizer, San Diego, CA, USA. [6]Discovery and Development Sciences, Bristol Myers Squibb, Cambridge, MA, USA.
*Corresponding author. Email: pbaran@scripps.edu
†These authors contributed equally to this work.
‡These authors contributed equally to this work.

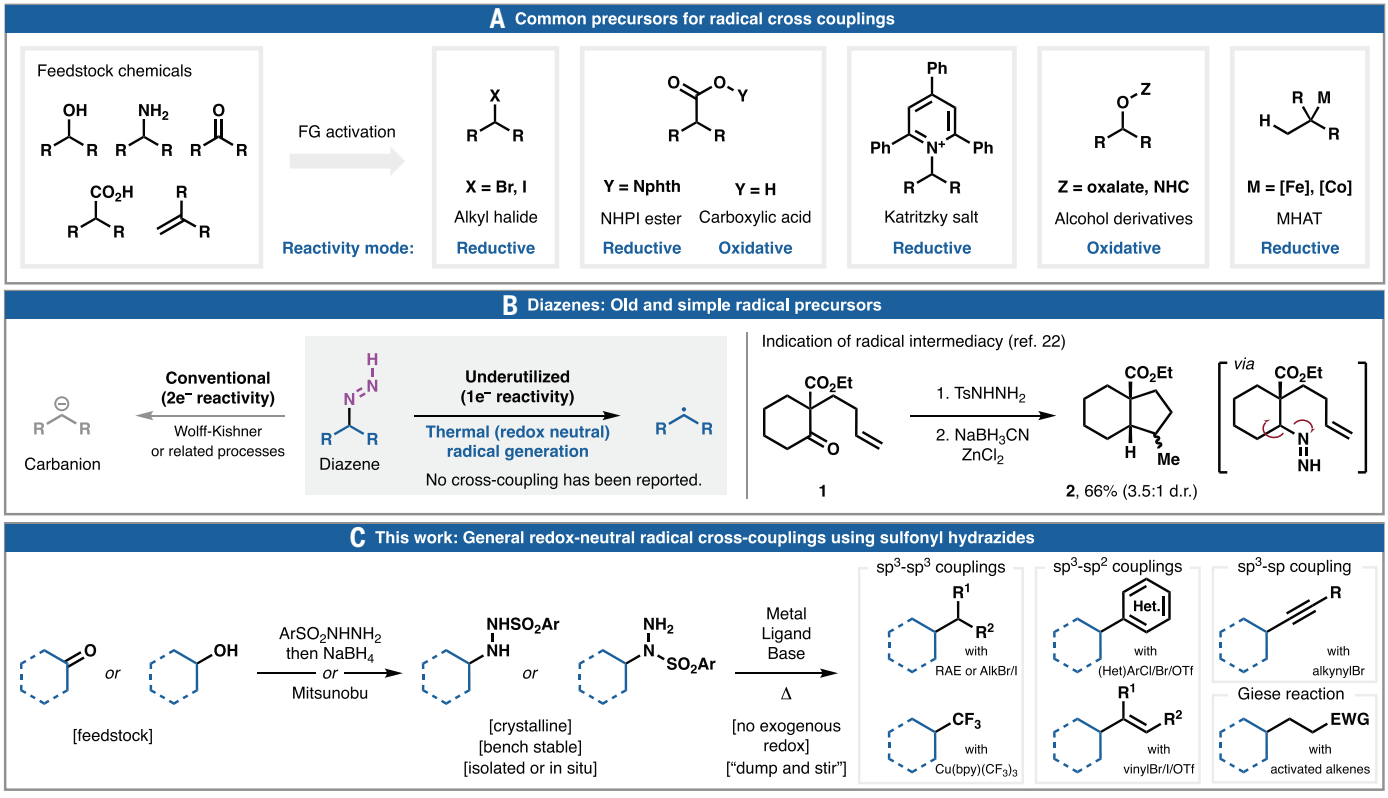

Fig. 1. Background and reaction development. (**A**) Common radical cross-coupling precursors. (**B**) Alkyl diazenes as potential leads for redox-neutral cross-coupling. (**C**) Realization of general redox-neutral cross-couplings using sulfonyl hydrazide precursors.

screening workflows because they are homogeneous and can be conducted on a very small scale in contrast to redox-based heterogeneous conditions, which create technical challenges for miniaturization. As discussed below, they can also be scaled up with ease as a result of their homogeneity. Explorations thus far have revealed most 2°-cyclic sulfonyl hydrazides to be bench-stable substances, particularly in the case of tosyl hydrazides. 2°-acyclic and 1°-tosyl hydrazides obtained after hydrazone reduction should be used shortly after preparation, whereas 1° hydrazides prepared through Mitsunobu (different NSO_2Ar regioisomer, Fig. 2B, box) are more stable (several days on a benchtop). A user guide based on current data is provided in the supplementary materials.

In situ sulfonyl hydrazide generation

From an operational perspective it may be desirable to proceed directly from a hydrazone to obtain a coupled product without isolation of the corresponding sulfonyl hydrazide, analogous to the widely used Barluenga coupling (*41*–*43*). In that reaction, a sulfonyl hydrazone is simply combined with a $C(sp^2)$-boronic acid to deliver useful $C(sp^2)$-$C(sp^3)$ linkages by way of a diazo-intermediate. After extensive exploration, a simple silane ($PhSiMe_2H$, ~2 USD per gram) could be added in situ to the standard reaction conditions, thereby enabling the equivalent of a reductive Barluenga coupling using more convenient (hetero)aryl halides, as illustrated in Fig. 3. Dozens of substrates were evaluated across a range of different hydrazones and aryl halides revealing the versatility of this method. In terms of the experimental protocol, it is operationally trivial to conduct because sulfonyl hydrazone formation is quantitative and isolation is optional. In cases where a hydrazone is used without purification, residual quantities of MeOH present after evaporation do not have a major effect on the ensuing coupling. With the hydrazone in hand (isolated or used after evaporation of MeOH), the remaining materials are added [ArX, Ni(dme)Cl_2, dNH_2-bpy], followed by DMF under N_2 or Ar (pre-stirring until homogenous), followed by base and silane. The reaction is heated to 75°C overnight (16 to 18 hours), followed by standard aqueous workup. In terms of the aryl electrophile scope, the trend is what one would expect based on known rates of Ni-oxidative addition into such systems. Using a highly electron-rich ligand (dNH_2-bpy) and elevated temperature helps to extend this scope even further. Thus, electron-rich aryl bromides are competent (**43** and **44**), but electron-poor aryl bromides work better (**45** and **47**). Electron-deficient aryl chlorides are suitable coupling partners (**17**, **18**, **54**, **58**, **60**, and **63** to **67**) as are aryl triflates (**18**). A wide variety of functional groups are tolerated, including valuable handles for further functionalization: Bpin (**46**), polyhalogenated arenes (**50**), free glutarimide NH (**76**), free amino pyridine (**55**), aryl fluorides (**54**), SMe (**59**), tetrazole (**48**), benzylic CHF_2 groups (**68** to **72**, **74**, and **79**), nitriles (**45**, **52**, and **57**), esters (**65** to **71**, **73**, **74**, and **77** to **79**), amides (**51**), ortho substituents (**52**), and challenging heterocycles such as pyrimidines (**58** to **60**), pyrazines (**65** to **67**), indazoles (**61**), and azaindole (**62**).

The array of suitable carbonyl coupling partners appears to be vast. Cyclic ketones with ring sizes ranging from 4 to 6 are easily used. Adjacent heteroatoms are tolerated (**63**, **71**, **72**, **78**, and **79**) and good to high diastereomeric ratio is observed with ketones bearing preexisting stereocenters (**68** and **69**). Complex bridged ketones also provide useful quantities of product in high diastereoselectivity (**67**, **70**, **71**, **73**, and **74**). Finally, aldehydes can be enlisted (**77** to **79**).

The ability to use simple carbonyl groups in complex cross-couplings as outlined above opens an opportunity for retrosynthetic planning because carbonyl groups are often used to generate carbon skeletons. Traditionally, the go-to strategy for such systems involves a sequence of vinyl-triflate or vinyl-boronic acid synthesis, Suzuki coupling, and hydrogenation, which, aside from being laborious (for example

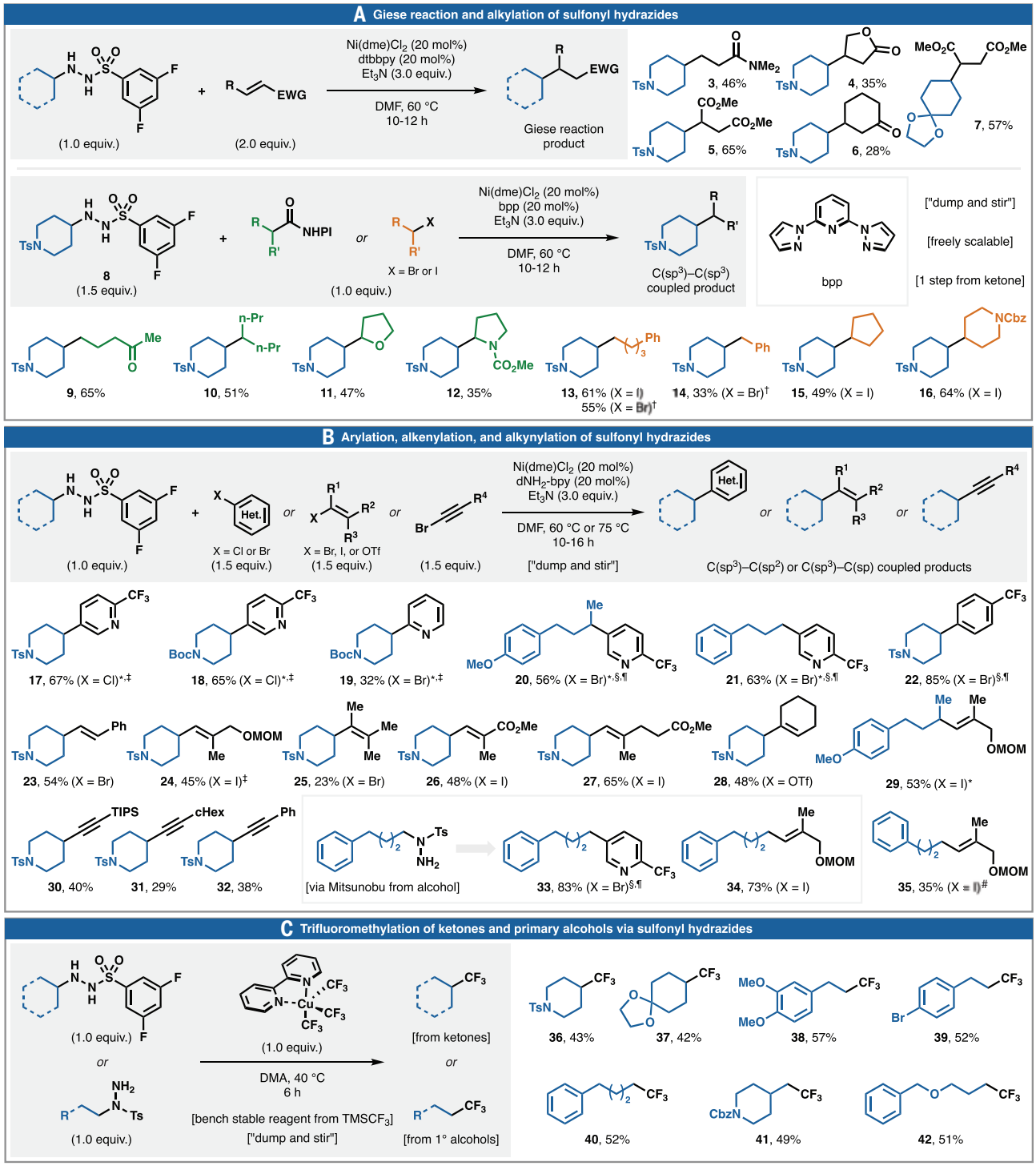

Fig. 2. Seven classes of redox-neutral reactions with sulfonyl hydrazides. (**A**) Giese addition and cross-coupling with alkyl halides and RAEs. (**B**) Cross-coupling with $C(sp^2)$ and C(sp) halides to create aryl-, alkenyl-, and alkynyl-alkyl linkages. (**C**) Trifluoromethylation with Grushin's reagent. *The corresponding Ts hydrazide was used instead of the depicted difluorinated. †NaI (2.0 equiv.) was added. ‡Pempidine was used as the base instead of Et_3N. §dtbbpy was used as ligand instead of dNH_2-bpy. ¶1.0 equiv. of ArBr was used instead of 1.5 equiv. #The compound is accessed from the linear Ts hydrazide. EWG, electron withdrawing group; dme, ethylene glycol dimethyl ether; dtbbpy, 4,4′-di-tert-butyl-2,2′-dipyridyl; DMF, dimethylformamide; dNH_2-bpy, 4,4′-diamino-2,2′-bipyridyl; DMA, dimethylacetamide; Ts, tosyl; Cbz, carbobenzyloxyl; Boc, tert-butyloxycarbonyl; MOM, methoxymethyl; TIPS, triisopropyl silyl; cHex, cyclohexyl.

furan **72**) and nonchemoselective, is impossible to employ on non-enolizable systems such as **70**. Another popular approach is to convert a carbonyl group into a halide and employ it in conventional or reductive cross-coupling approaches; however, this multistep process suffers from limitations in the halogenation of certain alcohols. In some cases, it is desirable to use a sulfonyl hydrazide directly rather than coupling a hydrazone directly (see supplementary materials for more details). Unlike the direct arylation of sulfonyl hydrazides presented in

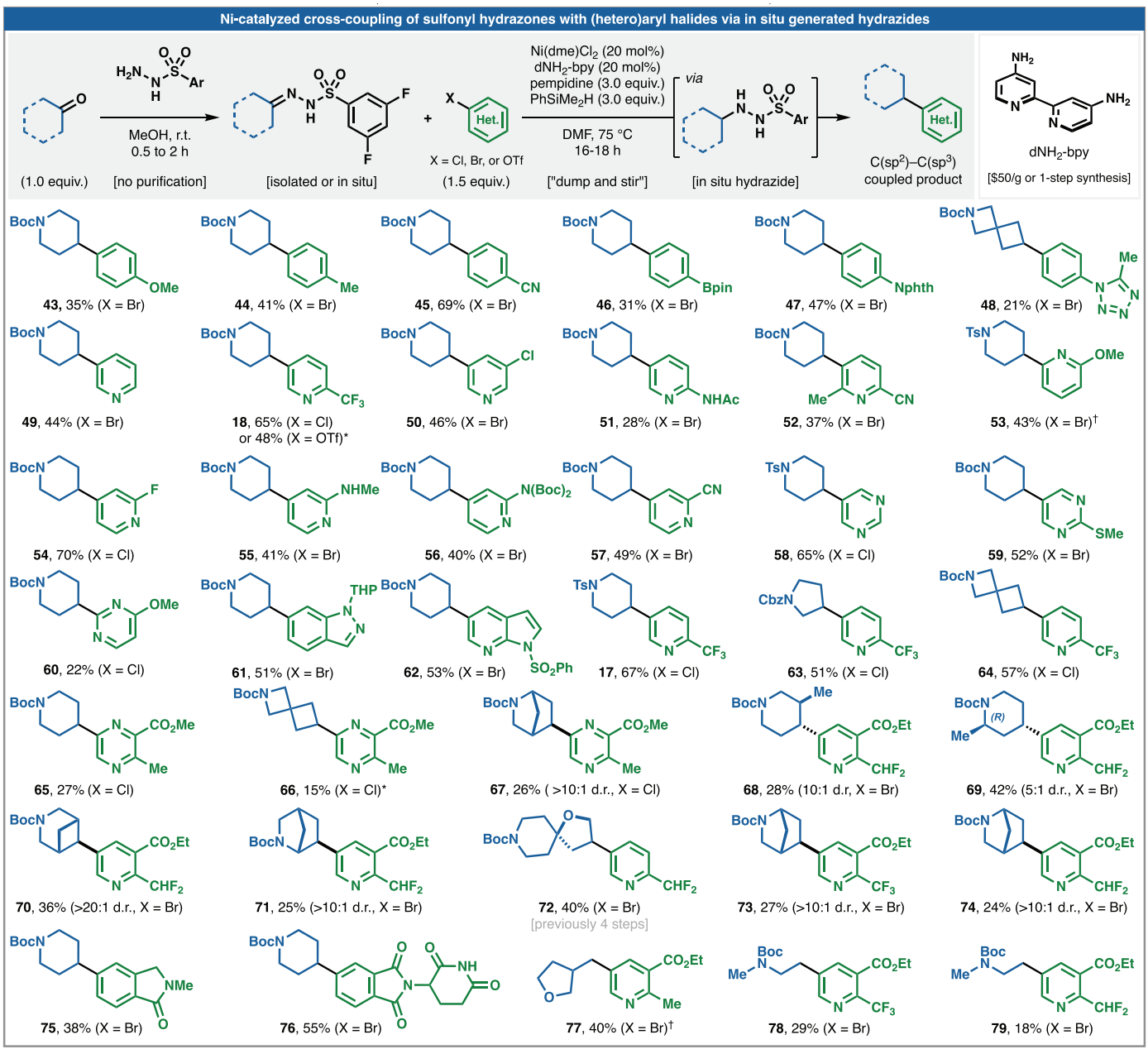

Fig. 3. A one-pot protocol for sulfonyl hydrazide couplings with aryl halides. The reaction proceeds through in situ reduction of hydrazones with an inexpensive silane. *Nuclear magnetic resonance (NMR) yield against 1,3,5-trimethoxybenzene or mesitylene as internal standard. †NaCl (1.0 equiv.) was added.

Fig. 2B, there are more by-products observed using hydrazones with in situ reduction stemming from protodehalogenation and products resulting from reaction with reduced sulfinate (see supplementary materials for more details). The arylation method of Fig. 3 is thus better for rapid screening campaigns in medicinal chemistry, where isolated yields are less important.

Late-stage and scale-up applications

Redox-neutral radical cross-couplings of alkyl sulfonyl hydrazides can considerably simplify access to numerous useful building blocks. For instance, hydroxyethylated pyridine **80** (Fig. 4A) is commercially available yet prohibitively expensive (~784 USD per gram, ChemScene LLC). Retrosynthetically, multiple options can be envisaged using a variety of hydroxyethyl surrogates such as ethylene oxide (**82**), β-hydroxy acid/RAE (**83**), Katritzky salt **84**, boronic acid donor **85**, stannane **86**, and chloroethanol **87** (*44*, *45*). Most of these building blocks are either unsuitable, unstable (**83**), inaccessible (**85** and **86**), or inconvenient to use (**82**). By contrast, commercial hydrazine **88** (0.2 USD per gram) and chloropyridine **81** (4 to 5 USD per gram) can be combined in a single-step process [chloropyridine **81**, TsCl, Ni(dme)Cl_2, and dNH_2-bpy are dissolved in DMF under Ar, then hydrazine **88** and Et_3N are added, stirred at room temperature for 30 min, followed by heating to 75°C for 6 hours] in 68% yield. The generally high chemoselectivity encountered in radical cross-couplings can be further leveraged for mild late-stage modifications such as in the case of the direct functionalization of ticagrelor (Fig. 4B). Without any protecting group chemistry, **89** can be subjected to Mitsunobu with $TsNHNH_2$ to install the sulfonyl hydrazide followed immediately (after aqueous workup) by radical cross-coupling to deliver arylated adduct **90** in 33% yield over two steps (along with ~20%

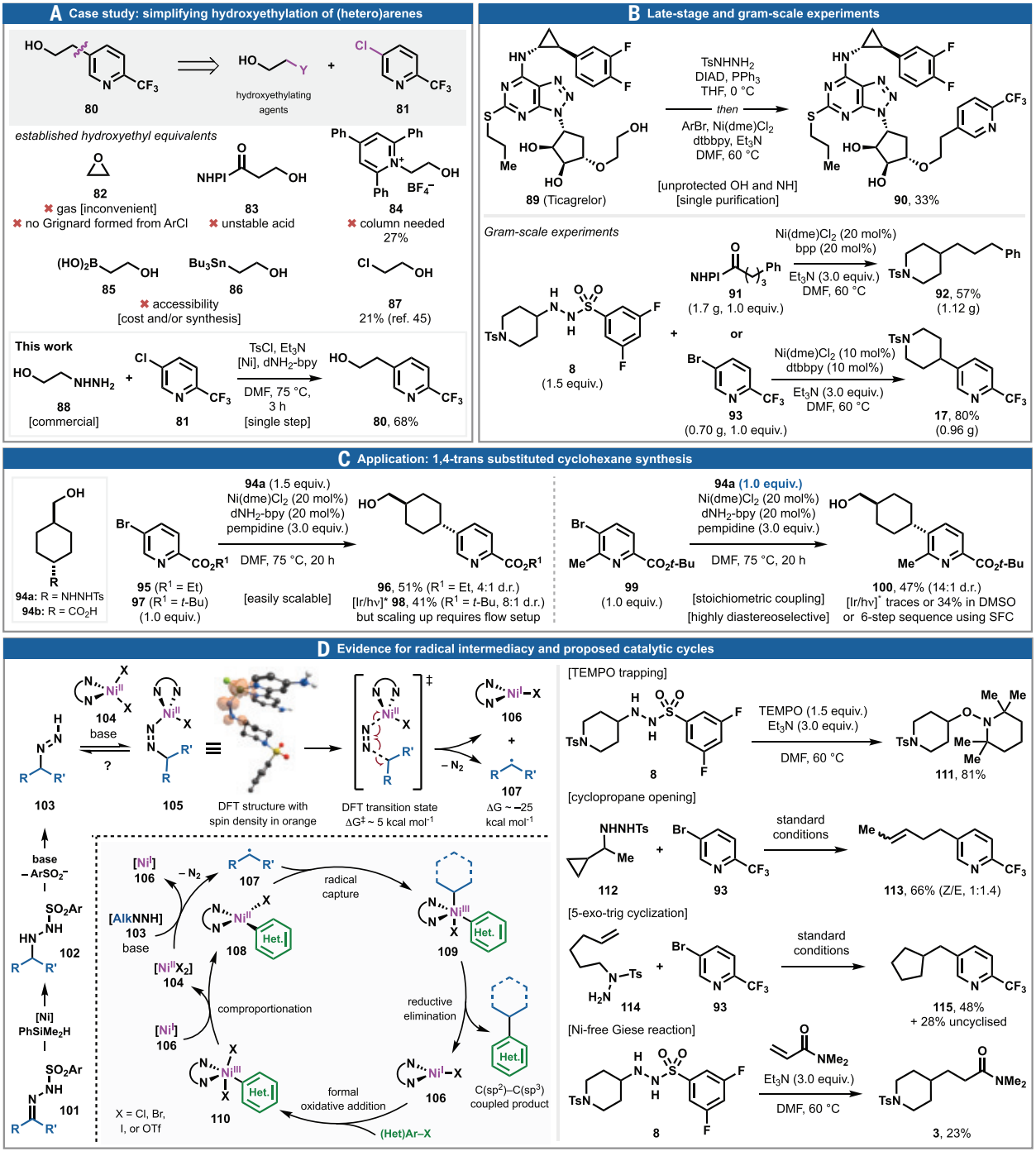

Fig. 4. Late-stage applications and mechanistic considerations. (**A**) Seemingly trivial hydroxyethylation of an aryl chloride can now be accomplished with ease. (**B**) Application to late-stage functionalization and gram-scale examples. (**C**) A case study to compare simplified redox-neutral cross-coupling with conventional photoinduced electron transfer–based decarboxylative coupling. (**D**) Current mechanistic working hypothesis and supporting studies. N–N ligand = 4,4′-diamino-2,2′-bipyridine. Löwdin spin density of **105** is shown, demonstrating radical character at the nickel, nitrogen, and carbon atoms; hydrogen atoms bound to carbon are omitted for clarity. Optimized geometries found at the (U)TPSSh-D3(BJ)/def2-TZVPP (Ni), def2-TZVP, ma-def2-TZVP (Cl) CPCM(DMF) level of theory; electronic energies computed with both (U)B3LYP-D3(BJ) and (U)M06-D3(0) with def2-QZVPP (Ni), def2-TZVPP, ma-def2-TZVPP (Cl) CPCM(DMF). See supplementary materials for more details. *__94b__ was used instead of __94a__ under the given photochemical conditions.

recovered tosyl hydrazide). It is difficult to conceive of a more direct and simple way to achieve such a transformation.

The utility of these reactions will likely extend beyond a medicinal chemistry setting, because their simple and homogenous nature bodes well for large-scale applications. To exemplify this, gram-scale preparation of substrates **17** and **92** was performed by treating sulfonyl hydrazide **8** with aryl bromide **93** and RAE **91**, respectively, in good yields. The clear advantages of eliminating exogenous redox in radical cross-coupling reach beyond reaction simplicity (no need for e-chem, photochem setups, or expensive sensitizers), thus

facilitating scale-up. For instance, as illustrated in Fig. 4C, 1,4-trans–substituted cyclohexanes **96** and **100** can be easily accessed in "dump-and-stir" homogenous reactions using sulfonyl hydrazide donor **94a** with arenes **95** and **99**, respectively (reactions run one time with no optimization). In the former case, a flow photochemical scaleup is required for decarboxylative coupling, and in the latter case, the reaction did not proceed in DMF [unless the solvent was changed to dimethyl sulfoxide (DMSO; unscalable), where 34% yield was observed], necessitating a laborious workaround (*46*).

Although the Ni-catalyst loading reported in this disclosure is usually 20 mol%, no deliberate effort was made to optimize yields when using reduced catalyst loadings (see supplementary materials, catalyst loadings as low as 1 mol% are viable). In the case of gram-scale coupling of **8** and **93**, a 10 mol% loading was used (delivering **17** in 80% yield), further suggesting that lower loadings of Ni are possible.

The seven reaction classes disclosed in this report can each be individually studied to unearth their guiding mechanistic principles. As such, a definitive mechanism for redox-neutral radical cross-coupling using sulfonyl hydrazides is beyond the scope of this work. Nevertheless, we provide a general mechanistic picture for the critical Ni-catalyzed, radical-forming step that initializes the reactions, then apply it to $C(sp^2)$-$C(sp^3)$ bond formation as a model example (Fig. 4D, left). As is well-precedented in the literature (*47*–*49*), a mild base undoubtedly liberates a diazene species **103** from the starting hydrazide **102** (which can be generated in situ from hydrazone **101** by $PhSiMe_2H$ reduction). Subsequently, carbon radical generation from **102** mediated by Ni is proposed. This hypothesis is supported by density functional theory (DFT) analysis conducted in ORCA 6 (*50*) (full details in the supplementary materials), revealing a pathway wherein the diazene associates to the high-spin Ni(II) complex **104** in a *Z* configuration. Abstraction of the proton by the base is nearly thermoneutral, affording intermediate **105**. Löwdin orbital population, and spin density analysis on **105** reveals radical character on both the Ni-bound nitrogen atom and N-bound carbon atom, priming the complex for thermally assisted homolysis by N_2 extrusion (*51*) (Fig. 4D, left, and fig. S15). Indeed, DFT analysis finds that liberation of dinitrogen and formation of the reduced Ni(I) species **106** and alkyl radical **107** requires only a modest barrier ($\Delta G^{\ddagger}$ ~5 kcal mol^{-1}) and is thermodynamically downhill by ~25 kcal mol^{-1} (table S12 and fig. S16). Subsequent formation of the square-planar Ni(II) complex **108** is well-established in the literature by formal oxidative addition of low-valent Ni(I) into (Het)Ar-X bonds (from **106** to **110**) and comproportionation (*25*, *52*). Radical capture by **108** has been shown to deliver high-valent Ni complexes such as **109** (*53*). Reductive elimination from **109** delivers the $C(sp^2)$-$C(sp^3)$–coupled product and returns low-valent species **106**, which in turn restarts the cycle.

Various experiments in support of radical intermediacy are presented (Fig. 4D, right). In accordance with findings in the literature, TEMPO (2,2,6,6-tetramethylpiperidin-1-oxyl) trapped the radical generated from a hydrazide even in the absence of a Ni-catalyst (**8** to **111**), demonstrating a radical background pathway. A productive radical pathway can be seen with cyclopropane opening/coupling of **112** with **93** to deliver linear adduct **113**, and with 5-exo-trig cyclization/coupling of **114** with **93** to afford cyclopentyl substrate **115** (*54*). In the latter case, the 5-exo-trig cyclization was only partially complete before coupling resulting in a mixture of cyclized product **115** and its linear counterpart (not shown) in a 1:1.4 ratio, respectively. The Giese reaction depicted in Fig. 2A to access **3** from **8** was facilitated with added Ni but in the absence of catalyst, it was also observed in lower yield (46 versus 23%, respectively).

Conclusions

Radical cross-coupling chemistry has had a profound impact on the practice of organic synthesis and has enabled simplification of radical retrosynthetic disconnections that did not exist a decade ago. Despite great strides in this field, the use of exogenous catalysts, stoichiometric reductants/oxidants, and photo/electrochemical setups diminishes its practical utility compared with conventional, redox-neutral C–C bond–forming cross-couplings such as the Suzuki reaction. The fundamental advance of this disclosure is the discovery that sulfonyl hydrazides can serve not only as versatile radical progenitors, but also act as their own electron donors, driven by the loss of N_2, to facilitate a metal-mediated catalytic cycle thereby obviating the need for external redox stimuli. From a practical perspective, sulfonyl hydrazides are generally stable, crystalline substances that do not need to be purified by chromatography and can often be used in crude form. Notably, these groups are not very polar and are well-behaved on silica gel (round spots on thin-layer chromatography; see supplementary materials for pictures). Catalysis is demonstrated with Ni, but the same principle should be applicable to many other organometallic systems. In fact, preliminary experiments suggest that other metals such as Cu, Co, Pd, and Fe, can provide varying levels of product in $C(sp^3)$-$C(sp^2)$ coupling (see supplementary materials). Because easily prepared sulfonyl hydrazides divorce redox chemistry from radical cross-couplings, reaction setup is greatly simplified (arguably as simple as a classic Suzuki coupling). It is likely that these C–C bond forming reactions will find application in nearly all branches of chemical synthesis.

REFERENCES AND NOTES

1. J. M. Smith, S. J. Harwood, P. S. Baran, *Acc. Chem. Res.* **51**, 1807–1817 (2018).
2. M. Yan, J. C. Lo, J. T. Edwards, P. S. Baran, *J. Am. Chem. Soc.* **138**, 12692–12714 (2016).
3. M. D. Palkowitz, M. A. Emmanuel, M. S. Oderinde, *Acc. Chem. Res.* **56**, 2851–2865 (2023).
4. G. Laudadio, M. D. Palkowitz, T. El-Hayek Ewing, P. S. Baran, *ACS Med. Chem. Lett.* **13**, 1413–1420 (2022).
5. Y. Gong, J. Hu, C. Qiu, H. Gong, *Acc. Chem. Res.* **57**, 1149–1162 (2024).
6. L.-M. Chen, S. E. Reisman, *Acc. Chem. Res.* **57**, 751–762 (2024).
7. S. B. Beil, T. Q. Chen, N. E. Intermaggio, D. W. C. MacMillan, *Acc. Chem. Res.* **55**, 3481–3494 (2022).
8. A. Y. Chan *et al.*, *Chem. Rev.* **122**, 1485–1542 (2022).
9. S. L. Rössler *et al.*, *Angew. Chem. Int. Ed.* **59**, 9264–9280 (2020).
10. A. Cook, S. G. Newman, *Chem. Rev.* **124**, 6078–6144 (2024).
11. J. Choi, G. C. Fu, *Science* **356**, eaaf7230 (2017).
12. D. J. Weix, *Acc. Chem. Res.* **48**, 1767–1775 (2015).
13. S. Payamifar, L. Behrouzi, A. P. Marjani, *Arab. J. Chem.* **17**, 105822 (2024).
14. E. M. Kosower, T. Tsuji, *J. Am. Chem. Soc.* **93**, 1992–1999 (1971).
15. T. Tsuji, E. M. Kosower, *J. Am. Chem. Soc.* **92**, 1429–1430 (1970).
16. A. A. Balandin, D. N. Vaskevich, *Zh. Obshch. Khim.* **6**, 1878–1891 (1936).
17. D. E. Lewis, *The Wolff-Kishner Reduction and Related Reactions: Discovery and Development* (Elsevier, 2019).
18. D. J. Cram, J. S. Bradshaw, *J. Am. Chem. Soc.* **85**, 1108–1118 (1963).
19. A. G. Myers, B. Zheng, *Tetrahedron Lett.* **37**, 4841–4844 (1996).
20. M. L. Shrestha, W. Qi, M. C. McIntosh, *J. Org. Chem.* **82**, 8359–8370 (2017).
21. S. Wang, B. König, *Angew. Chem. Int. Ed.* **60**, 21624–21634 (2021).
22. D. F. Taber, Y. Wang, S. J. Stachel, *Tetrahedron Lett.* **34**, 6209–6210 (1993).
23. T. Qin *et al.*, *Science* **352**, 801–805 (2016).
24. Z. Huang, M. E. Akana, K. M. Sanders, D. J. Weix, *Science* **385**, 1331–1337 (2024).
25. S. Al Zubaydi *et al.*, *Nature* **634**, 585–591 (2024).
26. X. C. Gan *et al.*, *Science* **384**, 113–118 (2024).
27. F. Juliá, T. Constantin, D. Leonori, *Chem. Rev.* **122**, 2292–2352 (2022).
28. J.-J. Chen, H.-M. Huang, *Tetrahedron Lett.* **102**, 153945 (2022).
29. Z. Zuo *et al.*, *Science* **345**, 437–440 (2014).
30. J. C. Tellis, D. N. Primer, G. A. Molander, *Science* **345**, 433–436 (2014).
31. T. B. Hamby, M. J. LaLama, C. S. Sevov, *Science* **376**, 410–416 (2022).
32. J. Twilton *et al.*, *Nature* **623**, 71–76 (2023).
33. X. Wang, S. Wang, W. Xue, H. Gong, *J. Am. Chem. Soc.* **137**, 11562–11565 (2015).
34. X. Wang *et al.*, *J. Am. Chem. Soc.* **140**, 14490–14497 (2018).
35. J. T. Edwards *et al.*, *Nature* **545**, 213–218 (2017).
36. J. M. Smith *et al.*, *Angew. Chem. Int. Ed.* **56**, 11906–11910 (2017).
37. J. Cornella *et al.*, *J. Am. Chem. Soc.* **138**, 2174–2177 (2016).
38. N. Nebra, V. V. Grushin, *J. Am. Chem. Soc.* **136**, 16998–17001 (2014).
39. H. Shen *et al.*, *J. Am. Chem. Soc.* **139**, 9843–9846 (2017).
40. Z.-Y. Liu, S. P. Cook, *Org. Lett.* **23**, 808–813 (2021).
41. J. Barluenga, M. Tomás-Gamasa, F. Aznar, C. Valdés, *Nat. Chem.* **1**, 494–499 (2009).
42. D. M. Allwood, D. C. Blakemore, A. D. Brown, S. V. Ley, *J. Org. Chem.* **79**, 328–338 (2014).
43. R. R. Merchant, J. A. Lopez, *Org. Lett.* **22**, 2271–2275 (2020).
44. J. Liao *et al.*, *Org. Lett.* **21**, 2941–2946 (2019).
45. S. Kim, M. J. Goldfogel, M. M. Gilbert, D. J. Weix, *J. Am. Chem. Soc.* **142**, 9902–9907 (2020).

46. R. Nallagonda *et al*., *ACS Catal.* **14**, 13439–13450 (2024).
47. A. G. Myers, M. Movassaghi, B. Zheng, *Tetrahedron Lett.* **38**, 6569–6572 (1997).
48. A. G. Myers, M. Movassaghi, *J. Am. Chem. Soc.* **120**, 8891–8892 (1998).
49. A. G. Myers, M. Movassaghi, B. Zheng, *J. Am. Chem. Soc.* **119**, 8572–8573 (1997).
50. F. Neese, *Wiley Interdiscip. Rev. Comput. Mol. Sci.* **12**, e1606 (2022).
51. Q. Liu *et al*., *J. Am. Chem. Soc.* **146**, 13629–13640 (2024).
52. D. A. Cagan, D. Bím, N. P. Kazmierczak, R. G. Hadt, *ACS Catal.* **14**, 9055–9076 (2024).
53. Q. Lin, E. H. Spielvogel, T. Diao, *Chem* **9**, 1295–1308 (2023).

ACKNOWLEDGMENTS

We thank L. Pasternack and G. J. Kroon for assistance with NMR spectroscopy. We are grateful for assistance with HRMS from E. Billings, B. Webb, C. Hoang (The Scripps Center for Metabolomics and Mass Spectrometry); A. Paiva (Discovery and Development Sciences, Bristol Myers Squibb); A. Pollatos; and B. Orzolek, B. Sanchez, Q. N. Wong, J. Lee (Scripps Automated Synthesis Facility). We thank M. Costantini, L. Massaro, F. Schneider, and A. Pollatos for helpful discussions. We thank A. Pollatos and G. Barnes for proofreading. The computations presented here were conducted in the Garibaldi High Performance Computing (HPC) cluster, a facility supported by Scripps Research, La Jolla. **Funding:** This project is financially supported by NIH (GM-118176). Á.P. acknowledges the European Union's Horizon Europe research and innovation program for a Marie Skłodowska-Curie postdoctoral fellowship (MSCA-GF grant 101110288). H.Z. acknowledges Nankai University for its financial support. **Author contributions:** Á.P. developed the in situ protocol described in Fig. 3 using hydrazones, initiated the project, and carried out underlying reactivity studies. J.S. developed coupling of sulfonyl hydrazides with aryl halides, redox active esters, alkyl halides, Giese addition, and carried out related reactivity studies. J.H. developed the Cu-mediated trifluoromethylation of sulfonyl hydrazides. J.T. developed the coupling of sulfonyl hydrazides with alkenyl and alkynyl halides. H.Z. assisted with all aspects of the work. D.A.C. assisted in the mechanistic analysis and performed the computational investigations. B.P.V., D.S.P., M.D.M., and M.D.P. contributed to field testing reactions in a medicinal chemistry setting and adding numerous substrates to the scope. Y.K. assisted in experimental design. All authors contributed to writing the paper. P.S.B. helped to conceptualize the project, write the paper, and secure funding. **Competing interests:** P.S.B. is a paid consultant at Bristol Myers Squibb. All other authors declare no competing financial interests. **Data and materials availability:** Supplementary Materials include extended reaction scope, experimental procedures including graphical guides, optimization studies, a user guide, spectroscopic data (^{1}H NMR spectra; ^{13}C NMR spectra, ^{19}F NMR spectra, HRMS), and DSC data. The x-ray crystallographic coordinates for compound **67** and **70** have been deposited at the Cambridge Crystallographic Data Centre (CCDC) with accession codes 2411748 (compound **67**) and 2411749 (compound **70**). Copies of the data can be obtained free of charge via https://www.ccdc.cam.ac.uk/structures/.

SUPPLEMENTARY MATERIALS

science.org/doi/10.1126/science.adu6406
Materials and Methods
Figs. S1 to S17
Tables S1 to S12
References (*54*–*86*)
NMR Spectra

Submitted 15 November 2024; accepted 19 February 2025
Published online 6 March 2025
10.1126/science.adu6406

HAPTICS

Full freedom-of-motion actuators as advanced haptic interfaces

Kyoung-Ho Ha[1]†, Jaeyoung Yoo[1,2]†, Shupeng Li[3]†, Yuxuan Mao[3,4], Shengwei Xu[3], Hongyuan Qi[3], Hanbing Wu[3], Chengye Fan[3], Hanyin Yuan[3], Jin-Tae Kim[1,5], Matthew T. Flavin[1,6], Seonggwang Yoo[1,7], Pratyush Shahir[8], Sangjun Kim[9], Hak-Young Ahn[1], Edward Colgate[3], Yonggang Huang[3,10,11]*, John A. Rogers[1,3,8,11,12]*

The sense of touch conveys critical environmental information, facilitating object recognition, manipulation, and social interaction, and can be engineered through haptic actuators that stimulate cutaneous receptors. An unfulfilled challenge lies in haptic interface technologies that can engage all the various mechanoreceptors in a programmable, spatiotemporal fashion across large areas of the body. Here, we introduce a small-scale actuator technology that can impart omnidirectional, superimposable, dynamic forces to the surface of skin, as the basis for stimulating individual classes of mechanoreceptors or selected combinations of them. High-bit haptic information transfer and realistic virtual tactile sensations are possible, as illustrated through human subject perception studies in extended reality applications that include advanced hand navigation, realistic texture reproduction, and sensory substitution for music perception.

The sense of touch conveys essential information about the physical environment, with critical roles in identifying and manipulating objects and in strengthening social interactions. Sensations arise from mechanical stimulation of cutaneous receptors that consist of specialized dendritic endings of afferent nerve fibers. These mechanoreceptors exist in complex distributions deep into the skin and across all regions of the body (*1*). Recent research focuses on the development of engineered systems that are capable of creating tactile sensations through these mechanisms in a fast, programmable manner with devices in thin, flexible formats that can interface with small or large areas of the skin, not limited to the fingertips (*2*–*5*). When combined with well-developed systems for visual and auditory inputs, such technologies can qualitatively enhance immersive experiences in extended reality (XR) environments, for applications that span entertainment, social media, medicine, and physical rehabilitation (*6*, *7*). The integration of sensors with these actuators offers the potential to provide closed-loop feedback for teleoperations (*8*, *9*) and remote health care (*10*). Specific opportunities include applications for amputees and those with visual or hearing impairments, where engagement with the somatosensory system can substitute and augment diminished natural capabilities for sensing (*11*, *12*).

The effectiveness of these systems depends on accurately reproducing the complex spatiotemporal patterns of activation of mechanoreceptors during the broad range of mechanical deformations that result from the natural processes of touch. Each of the four classes of mechanoreceptors that innervate various regions of the skin (*13*) responds to forces with specific combinations of directionality, magnitude, and frequency (Fig. 1A) (*14*–*16*). These receptors trigger action potentials with different timing responses to mechanical stimuli based on their rates of adaptation. The resulting pulses pass through sensory neurons to the brain to create distinct perceptions (*17*, *18*). Some schemes aim to generate programmable multidirectional forces on the skin by strategically arranging multiple types of actuators, including those based on electromagnetic motors (*19*–*21*), pneumatic systems (*22*, *23*), shape-memory alloys (*24*, *25*), and electrostatic assemblies (*26*). These approaches, however, have characteristics that are not ideally suited for immersive XR experiences owing to some combination of disadvantages in their relatively large sizes and masses, limited options in attachment locations, difficulty in distributing into programmable arrays, challenges in balancing requirements in forces and displacement distances, inability to achieve superimposable modes of actuation, and constraints in operating speeds and frequencies (table S1).

[1]Querrey-Simpson Institute for Bioelectronics, Northwestern University, Evanston, IL, USA. [2]Department of Semiconductor Convergence Engineering, Sungkyunkwan University, Suwon, Republic of Korea. [3]Department of Mechanical Engineering, Northwestern University, Evanston, IL, USA. [4]Institute of Biomedical Manufacturing and Life Quality Engineering, School of Mechanical Engineering, Shanghai Jiao Tong University, Shanghai, China. [5]Department of Mechanical Engineering, Pohang University of Science and Technology, Pohang, Republic of Korea. [6]School of Electrical Engineering and Computer Engineering, Georgia Institute of Technology, Atlanta, GA, USA. [7]College of Biomedical Science and Health, Inje University, Gimhae, Republic of Korea. [8]Biomedical Engineering, Northwestern University, Evanston, IL, USA. [9]Department of Mechanical Engineering, University of Texas at Austin, Austin, TX, USA. [10]Department of Civil and Environmental Engineering, Northwestern University, Evanston, IL, USA. [11]Department of Materials Science and Engineering, Northwestern University, Evanston, IL, USA. [12]Department of Neurological Surgery, Feinberg School of Medicine, Northwestern University, Chicago, IL, USA.
***Corresponding author. Email: y-huang@northwestern.edu (Y.H.); jrogers@northwestern.edu (J.A.R.)**
†These authors contributed equally to this work.

Fig. 1. Multisensory haptic interfaces with a full FOM actuator. (**A**) Various modes of mechanical stimuli and corresponding strain fields simulated for human skin. Diagram on the right shows the four main mechanoreceptors in the skin and their responses to distinct mechanical stimuli. (**B**) Disassembled view of the FOM actuator, with an IMU to enhance control methodologies. The inset shows an assembly of three coils into the nested tri-coil assembly. (**C**) Operating principles of the FOM actuator, illustrating the magnetic fields produced by current passing through the coils and the corresponding electromagnetic forces on the magnetic end effector. Simulated distributions of strain and their time-dependent propagation on and in the skin. (**D**) Photograph of the FOM actuators mounted on the fingertips, with a wireless control unit and battery in a wrist band. (**E**) Photograph of an FOM actuator mounted on the dorsal hand. (**F**) Photograph of a skin-integrated FOM actuator on a fingertip facilitated by a conformable thermoforming interface and a transparent strap. (**G**) State diagram that illustrates the use of wireless, battery-powered FOM actuator with integrated IMU in an XR environment.

Freedom-of-motion actuators

Here, we introduce a wireless, real-time haptic interface with full freedom of motion in generating programmable deformations at the surface of the skin. This engineering capability can reproduce the span of displacements and forces, both in magnitude and direction, necessary to engage all receptors in the skin in a targeted manner. Each actuator uses a collection of individually addressable wire coils to generate magnetic fields with user-defined directions and magnitudes. Lorentz forces produced by interaction with one or more fixed magnets that interface to the skin serve as the basis for operation. Figure 1A illustrates normal, shear, torsional, and vibrational stimuli that can be produced using this approach, through corresponding calculations of distributions of strain across the surface of the skin and into its depth. Normal forces stimulate three types of mechanoreceptors under specific conditions: Merkel cells respond to static forces with a small threshold, while Meissner and Pacinian corpuscles respond to low- and high-frequency vibrations, respectively. Stretching of the skin induced by shear or torsional motions activates Ruffini endings (*14*). The superposition of forces generated with a single actuator unit, which we refer to as a freedom-of-motion (FOM) actuator, can address a physiologically relevant range of magnitudes and time dynamics to engage each of these mechanoreceptors individually or in combination.

Figure 1B shows some details of the simplest form of actuator that uses these design principles, together with a sensor that enables advanced mechanisms for control. Two rectangular solenoid coils of different dimensions enable one (shear-x) to be inserted orthogonally into

the other (shear-y). Yet another coil, a short round solenoid (normal-z), inserts into the shear-x coil, resulting in a nested tri-coil assembly. A solid lubricating film serves as a low-friction interface that laminates beneath these coils, secured by a structure with supporting legs that can be customized in shape and materials on the basis of requirements for interfacing the FOM actuator with various regions of the skin. The end effector consists of a rectangular neodymium magnet positioned beneath the coils with a small air gap in between, coupled to the epidermis using a thin, compliant adhesive. An arm structure extends from the magnet in four orthogonal horizontal directions to ensure pure shear motions upon application of suitable currents through the shear-x and shear-y coils, by inhibiting out-of-plane torsional rotations (fig. S1). An inertial measurement unit (IMU) placed above the coils senses the egocentric coordinates and motion of the specific body part, as a reference for application of directional adaptive haptic stimuli.

Figure 1C illustrates the magnetic fields generated by passing current through the different coils, the resulting movements of the magnet, and the corresponding distributions of strains and propagation of them in the skin, for representative modes of mechanical stimulus. The normal-z coil can induce forces in the out-of-plane direction (relative to the surface of the skin), whereas the shear-x and shear-y coils can generate tangential forces in the two in-plane directions. Simultaneously operating these coils yields a sum of the individual orthogonal force vectors, thereby enabling omnidirectional forms of programmable actuation. Referring to the skin deformations in Fig. 1, A and C, normal force induces compressive strain deep within the skin rather than spreading laterally. Conversely, shear forces cause shallow, widespread deformations, with compressive strain in the forward direction and tensile strain in the rear. Vibrational stimuli, achieved by applying alternating current to

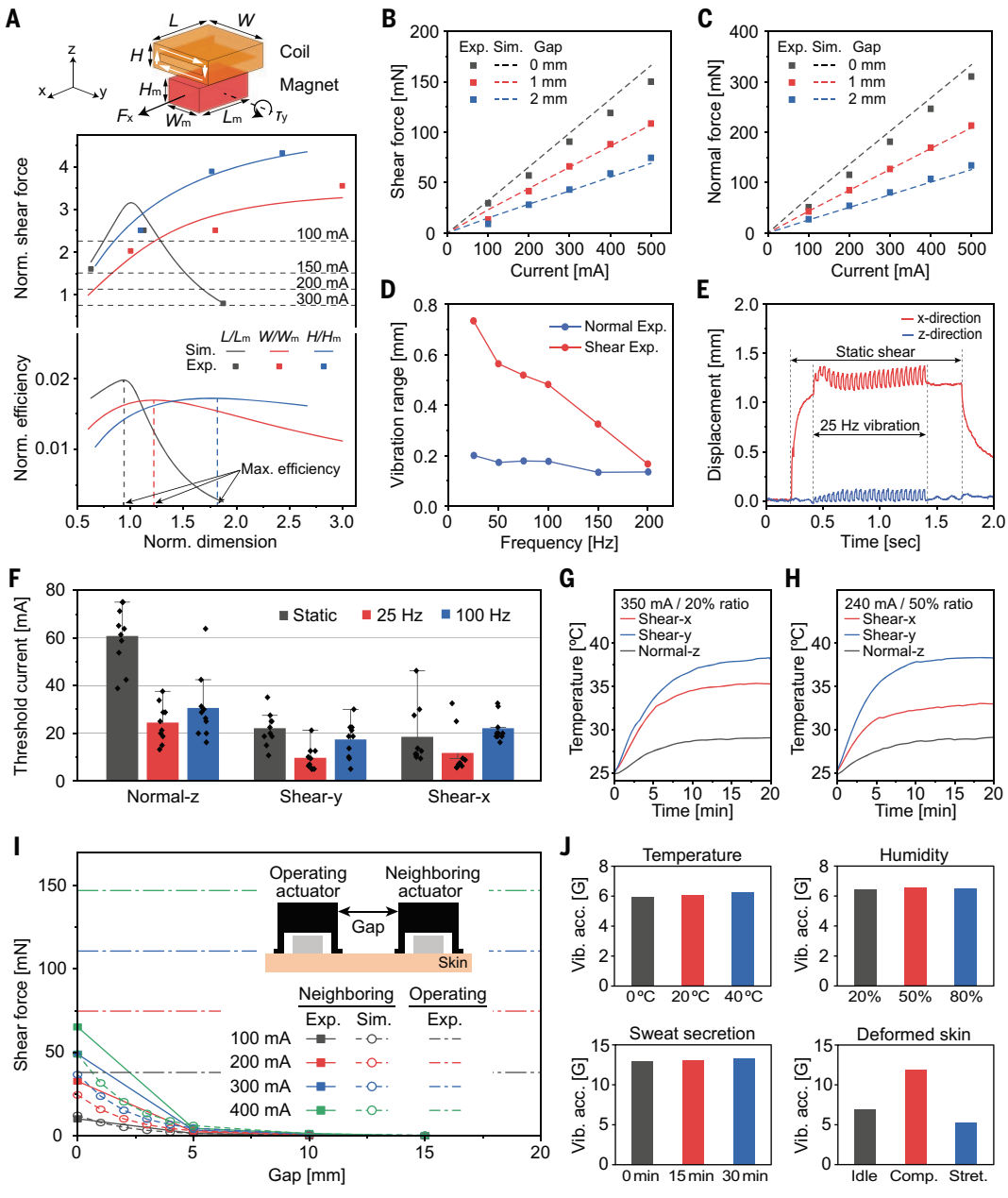

Fig. 2. Design strategies and characteristics of multimodal actuators by experiment and simulation. (**A**) Dimensional parametric analysis of the shear coil on force and efficiency. Parallel dashed lines indicate the threshold shear force, which are perceivable forces on human skin (2 kPa) at various operating currents. (**B**) Shear force as a function of the current and the gap between the shear coil and magnet. (**C**) Normal force as a function of the current and the gap between the normal coil and magnet. (**D**) Dynamic range of normal and shear vibrations depending on the frequency. (**E**) Simultaneous actuation of shear and normal coils to generate static shear force and 25 Hz of vibration. (**F**) Amplitude thresholds of human perception for the nested tri-coil FOM actuators across multiple modes (normal-z, shear-y, shear-x) and frequencies (static, 25 Hz, 100 Hz). (**G**) Temperature of the FOM actuator with a 20% duty cycle at 350 mA on each coil. (**H**) Temperature of the FOM actuator with a 50% duty cycle at 240 mA on each coil. (**I**) Interfering shear forces in neighboring actuators at various gap sizes compared with the shear forces on the operating actuator. The inset illustration depicts the definition of the gap. (**J**) Effects of environmental conditions on the performance of the FOM actuator (vibrational acceleration of the FOM actuator magnet, operated at 100 Hz and 100 mA): temperature, humidity, sweat secretion, and skin deformation (15% compression and 15% stretch).

the coils, produce waves of propagation into the depth and along the surface of the skin, with both longitudinal and shear content and varying waveforms depending on the direction of the vibrations.

The FOM actuator and sensor assembly, each equipped with a suitable mounting framework, can be positioned on nearly any body part, with wireless connectivity through a compact Bluetooth low-energy (BLE) electronic system and a small rechargeable battery (Fig. 1, D and E, and figs. S2 and S3). The result allows coordinated wireless operation in an array format or individually through a graphical user interface on a BLE-enabled external device. The photograph in Fig. 1F provides a magnified side view that shows a thermoformed soft structure and a strap to facilitate contact to curved surfaces of the skin, as a robust but comfortable interface. Skin-integrated single or multiple FOM actuators with sensors can provide realistic sensations or haptic information for various XR applications, referenced to real-time motions of the human body, in wireless coordination with portable XR devices, such as smart glasses, virtual reality headsets, and smartphones (Fig. 1G).

Design principles and characterization

Optimal designs to allow miniaturization of these concepts in power-efficient actuators require careful consideration of the direction and magnitude of forces and the displacements necessary for reliable human perception. Figure 2A and fig. S4 present an experimentally validated parametric analytical model that calculates a nondimensional (normalized) force and power efficiency metric, incorporating variables such as applied current, type of magnet, coil filling factor, and wire diameters. The analytical model evaluates the impact of each coil dimension individually with other parameters held constant (table S2).

The force generated by the normal-z coil, used exclusively in standard electromagnetic actuators (*4*, *27*–*29*), increases with its outer diameter and thickness of the coil and decreases with its inner diameter (fig. S4). The power efficiency, however, depends on the coil dimensions relative to those of the magnet, with a maximum when the outer radius is 1.4 times the effective radius of the magnet (R/R_m = 1.4), while monotonically decreasing with coil height. In the given coil dimensions and filling factor, force decreases, while efficiency linearly increases with the square of the wire diameter (see supplementary text in the supplementary materials).

Directional shear and torsional forces result from the shear-x and shear-y coils and their coordinated operation. As with the normal-z coil, the performance of these shear coils depends on their dimensions relative to those of the magnet (Fig. 2A). The shear force reaches its peak value when the coil length equals the magnet length (L/L_m = 1) and monotonically increases with both the width and height of the coil. The horizontal dashed lines in Fig. 2A denote design requirements for generation of perceivable stress (*30*) at operating currents ranging from 100 to 300 mA. The coil efficiency has an optimum value when the ratios of length (L/L_m), width (W/W_m), and height (H/H_m) are 0.93, 1.24, and 1.8, respectively. Additionally, similar lengths for the coil and magnet (L/L_m = 0.96) prevent unintentional torsional forces on the magnet during shear operations (fig. S5). For a wire diameter of 114 μm, and an N55 neodymium magnet, with $L/L_m \sim 1$ and with values of W and H that facilitate construction of the nested tri-coil assembly, optimal choices for the dimensions of the inner and outer shear coils are L/L_m = 1.13, W/W_m = 1.8, and H/H_m = 1.09 and L/L_m = 1.14, W/W_m = 2.22, and H/H_m = 1.96, respectively. The dimensions of the normal-z coil, with 79-μm-diameter wire, maximize its size within the available space constraints of the nested tri-coil assembly, specifically D_{out} = 7 mm, D_{in} = 3 mm, and H = 0.9 mm (fig. S6). The complete dimensions of an FOM actuator with these designs are 11.7 mm by 10.8 mm by 8.4 mm, and its weight are 3.19 g, including an 8 mm by 5 mm by 3 mm magnet and a packaging structure. Per simulation estimates, the size of the FOM actuator can be reduced to 5 mm by 5 mm by 3.5 mm while still generating human-perceivable normal and shear stress (2 kPa), under the given conditions of commercially available wire (0.079 μm diameter), a neodymium magnet, and operational currents up to 500 mA.

The operating parameters and the assembly structure, of course, also influence the dynamics of the system. Specifically, shear and normal forces linearly increase with the currents in the coils and nonlinearly decrease with the gap between coil and magnet (Fig. 2, B and C). Compared with the vertical distance (gap), the horizontal center-to-center distance causes a smaller reduction in forces (fig. S7). The chosen gap between the outermost coil and the magnet is 0.2 mm, as a balance to generate strong forces while avoiding unwanted contact between the coil and the magnet.

Time-varying currents create dynamic responses. For the case of vibrations, the amplitudes decrease with increasing frequency for motions in both normal and shear directions owing to a high damping ratio of the system, as shown in Fig. 2D and fig. S8. Amplitudes in the shear direction are typically larger than those in the normal direction, as the gap between the coil and magnet remains constant and coil does not interrupt the motion of the magnet in the shear case (movie S1). The FOM actuator can reproduce mixed forces, commonly encountered in practical, realistic scenarios, by simultaneously engaging multiple coils. For instance, concurrent operation of the shear and normal coils generates a mixed shear and 25-Hz vibrational motion of the end effector (Fig. 2E and movie S2). The simultaneous operation of static shear and vibrations is essential to reproduce sensation of texture, as described subsequently (*31*). The control system, driven by a 32-kHz high-frequency clock, precisely regulates the ac voltage with a resolution of 100 μs (fig. S9), enabling the FOM actuator to achieve frequency resolution across all operational frequencies that exceeds the resolution of human perception (fig. S10).

Figure 2F presents the threshold currents required for human perception for various stimuli generated by FOM actuators on the dorsal hand. Tests of normal and shear stimuli, both static and dynamic (25 and 100 Hz), involve responses from 10 human subjects. Except for the static normal stimulus, the average threshold currents for all stimuli are <31 mA. Vibrations at 25 Hz are perceivable with a lower current than both static stimuli and 100-Hz vibrations. The corresponding threshold forces, ranging from 2.5 to 15 mN, are listed in table S3 and are comparable to the perceptual threshold forces reported in the literature (*26*, *32*). While the perception threshold sets the minimum operational current, the temperature for safe operation on the skin defines the upper limit. The temperature of the actuator depends on the magnitude of the applied current, the coil resistance, the operational duration, and the duty cycle, as shown in Fig. 2, G and H, and fig. S11.

In an array configuration, the electromagnetic fields from neighboring actuators may interact, depending on their magnitudes and spacing (Fig. 2I and fig. S12). Simulations and experiments indicate that for spacing of 5 mm or more, electromagnetic interference is negligible. Environmental conditions, such as temperature, humidity, sweat secretion, and external load, do not significantly influence the performance of the actuator (Fig. 2J and figs. S13 and S14). Skin deformation around the actuators can affect the vibrations of the magnet by altering the dynamic system, caused by changes in effective skin modulus under deformed skin conditions (Fig. 2J). Specifically, compressive deformations can increase the vibrational amplitude through mechanical instabilities that lead to buckling of the skin. In contrast, tensile deformations can reduce the vibrational amplitude owing to the tension on the skin (fig. S15).

An extension of these ideas involves two sets of planar and normal coils, with the capability to generate normal, shear, and torsional forces across an array of four separate magnets (fig. S16). This design is beneficial in scenarios where there is a need for inducing three stimuli (normal, shear, and torsion) at a single point.

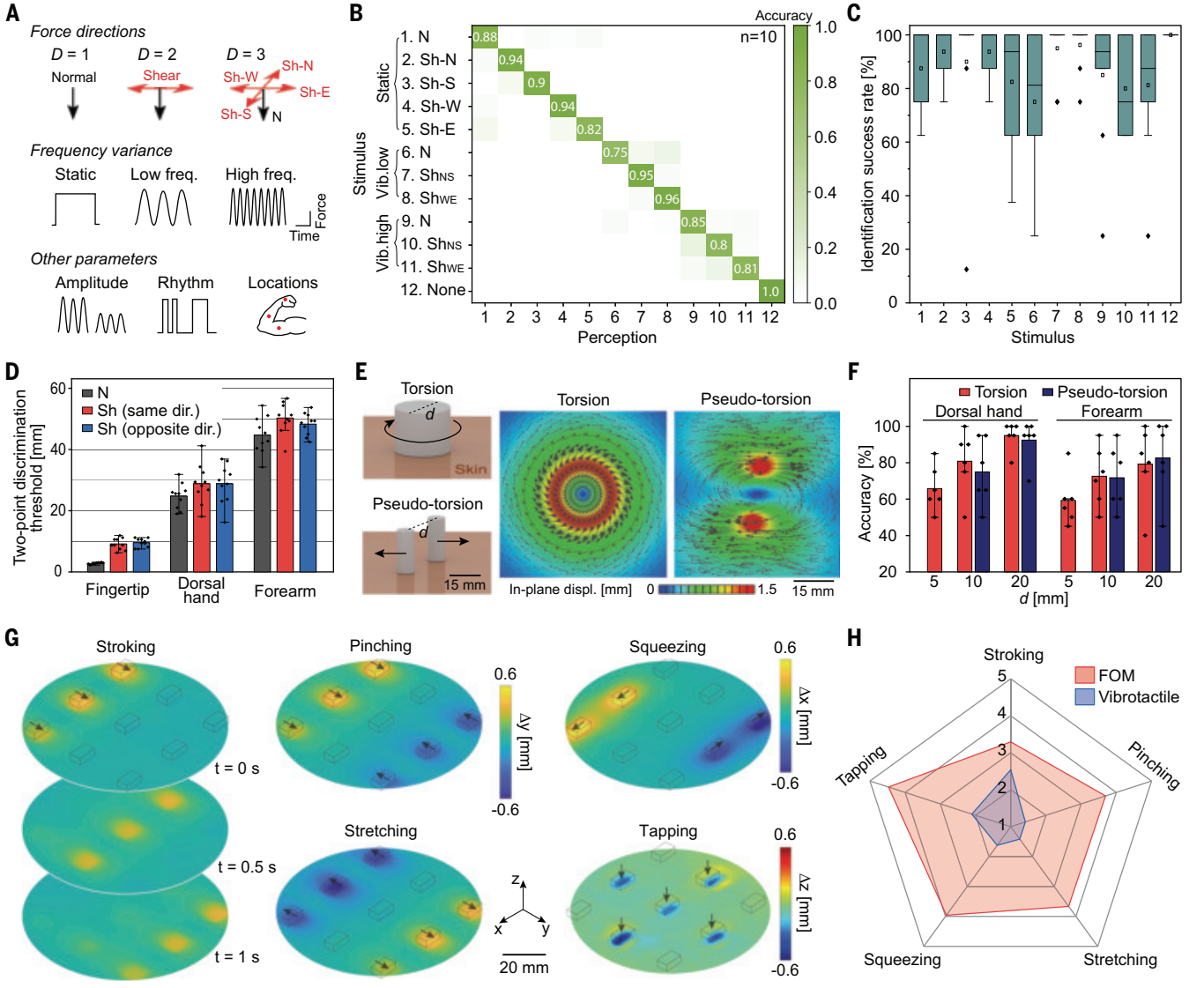

Fig. 3. Perception from FOM actuators. (**A**) Physical parameters of mechanical stimuli that support enhanced perceptual dimensions. (**B**) Accuracy in discriminating 12 mechanical stimuli applied by a single FOM transducer on a fingertip. (**C**) Variance in the success rate for identifying each stimulus. (**D**) Two-point discrimination threshold for normal, shear, and opposite shear forces on a fingertip, the dorsal hand, and the forearm. (**E**) Illustration of the application of torsion and pseudo-torsion on skin with corresponding simulations of the resulting deformations. (**F**) Success rate for directional perceptions of torsion and pseudo-torsion for different contact diameters [*d* specified in (E)] on the dorsal hand and forearm. (**G**) Representations of displacements evaluated by digital image correlation with a skin phantom and a 3-by-3 FOM actuator array programmed to encode various mechanical interactions: stroking, pinching, stretching, squeezing, and tapping. (**H**) Human perception for the appropriateness of the five different stimuli generated by FOM and vibrations: 5, appropriate; 4, nearly appropriate; 3, reminds of appropriateness; 2, confused appropriateness; and 1, unrelated. The plotted values represent an average of eight results.

Human perception—haptic information transfer and encoding daily interactions

The capabilities of the FOM actuator platform allow not only for the replication of everyday tactile experiences but also for the transfer of information through programmed activation of mechanoreceptors in the skin. A goal is in identifying the specific nature of a sensory stimulus, which involves a comprehensive perceptual process that is much more complex and subtle than simply determining the presence or absence of a stimulus (*33*). The direction of mechanical stimuli is an intuitive physical parameter that can extend perceptual dimensionality and enhance information transfer (*19*), particularly when paired with other parameters related to the stimulation, such as frequency, intensity, rhythm, and location (single or multiple) (Fig. 3A). The studies reported here involve 12 distinct stimuli, combining direction and frequency, evaluated on the fingertip. The experiments include five static forces (normal and four orthogonal shear directions), vibrations along three axes at frequencies of 10 and 50 Hz, and a control condition with no stimulation. The results of tests with 10 human subjects indicate an ability to identify 96 applied stimuli with an average success rate of 88% (Fig. 3B). This corresponds to an information transfer (IT) value of 2.8 bits, achieved by a single actuator without relying on variations in intensity or spatiotemporal patterns (movement illusions) that are commonly used to enhance IT in haptic interfaces (*34*). The result, in comparison to other haptic interfaces, enables a high IT per actuator with a reduced dimensionality (fig. S17 and table S4). Reductions in the required numbers of actuators and the perceptual dimensions needed to achieve

a given task improve wearability and energy efficiency, and they also minimize perceptual complexity. The variation in success rate for each stimulus (Fig. 3C) indicates no correlation with specific parameters; rather, it suggests considerable individual differences in the ability to identify stimuli, with individual IT values ranging from 2.64 to 3.53, as shown in fig. S18. Certain outliers with low success rates reflect failures in memory or in associating the stimulus with its correct name. Details on perception of multidirectional forces for various displacements, body locations, and other parameters are provided in fig. S19.

Arrays of FOM actuators can also replicate realistic sensations. Actuation at multiple points with appropriate spacing and relative timings can induce unified perceptions influenced by the concentration and receptive fields of mechanoreceptors in specific areas of the human body (*35*). The results in Fig. 3D demonstrate that the two-point discrimination thresholds (2PDTs) of shear forces in the same direction are 9.1, 28.8, and 50.3 mm at the fingertip, backhand, and forearm, respectively. These values are slightly larger than those observed for normal forces in our experiments (6.4, 4, and 5.6 mm, respectively) and in previous studies (table S5). This difference may be attributed to the comparatively large areas of skin deformation (fig. S20)

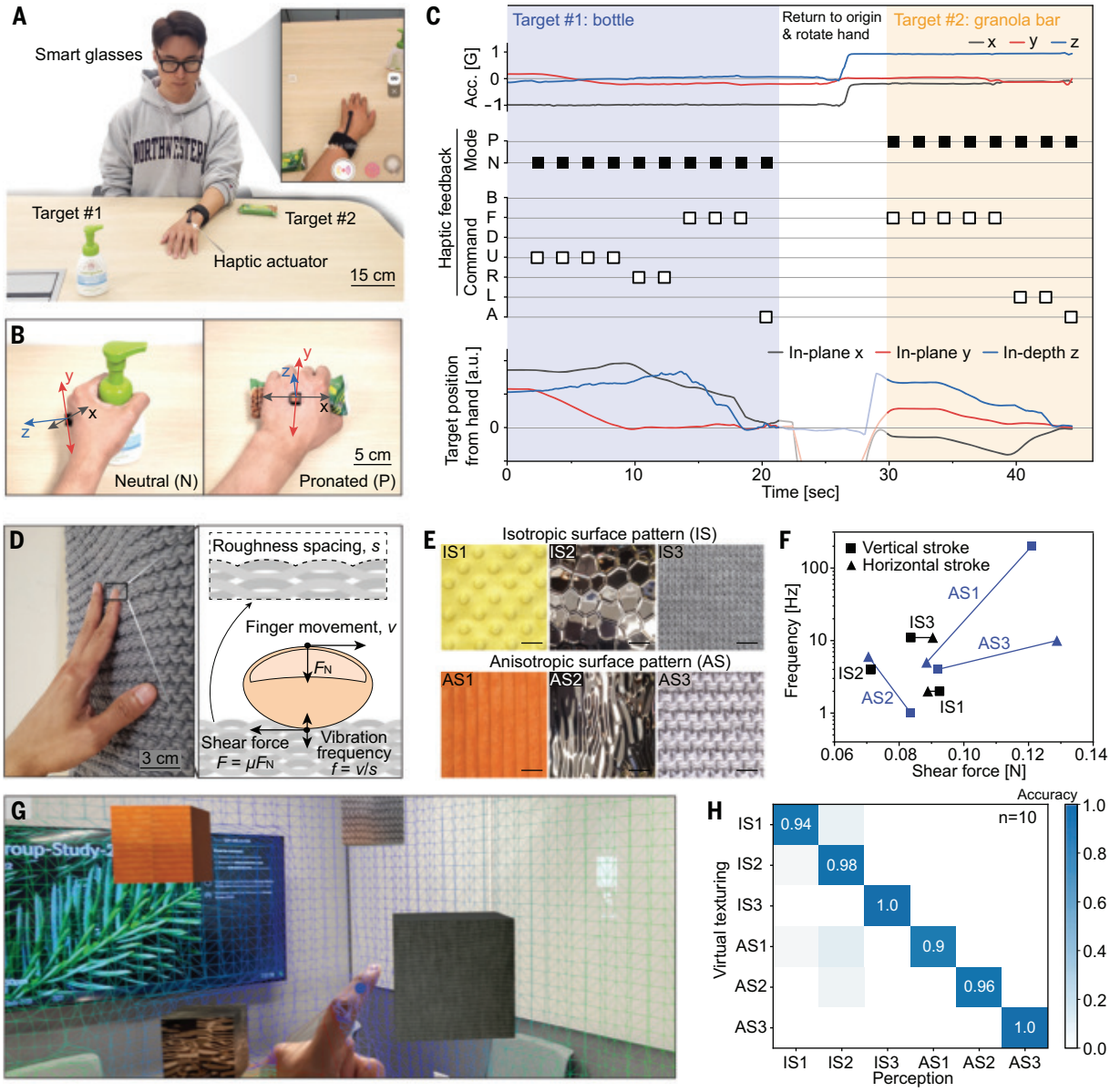

Fig. 4. Hand navigation system and reproduction of realistic textural sensations enabled by FOM actuators. (**A**) Photograph of a system for hand navigation based on a single FOM actuator. The inset photograph displays the corresponding view from the smart glasses. (**B**) Illustration of adaptation of the perceptual coordinate system depending on posture of the hand while grasping various items, enabled by outputs from the integrated IMU. (**C**) Data associated with haptic feedback during navigation to grasp two items: acceleration measured by the IMU, estimated hand posture on the basis of IMU data, haptic stimulus, and relative position of the target object from the hand based on data from a depth-sensing camera. P, pronated; N, neutral; B, back; F, forward; D, down; U, up; R, right; L, left; A, arrive. (**D**) Photograph of tactile engagement with a fabric, accompanied by a schematic illustration of the dynamics of the fingertip while stroking. (**E**) Examples of various textile and metal surfaces with isotropic and anisotropic features of surface relief and mechanical properties. Scale bars, 2 cm. (**F**) Vibration frequencies and static shear forces that create realistic virtual textural sensations, depending on the surfaces and stroke directions. (**G**) Photograph of an XR display as a user experiences the texture of virtual objects. (**H**) Confusion matrix that illustrates the ability to differentiate various surfaces on the basis of the haptic stimulus.

for the case of shear forces and the larger receptive fields of the corresponding mechanoreceptors (*13*, *36*). Opposing shear forces, which exhibit similar 2PDT values with the same directional shear, produce circular deformations of the skin that mediate a torsional perception, as an additional, distinct perceptual mode (Fig. 3E). Although pseudo-torsion generated by two opposite shears is mechanically different from true torsion, the perceptions of torsional direction relative to diameter are almost identical, as shown in Fig. 3F. This observation suggests that nested tri-coil FOM actuators in an array configuration can provide torsional perception.

Arrays of FOM actuators with spacing smaller than the 2PDT values can reproduce complex spatiotemporal stimuli, for everyday tactile experiences such as stroking, pinching, stretching, squeezing, and tapping (Fig. 3G and movie S3). Experimentally measured deformations of a skin phantom induced by operation of a 3-by-3 array of actuators demonstrate stimuli with distinct directions, areas, and timings for each sensation. The stimuli generated by FOM actuators produce more-realistic perceptions in humans than vibrotactile stimuli, which have been widely used in recent haptic applications (Fig. 3H and fig. S21). In a perception test where subjects rated the appropriateness of the stimuli reproduced by FOM and vibrations on a scale from 1 (unrelated) to 5 (appropriate), subjects found FOM stimuli to be more appropriate than vibrations for all types of stimuli.

Navigating hand positions with a single FOM actuator

Haptic interfaces can provide navigational or other inputs to individuals with visual impairments, of interest as a secondary sensory system without manual encumbrances or interferences with their primary hearing ability. Direct transfer of directional information with traditional haptic actuators requires arrays, which increases the overall size of the system. By contrast, the multimodal operation of the FOM actuator and its use with the integrated IMU described previously avoids this requirement, to provide effective information with real-time adaptation to changing body orientation. In a demonstration, a person wearing smart glasses reaches to grasp a bottle and a granola bar, guided by an FOM actuator placed on the dorsal hand (Fig. 4A and movie S4). A smartphone that shares the view with the smart glasses recognizes the positions of the hand and target objects and sends commands to the FOM actuator. When the visual data include in-depth information, such as from a depth-sensing camera or dual camera, the navigating system can provide more-detailed guidance (movie S5). The same command generates different haptic stimuli depending on the hand position, which serves as a perceptual reference coordinate. For example, the command to move the hand upward translates to positive x-directional haptic stimuli for a neutral hand posture, while it converts to positive z-directional stimuli for a pronated hand (Fig. 4B). The IMU in the actuator measures gravitational acceleration and determines the hand posture to issue the appropriate command. Figure 4C shows the measured acceleration, determined hand modes, haptic commands, and target positions during the demonstration. Movies S4 and S5 show that the individual successfully locates the bottle and granola bar using this form of haptic navigation.

Reproducing realistic virtual texture sensations using an array of FOM actuators

Realistic tactile sensations can represent essential aspects of an immersive experience in XR. Responses to surface textures result from complex patterns of deformation of the skin, where extension, compression, and vibration are key components (*31*). Limitations of traditional haptic actuators in this context follow from their inability to generate shear forces or torques or to mix these with normal forces in a fast, dynamic manner.

The FOM actuators can reproduce realistic texturing sensations on the fingertips when exploiting information from the IMU on the direction and speed of motion of the finger. Figure 4D and fig. S10 illustrate the connection between

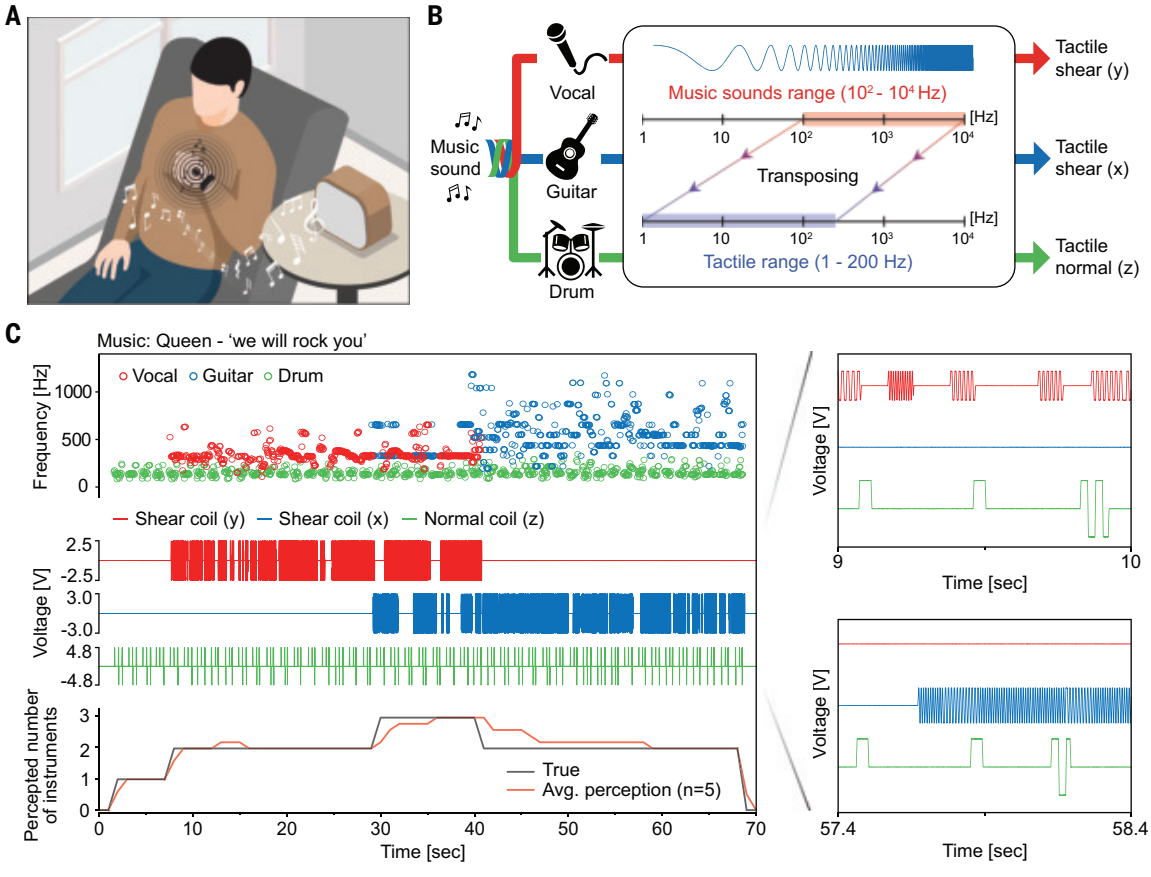

Fig. 5. Substitutional sensing: Tactile perception of music. (**A**) Illustration of a person perceiving music through tactile sensations. (**B**) Schematic diagram of the representation of music by means of distinct tactile stimuli corresponding to different musical instruments. (**C**) Auditory frequencies of various instruments and the corresponding voltages applied to each coil in the FOM device generate haptic sensations, allowing human subjects to recognize the number of instruments being played solely on the basis of haptic perceptions. Inset plots display the voltage signals over short time intervals.

the material properties, morphologies, and mechanical characteristics of the finger and the shear forces and vibrational frequencies that appear at the surface of the fingertip. Specifically, shear forces at the surface of the skin are proportional to the product of the friction coefficient between the skin and the target material and the normal force applied to the finger. Another key parameter for texture perception is vibration, with frequency determined by the spatial frequencies of roughness on the target surface and the finger and the speed of finger stroking. Demonstration experiments focus on reproduction of tactile sensations associated with six different objects, including those with both isotropic and anisotropic patterns of relief as shown in Fig. 4E and characterized in Fig. 4F and fig. S22.

These object-specific parameters allow programmable control of an FOM actuator to produce a virtual sensation in XR (Fig. 4G). On the basis of virtual vertical and horizontal stroking patterns, subjects can differentiate these six different surfaces with a 96% success rate (Fig. 4H).

Experiencing music through haptic interfaces

Haptic interfaces, as a substitutional sensory system, provide an opportunity for individuals with hearing impairments to experience music; additional interest lies in enhancing these experiences for those without impairments (Fig. 5A). Physical properties of sound waves, such as frequency and intensity, can be intuitively converted into tactile vibrational forces provided by the FOM actuator platform, through appropriate range control (*37*). A challenge in transposing sounds to haptic sensations is in reproducing distinct tone quality, which corresponds to timbre. Despite identical frequencies, sounds from different musical instruments have different timbre. The FOM actuator can produce various quality vibrations by using directional control, in a way that cannot be reproduced with conventional actuators. This capability enables a single FOM actuator unit to replicate music comprising different musical instruments.

Figure 5B illustrates the process flow for converting music into haptic vibrations. The first step isolates each instrument and vocal component using a machine learning–based algorithm, to allow physical parameters (frequency and intensity) of each sound to be analyzed. The analyzed audio frequencies, within the audible range of 10^2 to 10^4 Hz, are transposed into the perceivable vibrotactile frequency range of 1 to 200 Hz for use in haptic interfaces. In the third step, these frequencies and corresponding intensities convert into time-varying voltage applied to different coils, and thus vibrational directions, for different instruments.

An illustration of this scheme involves conversion of a sample piece of music consisting of voice, electric guitar, and drums into a haptic interface (movie S6). Figure 5C depicts the extracted frequencies of the vocal, guitar, and drums, along with the corresponding voltages applied to the coils. The right panels in Fig. 5C show the alternating voltages with varying frequencies at two time intervals on three coils. Perception tests confirm the ability to feel distinct tones of vibrations and to recognize a mixed collection of instruments by haptic interfaces conveyed through a single actuator.

Conclusions

The miniaturized, skin-integrated haptic actuator platforms introduced here are distinguished by their ability to deliver omnidirectional, superimposable, static and dynamic forces to the surface of the skin. This operation allows for programmable stimulation of various cutaneous mechanoreceptors, individually or in combination, as an essential aspect of future immersive XR experiences. Wireless, real-time operation, either as single units or as arrays distributed on desired body parts, yields various types of perceptible sensations in an efficient manner. Complete experimental and theoretical work identifies the physics of multicoil electromagnetics, including a validated analytical model that guides optimized choices in designs for compact, efficient operation. In comparison to conventional haptic interfaces, these technologies enable high-bit haptic information transfer and virtual tactile sensations with enhanced realism. Human perception tests and representative use cases highlight additional features. The latter include hand navigation for the visually impaired, textural sensation through mixed forces, and sensory substitution for music perception, all of which can be achieved with one or multiple actuators under closed-loop control by acoustic or motion feedback. Building on the FOM operation technology introduced in this work, future efforts may establish routes for further reducing the dimensions and the effective modulus of the FOM actuator for high-density, conformable haptic interfaces (figs. S23 to S25). The development of in-plane coil structures or related configurations, suitable for lithographic fabrication, may offer additional benefits in miniaturization.

REFERENCES AND NOTES

1. A. Zimmerman, L. Bai, D. D. Ginty, *Science* **346**, 950–954 (2014).
2. W. Lin *et al*., *Sci. Adv.* **8**, eabp8738 (2022).
3. Y. H. Jung *et al*., *Nat. Electron.* **5**, 374–385 (2022).
4. X. Yu *et al*., *Nature* **575**, 473–479 (2019).
5. E. Leroy, H. Shea, *Adv. Mater. Technol.* **8**, 2300242 (2023).
6. J. Yin, R. Hinchet, H. Shea, C. Majidi, *Adv. Funct. Mater.* **31**, 2007428 (2021).
7. Y. H. Jung, J. H. Kim, J. A. Rogers, *Adv. Funct. Mater.* **31**, 2008805 (2021).
8. E. Abdi, D. Kulić, E. Croft, *IEEE Trans. Biomed. Eng.* **67**, 3438–3451 (2020).
9. J. Bimbo, C. Pacchierotti, M. Aggravi, N. Tsagarakis, D. Prattichizzo, in *2017 IEEE/RSJ International Conference on Intelligent Robots and Systems (IROS)* (IEEE, 2017), pp. 3401–3408.
10. Y. S. Choi *et al*., *Science* **376**, 1006–1012 (2022).
11. P. B. Shull, D. D. Damian, *J. Neuroeng. Rehabil.* **12**, 59 (2015).
12. M. T. Flavin *et al*., *Nature* **635**, 345–352 (2024).
13. G. Corniani, H. P. Saal, *J. Neurophysiol.* **124**, 1229–1240 (2020).
14. A. Handler, D. D. Ginty, *Nat. Rev. Neurosci.* **22**, 521–537 (2021).
15. B. Delhaye, A. Barrea, B. B. Edin, P. Lefèvre, J.-L. Thonnard, *J. R. Soc. Interface* **13**, 20150874 (2016).
16. N. L. Neubarth *et al*., *Science* **368**, eabb2751 (2020).
17. S. Guest *et al*., *Atten. Percept. Psychophys.* **73**, 531–550 (2011).
18. J. Turecek, B. P. Lehnert, D. D. Ginty, *Nature* **612**, 310–315 (2022).
19. K. T. Yoshida *et al*., *IEEE Trans. Haptics* **17**, 483–495 (2024).
20. M. Sarac *et al*., *IEEE Robot. Autom. Lett.* **7**, 6099–6106 (2022).
21. S. R. Williams, J. M. Suchoski, Z. Chua, A. M. Okamura, *IEEE Robot. Autom. Lett.* **7**, 3310–3317 (2022).
22. Z. Zhakypov, A. M. Okamura, in *2022 IEEE 5th International Conference on Soft Robotics (RoboSoft)* (IEEE, 2022), pp. 938–944.
23. M. Zhu *et al*., in *Proceedings of the 2020 CHI Conference on Human Factors in Computing Systems* (Association for Computing Machinery, 2020), pp. 1–12.
24. P. Zhang, M. Kamezaki, Y. Hattori, S. Sugano, in *2022 International Conference on Robotics and Automation (ICRA)* (IEEE, 2022), pp. 8869–8875.
25. N. A.-h. Hamdan, A. Wagner, S. Voelker, J. Steimle, J. Borchers, in *Proceedings of the 2019 CHI Conference on Human Factors in Computing Systems* (Association for Computing Machinery, 2019), pp. 1–14.
26. E. Leroy, R. Hinchet, H. Shea, *Adv. Mater.* **32**, e2002564 (2020).
27. J. Wan *et al*., *Sci. Adv.* **10**, eadm9314 (2024).
28. Y. Luo *et al*., *Nat. Commun.* **15**, 868 (2024).
29. Y. Huang *et al*., *Nat. Electron.* **6**, 1020–1031 (2023).
30. A. Kaneko, N. Asai, T. Kanda, *J. Hand Ther.* **18**, 421–425 (2005).
31. Z. Liu, J.-T. Kim, J. A. Rogers, R. L. Klatzky, J. E. Colgate, *IEEE Trans. Haptics* **17**, 441–450 (2024).
32. S.-A. Abad, N. Herzig, D. Raitt, M. Koltzenburg, H. Wurdemann, *Nat. Commun.* **15**, 7631 (2024).
33. M. W. Brown, J.-Z. Xiang, *Prog. Neurobiol.* **55**, 149–189 (1998).
34. H. Z. Tan, S. Choi, F. W. Lau, F. Abnousi, *Proc. IEEE* **108**, 945–965 (2020).
35. C. Pasluosta, P. Kiele, T. Stieglitz, *Clin. Neurophysiol.* **129**, 851–862 (2018).
36. Y. Roudaut *et al*., *Channels (Austin)* **6**, 234–245 (2012).
37. M. D. Fletcher, *Front. Neurosci.* **15**, 723877 (2021).

ACKNOWLEDGMENTS

The authors thank Y. Wang for preliminary assistance in fabricating devices. **Funding:** This work was funded by the Querrey-Simpson Institute for Bioelectronics. J.Y. acknowledges funding from the Basic Research Laboratory (BRL) Project from the National Research Foundation (RS-2024-00406674) funded by the Ministry of Science and ICT of Korea, as well as the Technology Innovation Program (RS-2024-00443121) funded by the Ministry of Trade, Industry and Energy (MOTIE, Korea). **Author contributions:** Conceptualization: K.-H.H., J.A.R.; Formal analysis: K.-H.H., S.L., Y.M., S.X., H.Q., H.W., C.F., H.Y., P.S., S.K., E.C.; Funding acquisition: Y.H., J.A.R.; Investigation: K.-H.H., J.Y., S.L., Y.M., S.X., H.Q., H.W., C.F., H.Y., J.-T.K., P.S.; Methodology: K.-H.H., J.Y., S.L., Y.M., M.T.F., E.C.; Project administration: Y.H., J.A.R.; Software: K.-H.H., J.Y.; Supervision: K.-H.H., Y.H., J.A.R.; Validation: K.-H.H., Y.M., S.X.; Visualization: K.-H.H., J.Y., S.L., Y.M., S.X., H.Q., J.-T.K., S.Y.; Writing – original draft: K.-H.H.; Writing – review & editing: K.-H.H., J.Y., S.L., Y.M., H.Q., H.-Y.A., Y.H., J.A.R. **Competing interests:** The authors declare that they have no competing interests. **Data and materials availability:** All data are available in the main text or the supplementary materials.

SUPPLEMENTARY MATERIALS

science.org/doi/10.1126/science.adt2481
Materials and Methods
Supplementary Text
Figs. S1 to S29
Tables S1 to S8
References (*38*–*68*)
Movies S1 to S6

Submitted 18 September 2024; accepted 14 February 2025
10.1126/science.adt2481

POPULATION GENETICS

A geographic history of human genetic ancestry

Michael C. Grundler[1], Jonathan Terhorst[2], Gideon S. Bradburd[1]*

Describing the distribution of genetic variation across individuals is a fundamental goal of population genetics. We present a method that capitalizes on the rich genealogical information encoded in genomic tree sequences to infer the geographic locations of the shared ancestors of a sample of sequenced individuals. We used this method to infer the geographic history of genetic ancestry of a set of human genomes sampled from Europe, Asia, and Africa, accurately recovering major population movements on those continents. Our findings demonstrate the importance of defining the spatiotemporal context of genetic ancestry when describing human genetic variation and caution against the oversimplified interpretations of genetic data prevalent in contemporary discussions of race and ancestry.

Present-day genomes are inherited from an unbroken chain of ancestors who lived in different geographic locations at different times, creating spatial patterns of genetic relatedness (*1*). Understanding these patterns is vital both for the identification of the genomic basis of phenotypic variation (*2*) and for knowledge of the demographic history of a species (*3*). Conversely, ignoring spatial demographic history can have serious implications for genome-wide association studies or the identification of loci involved in local adaptation (*4*).

Genetic variation in humans is often summarized with discrete labels, but these can be inaccurate and misleading (*5*, *6*). Even when based on geographic history, genetic ancestry labels oversimplify a complex picture because they implicitly focus on only a single point in time. For example, based on our current understanding of human origins, all living individuals are "African" (regardless of the geography of their recent ancestors) when considering their ancestry ~200,000 years before present. Advances in the study of ancient DNA have revealed a lack of genetic continuity within geographic regions (*7*–*10*), further highlighting the shortcomings of genetic ancestry labels. The fact that these labels are generated using statistical genetics approaches gives them the veneer of authenticity, further reifying problematic notions of race and ancestry in society (*6*, *11*).

At a technical level, many of the existing methods for quantifying ancestry average over the ages of shared ancestors in the sample, effectively "flattening" the temporal component of the genealogy that connects all individuals within a species (*12*, *13*). In reality, any pair of individuals is connected by many shared ancestors from whom each has inherited some portion of their genome (*14*). This flattening has the effect of painting a static notion of ancestry rather than one that changes as it proceeds backward in time.

If we knew the identities, locations, and ages of the ancestors of a sample, we could more precisely and accurately report their geographic ancestry through time. Moreover, we could learn about their history of dispersal, identifying major population movements, demographic events, and barriers to migration. Although such detailed pedigree information is rare [but see (*15*) and (*16*)], it is nevertheless possible to learn about pedigree ancestors that are shared among individuals in a sample. This is because genetic relationships between samples, as well as the identities of the shared ancestors with whom they are related, are encoded in an interwoven collection of gene genealogies called an ancestral recombination graph (ARG) (*17*–*19*).

Recent advances in statistical and computational population genetics (*20*–*23*) have facilitated the inference of an ARG from large numbers of genomes. The ARG is a record of all coalescence and recombination events since the divergence of the sequences under study, and therefore it specifies a complete genealogy of the sample at each genomic position. This record can be represented as a tree sequence (*24*, *25*), an ordered set of trees localized to adjacent regions of the genome describing the gene genealogies of a set of samples at every genomic position. Each internal node in a local genealogy represents a haplotype within an ancestor from whom two or more sampled individuals have coinherited a portion of their genome. By estimating where and when each of these ancestors lived, we can reconstruct the geographic history of a set of modern-day individuals, documenting the path through space and time by which their genomes came to them.

Here, we present and validate a method for achieving this goal. Our method, called GAIA (geographic ancestor inference algorithm), efficiently infers the geographic locations of the shared ancestors of a modern, georeferenced sample. We applied GAIA to a tree sequence of humans sampled in Europe, Asia, the Middle East, and Africa (*22*) and reconstructed the geographic history of human ancestry over the past 2 million years.

Inferring the locations of shared ancestors

Conceptually, GAIA is like many tree-based methods in phylogeography that attempt to reason about the locations and movements of genetic ancestors based on the geographic distribution of modern-day samples and the phylogenetic relationships among them (*26*–*28*). Instead of working with a single gene tree or with a collection of independent gene trees, GAIA generates inferences using a sequence of locally correlated gene trees. It is similar to several recent existing methods in this regard. For example, Wohns *et al.* (*22*) introduced a nonparametric approach that estimates ancestor locations by successively averaging the coordinates of sample locations in a postorder traversal of a tree sequence. In addition, Osmond and Coop (*29*) described a likelihood method for locating genetic ancestors and estimating migration rates based on a model of branching Brownian motion using a sample of gene trees from a tree sequence, an approach that was recently extended by Deraje *et al.* (*30*) to the full ARG. GAIA differs from these approaches, both in its choice of optimality criterion and in its flexible representation of geographic space, which can be continuous or discrete.

GAIA works by fitting a minimum migration cost function to each genomic position in an ancestral haplotype using the generalized parsimony algorithm (Fig. 1). Because neighboring gene genealogies in a tree sequence are highly correlated, we were able to efficiently maintain the state of parsimony calculations as we iterated over the local genealogies in a tree sequence containing the ancestral haplotype. Once these cost functions were computed for all genomic positions, we averaged them and assigned the ancestral haplotype to the geographic location that minimized its average cost function. These assignments then have a straightforward interpretation: They correspond to the geographic location that minimizes the overall migration cost of an average ancestral base pair. In our implementation, migration cost is a function of geographic distance, and the overall migration cost in a local genealogy is simply the sum of all ancestor-descendant migration costs.

A minimum migration optimality criterion may miss migration events because ancestors in distinct geographic locations can sometimes be assigned to a single geographic location to lower the overall migration cost given the sampling configuration. This can create a simplified picture of ancestry when the reality is more complex (*31*). Additionally, variance in the coalescent process itself can interact with the sampling configuration such that ancestors in the same location are inferred to be in different locations, potentially resulting in mistaken

[1]Department of Ecology and Evolutionary Biology, University of Michigan, Ann Arbor, MI, USA. [2]Department of Statistics, University of Michigan, Ann Arbor, MI, USA.
*Corresponding author. Email: bradburd@umich.edu

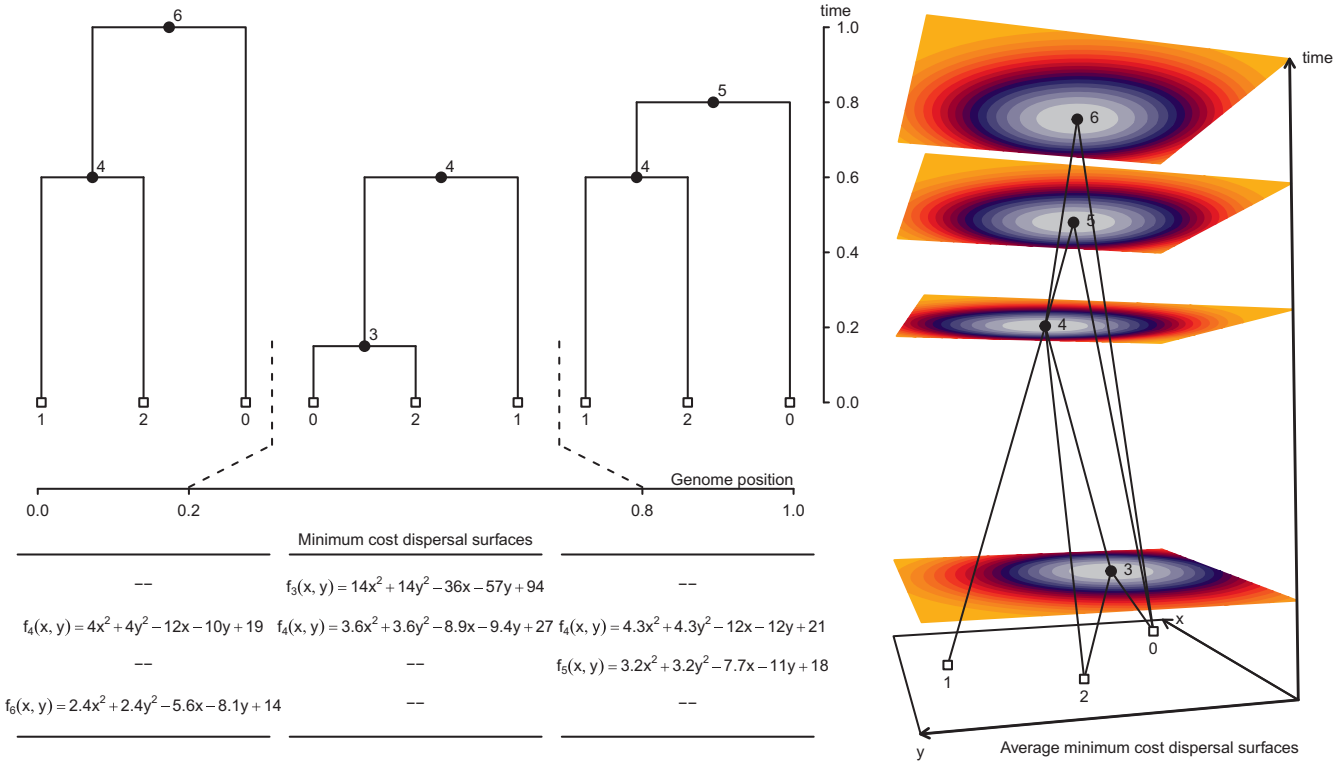

Fig. 1. Conceptual overview of GAIA. For each local tree, we used the dynamic programming method of Sankoff and Rousseau (*38*) to fit a minimum cost dispersal surface to the genealogical relationships of the georeferenced sample nodes. In this example, we used squared Euclidean distance as the cost function, and $f_u(x, y)$ returns the smallest sum of squared dispersal distances between all ancestor-descendant node pairs that can be obtained when node u is at location (x, y). Using the genomic spans of local trees as weights, we then took a weighted average of local surfaces to assign each node a single average minimum cost dispersal surface. Here, node 4 appears in all three local trees, and its final fitted surface is the weighted average of the three local surfaces. By contrast, nodes 3, 5, and 6 appear in a single local tree, and their final fitted surfaces are identical to the surface in the local tree in which they appear. The perspective plot in the rightmost panel displays the ancestral recombination graph encoding the local trees along with the final fitted surface for each node. Nonsample nodes are positioned at the minimum cost point on the surface. Warmer colors denote higher costs.

inferences of migration. Because GAIA is principally an exploratory tool, we did not attempt exhaustive exploration of these biases, but users of GAIA should bear them in mind when interpreting results.

To validate GAIA's performance, we simulated genetic data under different spatial models using SLiM (*32*). GAIA performs well under a variety of demographic histories and over a range of dispersal kernels (both magnitude and shape), achieving greater accuracy and faster computation times than related nonparametric methods (figs. S3 to S6), and it is able to accurately reconstruct pairwise distributions of ancestor distances over a range of temporal scales (fig. S13). We also demonstrate that we can use the reconstructed geographic distances between nodes in the tree sequence to estimate the parent-offspring dispersal distance for both Gaussian and non-Gaussian dispersal kernels (figs. S1 and S2).

Tracking human ancestors through space and time

We inferred the geographic locations of ancestors of a contemporary sample of 2140 georeferenced human genomes from the Human Genome Diversity Project (*33*, *34*) using a dated tree sequence inferred for chromosome 18 by Wohns *et al.* (*22*) (Fig. 2). To avoid the complexity introduced by large-scale postcolonial migrations, we focused on ancestry of the subset of individuals sampled from the continents of Europe, Asia, and Africa, consisting of 1070 contemporary individuals. The tree sequence for these individuals consists of 28,154 local genealogies containing 114,606 ancestral nodes and spanning ~80,000 generations of human history. An equal area discrete global grid (*35*) (cell spacing ~800 km) intersected with Earth's landmass provided a set of habitable areas; individual sample locations were assigned to the nearest grid cell. Although a variety of complex migration cost matrices can be envisioned, we opted for the simplest model that only allows migration between neighboring grid cells and assigns a unit cost to each migration event. We used GAIA to locate ancestral nodes to the grid cells with the lowest migration cost. For many ancestral nodes, especially older nodes, multiple grid cells may be optimal or near optimal (fig. S7). Because our summaries ignore near-optimal solutions, they do not explore the full range of uncertainty in ancestral locations and should be viewed, not as precise statements on where ancestors lived and how they moved, but rather as summaries of major trends.

Our inferred geographic chronology of the ancestors of the sample largely reconstructs major population movements in human prehistory, including the out-of-Africa expansion and the peopling of Eurasia (Fig. 3). Our estimates place some genetic ancestors of the sample in Asia and the Middle East well before the earliest fossil evidence of human dispersal out of Africa. The oldest nodes in the tree sequence are estimated to have occurred ~2 million years before present, and a small minority of these are inferred to be located in Asia and the Middle East. A similar pattern was observed by Wohns *et al.* (*22*) in their analysis of chromosome 20. Geographic estimates of ancient ancestry must be viewed with caution because phylogenetic signal is highly attenuated at deep timescales. In the extreme case of complete loss of phylogenetic signal, estimates from GAIA will be no better than random

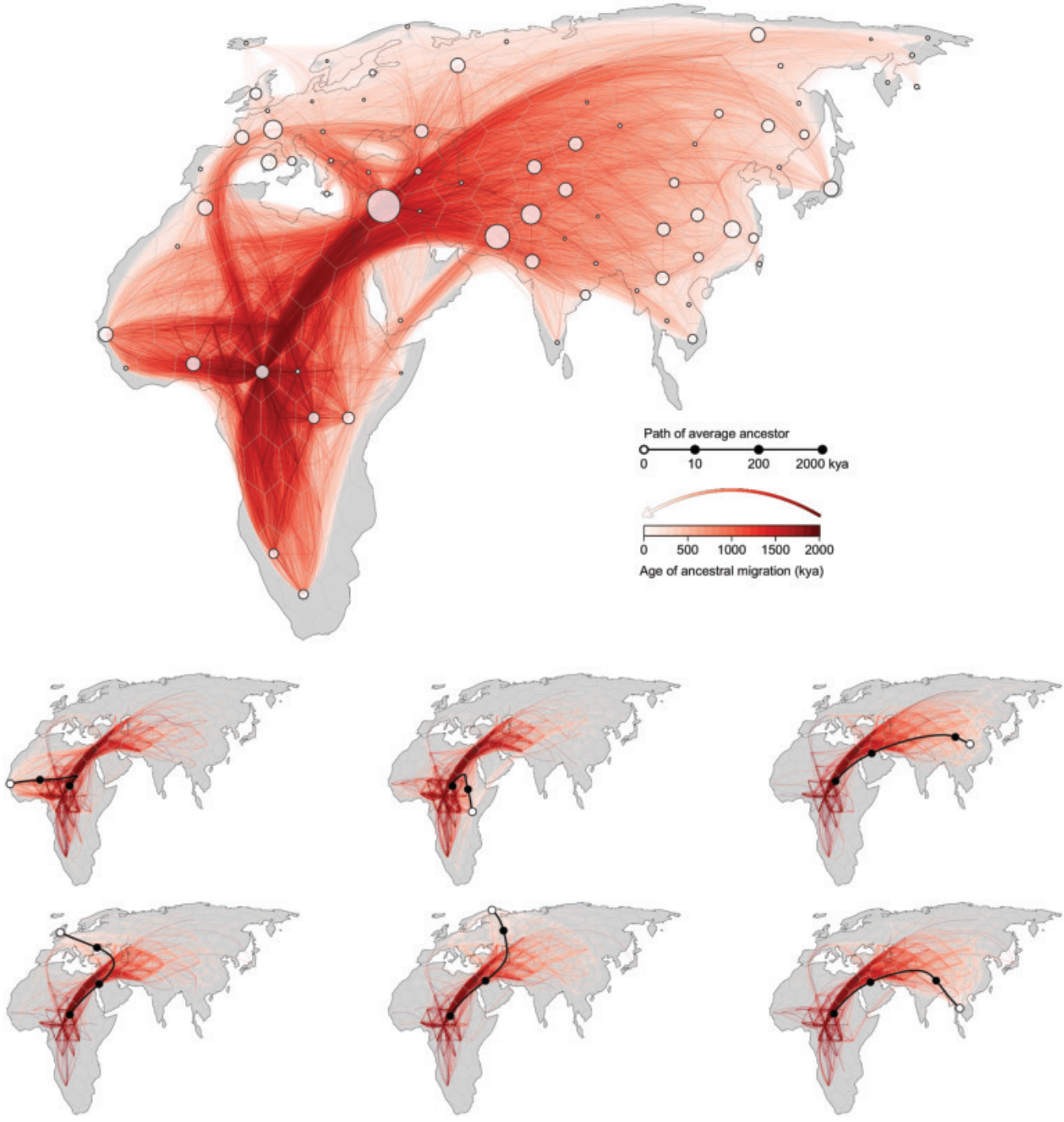

Fig. 2. A georeferenced ARG. Red lines trace the inferred historical migrations of genetic ancestors of the sample (white points), with darker shading used to indicate movements that took place in the more distant past. Six contemporary samples are highlighted in the bottom panels. Black lines trace the average position of their genetic ancestors back through time, and red lines denote the subset of edges in the ARG that are ancestral to the samples.

guessing and will tend to be pulled toward a majority rule geographic centroid location. Although this is not a concern for the dataset as a whole (where the geographic centroid occurs in central Asia), it may contribute to GAIA's placement of the oldest genetic ancestors in central Africa (fig. S12). These concerns notwithstanding, from ~2 million to 200,000 years before present, the average positions of genetic ancestors to the geographic subsets of samples from Europe, Asia, the Middle East, and Africa are all inferred to be in Africa. This coincides with the period when most genome positions in these geographic subsets trace their descent to an ancestor in Africa. Between 200,000 years ago and the present, the average location of ancestors to the geographic subsets of samples from Europe, Asia, and the Middle East diverge from one another and begin to move toward the average of position of samples from those regions, whereas the average position of ancestors to the African subset of samples remains in Africa (Fig. 4).

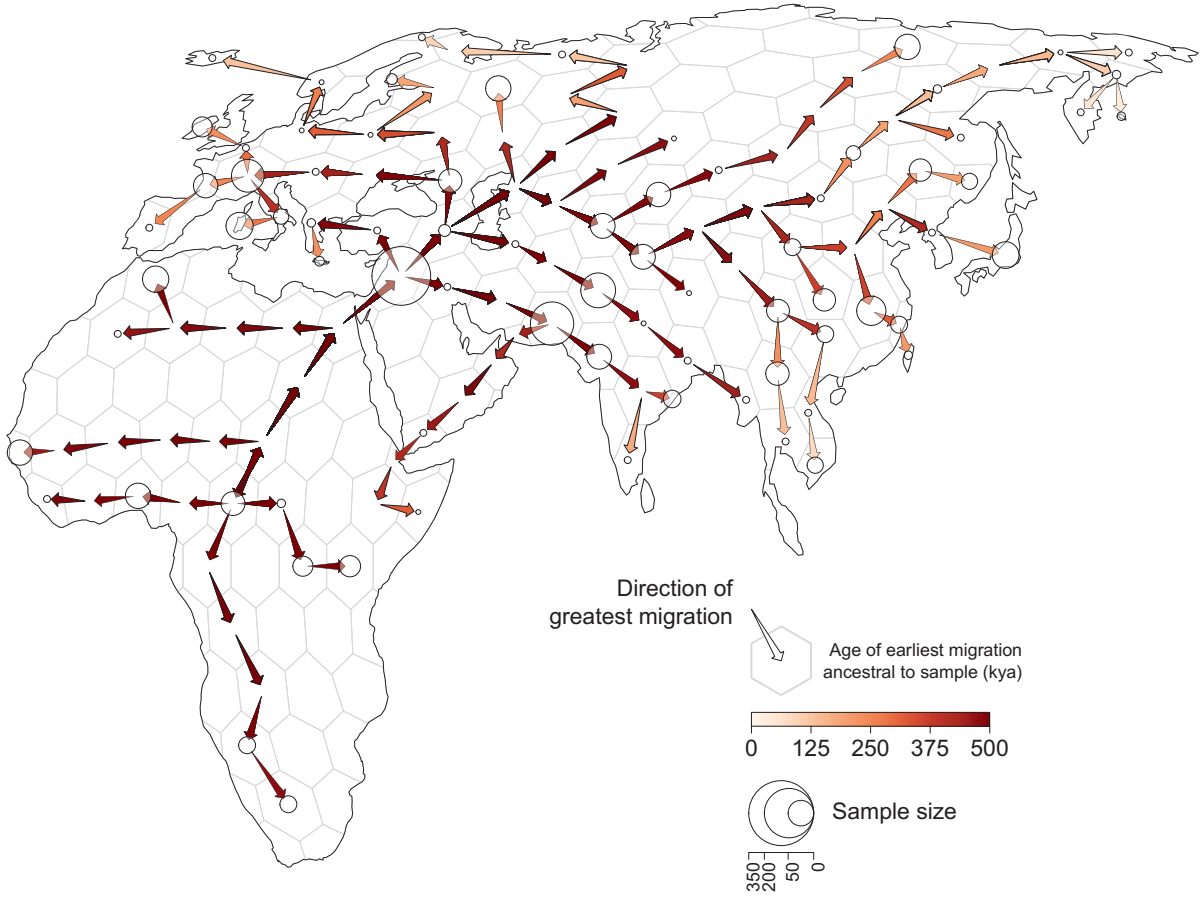

Fig. 3. Geographic chronology of human genetic ancestry. Arrows point in the direction of the greatest migration of the shared genetic ancestors of the sample and are colored according to the age of the earliest migration. Points show the distribution of sampled modern-day genomes. Point size is proportional to the number of samples from each locality.

Geographic history of human ancestry

We used the georeferenced tree sequence to define a spatiotemporally explicit ancestry coefficient, which we then tracked across space and time to understand and quantify the genetic and geographic history of our sample. Only a subset of any given contemporary individual's genome, $A_i(t)$ in individual i, is found in the ancestral nodes or branches in the tree sequence at a given point in time t (once the local genealogy in a particular genomic region has coalesced, that portion of the genome is no longer represented in deeper sections of the tree sequence; therefore, the farther back in time we look, the less of any modern-day individual's genome can be found). We define this spatiotemporally explicit ancestry coefficient, which we call $z_{ik}(t)$, as $A_{ik}(t)/A_i(t)$: the proportion of individual i's genome that exists in its ancestors in the tree sequence at time t and that is inherited from ancestors living within some prescribed geographic region k. This ancestry coefficient can be broadly understood as the proportion of a sample's genome inherited from individuals living within a specified geographic region at a specific time.

Unlike ancestry labels, $z_{ik}(t)$ is explicitly associated with both a point in time and a region of space. Therefore, we can use it to understand how a sample's ancestry has changed across space and time. At the present moment, the distribution of z_{ik} simply reflects the geography of modern-day sampling. By 100,000 years ago, we find that only 2% of modern-day samples are inheriting their genomes from ancestors in Europe (Fig. 4); almost all ancestors contributing genomic material to the modern-day sample are inferred to have lived in Africa, Asia, and the Middle East. The spatiotemporal ancestry coefficients show similar trajectories for modern-day samples from Asia. During this same period, the proportion of sample ancestors found in Africa increases almost monotonically backward in time, from 16% at the present (again, reflecting the geography of modern-day sampling) to ~95% by 1 million years ago. The proportion of the genomes of the sample inherited from ancestors inferred to be in Africa plateaus at ~95%, with ~5% of genome continuing to be inherited from ancestors in the Middle East along the eastern Mediterranean (fig. S8). Randomly downsampling the data so that each population is represented by only a single individual does not change this result (fig. S9). However, because attenuation of phylogenetic signal at deep timescales can cause misplacement of genetic ancestors, this result should be viewed with caution.

Large-scale movement in human ancestry

To study large-scale movements of human ancestry, we introduce a new statistical summary of the georeferenced tree sequence: ancestry flux. Formally, if $A_i(t_l, t_r)$ is the amount of individual i's genome that inherits from ancestors alive between $[t_l, t_r)$, and $A_{ijk}(t_l, t_r)$ is the same amount that inherits from ancestors who moved from j to k, we define ancestry flux as $\phi_{ijk}(t_l, t_r) = A_{ijk}(t_l, t_r)/A_i(t_l, t_r)$: the proportion of i's genome that exists in its ancestors in the tree sequence during the period $[t_l, t_r)$ and that is inherited from ancestors who moved from j to k during that same period. This coefficient can be broadly understood as the proportion of a sample's genome inherited from ancestors who moved between specified geographic regions during a particular period. However,

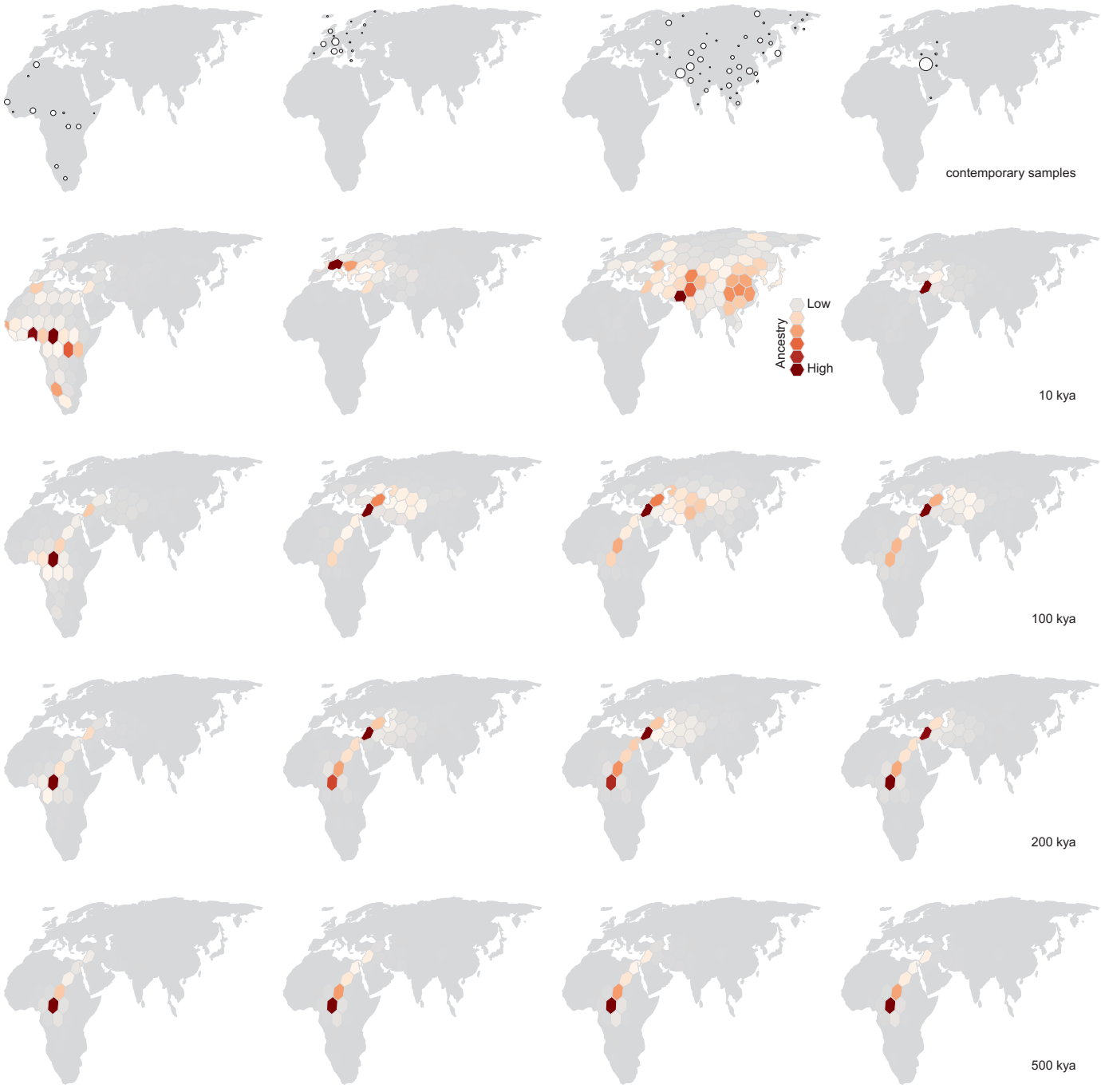

Fig. 4. Inferred spatiotemporal ancestry coefficients through time. The fraction of genomic positions in each geographic subset of samples (top row) that trace ancestry to different geographic regions at different times in the past is represented by shades of red, with darker shading indicating greater ancestry (i.e., a larger fraction). Point size is proportional to the number of sampled genomes from each locality.

because of the nature of the coalescent process, we expect that the movement of genetic ancestry quantified in this fashion will predate the movement of individuals carrying that ancestry. Additionally, estimates of ancestry flux are subject to error in ancestor location estimates and error incurred by interpolating migration routes between estimated locations (fig. S14), so care is warranted when interpreting the directions and timings associated with the coefficients.

We discretized Europe, Asia, and Africa into approximately equal-area hexagons (each ~800 km^2) and quantified ancestry flux between them in 2500-year intervals between the present and 0.5 million years ago. We found consistent ancestry flux out of Africa into the Middle East during this time, with a peak occurring between 100,000 and 150,000 years ago (Fig. 5). Nearly all ancestry flux out of Africa is estimated to have occurred through a northern route across the Sinai Peninsula rather than a southern route across the strait at Bab-el-Mandeb. Approximately 30% of genomic positions in the modern-day sample trace ancestry to a northerly migration out of Africa, but only 0.1% trace ancestry to a southerly migration

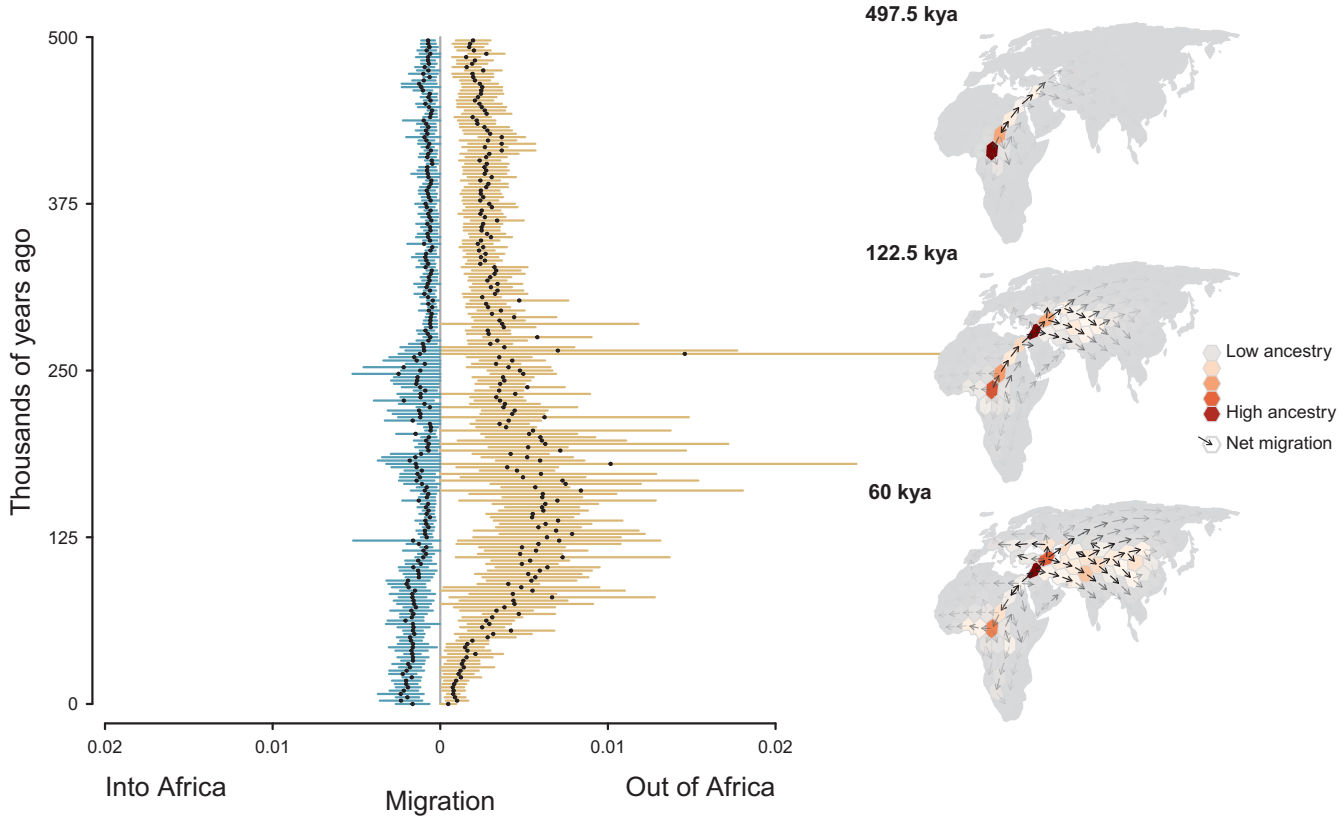

Fig. 5. Inferred flux in spatiotemporal ancestry coefficients through time. Each point is the mean estimate (computed from random subsets of the data and bracketed by the SD) of the amount of historical migration of shared genetic ancestors of the modern-day sample into or out of Africa over time. Inset maps highlight three different time intervals. Cells are colored by the fraction of genomic positions that find ancestry in them at that time, and arrows depict the direction of greatest migration, with opacity scaled by the magnitude of migration.

route out of Africa. However, this result should be viewed with caution, because simulations indicate that GAIA would detect such a pattern even if the true route had been through the south (fig. S11).

Discussion

We have described a simple heuristic approach for reconstructing the geographic genetic history of a sample, which can be used to explore the timing and location of demographic events. Patterns of diversity and relatedness between individuals are created by a complex interplay between evolutionary forces acting over the history of a population. By uncovering these patterns, our method enables researchers to go beyond the standard practice of grouping individuals into a small number of static and ill-defined "populations." Although this practice may be useful in some limited scenarios (e.g., for conservation and management), our results illustrate that it discards an immense amount of additional information. Furthermore, when applied to humans, population assignment has the potential to lead to greater harm and confusion by conflating race, ethnicity, geography, and ancestry (*5*). A spatiotemporal summary of ancestors offers an intuitive and informative path toward understanding ancestry, demography, and major population movements through time.

Of course, the geographic histories inferred by GAIA are not perfectly accurate; individual dispersal decisions are the result of countless factors that we cannot capture using a simple heuristic model. For example, GAIA assumes that lineages disperse independently of one another and that the dispersal process is independent of the coalescent process in a reconstructed gene tree, and both of these assumptions are certainly violated in empirical datasets. Moreover, errors in the tree sequences inferred by upstream tools such as RELATE (*20*) and TSINFER (*21*) have the potential to propagate into the output of GAIA. Additionally, the sampling process itself may affect our results insofar as the accuracy of geographic inference of ancestor locations depends on the distribution of sampled individuals relative to that of their ancestors. Finally, we caution that GAIA sheds light on the geographic and temporal distribution of shared genetic ancestors. Even if we had perfect information on the geographic locations of all ancestors, it would not necessarily inform our understanding of the distribution of the census population alive at any point in the past. As with all population genetic approaches, historical individuals who contributed no ancestry to the modern-day sample remain inscrutable. We therefore present GAIA as an exploratory data analysis tool rather than a formal approach for explicitly comparing different models of geographic history.

Despite these limitations, the ability to infer the locations of ancestors in the tree sequence opens exciting avenues for research. Simply summarizing the georeferenced tree sequence can yield valuable insights about the history of a population, including identifying barriers to dispersal, shifts in dispersal regimes through time, and the geography of ecological dynamics (at least with respect to genetic ancestry). A straightforward direction for extending GAIA would be to explicitly incorporate some of these elements. Because the transitions between different geographic states occur on an arbitrary network, we can easily incorporate different geographies, such as dispersal routes that connect far-flung regions that may be of interest when species occasionally experience human-mediated dispersal (*36*). More broadly, the ability to study the geography of genealogies heralds an exciting growth in the ability of

the field of population genetics to shed light on population ecological processes governing the movement, distribution, and density of individuals across space and time.

REFERENCES AND NOTES

1. G. S. Bradburd, P. L. Ralph, *Annu. Rev. Ecol. Evol. Syst.* **50**, 427–449 (2019).
2. C. J. Battey, P. L. Ralph, A. D. Kern, *Genetics* **215**, 193–214 (2020).
3. P. Ralph, G. Coop, *PLOS Biol.* **11**, e1001555 (2013).
4. A. A. Zaidi, I. Mathieson, *eLife* **9**, e61548 (2020).
5. G. Coop, Genetic similarity and genetic ancestry groups. arXiv: 2207.11595 [q-bio.PE] (2022).
6. A. C. F. Lewis *et al.*, *Perspect. Biol. Med.* **66**, 225–248 (2023).
7. W. Haak *et al.*, *Nature* **522**, 207–211 (2015).
8. M. E. Allentoft *et al.*, *Nature* **522**, 167–172 (2015).
9. F. Racimo *et al.*, *Proc. Natl. Acad. Sci. U.S.A.* **117**, 8989–9000 (2020).
10. T. M. Mattila *et al.*, *Commun. Biol.* **6**, 793 (2023).
11. J. Carlson, B. M. Henn, D. R. Al-Hindi, S. Ramachandran, *Nature* **610**, 444–447 (2022).
12. D. J. Lawson, G. Hellenthal, S. Myers, D. Falush, *PLOS Genet.* **8**, e1002453 (2012).
13. J. K. Pritchard, M. Stephens, P. Donnelly, *Genetics* **155**, 945–959 (2000).
14. I. Mathieson, A. Scally, *PLOS Genet.* **16**, e1008624 (2020).
15. S. M. Aguillon *et al.*, *PLOS Genet.* **13**, e1006911 (2017).
16. L. Anderson-Trocmé *et al.*, *Science* **380**, 849–855 (2023).
17. R. C. Griffiths, P. Marjoram, in *Progress in Population Genetics and Human Evolution* (Springer, 1997), pp. 257–270.
18. A. L. Lewanski, M. C. Grundler, G. S. Bradburd, *PLOS Genet.* **20**, e1011110 (2024).
19. Y. Wong *et al.*, *Genetics* **228**, iyae100 (2024).
20. L. Speidel, M. Forest, S. Shi, S. R. Myers, *Nat. Genet.* **51**, 1321–1329 (2019).
21. J. Kelleher *et al.*, *Nat. Genet.* **51**, 1330–1338 (2019).
22. A. W. Wohns *et al.*, *Science* **375**, eabi8264 (2022).
23. Y. Deng, R. Nielsen, Y. S. Song, Robust and accurate Bayesian inference of genome-wide genealogies for large samples. bioRxiv [Preprint] (2024); https://doi.org/10.1101/2024.03.16.585351.
24. J. Kelleher, A. M. Etheridge, G. McVean, *PLOS Comput. Biol.* **12**, e1004842 (2016).
25. J. Kelleher, K. R. Thornton, J. Ashander, P. L. Ralph, *PLOS Comput. Biol.* **14**, e1006581 (2018).
26. J. Avise, *Phylogeography: The History and Formation of Species*, (Harvard Univ. Press, 2000), **vol. 447**.
27. L. L. Knowles, W. P. Maddison, *Mol. Ecol.* **11**, 2623–2635 (2002).
28. L. L. Knowles, *Annu. Rev. Ecol. Evol. Syst.* **40**, 593–612 (2009).
29. M. Osmond, G. Coop, *eLife* **13**, e72177 (2024).
30. P. Deraje, J. Kitchens, G. Coop, M. M. Osmond, Inferring the geographic history of recombinant lineages using the full ancestral recombination graph. bioRxiv [Preprint] (2024); https://doi.org/10.1101/2024.04.10.588900.
31. E. M. L. Scerri, L. Chikhi, M. G. Thomas, *Nat. Ecol. Evol.* **3**, 1370–1372 (2019).
32. B. C. Haller, P. W. Messer, *Am. Nat.* **201**, E127–E139 (2023).
33. H. M. Cann *et al.*, *Science* **296**, 261–262 (2002).
34. J. Z. Li *et al.*, *Science* **319**, 1100–1104 (2008).
35. R. Barnes, K. Sahr, "dggridR: Discrete Global Grids" (r package version 3.0.0., 2023); https://cran.r-project.org/package=dggridR.
36. S. H. Zhan *et al.*, Towards pandemic-scale ancestral recombination graphs of SARS-CoV-2. bioRxiv [Preprint] (2023); https://doi.org/10.1101/2023.06.08.544212.
37. M. C. Grundler, J. Terhorst, G. S. Bradburd, Data for: A geographic history of human genetic diversity, Dryad (2024); https://doi.org/10.5061/dryad.p5hqbzkwz.
38. D. Sankoff, P. Rousseau, *Math. Program.* **9**, 240–246 (1975).

ACKNOWLEDGMENTS

We thank Y. Brandvain, J. Carlson, G. Coop, P. Deraje, D. Edge, J. Kitchens, M. Weber, and members of the Bradburd lab for comments and discussion that helped improve the research presented here. **Funding:** This work was supported by the National Science Foundation (award number DMS- 2052653 to J.T.) and the National Institute of General Medical Sciences of the National Institutes of Health under award numbers R35GM151145 (J.T.) and R35GM137919 (G.S.B.). The content is solely the responsibility of the authors and does not necessarily represent the official views of the National Institutes of Health. **Author contributions:** Conceptualization: M.C.G., J.T., G.S.B.; Data curation: M.C.G.; Formal analysis: M.C.G.; Funding acquisition: J.T., G.S.B.; Methodology: M.C.G., J.T., G.S.B.; Software: M.C.G.; Supervision: G.S.B.; Validation: M.C.G.; Writing – original draft: M.C.G., G.S.B.; Writing – review & editing: M.C.G., J.T., G.S.B. **Competing interests:** The authors declare no competing interests. **Data and materials availability:** All publicly available datasets used in this paper are available from their original publications. GAIA is available at https://github.com/blueraleigh/gaia under the MIT license. All code and data files used to perform analyses in this paper are available on GitHub at https://github.com/blueraleigh/gaia-paper and on Dryad (*37*). **License information:** Copyright © 2025 the authors, some rights reserved; exclusive licensee American Association for the Advancement of Science. No claim to original US government works. https://www.science.org/about/science-licenses-journal-article-reuse

SUPPLEMENTARY MATERIALS

science.org/doi/10.1126/science.adp4642
Materials and Methods
Supplementary Text
Figs. S1 to S16
References (*39*–*43*)
MDAR Reproducibility Checklist

Submitted 26 March 2024; accepted 24 January 2025
10.1126/science.adp4642

POLICING

High-frequency location data show that race affects citations and fines for speeding

Pradhi Aggarwal[1], Alec Brandon[2]*, Ariel Goldszmidt[3], Justin Holz[4], John A. List[3], Ian Muir[5], Gregory Sun[6], Thomas Yu[7]

Prior research on racial profiling has found that in encounters with law enforcement, minorities are punished more severely than white civilians. Less is known about the causes of these encounters and their implications for our understanding of racial profiling. Using high-frequency location data of rideshare drivers in Florida (*N* = 222,838 individuals), we estimate the effect of driver race on citations and fines for speeding using 19.3 million location pings. Compared with a white driver traveling the same speed, we find that racial or ethnic minority drivers are 24 to 33% more likely to be cited for speeding and pay 23 to 34% more money in fines. We find no evidence that accident and reoffense rates explain these estimates, which suggests that an animus against minorities underlies our results.

Racial profiling is one of the most important social issues in the United States. To better understand the extent of this issue and motivate policy interventions to mitigate it, social scientists have extensively examined administrative data collected by law enforcement agencies, such as records of police encounters with motorists and pedestrians, responses to 911 calls, and criminal trials. Broadly speaking, this research has found that, relative to the white civilians who appear in the data, police officers and judges are more likely to search, fine, use force, charge, detain, and incarcerate civilians who belong to a racial or ethnic minority group (*1*–*16*).

A basic concern with this research is that because race or ethnicity likely affect whether a civilian is cited in the administrative data, the results are unlikely to capture the full extent of racial profiling (*17*–*22*). The direction in which this would bias prior findings depends on why race or ethnicity affects the likelihood of appearing in the data. One possibility is that civilians who belong to a racial or ethnic minority group are more likely to be cited compared with their white counterparts for the same violation of the law, potentially because they are targeted by police or because their communities are overpoliced. Under this possibility, analyses of administrative records would understate the extent of racial profiling. Another possibility is that minority civilians are more likely to be cited because they break the law more frequently, which would cause analyses of the administrative data to overstate the extent of racial profiling.

Without additional data that allow social scientists to control for possibilities such as these, it is hard to make progress on policy interventions to mitigate racial profiling. A subset of the prior research has suggested that interventions should target "taste-based discrimination" (*23*)—because underlying the evidence of racial profiling is an animus against racial and ethnic minority groups—not "statistical discrimination" (*24*, *25*), where police and judges use civilian race or ethnicity as predictors that help accomplish objectives, such as deterrence. However, it is possible that this suggestion is only partially true and that an analysis of the full extent of racial profiling would find evidence for targeting statistical discrimination too.

In this Research Article, we examine the full extent of racial profiling in the enforcement of speed limits. Prior research on this question is emblematic of the broader literature on racial profiling. Among motorists cited in the

[1]Sloan School of Management, Massachusetts Institute of Technology, Cambridge, MA, USA. [2]Carey Business School, Johns Hopkins University, Baltimore, MD, USA. [3]Kenneth C. Griffin Department of Economics, University of Chicago, Chicago, IL, USA. [4]Gerald R. Ford School of Public Policy, University of Michigan, Ann Arbor, MI, USA. [5]Wal-Mart Inc., Bentonville, AR, USA. [6]Olin Business School, Washington University in St. Louis, St. Louis, MO, USA. [7]Department of Economics, Yale University, New Haven, CT, USA.
***Corresponding author. Email: alec.brandon@jhu.edu**

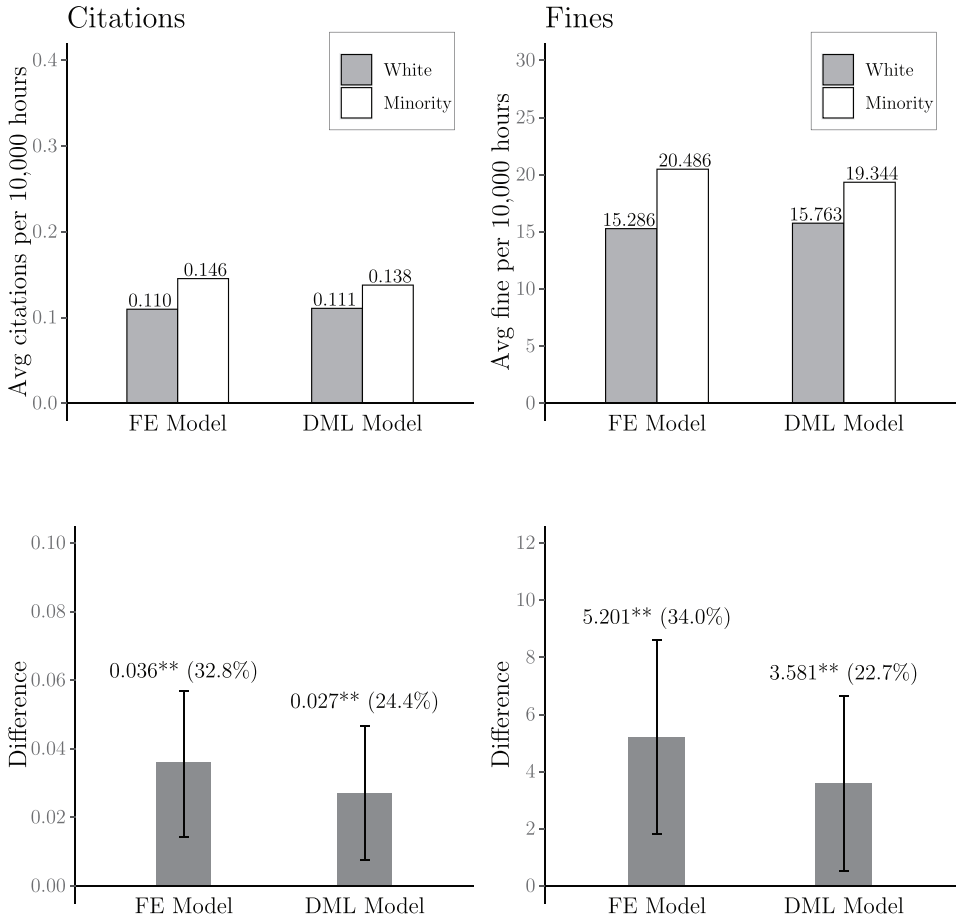

Fig. 1. Effect of driver race on citations and fines for speeding. In the top row, the rate of citations and cost of fines for white and minority drivers is plotted. In each column of the top row, the left pair of estimates are adjusted for the variation explained by the control variables in the FE model, and the right pair of estimates account for variation explained by controls in the DML model. In the bottom row, the differences between white and minority citation rates and fines are plotted. For each outcome, the left estimate controls for the covariates in the FE model, and the right estimate controls for the covariates selected by the DML model. 95% confidence intervals constructed with robust standard errors clustered by driver are included on the estimated differences. In parentheses, the estimated difference is normalized by the rate of citations and fines for white drivers. *P < 0.10; **P < 0.05; ***P < 0.01.

administrative data, minority drivers receive harsher punishments for speeding (*5*, *7*, *12*–*14*), and these harsher punishments are attributed to taste-based, not statistical, discrimination because they cannot be explained by an objective, such as deterring future citations for speeding (*13*). There is also evidence that minority drivers are more likely to appear in these data, although why they are overrepresented is multivariate. There is evidence that police officers target minority drivers in traffic stops (*12*) and that minority communities are overpoliced (*26*, *27*). However, there are also data collected by researchers (*28*) and automated speed cameras (*29*) that suggest that drivers who belong to a racial or ethnic minority group are more likely to exceed the speed limit. One way to better understand the full extent of racial profiling in this context would be to analyze administrative records on speeding violations that are linked to data on whether a motorist was driving, their driving speed relative to the limit, their race or ethnicity, and other potentially important controls such as driving location.

We constructed a dataset of this form by linking (i) high-frequency location (HFL) data [i.e., global positioning system (GPS) pings communicated from a driver's smartphone] of motorists with (ii) official government administrative records on their speeding violations and (iii) inference of their race or ethnicity. To the best of our knowledge, this is the first study to construct such a dataset (*30*). Using these data, we conduct analyses to answer the following research questions (RQs). RQ1: Compared with white drivers, are minority drivers more likely to be cited and pay more in fines for speeding? RQ2: Which mechanism, taste-based or statistical discrimination, underlies our answer to RQ1?

Methods

We answer these questions using data from a collaboration with the rideshare platform Lyft. This study's sample included Lyft drivers (N = 222,838 individuals) operating in the state of Florida. Much like its competitor Uber, Lyft runs a platform that matches customers with drivers offering rides. To offer rides, drivers log into an application on their smartphone that communicates pings of a driver's precise location and driving speed to Lyft's platform every 10 s.

Measures

Driver speed, speeding, and reoffense of speeding

The HFL pings that Lyft receives denote the time and location of a driver using their smartphone's clock and GPS. We calculate average driving speed between pings by dividing the distance and time between each ping. After merging the location of the pings onto Florida records of the location of road segments and their attributes, such as speed limit, we can infer whether and the extent to which a driver exceeds the speed limit. Following the relationship between speeding and fines in Florida, we group speeding into the following discrete categories: 0 to 9, 10 to 14, 15 to 19, 20 to 29, and 30+ miles per hour (mph) over the speed limit.

Citations, fines, and accidents

In partnership with Lyft, we obtained access to the pings of the population of Lyft drivers operating in Florida between August 2017 and August 2020. We link each ping to Florida's government records of speeding violations and accidents with information on timing and driver's license number. We infer when an accident occurred or when a driver was stopped by police for a speeding citation by searching for the largest reduction in driving speed within 3 min of the approximate time in the Florida records.

Race or ethnicity

To infer driver race or ethnicity, we fit a model that relates the self-reported race or ethnicity

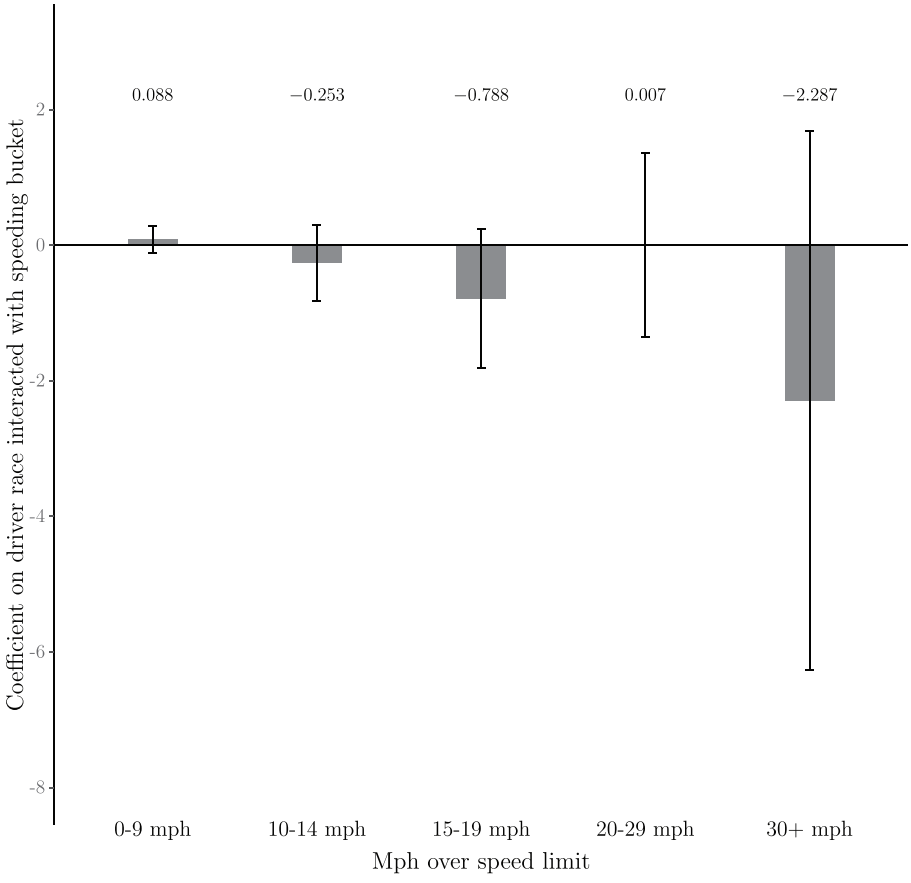

Fig. 2. Effect of driver race on relationship between driving speed and accidents. Difference between white and minority driver accident rates by level of speeding. The estimated differences control for the covariates in the FE model. Brackets indicate the 95% confidence intervals, which are constructed with standard errors clustered by driver.

of the 45.7% of drivers who are registered voters in Florida to a picture that each driver submits when they apply to drive on Lyft's platform. This fitted model is then used to infer the race or ethnicity from the picture submitted by the 54.3% of drivers who are not registered voters. Our main analysis assigns drivers to one of two racial and ethnic categories: white or minority, where minority includes Asian and Pacific Islander, Black, or Hispanic (*31*). See the supplementary materials, sections 1.1 to 1.6, for construction of analysis sample.

To determine whether there is evidence of racial profiling, we would ideally compare white and minority drivers while controlling for all other factors that are related to driver race and affect speeding citations and fines. Under the first strategy, we select the controls that are likely relevant. We refer to this strategy as the "FE model" because we primarily select fixed effects (FEs) to control for the nonrace factors that could influence the receipt of citations and fines. Second, a machine learning algorithm selects the factors to control. We refer to this strategy as the "DML model" because it relies on a technique called double machine learning (DML) (*32*). See the supplementary materials for variables in the FE model (section 2.1) and for the DML model's selection of controls (section 2.2).

Taste-based versus statistical discrimination

To understand whether the racial profiling of minorities is attributable to statistical or taste-based discrimination by police, we adopt the following strategy. We test for statistical discrimination by examining whether, compared with white drivers, speeding citations for minority drivers are more predictive of other traffic violations. If we find evidence that minority status is predictive, then we would attribute racial profiling to statistical discrimination because it would suggest that police profile to deter traffic violations that happen to be more prevalent amongst minority drivers versus white motorists. Otherwise, we would attribute the evidence to taste-based discrimination.

We consider two types of traffic violations with which a citation for speeding is likely related: reckless driving (using accidents as a proxy) and reoffenses (of speeding). With accidents, we test for whether minority status is predictive by regressing whether an accident occurs on minority status interacted with speeding and the controls used in the FE model described above. With reoffenses, we test for whether minority status is predictive by regressing the portion of time in a week spent driving more than 10 mph over the speed limit on the interaction between minority status and weeks since a citation for speeding, driver FEs, and weeks since a citation FEs (*33*). If both tests find that minority status is a statistically significant predictor, then we would attribute an effect of minority race or ethnicity to statistical discrimination by police; by contrast, if both tests find no such statistical significance, then we would attribute an effect of minority status to taste-based discrimination.

Results

Our empirical analysis of racial profiling controls for location, time, features of the road, car, driver age and gender, the phase of a trip that the driver was completing (i.e., waiting to be paired with a passenger, picking up a passenger, or dropping off a passenger), and the extent to which the driver was exceeding the speed limit. See the supplementary materials, sections 2.1 to 2.2, for details.

RQ1: Race, citations, and fines

We find that compared with white drivers, minority drivers are significantly more likely to be cited for speeding, and they pay significantly more in fines. Notably, this comparison controls for whether and the extent to which a driver was speeding, where they were driving, features of the car being driven, and other potentially relevant covariates. Figure 1 presents these findings by plotting the rates of citations and costs of fines for white and minority drivers as well as the estimated effect of driver race on citations and fines for speeding. Across the two outcomes and models in the top row of Fig. 1, we see that the average rate of citations and cost of fines is low. For every 10,000 hours of driving, which is about a half decade of working 40 hours per week, drivers have an 11 to 15% chance of receiving a citation for speeding, and the average cost of these citations is $15 to $20. Yet, despite how rare speeding citations are, differences between white and minority drivers appear across both outcomes and both models.

The bottom row of Fig. 1 plots the average effect of minority status on citation rates and fines. Starting from the left, the FE and DML models, respectively, find that for every 10,000 hours of driving, minority drivers are 3.6 and 2.7 percentage points more likely to be cited for speeding compared with white drivers.

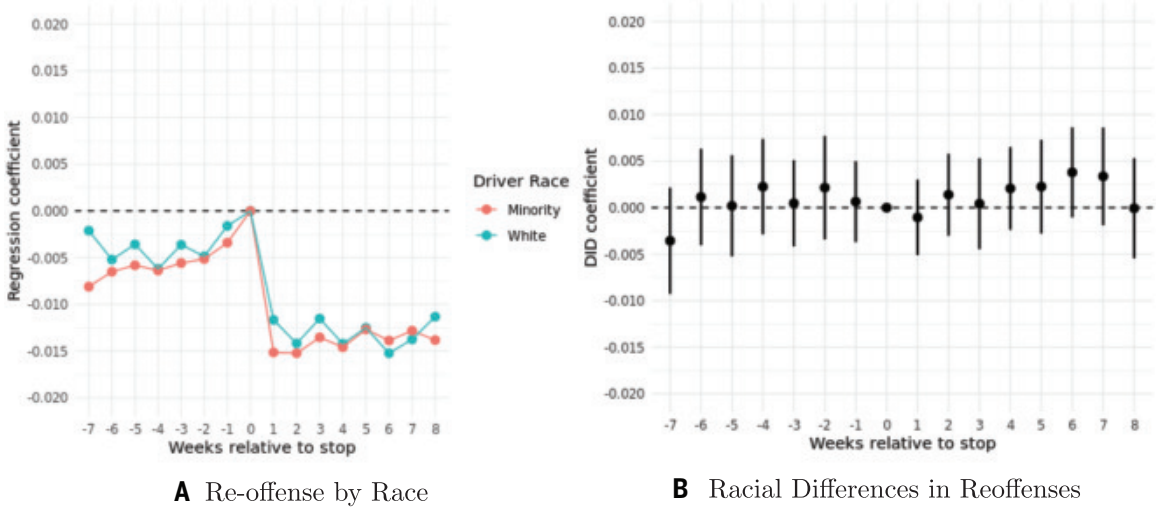

A Re-offense by Race

B Racial Differences in Reoffenses

Fig. 3. Effect of speeding citations on reoffending. (**A**) The proportion of driving time over the speed limit in the weeks before and after a white and minority driver is cited for a speeding ticket. Estimates are relative to time spent speeding during the week that a speeding ticket was received and control for driver FEs. (**B**) The estimated differences and 95% confidence intervals constructed with robust standard errors clustered by driver.

Moving to the right, we report a similar relationship between minority status and fines, with the FE and DML models, respectively, finding that the average effect of minority status on speeding fines per 10,000 hours of driving is $5.20 and $3.58. Relative to how rare citations and fines are, these effects are quite large. In percentage terms, minority drivers are 24 to 33% more likely to be cited for speeding and pay 23 to 34% more in fines. Furthermore, the four estimated effects shown in the bottom two panels of Fig. 1 are statistically significantly different from zero at the conventional level of 5%. The supplementary materials, sections 3.1 to 3.2, present these results in table form. The results from a series of robustness and heterogeneity analyses can be found in the supplementary materials, sections 4.1 to 4.6; these include the effect of minority status at discrete levels of speeding and the effect of each race or ethnicity.

RQ2: Mechanisms—taste-based versus statistical discrimination

Having established that minority drivers are more likely to be cited and fined for speeding compared with white drivers, we next consider mechanisms (i.e., taste-based versus statistical discrimination). Our analysis finds that, contrary to the statistical discrimination mechanism, police do not racially profile in their enforcement of speeding tickets to deter reckless driving (accidents) or reoffending speed limits. We find that white and minority drivers have statistically indistinguishable accident rates and rates of reoffending, which suggests that statistical discrimination does not underlie the evidence of racial profiling. As a result, we attribute the effect of minority status on citations and fines to taste-based discrimination by police officers. Figure 2 presents the results of an analysis that considers whether police officers are more likely to penalize minority drivers for speeding because their speeding is more predictive of accidents than for white drivers. The effect of minority status on accident rates is reported for several discrete levels of driving speed exceeding the speed limit, with brackets around each estimated effect illustrating the 95% confidence interval. When traveling 0 to 9 mph over the speed limit, minority drivers are marginally more likely to be cited for an accident than white drivers; at nearly every higher level of speeding, the direction reverses, and white drivers are more likely to be cited for an accident. Furthermore, none of these estimates are statistically distinguishable from zero at the conventional level of 5% significance.

Figure 3 presents the results of a complementary analysis that considers whether police officers are more likely to penalize minority drivers because their speeding is more predictive of reoffending. This figure shows that being a minority does not predict speeding around a citation because the difference has an ambiguous sign in the weeks before and after a speeding ticket is received. Furthermore, the differences are statistically indistinguishable from zero at the conventional level of 5% significance. Regression results can be found in the supplementary materials, sections 3.3 to 3.4.

Discussion

Using data on active Lyft drivers in Florida, we estimate the effect of racial profiling on citations and fines for speeding. Across two empirical strategies that control for speeding, location, and a battery of other covariates, we find that racial or ethnic minority drivers are significantly more likely to be cited for speeding and to pay significantly more money in fines. Our complementary analyses of reoffense and accident rates fail to find evidence that these effects can be attributed to differences in speeding behavior or traffic violations across white versus minority drivers (i.e., statistical discrimination); therefore, our findings suggest that police racial profiling of drivers is due to police having animus or prejudice against minority drivers (i.e., taste-based discrimination).

These results suggest concrete prescriptions for policy-makers and business leaders interested in mitigating racial profiling. For policymakers, our findings suggest that compared with enforcement by police officers, appropriately located automated technologies, such as speeding cameras, could help reduce selective enforcement of traffic violations. For business leaders, our findings indicate that race-blind approaches to disincentivizing risky behavior may not be so blind. For example, car insurance rates typically increase when drivers are cited for speeding (*34*), but our findings indicate that such citations are not blind to driver race. Accounting for race in the relationship between citations and insurance rates could help diminish the effect of racial profiling.

More generally, we present a methodological advance. We view our analysis as a proof of concept for an approach to measuring the full extent of racial profiling's effects. A basic concern with prior research is that it can only evaluate racial profiling after an encounter with police has begun; however, failing to control for the previous events that led to these encounters (e.g., speeding) can bias evaluations for or against finding evidence of racial profiling. Our analysis demonstrates that these events can be controlled in the context of enforcement of speed limits. With sufficiently large

datasets of motorists or pedestrians, it is likely possible to extend our approach to the analysis of outcomes that follow traffic and pedestrian stops, such as use of force, detainment, and incarceration. Although citations for speeding are too rare in our data to investigate outcomes that follow, progress would likely be possible with larger samples of HFL data. A similar analysis of racial profiling in the setting of stop-and-frisk would likely be possible with HFL data that could link pedestrians to their encounters with police.

We also conjecture that, with a more representative sample of HFL data, applications of our approach would be superior to existing alternatives. The "veil of darkness" test (*12*, *18*), which compares the racial composition of citations before and after the sun sets, is useful for determining whether there is more racial profiling during evening hours but cannot address profiling at other times of the day. Similarly, a more recent alternative compares the racial composition of citations issued by police with those issued by automated cameras (*29*, *35*); however, this approach is also limited because it only evaluates racial profiling in the locations where cameras are installed.

Limitations

This article has several important limitations. First, we study a very specific sample of motorists that is almost certainly not representative of drivers in Florida or the US. For example, to drive on Lyft's platform, motorists must pass a background check that excludes applicants convicted of violent offenses, sexual offenses, and driving under the influence of drugs or alcohol. Lyft drivers are incentivized to avoid traffic violations, and these incentives appear to work. Compared with the general population of motorists, our sample is less prone to speed, especially more than 10 mph over the limit (*26*). As a result, our analysis examines only 1423 citations for speeding, which limited the scope of analyses that we could conduct. With more citations, researchers could build on our analyses to learn more about the nature of the taste-based discrimination that we find underlies racial profiling. Of particular interest would be analyses that precisely estimate the effect of driver race or ethnicity on speeding citations as a function of ambient light (e.g., daytime versus evening), driving in overpoliced communities of color versus predominantly white neighborhoods, and motor vehicle characteristics.

Second, our sample of Lyft drivers was observed in Florida during 2017 to 2020. In terms of racial and ethnic demographics, Florida is similar to the rest of the country (*36*) but is more politically conservative, and Florida's police are less likely to search a car during a stop; those searches largely target Black drivers (*12*). Although we only studied a specific time frame, the supplementary materials show that omitting data after COVID-19 lockdowns and protests over George Floyd's killing did not affect results.

Third, we still rely on some administrative data from law enforcement that may mask important forms of racial profiling. Most important is the possibility that police officers use civilian race as a pretext to stop civilians and do not document these stops in their records. However, we conjecture that progress on unrecorded stops would require combining data such as ours with data reported by drivers or HFL data on police officers (*27*). A related limitation of our HFL data is that they are proprietary and can only be accessed with permission from Lyft.

REFERENCES AND NOTES

1. J. Knowles, N. Persico, P. Todd, *J. Polit. Econ.* **109**, 203–229 (2001).
2. S. Anwar, H. Fang, *Am. Econ. Rev.* **96**, 127–151 (2006).
3. A. Gelman, J. Fagan, A. Kiss, *J. Am. Stat. Assoc.* **102**, 813–823 (2007).
4. K. Antonovics, B. Knight, *Rev. Econ. Stat.* **91**, 163–177 (2009).
5. M. D. Makowsky, T. Stratmann, *Am. Econ. Rev.* **99**, 509–527 (2009).
6. D. Abrams, M. Bertrand, S. Mullainathan, *J. Legal Stud.* **41**, 347–383 (2012).
7. N. Anbarci, J. Lee, *Int. Rev. Law Econ.* **38**, 11–24 (2014).
8. M. D. Makowsky, T. Stratmann, *J. Law Econ.* **54**, 863–888 (2011).
9. A. Gupta, C. Hansman, E. Frenchman, *J. Legal Stud.* **45**, 471–505 (2016).
10. D. Arnold, W. Dobbie, C. S. Yang, *Q. J. Econ.* **133**, 1885–1932 (2018).
11. R. Fryer Jr., *J. Polit. Econ.* **127**, 1210–1261 (2019).
12. E. Pierson *et al*., *Nat. Hum. Behav.* **4**, 736–745 (2020).
13. F. Goncalves, S. Mello, *Am. Econ. Rev.* **111**, 1406–1441 (2021).
14. S. Anwar, P. Bayer, R. Hjalmarsson, M. L. Mizel, "Racial Disparities in Misdemeanor Speeding Convictions" (RAND Corporation Report, 2021).
15. M. Hoekstra, C. Sloan, *Am. Econ. Rev.* **112**, 827–860 (2022).
16. D. Arnold, W. Dobbie, P. Hull, *Am. Econ. Rev.* **112**, 2992–3038 (2022).
17. I. Ayres, J. Waldfogel, *Stanford Law Rev.* **46**, 987–1047 (1994).
18. J. Grogger, G. Ridgeway, *J. Am. Stat. Assoc.* **101**, 878–887 (2006).
19. C. Simoiu, S. Corbett-Davies, S. Goel, *Ann. Appl. Stat.* **11**, 1193–1216 (2017).
20. S. N. Durlauf, J. J. Heckman, *J. Polit. Econ.* **128**, 3998–4002 (2020).
21. I. Canay, M. Mogstad, J. Mountjoy, *Rev. Econ. Stud.* **91**, 2135–2167 (2024).
22. D. Knox, W. Lowe, J. Mummolo, *Am. Polit. Sci. Rev.* **114**, 619–637 (2020).
23. G. S. Becker, *The Economics of Discrimination* (Univ. Chicago Press, 1957).
24. K. J. Arrow, in *Discrimination in Labor Markets*, O. Ashenfelter, A. Rees, Eds. (Princeton Univ. Press, 1972).
25. E. S. Phelps, *Am. Econ. Rev.* **62**, 659–661 (1972).
26. W. Cai *et al*., *PNAS Nexus* **1**, pgac144 (2022).
27. M. K. Chen, K. L. Christensen, E. John, E. Owens, Y. Zhuo, *Rev. Econ. Stat.* **2023**, 1–29 (2023).
28. R. Tillyer, R. Engel, *J. Crim. Justice* **40**, 285–295 (2012).
29. W. Xu *et al*., *Proc. Natl. Acad. Sci. U.S.A.* **121**, e2402547121 (2024).
30. Earlier research with HFL data did not link the data to individual-level data on race or ethnicity and speeding violations (*26*, *29*).
31. Registration forms in Florida have voters indicate that whether they are White, Not Hispanic, or Hispanic, so White Hispanics are classified as Hispanic in our data.
32. V. Chernozhukov *et al*., *Econom. J.* **21**, C1–C68 (2018).
33. Our reoffenses test depends on whether minority status is predictive of speeding both before and after a citation because, in isolation, indistinguishable postcitation differences in speeding could be a consequence of racial profiling more powerfully deterring the speeding of minority drivers. However, if these differences are indistinguishable both before and after a citation, then it is not straightforward to reconcile with a statistically motivated deterrence policing strategy.
34. A. Carrns, "What That Speeding Ticket May Really Cost You," *New York Times* (2012); https://archive.nytimes.com/bucks.blogs.nytimes.com/2012/05/17/what-that-speeding-ticket-may-really-cost-you/.
35. S. Quintanar, *J. Appl. Econ.* **20**, 1–28 (2017).
36. A. Van Dam, "What state best represents America?" *Washington Post* (2024); https://www.washingtonpost.com/business/2024/05/10/most-representative-most-unique-places-america/.
37. P. Aggarwal *et al*., High-frequency location data show that race affects citations and fines, Dryad (2025).

ACKNOWLEDGMENTS

B. Ba, R. Fryer, J. Grogger, and M. Mogstad provided helpful comments and suggestions. A. Adams, J. Alferness, K. Ashorn, S. Carpenter, N. Chamandy, P. Day, B. Emeott, K. Falcon, H. Foster, L. Green, T. Hayes, S. Kapur, C. Martin, B. McClure, S. Reddick-Smith, B. Stevenson, A. Wang, and J. Zimmer provided invaluable assistance in advancing this study. **Funding:** The authors received no funding in support of this project. **Author contributions:** Conceptualization: A.B., J.H., J.A.L., T.Y.; Investigation: J.A.L., I.M., T.Y.; Methodology: A.B., P.A., A.G., J.H., J.A.L., G.S., T.Y.; Project administration: A.B., J.H., I.M.; Supervision: J.A.L., I.M.; Visualization: P.A., T.Y.; Writing – original draft: A.B., J.H., T.Y.; Writing – review & editing: A.B., J.A.L., T.Y. **Competing interests:** This study was conducted while P.A., A.G., J.A.L., I.M., G.S., and T.Y. were employed by Lyft. None are currently employed by Lyft. The authors declare no other competing interests. **Data and materials availability:** All code and nonproprietary data used to conduct our analysis are stored on Dryad (*37*). The nonproprietary data are stored on Dryad in a redacted form that removes personally identifying information. The proprietary data that are not stored on Dryad are the HFL data from Lyft (i.e., the smartphone pings from active Lyft drivers) and the voter data, which were obtained from a third-party vendor. A full replication of the merges that created the dataset used to conduct our analysis is not guaranteed because Lyft does not store its HFL data indefinitely. The dataset used to conduct our analysis remains on Lyft's servers, and we have requested that Lyft retain the data for at least 5 years. Researchers seeking replication with this dataset should submit an emailed request to bemeott@lyft.com and kfalcon@lyft.com, clearly stating the analyses that they would like to reproduce, the names and organizational affiliations of the researchers, and a proposed data use agreement. Lyft will review and consider all such requests but may not necessarily grant access. If the aforementioned email addresses become disabled, then contact A.B., the corresponding author.

SUPPLEMENTARY MATERIALS

science.org/doi/10.1126/science.adp5357
Supplementary Text
Figs. S1 to S5
Tables S1 to S15
References (*38*, *39*)
MDAR Reproducibility Checklist

Submitted 29 March 2024; accepted 24 February 2025
10.1126/science.adp5357

PLANT PATHOLOGY

A wheat tandem kinase activates an NLR to trigger immunity

Renjie Chen[1]†, Jian Chen[2]†, Oliver R. Powell[1]†, Megan A. Outram[2]†, Taj Arndell[2], Karthick Gajendiran[1], Yan L. Wang[1], Jibril Lubega[3], Yang Xu[4], Michael A. Ayliffe[2], Cheryl Blundell[2], Melania Figueroa[2], Jana Sperschneider[2], Thomas Vanhercke[2], Kostya Kanyuka[3], Dingzhong Tang[4], Guitao Zhong[4], Catherine Gardener[1], Guotai Yu[1], Spyridon Gourdoupis[5], Łukasz Jaremko[5], Oadi Matny[6], Brian J. Steffenson[6], Willem H. P. Boshoff[7], Wilku B. Meyer[7], Stefan T. Arold[5], Peter N. Dodds[2]*, Brande B. H. Wulff[1]*

The role of nucleotide-binding leucine-rich repeat (NLR) receptors in plant immunity is well studied, but the function of a class of tandem kinases (TKs) that confer disease resistance in wheat and barley remains unclear. In this study, we show that the *SR62* locus is a digenic module encoding the $Sr62^{TK}$ TK and an NLR ($Sr62^{NLR}$), and we identify the corresponding AvrSr62 effector. AvrSr62 binds to the N-terminal kinase 1 of $Sr62^{TK}$, triggering displacement of kinase 2, which activates $Sr62^{NLR}$. Modeling and mutation analysis indicated that this is mediated by overlapping binding sites (i) on kinase 1 for binding AvrSr62 and kinase 2 and (ii) on kinase 2 for binding kinase 1 and $Sr62^{NLR}$. Understanding this two-component resistance complex may help engineering and breeding plants for durable resistance.

Plant diseases cause about 20 to 30% losses in crop production annually (*1*). Limiting such losses without recourse to chemicals relies on breeding for disease resistance traits. Most known plant resistance (*R*) genes encode nucleotide-binding leucine-rich repeat (NLR) immune receptor proteins, which recognize pathogen effector proteins that are delivered into host cells during infection (*2*, *3*). Such immune-recognized effectors are known as avirulence (Avr) proteins because their recognition triggers immune responses that prevent disease. Many NLRs containing an N-terminal coiled coil (CC) domain directly trigger immune responses upon Avr detection by forming an oligomeric resistosome that acts as a Ca^{2+} channel (*4*–*6*). Avr recognition by NLRs can occur either through direct interaction with the Avr (*6*, *7*) or indirectly through detection of other host proteins modified by effectors, such as the decoy kinases PBL2 and Pto that are "guarded" by the NLRs ZAR1 and Prf, respectively (*5*, *8*). Other NLRs function in pairs, usually encoded by adjacent genes at a digenic resistance locus, wherein one NLR acts as a "sensor" to detect an Avr protein, while the second acts as a "helper" or "executor" NLR to trigger downstream responses (*9*, *10*). In some species, complex networks of sensor and helper NLRs have evolved to confer resistance to a variety of pathogens (*11*). Another class of NLRs contains an N-terminal TIR domain that, upon activation, catalyzes the production of small molecules detected by EDS1 family protein complexes to activate downstream helper CC-NLRs (*2*, *12*).

In *Triticeae* species, 18 of the 85 (20%) cloned wheat and barley *R* genes were found to encode a different type of receptor based on kinase fusion proteins (*13*, *14*). Most of these proteins consist of two kinase domains and are known as tandem kinase (TK) proteins, although a few, such as Sr43 (*15*), contain a single kinase domain fused to other domains. It is not known how TK proteins confer pathogen recognition or induce immune responses. Corresponding Avr proteins are unknown, except for RWT4, which recognizes PWT4 from *Pyricularia oryzae* to confer wheat blast resistance (*16*, *17*). *Sr62* is derived from the wheat relative *Aegilops sharonensis* and confers resistance to stem rust disease caused by the fungus *Puccinia graminis* f. sp. *tritici* (*Pgt*) (*18*), including against highly virulent strains, such as Ug99, that have caused significant losses worldwide (*19*). Mutational analysis showed that a TK gene at the *SR62* locus ($Sr62^{TK}$) was required for stem rust resistance in the Zahir-1644 introgression line, and transgenic expression of $Sr62^{TK}$ was sufficient to confer resistance in the susceptible wheat cultivar Fielder (*18*). In this study, we show that the $Sr62^{TK}$ protein directly detects a corresponding AvrSr62 protein from *Pgt* and activates a CC-NLR, also encoded at the *SR62* locus.

[1]Plant Science Program, Biological and Environmental Science and Engineering Division (BESE), King Abdullah University of Science and Technology (KAUST), Thuwal, Saudi Arabia. [2]CSIRO Agriculture and Food, Canberra, Australian Capital Territory, Australia. [3]National Institute of Agricultural Botany (NIAB), 93 Lawrence Weaver Road, Cambridge, UK. [4]State Key Laboratory of Agricultural and Forestry Biosecurity, Key Laboratory of Ministry of Education for Genetics, Breeding and Multiple Utilization of Crops, Plant Immunity Center, Fujian Agriculture and Forestry University, Fuzhou, China. [5]Bioscience Program, Smart Health Initiative, BESE, KAUST, Thuwal, Saudi Arabia. [6]Department of Plant Pathology, University of Minnesota, St. Paul, MN, USA. [7]Department of Plant Sciences, University of the Free State, Bloemfontein, South Africa.
*Corresponding author. Email: peter.dodds@csiro.au (P.N.D.); brande.wulff@kaust.edu.sa (B.B.H.W.)
†These authors contributed equally to this work.

$Sr62^{TK}$ recognizes AvrSr62 protein variants encoded at a complex locus in *Pgt*

To identify corresponding *Avr* genes, we used $Sr62^{TK}$ to screen a *Pgt* effector library (*20*) by coexpression in wheat protoplasts. Four effector constructs (clone nos. 0469, 0472, 0483, and 0490) showed significantly reduced expression in the presence of $Sr62^{TK}$ relative to an empty vector control (fig. S1), suggesting immune recognition-induced protoplast cell death. These four *Avr* gene candidates belong to a gene family of seven members, designated *AvrSr62-1* to *AvrSr62-7*, that are encoded at a complex locus on chromosome group 5 of *Pgt* strain Pgt21-0. Four of these reside in a ~70–(kilo–base pair) kbp region on chromosome 5A with the other three spanning ~35 kbp on chromosome 5B (Fig. 1A and fig. S2A). All seven genes were present in the effector library, but three of them, *AvrSr62-2*, *AvrSr62-3*, and *AvrSr62-6*, were not detected in the screen. AlphaFold-predicted structures of AvrSr62-1 to AvrSr62-7 proteins are highly similar (fig. S3) but show no similarity to other protein structures in public databases. EffectorP3.0 (*21*) predicted the AvrSr62 proteins as cytoplasmic effectors, and RNA sequencing (RNA-seq) data (*22*) indicated preferential expression in haustoria and during in planta infection but not in germinated spores (fig. S2B), similar to other characterized *Avr* genes in *Pgt* (*23*). *AvrSr62-1* to *AvrSr62-7* genes were tested individually for recognition by $Sr62^{TK}$ in wheat protoplasts. Expression of $Sr62^{TK}$ alone resulted in reduced yellow fluorescent protein (YFP) accumulation, indicating some autoactive cell-death induction (fig. S4). Nevertheless, coexpression of the four positively identified *AvrSr62* genes resulted in enhanced $Sr62^{TK}$-dependent cell death, whereas *AvrSr62-3* induced an intermediate response and *AvrSr62-2*, and *AvrSr62-6* gave no response (Fig. 1B). Recombinant barley stripe mosaic virus (BSMV) expressing *AvrSr62-5* or *AvrSr62-7* was unable to infect Zahir-1664 containing *Sr62*, whereas BSMV expressing *AvrSr62-1* or *AvrSr62-4* remained infective (fig. S5). All BSMV strains could infect a susceptible mutant derived from Zahir-1644. Yeast two-hybrid assays showed interaction between $Sr62^{TK}$ and the four recognized AvrSr62 proteins but not the nonrecognized variants (Fig. 1C). AvrSr62-5 and AvrSr62-7 showed stronger interaction than AvrSr62-1 and AvrSr62-4, consistent with the results from the viral infection assays (fig. S5). In planta two-hybrid assays (*24*) also supported these interactions (fig. S6, A and B), whereas coimmunoprecipitation (co-IP) assays detected an interaction between $Sr62^{TK}$ and AvrSr62-5 only (fig. S6C). These data confirmed specific recognition of AvrSr62 proteins by $Sr62^{TK}$, suggesting that it

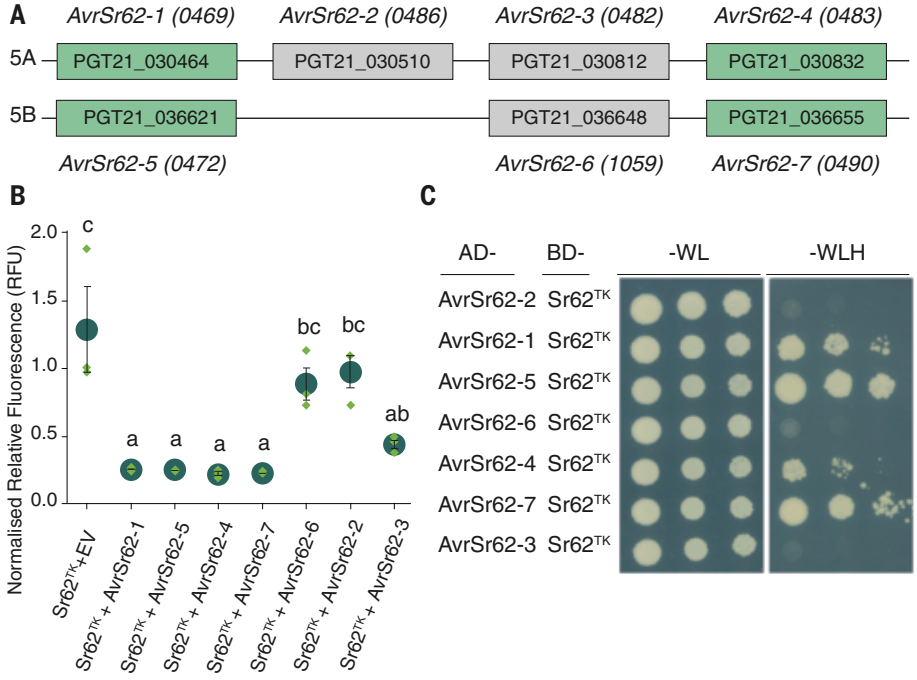

Fig. 1. Identification of candidate avirulence effectors for Sr62^{TK} using a high-throughput effector library screening platform in wheat Fielder protoplasts. (**A**) Genomic arrangement of *AvrSr62* genes in the Pgt21-0 genome assembly (*22*). Genes shown in green are recognized by *Sr62^{TK}*, whereas those shown in gray are not recognized. (**B**) Protoplasts from wheat cv. Fielder were cotransformed with YFP and combinations of individual *AvrSr62* genes, *Sr62^{TK}* and an empty vector (EV = pTA22) as indicated. YFP fluorescence (*y* axis) was measured after 24 hours and normalized to Sr62^{TK} alone. Results represent the means (dark green circles) of three biological replicates (green diamonds), with error bars indicating the standard error. Samples marked by identical letters in the plots do not differ significantly [$P < 0.05$; analysis of variance (ANOVA), Tukey post hoc test]. RFU, relative fluorescence units. (**C**) Growth of yeast strains cotransformed with AvrSr62 variants fused to the GAL4 activation domain (AD) and Sr62^{TK} fused to GAL4 binding domain (BD). Yeast suspensions at an OD_{600} = 1.0 and two serial dilutions of 1/10 and 1/100 were spotted on synthetic medium lacking tryptophan and leucine (−WL, growth control) and on synthetic medium lacking tryptophan, leucine, and histidine (−WLH, interaction selection). Pictures were taken after 5 days of growth. Immunoblot of AvrSr62 variants shown in fig. S6D.

acts as the primary receptor for these effectors in wheat. However, coexpression of *Sr62^{TK}* and *AvrSr62* variants in *Nicotiana benthamiana* leaves or oat (*Avena sativa*) protoplasts did not cause cell death (fig. S7). This suggests that the Sr62^{TK}-induced immune response in wheat may require other proteins that are not conserved in these more distantly related species.

The *SR62* locus comprises a digenic module encoding a TK and an NLR

To identify other wheat genes involved in *Sr62* resistance, we reexamined seven putative ethyl methanesulfonate (EMS)–induced susceptible mutants derived from the wheat *Aegilops sharonensis* introgression line Zahir-1644 that appeared to maintain wild-type *Sr62^{TK}* sequences based on RNA-seq analysis (*18*). We reevaluated the phenotypes and sequences of these mutants aided by additional whole genome shotgun sequencing and a high-quality Zahir-1644 genome assembly (Contig N50, 21 Mb) (tables S1 and S2). Four partially or completely susceptible mutants were confirmed to encode intact *Sr62^{TK}* open reading frames (mutants 119d, 267d, 200h, and 1298e; Fig. 2A, tables S3 and S4, and data S1). All four mutants contained missense (119d and 1298e) or nonsense (267d and 200h) mutations in an NLR-encoding gene 20.4 kbp distal to *Sr62^{TK}* (*18*) (Fig. 2, B and C; table S4; and data S1). This gene encodes a predicted 1040–amino acid protein with domains resembling a CC domain, two nucleotide-binding domains (NBD1 and NBD2), a helix domain (HD1), a winged helix domain (WHD), and 12 leucine-rich repeats (Fig. 2, B to D; fig. S8, A and B; and table S5). We backcrossed the four mutant lines with Zahir-1644 and genotyped susceptible and resistant BC_1F_2 plants (table S6) by bulk exome-capture sequencing and/or polymerase chain reaction and Sanger sequencing of individual plants. In all cases, we observed complete cosegregation between susceptibility and the NLR mutations (table S7 and data S1). No other genes containing mutations in three or four mutants were identified (table S8). Phylogenetic analysis of NLRs in wheat landrace "Chinese Spring" showed that *Sr62^{NLR}* belongs to a clade of NLRs each containing an additional NBD (fig. S9).

Transient expression of *AvrSr62-7* induced cell death in wild-type Zahir-1644 protoplasts but not in protoplasts of NLR-mutant Zahir-1644 lines (Fig. 2E and figs. S10, A and B, and S11). However, coexpression of the wild-type NLR gene with *AvrSr62-7* did induce cell death in protoplasts from 267d, 1298e, and 200h mutant lines (Fig. 2E and fig. S10, A and B). These experiments confirmed the requirement of this NLR for *Sr62* function. Previously, we transformed *Sr62^{TK}* into wheat cultivar (cv.) Fielder and recovered disease-resistant transgenics (*18*), suggesting that the ortholog of this NLR gene on chromosome 1D of Fielder (94.6% amino acid identity; fig. S8C) supports *Sr62^{TK}* resistance function. We confirmed this by transient complementation with the Fielder NLR in protoplasts from the 267d mutant line (Fig. 2E). Lastly, transient coexpression of Sr62^{TK}, the Fielder NLR, and recognized AvrSr62 variants resulted in cell death in *N. benthamiana* and *N. tabacum* (Fig. 2F and fig. S10, C to E). The AvrSr62-5 and AvrSr62-7 variants induced significantly stronger cell death responses than AvrSr62-1 and AvrSr62-4 (fig. S10C), consistent with the protein interaction and viral infection data (Fig. 1C and figs. S5 and S6). These results indicate that the *SR62* locus comprises a digenic module encoding a TK and a linked NLR, which we designated *Sr62^{TK}* and *Sr62^{NLR}*, respectively.

Sr62^{TK} and Sr62^{NLR} work together in AvrSr62 detection

Split luciferase complementation assays (*25*) showed that coexpression of AvrSr62-7 with Sr62^{TK} and Sr62^{NLR} fused to the N- and C-terminal domains of luciferase, respectively, induced an interaction resulting in strong luminescence (Fig. 3A and fig. S12, A and B). Coexpression of the unrecognized AvrSr62-2 did not result in luciferase activity, and AvrSr62-7 did not induce interaction between Sr62^{TK} and the unrelated NLR Sr35 (fig. S12A). Similarly, coexpression of the recognized AvrSr62-5 and AvrSr62-7 proteins led to enhanced co-IP of Sr62^{NLR} by Sr62^{TK} compared with coexpression with unrecognized AvrSr62-2 and AvrSr62-6 or control proteins (fig. S12, C and D). These results suggest that recognized AvrSr62 proteins promote an interaction between the Sr62^{TK} and Sr62^{NLR} that activates immunity.

The recognized AvrSr62 variants interacted with the N-terminal kinase 1 domain of Sr62^{TK}, but not with the C-terminal kinase 2 domain in yeast-two-hybrid (Fig. 3B), in planta two-hybrid and co-IP assays (figs. S13 and S14). No interaction was detected between AvrSr62 proteins and Sr62^{NLR} in yeast or in planta two-hybrid experiments (Fig. 3B and fig. S15). The individual kinase 1 and kinase 2 domains

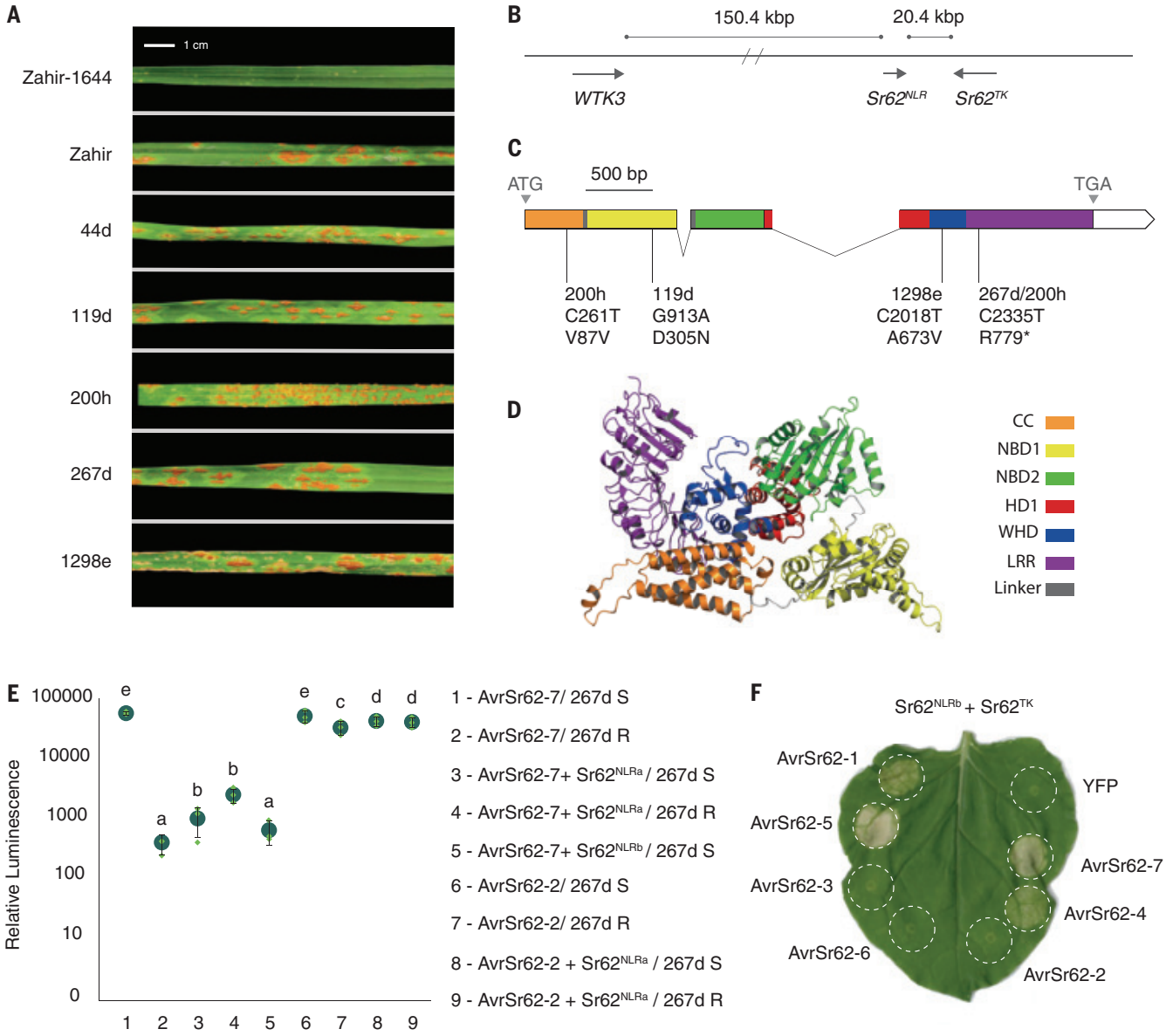

Fig. 2. Discovery of an NLR essential for the function of the *Sr62* TK. (**A**) Infection types of the wheat *Ae. sharonensis* introgresion line Zahir-1644, the recurrent parent cv. Zahir, and EMS-derived mutants inoculated with *Puccinia graminis* f. sp. *tritici* (*Pgt*) race TTKSK. Scale bar, 1 cm. (**B**) The $Sr62^{NLR}$ is flanked by the paralogous $Sr62^{TK}$ and *WTK3* (*Pm24/Rwt4* orthologs). (**C**) $Sr62^{NLR}$ gene structure with predicted nucleotide changes caused by EMS-derived loss-of-function mutations (top two lines) and corresponding amino acid changes (bottom line). Colored and white boxes represent predicted translated and untranslated exons, respectively, whereas black connecting lines represent introns. The predicted structural domains encoded by the exons are colored and labeled: CC, orange; NBD1, yellow; NBD2, green; HD1, red; WHD, blue; and leucine-rich repeat (LRR), purple. (**D**) AlphaFold-predicted structure of $Sr62^{NLR}$ colored by domains as in (C). (**E**) Protoplasts of BC1F2 lines derived from the Zahir-1644 $Sr62^{NLR}$ 267d mutant line and either homozygous susceptible (267d S) or resistant (267d R) were cotransformed with a *Luciferase* construct and either *AvrSr62-2* or *AvrSr62-7* with or without $Sr62^{NLR}$. Graph shows the mean (dark green circle) luminescence of three biological replicates (green diamonds) with the standard error indicated (black line) on a logarithmic scale. Samples marked by identical letters in the plots do not differ significantly ($P < 0.05$; ANOVA, Tukey post hoc test). $Sr62^{NLRa}$ and $Sr62^{NLRb}$ denote *Ae. sharonensis* and *T. aestivum* cv. Fielder chromosome 1D alleles, respectively. (**F**) Coexpression of $Sr62^{TK}$, $Sr62^{NLRb}$, and *AvrSr62* induces cell death in *N. benthamiana*. $Sr62^{TK}$ and $Sr62^{NLR}$ are fused to 3 × hemagglutinin tag at the C terminus. AvrSr62 effectors are fused to a YFP tag at the N terminus and immunoblot detection of protein accumulation is shown in fig. S7C. Quantification of cell death results shown in fig. S10C.

interacted with each other in co-IP and in planta two-hybrid assays (Fig. 3C and fig. S16), and full-length $Sr62^{TK}$ and the kinase 1 domain self-associated (Fig. 3D and fig. S17). Coexpression of the recognized AvrSr62-5 or AvrSr62-7 proteins suppressed the association between kinase 1 and kinase 2 fragments, whereas the unrecognized AvrSr62-2 had no effect on this interaction (Fig. 3C and fig. S16), and kinase 2 expression did not affect the kinase 1–AvrSr62 interaction (fig. S18). $Sr62^{TK}$ self-association was not affected by AvrSr62 coexpression, whereas kinase 1 self-association was enhanced in the presence of AvrSr62-5 but not AvrSr62-2 (fig. S17).

We next investigated molecular interactions between $Sr62^{TK}$ and $Sr62^{NLR}$. Coexpression of kinase 2, but not kinase 1, with

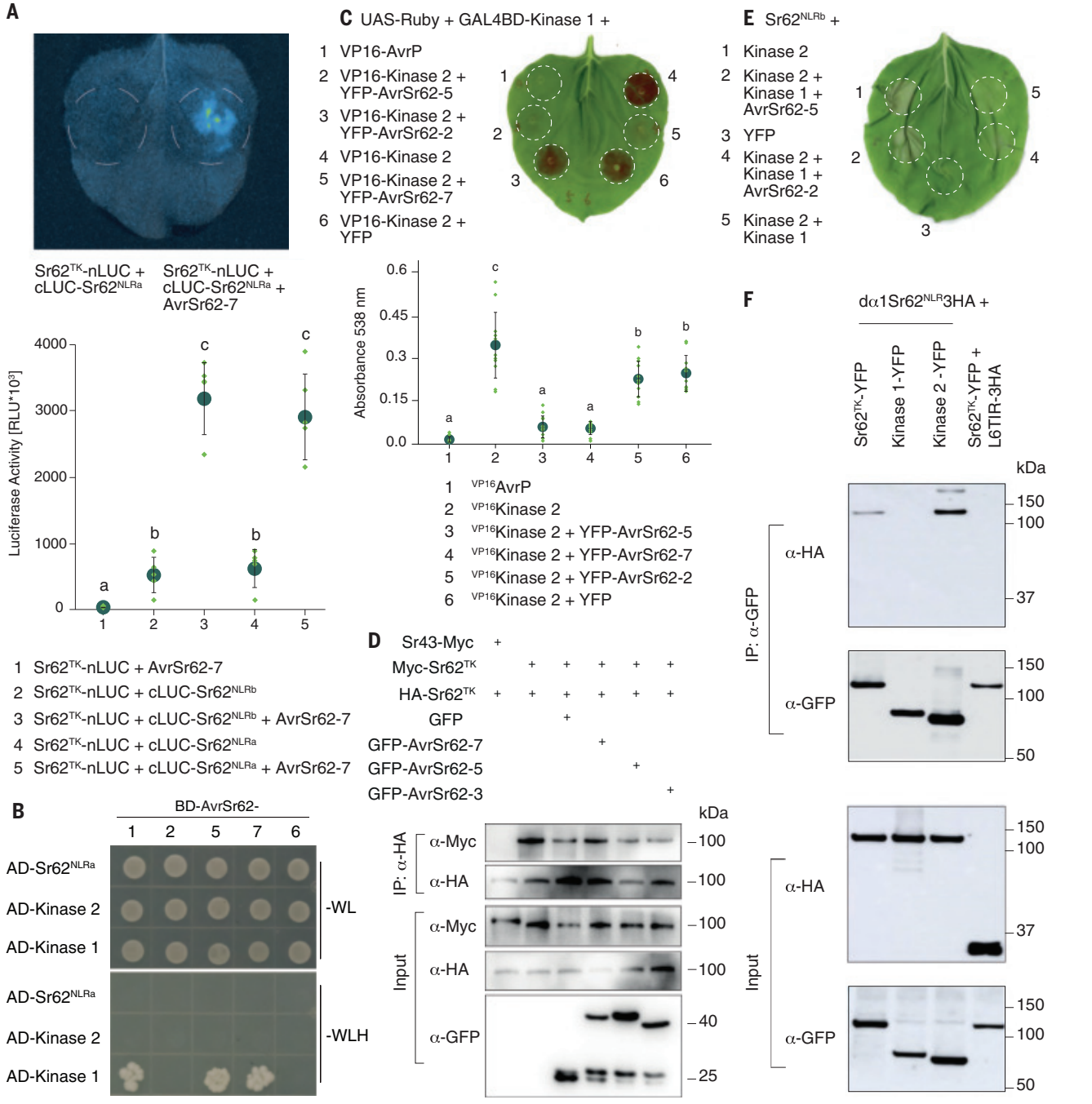

Fig. 3. Sr62^{TK} kinase 1 and kinase 2 regulate AvrSr62-induced recruitment of Sr62^{NLR} to induce cell death. (**A**) Split-luciferase complementation in *N. benthamiana* leaves coinfiltrated with Agrobacteria containing different constructs were imaged at 48 hours postinfiltration (example, top) and quantified (bottom): mean (green circle) of three biological replicates (green diamonds) with standard error shown as error bars. Identical letters indicate no significant difference ($P < 0.05$; ANOVA, Tukey post hoc test). This was repeated with more controls in fig. S12. nLUC, N-terminal luciferase; cLUC, C-terminal luciferase; RLU, relative light units. (**B**) Yeast two-hybrid assay of *Sr62^{NLR}* and *Sr62^{TK}* kinase 1 and kinase 2 fused to GAL4 AD and *AvrSr62* fused to GAL4 DNA BD. (**C**) Plant two-hybrid betalain accumulation observed in leaves expressing UAS-Ruby with kinase 1 fused to BD and kinase 2 fused to VP16 and expressed with AvrSr62 variants or VP16-AvrP (negative control). Imaged at 3 days postinfiltration (top). Extracted betalain was quantified (bottom) from ≥6 biological replicates (diamonds) with the average (circle) and standard error shown as error bars. Identical letters indicate no significant difference ($P < 0.05$; ANOVA, Tukey post hoc test). (**D**) Coimmunoprecipitation of myc-tagged *Sr62^{TK}* and *Sr43* (negative control) transiently expressed in *N. benthamiana* with HA-tagged *Sr62^{TK}*, green fluorescent protein (GFP), and GFP-tagged AvrSr62 variants. Total protein extracts immunoprecipitated with an anti-HA antibody were immunoblotted with anti-GFP, anti-Myc, or anti-HA antibodies. (**E**) Sr62^{NLR} transiently expressed in *N. benthamiana* with kinase 1, kinase 2, AvrSr62 variants, or YFP. Sr62^{NLR}, kinase 1, and kinase 2 were tagged with HA at the C terminus, whereas AvrSr62s were tagged with YFP at the N terminus. Fig. S20A shows cell death quantification. (**F**) Co-IP of YFP-tagged Sr62^{TK}, kinase 1, and kinase 2 transiently expressed in *N. benthamiana* with HA-tagged Sr62^{NLRb} lacking the first α helix (dα1Sr62^{NLR}). Total protein extracts were immunoprecipitated with anti-GFP beads (IP), followed by immunoblotting with anti-GFP and anti-HA antibodies. HA-tagged L6TIR Glu^{135}Ala (*42*) was used as negative control. Protein expression immunoblots are shown in figs. S15A [for (B)], S7D and S13D [for (C)], and S6C and S17A [for (E)].

Sr62^{NLR} induced a strong cell death response in *N. benthamiana* and *N. tabacum* (Fig. 3E and fig. S19A). This effect was dependent on an intact α1 helix in Sr62^{NLR} (fig. S19B), which is required for NLR resistosome signaling (*4*) and was not observed with unrelated NLRs, Sr33 and Sr50 (fig. S19C). However, coexpression of kinase 1 with kinase 2 and Sr62^{NLR} strongly suppressed cell death (Fig. 3E and fig. S19A), suggesting that kinase 1 negatively regulates kinase 2 activation of Sr62^{NLR}. Additional coexpression of the recognized AvrSr62-5, but not the unrecognized AvrSr62-2, restored the cell death response. This indicates that AvrSr62-5 detection by kinase 1 releases its inhibition of kinase 2 (Fig. 3E and fig. S20A). Similar results were observed in wheat protoplast assays (fig. S20, B and C), and co-IP experiments showed interactions between kinase 2 and Sr62^{NLR} (Fig. 3F). Overall, these data suggest that interaction of a recognized AvrSr62 protein with the kinase 1 domain disrupts an intramolecular interaction in Sr62^{TK}, which allows kinase 2 to interact with and activate Sr62^{NLR}.

AlphaFold (*26*) was used to predict three-dimensional protein structures and interactions (Fig. 4 and figs. S21 and S22). The predicted scores for the structures and their interactions (fig. S21 and tables S9 and S10) supported our experimentally derived model by confidently predicting kinase 1 homodimerization, kinase 1 and kinase 2 heterodimerization, and kinase 2 and Sr62^{NLR} heterodimerization. AlphaFold also predicted associations between kinase 1 and the recognized AvrSr62-1, AvrSr62-4, AvrSr62-5 and AvrSr62-7 effectors, whereas the predictions with the other family members showed weaker scores (fig. S22, E to H versus I to K, respectively, and table S10). The predicted kinase 1 structure contains all features needed for catalysis (including a P-loop and catalytic residues Lys^{86} and Glu^{83}), whereas key catalytic features were absent in kinase 2, suggesting that it is a pseudokinase (*15*).

Compared with canonical kinase folds, the last two β strands of the predicted kinase 1 N-lobe extend by eight residues each, forming an unusual β hairpin finger structure (termed β finger; residues 100 to 128). (Fig. 4, B and C). The first strand of this β finger contributes to the predicted homodimerization interface of kinase 1 (Fig. 4C and fig. S22L), whereas the second strand plays a key role in the predicted binding of the effector molecules through a mostly hydrophobic interaction (Fig. 4B and fig. S23). The position of kinase 2 in the highest-scoring AlphaFold Sr62^{TK} homodimer predictions largely overlapped with the position of the effectors (Fig. 4 and fig. S22, L and N), suggesting that recognized AvrSr62 effectors compete with kinase 2 for the same site on kinase 1. The relevance of predicted interaction

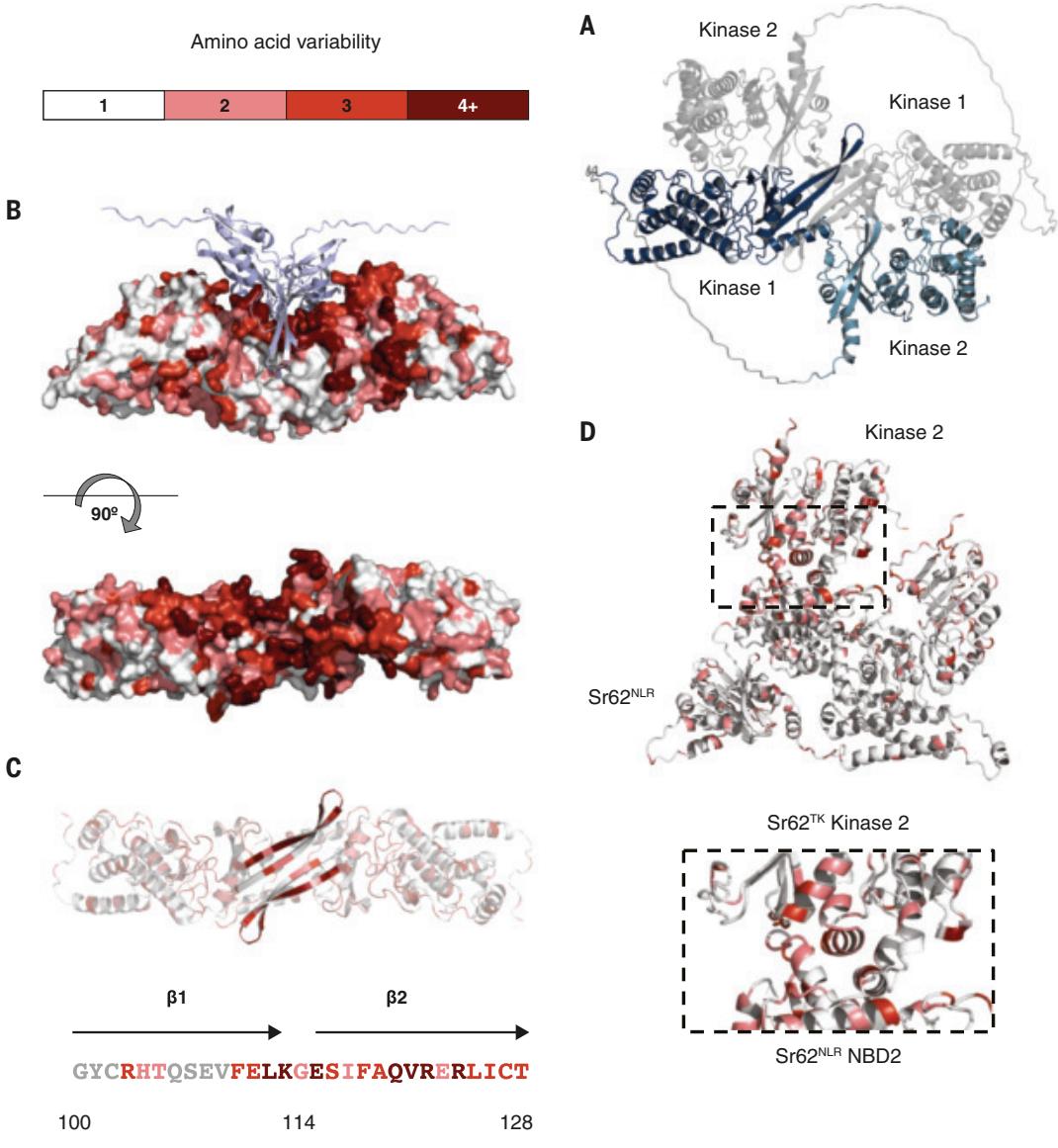

Fig. 4. Predicted structures, interactions, and amino acid variability in the "Sr62 complex." (**A**) AlphaFold-predicted structure of the Sr62^{TK} homodimer, with each monomer subunit represented in gray or blue. Sr62^{TK} dimerization is mediated by kinase 1–kinase 2 and kinase 1–kinase 1 interactions. (**B**) Interaction of two AvrSr62-5 proteins (light purple) with the Sr62^{TK} kinase 1 homodimer, colored according to amino acid variability. (**C**) The extended β finger structure mediating Sr62^{TK} homodimerization through the conserved β1 and effector interaction through the variable β2. (**D**) Interaction of Sr62^{TK} kinase 2 with Sr62^{NLR} between the NBD2 domain of the Sr62^{NLR}. The distribution of amino acid variability [(B) to (D)] is based on sequence comparison of *Triticum* and *Aegilops* homologs.

sites was supported by EMS-induced mutations of *Sr62^{TK}* and *Sr62^{NLR}* (fig. S24). For example, Glu^{10}Lys in Sr62^{TK} disrupts the putative homodimer interaction surface, whereas Thr^{627}Met perturbs the kinase 2 surface that binds to kinase 1 and Sr62^{NLR}.

We further tested these structural models by generating mutants with multiple amino acid substitutions in the predicted interaction sites (figs. S25 to S27). Sr62^{TK} mutants Phe^{6}Ala/Trp^{31}Asp (fig. S25A) and Lys^{24}Glu/Ser^{27}Tyr/Tyr^{101}Ala (fig. S25B) in the predicted kinase 1–kinase 1 interface (fig. S25C) disrupted self-association of Sr62^{TK} in co-IP and in planta two-hybrid assays (fig. S28, A and B), supporting their role in homodimerization. Sr62^{TK}–Phe^{6}Ala/Trp^{31}Asp also lost the capacity to respond to AvrSr62-5, whereas Sr62^{TK}–Lys^{24}Glu/Ser^{27}Tyr/Tyr^{101}Ala was autoactive (fig. S28C), possibly because it disturbs the position of the β finger and disrupts the kinase 2 interaction. Mutations of the predicted kinase 1–effector interaction site in Sr62^{TK} (Phe^{110}Asp/Leu^{112}Ala/Lys^{113}Ala) (fig. S27, A and B) or AvrSr62-5 (Ile^{60}Asp/Val^{67}Asp/Trp^{69}Asp) blocked or attenuated the interaction between these two proteins in yeast and in planta two-hybrid experiments and by co-IP (fig. S29 and S30). The mutated AvrSr62-5 also failed to trigger cell death when coexpressed with Sr62^{TK} and Sr62^{NLR} in *N. benthamiana* (fig. S31), whereas the Sr62^{TK}–Phe^{110}Asp/Leu^{112}Ala/Lys^{113}Ala mutant was autoactive, likely because it also disrupted the Kinase 1–Kinase 2 interaction (figs. S26, A and B, and S31), which also involves the β finger region. Mutations in other kinase 1 sites predicted to interact with kinase 2 also resulted in autoactivity of Sr62^{TK} (fig. S32). These mutations also disrupted interaction between kinase 1 and kinase 2 fragments in in planta two-hybrid assays (fig. S33) and disrupted the ability of kinase 1 to suppress kinase 2 autoactivity (fig. S34). Similarly, mutations in the corresponding regions of kinase 2 also disrupted the kinase 1–kinase 2 interactions (figs. S26C and S35). However, in the context of the full-length Sr62^{TK}, three of the four kinase 2 mutations led to loss of (Val^{422}Asp/Val^{590}Asp, Lys^{584}Ala/Lys^{592}Ala/Lys^{593}Ala) or reduced (Ser588Gly/Val589Gly/Val590Gly) function rather than autoactivity (fig. S36A). This is likely because these residues are also involved in interaction with the Sr62^{NLR}, as these mutations also led to loss of or reduced cell death induction by the kinase 2 fragment when coexpressed with Sr62^{NLR} (fig. S36B) and also disrupted interaction of the kinase 2 fragment with Sr62^{NLR} (fig. S37A). This is consistent with the AlphaFold prediction that kinase 2 uses overlapping surfaces to bind to both kinase 1 and the NBD2 and HD1 domains of Sr62^{NLR}. The exception was the Asp^{405}Ala/Gln^{493}Ala/Lys^{496}Ala mutation which had no effect on Sr62^{TK} or kinase 2 function. Co-IP experiments with different fragments of the Sr62^{NLR} supported an interaction between kinase 2 and the NBD1+NB2 region (fig. S37B). Lastly, a Leu^{430}Ala mutation in the predicted kinase 2 interaction surface of the Sr62^{NLR} NB2 region abolished its ability to induce cell death (fig. S38).

Sr62^{TK} and Sr62^{NLR} homologs showed substantial natural variation in 76 genome assemblies from *Triticum* and *Aegilops* genera, with 19 and 25 distinct variants, respectively (figs. S39 and S40 and table S11). A polymorphic hotspot in kinase 1 coincides with the putative AvrSr62 interaction surface (Fig. 4, B and C), suggesting that effector variation drives selection for variation at this site. By contrast, Kinase 2 and the NLR are largely conserved (Fig. 4D).

Discussion

The present computational and experimental analysis of the digenic wheat stem rust resistance locus *SR62* are consistent with the workings of a new multistep immune switch (fig. S41). In our model, Sr62^{TK} exists as a homodimer in which the N- and C-terminal kinases interact with each other in the inactive state. AvrSr62 effector binding to the N-terminal kinase 1 β finger ("sensor") competitively inhibits the kinase 1 ("repressor") interaction with the kinase 2 pseudokinase domain ("activator"). This allows kinase 2 to recruit and activate Sr62^{NLR} ("executor") to trigger immune signaling. In this model, the recognition step is facilitated by an overlap in the binding site on kinase 1 for binding AvrSr62 and kinase 2, and the activation step, by an overlapping binding site on kinase 2 for binding kinase 1 and Sr62^{NLR}. Given that the kinase 1 catalytic site mutation Asp^{177}Asn disrupts Sr62^{TK} function (*18*), phosphorylation events may also contribute to the activation process. *Sr62^{TK}* is located 20.4 kbp proximal to the *Sr62^{NLR}*. The allelic powdery mildew– and wheat blast–resistance genes *Pm24* and *Rwt4*, respectively, are *Sr62^{TK}* paralogues that reside 151.4 kbp distal to the *Sr62^{NLR}* (*16*, *27*) (Fig. 2B). Concomitantly, Lu *et al.* (*28*) found that Pm24 and Rwt4 signal through the same NLR as Sr62^{TK}.

Kinases play important roles in plant signaling, including in pathogen-associated molecular pattern–triggered immunity (*29*), making them prime targets of pathogen virulence effectors (*30*). In some cases, these effectors can be recognized indirectly by kinase decoys guarded by NLRs to induce immunity (*2*, *3*). Thus, wheat TKs may represent decoys that activate a guard NLR when targeted by a pathogen effector. This would be akin to the tomato Prf/Pto system, in which the *Prf* NLR-encoding gene is embedded within a locus of *Pto* kinase homologs, which act as decoys for bacterial effectors that target host kinases (*8*). However, the observation that Sr62^{TK} uses an unusual β finger extension to recognize AvrSr62 and adopts a multistep activation process involving separate recognition and activation domains (fig. S41) suggests a specialized role of this TK in effector recognition and transfer of a signal to the NLR. Sung *et al.* (*31*) also found that RWT4 binds to its ligand AvrPWT4 through a similar extended β finger. Thus, these proteins may represent a specialized sensor TK and helper NLR immune recognition system similar to paired sensor and helper NLRs (*11*, *32*), which has expanded in the Triticeae family as genetic determinants of resistance to diverse fungi. This distinction may be resolved through identification of host targets of AvrSr62 and AvrPWT4. It is not known whether other wheat TK and kinase fusion proteins require NLRs for their function or whether such NLRs are encoded by physically linked genes.

We observed extensive haplotype variation at the *SR62* locus in wheat. It is possible that not all the *Sr62^{NLR}* variants would support *Sr62^{TK}* function. In natural populations and breeding programs, digenic modules ensure coinheritance of functionally coadapted genes. By extension, when using two-component resistance determinants in multiresistance gene stacks (*33*), it will be important to ensure inclusion of both components in the stack. Although both alleles of the *AvrSr62* locus in the Pgt21-0 and Ug99 strains encoded recognized variants of AvrSr62, the AvrSr62-1 and AvrSr62-4 variants in the shared A nuclear haplotype showed weaker recognition in several assays than the AvrSr62-5 and AvrSr62-7 variants encoded by the B and C haplotypes. Thus, it is unclear whether these strains are homozygous or heterozygous for functional avirulence alleles. In conclusion, Sr62^{TK} and Pm24/Rwt4 represent a pathogen resistance mechanism characterized by the interaction of kinase fusion proteins and NLRs.

REFERENCES AND NOTES

1. S. Savary *et al.*, *Nat. Ecol. Evol.* **3**, 430–439 (2019).
2. P. N. Dodds, J. Chen, M. A. Outram, *Plant Cell* **36**, 1465–1481 (2024).
3. B. P. M. Ngou, P. Ding, J. D. G. Jones, *Plant Cell* **34**, 1447–1478 (2022).
4. J. Wang *et al.*, *Science* **364**, eaav5870 (2019).
5. J. Wang *et al.*, *Science* **364**, aav5868 (2019).
6. A. Förderer *et al.*, *Nature* **610**, 532–539 (2022).
7. J. Chen *et al.*, *Science* **358**, 1607–1610 (2017).
8. J. R. Gutierrez *et al.*, *Plant J.* **61**, 507–518 (2010).
9. S. Césari *et al.*, *EMBO J.* **33**, 1941–1959 (2014).
10. S. J. Williams *et al.*, *Science* **344**, 299–303 (2014).
11. H. Adachi, L. Derevnina, S. Kamoun, *Curr. Opin. Plant Biol.* **50**, 121–131 (2019).
12. F. Locci, J. Wang, J. E. Parker, *Curr. Opin. Plant Biol.* **74**, 102373 (2023).
13. P. M. Dracatos, J. Lu, J. Sánchez-Martín, B. B. H. Wulff, *Plant Biotechnol. J.* **21**, 1938–1951 (2023).
14. T. Fahima, G. Coaker, *Nat. Genet.* **55**, 908–909 (2023).
15. G. Yu *et al.*, *Nat. Genet.* **55**, 921–926 (2023).
16. S. Arora *et al.*, *Nat. Plants* **9**, 385–392 (2023).
17. Y. Inoue *et al.*, *Science* **357**, 80–83 (2017).
18. G. Yu *et al.*, *Nat. Commun.* **13**, 1607 (2022).
19. R. P. Singh *et al.*, *Phytopathology* **105**, 872–884 (2015).
20. T. Arndell *et al.*, *Nat. Plants* **10**, 572–580 (2024).
21. J. Sperschneider, P. N. Dodds, *Mol. Plant Microbe Interact.* **35**, 146–156 (2022).

22. F. Li *et al*., *Nat. Commun.* **10**, 5068 (2019).
23. N. M. Upadhyaya *et al*., *Nat. Plants* **7**, 1220–1228 (2021).
24. J. Chen *et al*., *Plant J.* **114**, 1209–1226 (2023).
25. Z. Zhou, G. Bi, J.-M. Zhou, *Curr. Protoc. Plant Biol.* **3**, 42–50 (2018).
26. J. Jumper *et al*., *Nature* **596**, 583–589 (2021).
27. P. Lu *et al*., *Nat. Commun.* **11**, 680 (2020).
28. P. Lu *et al*., *Science* **387**, eadp5469 (2025).
29. X. Liang, J.-M. Zhou, *Annu. Rev. Plant Biol.* **69**, 267–299 (2018).
30. M. Khan, D. Seto, R. Subramaniam, D. Desveaux, *Plant J.* **93**, 651–663 (2018).
31. Y.-C. Sung *et al*., bioRxiv, 2024.2004.2030.591956 (2024).
32. S. Cesari, M. Bernoux, P. Moncuquet, T. Kroj, P. N. Dodds, *Front. Plant Sci.* **5**, 606 (2014).
33. M. Luo *et al*., *Nat. Biotechnol.* **39**, 561–566 (2021).
34. T. Florio, FlozBox Science (2024); www.Flozbox-Science.com.
35. O. Powell, SABAT, Zenodo (2024); https://zenodo.org/records/13902586.
36. O. Powell, SABAT_NF, Zenodo (2024); https://zenodo.org/records/13902590.
37. O. Powell, conservation_mapper, Zenodo (2024); https://zenodo.org/records/13902609.
38. O. Powell, NLR-Finder, Zenodo (2024); https://zenodo.org/records/13981323.
39. J. Sperschneider, P. Dodds, Effector screen, CSIRO Data Collection (2024); https://doi.org/10.25919/j0vh-ve59.
40. B. B. H. Wulff, Zahir-1644 genome assembly, Dryad (2024); https://doi.org/10.5061/dryad.hdr7sqvr9.
41. O. Powell, AlphaFold Structures for: A wheat tandem kinase activates an NLR to trigger immunity, https://zenodo.org/records/14184379, (2024).
42. S. Horsefield *et al*., *Science* **365**, 793–799 (2019).

ACKNOWLEDGMENTS

This research used the Ibex HPC cluster and the Shaheen Supercomputer managed by the Supercomputing Laboratory at King Abdullah University of Science and Technology (KAUST). We are grateful to Z. Liu (Chinese Academy of Sciences) and P. Brodersen (Copenhagen University) for helpful discussions, T. Florio (*34*) for figure artwork, H. Cui (Shandong Agricultural University) for Golden Gate plasmids, B. Steuernagel (JIC) for bioinformatics advice, A. Belén Perrera Rodríguez (KAUST) for greenhouse assistance, G. Huijuan (Novogene) and D. Copetti (Arizona Genomics Institute) for NGS services, and D. Snyman and R. Prins (CenGen Pty Ltd.) for DNA extractions. The seed of cv. Fielder was obtained from A. Carlson (University of Wisconsin) under a materials agreement. **Funding:** KAUST baseline and awards CRG10-2021-4735 and CRG11-2022-5087 (B.B.H.W.); KAUST baseline and awards FCC/1/1976-33 and REI/1/4446-01 (S.T.A.); The National Research Foundation, SARChI chair UID 8464 (W.H.P.B.); The Lieberman-Okinow Endowment at the University of Minnesota (B.J.S.); The National Natural Science Foundation of China (31830077) (D.T.); CSIRO Research Office, OD-213047, OD-225629, OD-227545 (P.N.D., M.F., J.S., T.V., M.A.A.); CSIRO SynBio Future Science Platform OD-206702 (T.V.); Biotechnology and Biological Sciences Research Council award BB/W018403/1 (K.K.). **Author contributions:** Conceptualization: R.C., J.C., O.R.P., M.A.O., T.A., M.F., J.S., T.V., M.A.A., P.N.D., B.B.H.W.; Investigation: R.C., J.C., O.R.P., M.A.O., T.A., K.G., Y.L.W., J.L., C.B., J.S., Y.X., G.Z., C.G., G.Y., S.G., O.M., W.H.P.B., W.B.M., S.T.A.; Visualization: R.C., J.C., M.A.O., O.R.P., K.G., Y.L.W., J.S., J.L., S.T.A., P.N.D., B.B.H.W.; Funding acquisition: M.A.A., M.F., J.S., T.V., D.T., L.J., B.J.S., K.K., W.H.P.B., S.T.A., P.N.D., B.B.H.W.; Project administration: D.T., L.J., B.J.S., W.H.P.B., K.K., P.N.D., B.B.H.W.; Writing – original draft: R.C., J.C., M.A.O., O.R.P., S.T.A., P.N.D., B.B.H.W.; Writing – review and editing: R.C., J.C., M.A.O., O.R.P., T.A., M.A.A., M.F., J.S., T.V., S.T.A., P.N.D., B.B.H.W. **Competing interests:** G.Y. and B.B.H.W. are inventors on patent application WO2023056269A1 filed by 2Blades and relating to the use of *Sr62*^{TK} in transgenic wheat. P.N.D., T.V., T.A., M.F., M.A.A., and J.S. are inventors on patent application WO2024103117 filed by CSIRO and relating to the identification of protein-protein interactions by protoplast screening. The remaining authors declare that they have no competing interests. **Data and materials availability:** Selected wheat cultivars and EMS-derived mutants are available from SeedStor or Alvar Carlson at University of Wisconsin under a material agreement (table S3). The code for SABAT (*35*), SABAT_NF (*36*), Conversation Mapper (*37*), and NLR-Finder (*38*) can be accessed on Zenodo. Sequence data are available from ENA project ID PRJEB74232, except for the wheat protoplast RNA-seq data which can be accessed at the CSIRO data access portal (*39*). The *Sr62*^{NLR} and *AvrSr62* variant sequences and annotations are available from NCBI with GenBank accession numbers PP537390 (*Sr62*^{NLR}) and PP623079 to PP623085 (*AvrSr62-1* to *AvrSr62-7*). The Zahir-1644 genome assembly can be downloaded from the Dryad data repository (*40*). The AlphaFold protein structures (PDB) files are available on Zenodo (*41*).

SUPPLEMENTARY MATERIALS

science.org/doi/10.1126/science.adp5034
Materials and Methods
Figs. S1 to S41
Tables S1 to S14
References (*43*–*77*)
Data S1 and S2

Submitted 3 April 2024; resubmitted 26 November 2024
Accepted 14 February 2025
10.1126/science.adp5034

HYDROLOGY

Abrupt sea level rise and Earth's gradual pole shift reveal permanent hydrological regime changes in the 21st century

Ki-Weon Seo[1]*†, Dongryeol Ryu[2]*†, Taehwan Jeon[3], Kookhyoun Youm[1], Jae-Seung Kim[1,3], Earthu H. Oh[1], Jianli Chen[4,5,6], James S. Famiglietti[7], Clark R. Wilson[8]

Rising atmospheric and ocean temperatures have caused substantial changes in terrestrial water circulation and land surface water fluxes, such as precipitation and evapotranspiration, potentially leading to abrupt shifts in terrestrial water storage. The European Centre for Medium-Range Weather Forecasts (ECMWF) Reanalysis v5 (ERA5) soil moisture (SM) product reveals a sharp depletion during the early 21st century. During the period 2000 to 2002, soil moisture declined by approximately 1614 gigatonnes, much larger than Greenland's ice loss of about 900 gigatonnes (2002–2006). From 2003 to 2016, SM depletion continued, with an additional 1009-gigatonne loss. This depletion is supported by two independent observations of global mean sea level rise (~4.4 millimeters) and Earth's pole shift (~45 centimeters). Precipitation deficits and stable evapotranspiration likely caused this decline, and SM has not recovered as of 2021, with future recovery unlikely under present climate conditions.

Drought is an emerging climatic and hydrologic disaster that has affected humans and ecosystems over the past several decades (*1*–*3*). Extended periods of precipitation deficit, associated with abnormally high barometric pressure over the continents and with anomalous sea surface temperatures, are main contributors to drought conditions (*4*, *5*). Increasing air temperature also increases evapotranspiration as an additional contributor to drought (*6*, *7*). The frequency of once-in-a-decade agricultural and ecological droughts has increased by a factor of about 1.7 compared with the 1850–1990 mean. Drought frequency is projected to further rise in accordance with various warming scenarios (*8*).

Unlike other natural disasters such as earthquakes and floods, drought events develop more gradually (*9*). Generally, droughts commence with precipitation deficits, leading to the depletion of terrestrial water storage (TWS), including soil moisture (SM), groundwater, and water in streams and lakes (*10*). However, challenges in measuring TWS, especially groundwater and root-zone SM, limited understanding of hydrological depletion at continental scales until the development of satellite gravity missions. Observations from the Gravity Recovery and Climate Experiment (GRACE) (May 2002 to May 2017) and GRACE Follow-On (June 2018 to present) provide continental-scale observations of TWS variations, serving as an indicator of hydrological drought (*11*). GRACE observed a gradual global depletion of TWS from 2005 to 2015 of approximately 1287 gigatonnes (Gt) of water, equivalent to about 3.52 mm of global mean sea level (GMSL) rise (*12*). An important question is whether global TWS depletion is linked to decadal climate variations or to longer-term changes associated with a warming climate. Since the late 1990s, there have been reports of considerable declines in evapotranspiration associated with decreasing SM (*13*) and increasing atmospheric vapor pressure deficit (VPD) (*14*). These abrupt changes imply a gradual decline in global TWS and a more permanent shift

[1]Department of Earth Science Education, Seoul National University, Seoul, South Korea. [2]Department of Infrastructure Engineering, The University of Melbourne, Parkville, VIC, Australia. [3]Center for Educational Research, Seoul National University, Seoul, South Korea. [4]Department of Land Surveying and Geo-Informatics, The Hong Kong Polytechnic University, Hong Kong, China. [5]Research Institute for Land and Space, The Hong Kong Polytechnic University, Hong Kong, China. [6]The Hong Kong Polytechnic University Shenzhen Research Institute, Shenzhen, China. [7]School of Sustainability, Arizona State University, Tempe, AZ, USA. [8]Center for Space Research and Department of Earth and Planetary Sciences, University of Texas at Austin, Austin, TX, USA.
***Corresponding author. Email: seokiweon@snu.ac.kr (K.-W.S.); dryu@unimelb.edu.au (D.R.)**
†These authors contributed equally to this work.

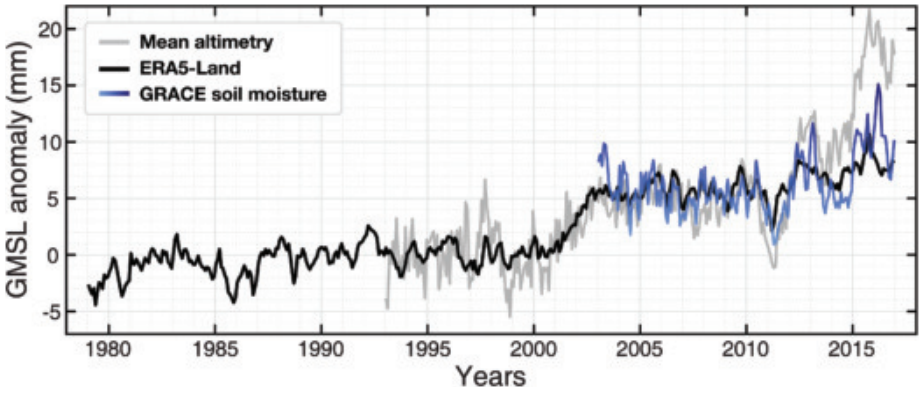

Fig. 1. GMSL anomalies observed and derived from SM change. GMSL variations due to ERA5-Land SM change (black) and GRACE-derived SM change (blue) and from 30-day means of altimetry datasets from AVISO, NOAA, and CU (gray). The January 1993 to December 1999 trend was removed from the altimetry time series. Annual components were removed from the three curves. Vertical offsets were added to the blue and black curves to facilitate comparison with the gray line.

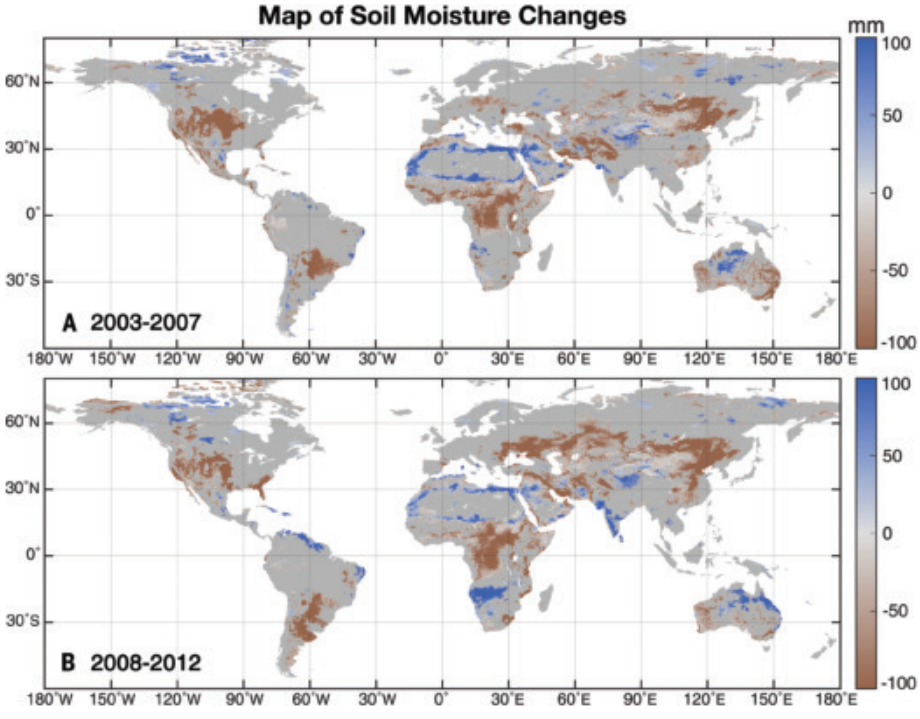

Fig. 2. Maps of global SM changes. (**A** and **B**) Mean SM variations during (A) 2003–2007 and (B) 2008–2012 relative to 1995–1999. Dark gray indicates areas where the change in SM was statistically not significant ($p > 0.05$).

in other TWS components, such as streamflow, during the same period (*15*). A limitation of using satellite gravity observations to address these questions is that they have only been available since 2002.

Variations in GMSL observed by satellite altimeters are likely an important indicator of permanent TWS changes, because ocean mass increases as TWS declines (*16*). Additionally, TWS changes before the GRACE era can be inferred from observations of Earth's polar motion (PM). For example, groundwater extraction that led to TWS changes during the pre-GRACE era was confirmed by PM changes (*17*). Given that PM is influenced by mass redistribution within the Earth system, a comprehensive approach involving diverse models and observations of the atmosphere, hydrosphere, and lithosphere is essential for understanding observed PM. In this study, we used both GMSL and PM data from 1992 to 2016 to understand global TWS depletion patterns in the European Centre for Medium-Range Weather Forecasts (ECMWF) Reanalysis v5 (ERA5) Land SM product (*18*).

Depletion of TWS

We calculated global SM variation, excluding Antarctica and Greenland, using the ERA5-Land SM data, averaged monthly from January 1979 to December 2016 (*19*). This ERA5 product estimates water within the upper 289 cm in four discrete soil layers simulated by the Carbon-Hydrology-Tiled ECMWF Scheme for Surface Exchanges over Land (CHTESSEL). Soil water leaving the bottom layer is treated as subsurface runoff because there is no provision for groundwater storage in aquifers. Groundwater recharge and abstraction were estimated by the global hydrological model PCR-GLOBWB separately (*20*, *21*). Comparison of the ERA5-Land SM (top layer, 0 to 7 cm) with microwave satellite SM retrievals (v202212) from Copernicus Climate Change Service (C3S) Climate Data Store (CDS) over 1979 to 2022 shows consistent temporal patterns between them, indicating no artificial changes in ERA5-Land SM from the reanalysis scheme (fig. S1). Other commonly used land surface models—Noah version 3.6, VIC version 4.1.2, and CLSM version 3.6 of NASA's Global Land Data Assimilation (GLDAS, versions 2.0 and 2.1), as well as MERRA-2 of Global Modeling and Assimilation Office (GMAO)—resulted in large discrepancies in SM contributions to GMSL and PM, particularly before the GRACE monitoring period, and were consequently excluded from our analysis (see section Discussion and conclusion).

The black line in Fig. 1 shows ERA5-Land SM contributions (relative to the mean value for 1993–1999) to change in GMSL (see methods). Annual components were removed. During the period 1979–2016, the increase in GMSL from SM depletion is estimated at 10.78 mm, corresponding to a loss of 3941 Gt of water from the continents. A substantial portion of SM depletion (1614 Gt) occurred within the short period 2000–2002. From 2003 to 2016, Fig. 1 shows that depleted SM has not returned to its previous level and that the depletion has even steadily intensified, yielding an additional 2.76 mm of GMSL rise (equivalent to 1009-Gt SM depletion).

The rapid GMSL rise (2000–2002) is evident in satellite radar altimetry observations. The gray line in Fig. 1 shows satellite radar altimetry GMSL from January 1993 to December 2016. The altimetry series is the 30-day mean of estimates from three groups: Archiving, Validation and Interpretation of Satellite Oceanographic data (AVISO); the National Oceanic and Atmospheric Administration (NOAA); and the University of Colorado (CU) (fig. S2). We removed the linear trend of the period 1993–1999 from the altimetry time series to show the anomalies of interest. The trend includes effects from

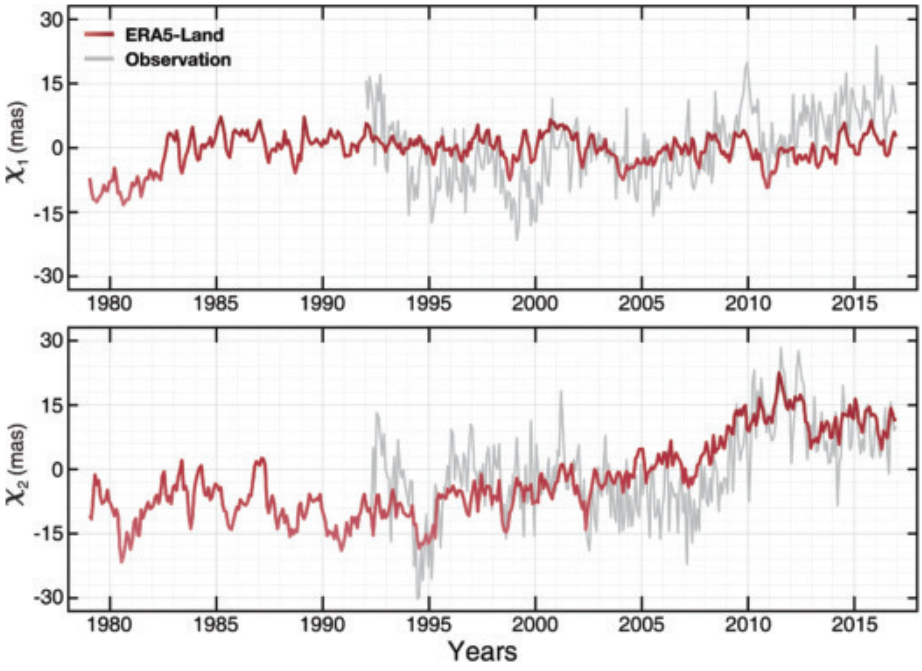

Fig. 3. PM excitation components derived from SM changes. Gray lines show the two components of residual PM excitation (difference between observed and estimated) in fig. S5. SM contributions to χ_1 and χ_2 were excluded in the estimation. The red lines are excitations derived from ERA5-Land SM variation.

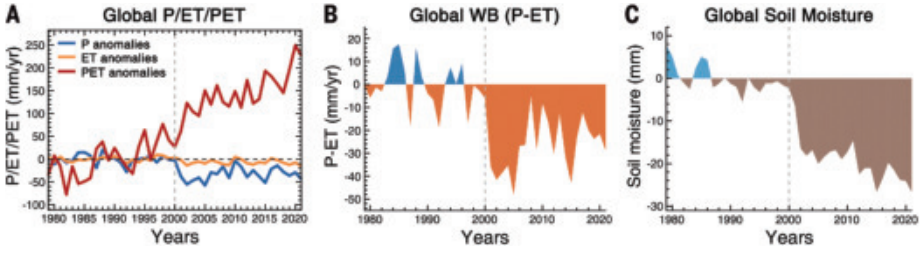

Fig. 4. Anomalies of global water balance components in 1979–2021 derived from ERA5-Land, excluding Greenland and Antarctica. (**A**) P, ET, and PET anomalies. (**B**) Water balance (WB) estimated as P-ET. (**C**) SM content. Anomaly values were calculated by subtracting the mean of each variable for 1979–1999. Here, positive values for ET indicate evaporation, and negative values indicate condensation to the ground.

land ice mass loss and steric sea level changes. The detrended altimetry series also shows anomalies due to other causes such as El Niño–Southern Oscillation (ENSO) events (e.g., 1997–1998, 2010–2012, and 2014–2016) (*8*) and other sources. Nevertheless, the altimetry series shows an increase for 2000–2002, consistent with variations derived from the ERA5-Land SM data. Note that the increasing deviation of the gray line (altimetry sea level change) from the black line after 2010 is due mostly to larger GMSL rise resulting from ice mass loss acceleration in Greenland and Antarctica (*22*).

The steady decline of SM (2003 and onward) after the abrupt loss of SM in 2000–2002 is also supported by GRACE observations (see fig. S3). The blue line in Fig. 1 shows GMSL variations associated with SM estimated from GRACE (*12*) during 2003–2016 after correction for other effects, including the Greenland and Antarctic ice sheets (*22*), mountain glaciers (*23*), snow (*18*), groundwater (*20*), and dams (*24*). The estimated SM contribution to GMSL rise is about 0.23 ± 0.09 mm/year, close to that from ERA5-Land SM data (0.19 ± 0.04 mm/year) during the same period, confirming that depletion intensified after the abrupt loss of SM during 2000–2002.

Apparently, SM depletion during the early 21st century was a global event. Figure 2A shows mean SM for 2003–2007 relative to that for 1995–1999, estimated by ERA5-Land. Large regions in East and Central Asia, Central Africa, and North and South America show pronounced depletion. By contrast, replenishment of SM occurred in relatively small portions of South America, India, Australia, and North America. Between 2000 and 2002, the estimated loss of SM was approximately 1614 Gt, contributing to a GMSL rise rate of about 1.95 ± 0.29 mm/year. Considering a GMSL increase of around 0.8 mm/year from Greenland ice loss (*25*), recognized as the largest source of GMSL rise over the past few decades, a rapid global SM decline and consequent GMSL rise during the early 21st century is notable.

The regions of pronounced SM decline expanded further in Central Asia and South America during 2008–2012 (Fig. 2B). As a result, when the comparison periods are extended to 2003–2021 for test and 1979–1999 for reference (see fig. S4), areas of SM depletion grow much larger to cover East and Central Asia, Europe, Central Africa, Eastern US, and South America. This is consistent with observed GMSL that indicates continued decline of global SM after the abrupt loss in 2000–2002.

To substantiate the ERA5-Land SM shift and corresponding GMSL variations, we examined PM, measuring changes in Earth's rotational pole relative to its geographic pole. PM was shown to undergo an observable change from global groundwater loss during the period 1993–2010 (*17*). The red lines in Fig. 3 are two PM excitation terms, χ_1 and χ_2, calculated from SM variations that are shown in Figs. 1 and 2. The PM excitation terms are given in milliarcsecond (mas) along the Greenwich meridian and 90° east longitude, respectively. The estimated χ_1 and χ_2 from ERA5-Land SM variations are compared with the observed PM excitation terms after removing all contributing factors except for SM in the gray lines. The observed PM excitation terms and their estimates from all contributing factors, excluding SM, are shown in fig. S5 as gray and red lines, respectively (see methods). The "residual" in Fig. 3 (gray lines) is the difference between the observed (gray lines) and estimated (excluding SM, red lines) PM excitation terms from fig. S5. The PM excitation terms estimated from SM (red line in Fig. 3) vary closely with the residual excitation terms (gray lines), supporting our hypothesis that the global SM variation estimated by ERA5-Land is consistent with the observed PM changes.

Gray and red lines for χ_2 show that Earth's pole shifted about 45 cm (~15 mas) up to 2012. Variations of χ_1 and χ_2 associated with SM variations may not necessarily correlate with GMSL variations in Fig. 1. This is because χ_1 and χ_2 are sensitive to both the amount and location of mass changes (see figs. S6 to S8), whereas GMSL only accounts for the overall amount. A similar increase during 2000–2002 in GMSL is not evident in χ_2 because SM declined globally. For instance, although a SM decrease in North America during that period shifted Earth's pole 90° toward west longitude (i.e., χ_2 decreased), a similar decline in Eurasia had the

opposite effect, moving Earth's pole toward 90° east longitude (i.e., χ_2 increased) (see figs. S6 and S8). The steady increase in χ_2 from 2008 to 2012 shown in Fig. 2B is mostly driven by SM variations in Eurasia that are evident in changes in mean SM during the two different periods, 2003–2007 and 2008–2012, relative to 1995–1999 in Fig. 2. The region experienced a consistent decline in SM, which extended toward mid-latitude regions where PM is the most sensitive (see fig. S6).

There is a relatively larger difference between gray and red lines for χ_1 because it is mostly affected by ocean mass rather than SM changes (see fig. S6, which shows the modes of χ_1 primarily located in the oceans). The effect of SM on PM is more strongly reflected in χ_2 as a result. The coefficient of determination (R^2) between observed and estimated χ_2 is 0.72 when the contribution of SM is not accounted for, which improves to 0.82 with the SM effect included.

Both GMSL and PM excitation affirm the distinct SM variations shown in Figs. 1 and 2. This reflects a transition to a drier hydrologic regime since the early 21st century, which steadily intensifies.

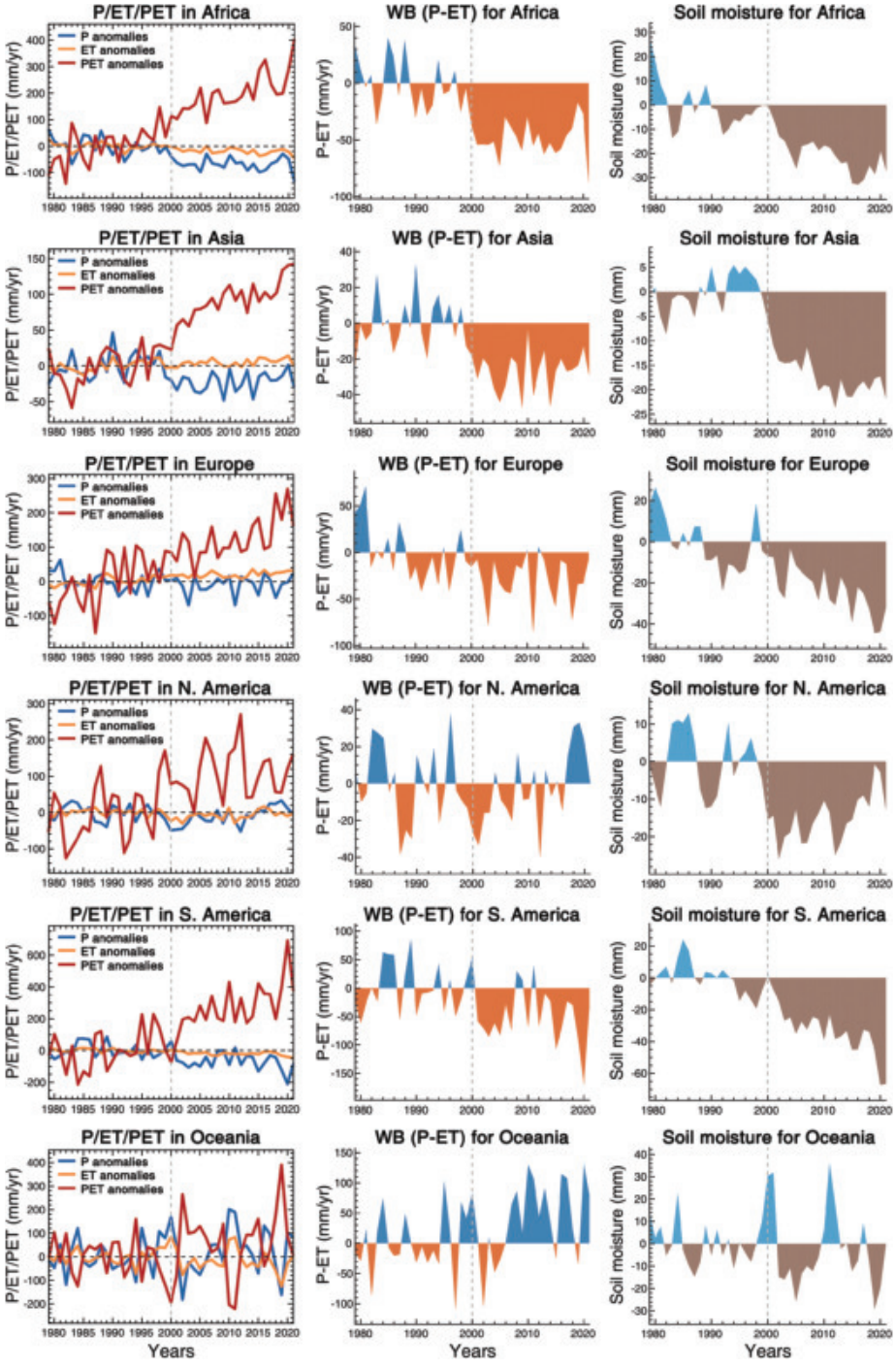

Fig. 5. Anomalies of water balance components for six continents in 1979–2021 derived from ERA5-Land. (Left) P, ET, and PET anomalies. (Middle) Water balance (WB) estimated as P-ET. (Right) SM content. Anomaly values were calculated as in Fig. 4.

Drivers of the shift in TWS

The ERA5 global land precipitation (P) anomaly in Fig. 4A, relative to 1979–1999, shows a steep decline after 2000 and remains below the average 1979–1999 level. The rapid decline of land precipitation from 2000 to 2002 in ERA5 is consistent with the sharp decline shown in the gauge-based precipitation data from the Global Precipitation Climatology Centre (GPCC) and the blended gauge-satellite estimates from the Global Precipitation Climatology Project (GPCP) during the same period (*26*). The declining trend in land precipitation from the late 1990s, particularly in Africa and Australia, resulted in a reduction in global land evapotranspiration from 1998 to 2008 (*13*). Concurrently, the global VPD experienced a sharp and steady increase from the late 1990s (*14*).

Global evapotranspiration declines with precipitation but with a smaller magnitude. Consequently, the global water balance [precipitation-evapotranspiration (P-ET)] anomaly drops steeply from 2000 (Fig. 4B), mirroring the interannual pattern of precipitation. By contrast, the potential evapotranspiration (PET) anomaly has increased significantly since the late 1990s, displaying a consistent long-term pattern of increase reported in a separate study of VPD trend (*14*). Note that the PET in ERA5-Land is calculated separately from the CHTESSEL outputs by making a second call to the input forcing data from ERA5, assuming an open water surface (*19*). The PET anomaly is presented to show increasing atmospheric demand for evapotranspiration in recent decades (*14*, *27*).

Conversely, the ERA5-Land SM anomaly exhibits a gradual decline from 2000 to 2021 after the sharp drop in 2000–2002, with diminished interannual variability compared to P or P-ET owing to SM's inherent effect of buffering short-term climate variability. This trend may be attributed to increased precipitation intensity (*8*, *26*) in recent decades, which typically leads to increased runoff and reduced infiltration.

It is important to note that ERA5-Land uses static monthly climatological mean values for the leaf area index and surface albedo with fixed land cover (*19*). Consequently, the impact of growing agricultural irrigation in regions such as northeast China and the Western US (*28*, *29*) and global greening trends (*30*, *31*) is not considered in the ERA5 results used in this work. The inclusion of agricultural intensification

and greening in semiarid regions may contribute to a further decline in global SM.

The global pattern of ERA5-Land SM changes, characterized by a sharp depletion in 2000 followed by a gradual decline, is influenced by changes in Africa, Asia, Europe, and South America (Fig. 5). In Africa and South America, continental-scale P anomalies exhibit a declining trend, whereas the P anomaly in Asia shows a flat trend after a distinctive shift (decline) around the year 2000. The ET anomaly in Africa and South America remains mostly negative as for P anomalies, exhibiting the P versus ET behavior of the water-limited ET regime. The P-ET anomaly in Africa and South America is still determined by the anomaly of precipitation that varies with large amplitudes. In comparison, the ET anomaly in Asia and Europe stayed in the positive range for 2000–2021, even in the years of large negative anomalies of P, indicating the P versus ET pattern of the energy-limited regime. The opposite trend in P and ET anomalies in Asia and Europe contributes to amplifying the influence of P anomalies on the overall water balance (P-ET) in the regions. Resulting large interannual variations of P-ET in Europe since 2000 clearly depict the extreme drought events in the years 2003, 2007, 2011, 2015, and 2018 (*32*, *33*).

Discussion and conclusions

Satellite gravity observations over land, excluding Antarctica and Greenland, with corrections for mountain glaciers (*23*), reveal a decline in TWS from 2005 to 2015, contributing to a GMSL rise of 0.32 ± 0.02 mm/year (*12*). Similarly, analysis of ERA5-Land SM data indicates a corresponding TWS depletion, with a notable abrupt decline in SM during the early 21st century, preceding the satellite gravity observation period. This sudden decrease in TWS, estimated at approximately 1614 Gt, led to a substantial GMSL rise of 1.95 ± 0.29 mm/year over 3 years (2000–2002). This rate of GMSL rise is unprecedented when compared with the rate attributed to Greenland ice mass loss, which is approximately 0.8 mm/year and widely considered to be the largest source (*25*). Importantly, TWS has not recovered to its previous state since the apparent SM decrease.

Anomalous SM variations observed in ERA5-Land data were mirrored in sea surface height observations. Although sea surface height variations are influenced by various factors (such as ice sheet mass loss and sea water density change), satellite altimetry observations clearly reveal variations consistent with those predicted from ERA5-Land SM data.

PM excitation data also support the existence of anomalous SM variations since the beginning of the 21st century. Because PM excitation is influenced by both the amount and location of mass redistribution, the expected variations associated with anomalous SM differ from those of sea level. For example, although global trends in SM anomalies in Fig. 4 are mostly influenced by trends in Africa, Asia, Europe, and, to a greater extent, in South America, declining SM in Asia makes a larger contribution to PM as a result of its mid-latitude location, as shown in figs. S6 and S8. Residual excitations, calculated by removing estimated excitation sources except SM, are similar to estimated contributions from ERA5-Land SM data. Thus, both sea surface height and PM observations support the conclusion that the abrupt change in SM is genuine. If the abrupt shift in SM and TWS is driven by a warming climate and associated changes, the diminished TWS may not be recoverable in the foreseeable future.

Variations in SM from other commonly used land surface models (GLDAS-Noah, GLDAS-VIC, GLDAS-CLSM, MERRA-2) exhibit interannual patterns similar to those of ERA5-Land and depict declining TWS during 2000–2002, but with smaller magnitudes. As a result, in contrast to ERA5-Land, TWS is replenished in subsequent years, which is inconsistent with observations of sea surface heights (fig. S9) and PM (fig. S10). Conversely, the GLDAS 2.1 CLSM model appears to more closely agree with sea surface height observations with a larger contribution to GMSL from 2009 (fig. S9). However, because sea surface height observations incorporate more substantial effects from polar ice sheets after 2005, CLSM's recent trend indicates an overestimation of the decline in SM. This is confirmed by the comparison between GMSL rise associated with SM variations and GRACE observations in fig. S11.

Changes in precipitation patterns since 2000, combined with relatively stable evapotranspiration and steeply increasing VPD during the same period, are likely the main factors for the TWS depletion reported in our analysis. Given that the ERA5-Land model used in this work does not consider global greening trends (*30*) and expansion of agricultural irrigation (*28*, *29*), the estimated change in SM is driven mainly by the changes in precipitation and evaporative demand during the analysis period. This is consistent with previous studies that suggest a global decline of SM over recent decades, with expectations of further reductions as the climate continues to warm (*34*–*37*). Although a warming climate favors increased vapor in the atmosphere, leading to an increase in precipitation, the actual trend of precipitation varies regionally. Conversely, the increasing evaporative demand driven by a warming climate is more uniformly distributed across the globe, suggesting a more consistent and widespread trend toward drying as temperatures rise (*38*).

However, the complex interplay between precipitation and evapotranspiration, influenced by a broad range of factors, renders the impact of a warming climate on SM highly unpredictable. For example, although precipitation intensification due to climate change generally increases runoff and reduces soil infiltration (*39*, *40*), an increase in peak rainfall may also lower peak runoff and increase infiltration when the intensification occurs with drying soil conditions (*41*). Declining pan evaporation under a warming climate in the late 20th century, known as the pan evaporation paradox (*42*), demonstrates that reduced solar radiation (*43*) and wind speed (*44*) can offset the effect of warming. However, the trend has reversed to positive in the 21st century, driven by sharply increasing VPD (*45*, *46*). Analysis of general circulation model simulations shows that rising VPD and PET in a warming climate not only exacerbate drying in regions with reduced precipitation but can also trigger drought in areas experiencing small or even positive changes in precipitation (*35*). However, the commonly used Penman-Monteith approach may severely overestimate PET owing to the reduced plant stomatal conductance with increasing atmospheric CO_2 concentration and subsequent improvement of plant water use efficiency, known as the CO_2 fertilization (*38*, *47*). Interestingly, a recent study reports that global ecosystem water use efficiency has not risen since 2001, owing to the steeper increase of VPD in comparison with the effect of CO_2 fertilization, which implies continued increase of evapotranspiration with a warming climate (*27*). Accurate representation of the key factors that influence changes in SM under a changing climate would require substantial improvement in present land surface and hydrological models. This study presents innovative methods to estimate changes in global SM, which can provide opportunities to evaluate and improve the present status of modeling at continental and global scales.

REFERENCES AND NOTES

1. C. P. Kelley, S. Mohtadi, M. A. Cane, R. Seager, Y. Kushnir, *Proc. Natl. Acad. Sci. U.S.A.* **112**, 3241–3246 (2015).
2. M. Zhao, S. W. Running, *Science* **329**, 940–943 (2010).
3. S. Madadgar, A. AghaKouchak, A. Farahmand, S. J. Davis, *Geophys. Res. Lett.* **44**, 7799–7807 (2017).
4. A. Giannini, R. Saravanan, P. Chang, *Science* **302**, 1027–1030 (2003).
5. K. E. Trenberth, G. W. Branstator, P. A. Arkin, *Science* **242**, 1640–1645 (1988).
6. S. Huang *et al*., *Sci. Total Environ.* **845**, 157203 (2022).
7. L. E. Condon, A. L. Atchley, R. M. Maxwell, *Nat. Commun.* **11**, 873 (2020).
8. Intergovernmental Panel on Climate Change (IPCC), *Climate Change 2021: The Physical Science Basis. Contribution of Working Group I to the Sixth Assessment Report of the Intergovernmental Panel on Climate Change*, V. Masson-Delmotte *et al*., Eds. (Cambridge University Press, 2021).
9. A. F. Van Loon, *WIREs Water* **2**, 359–392 (2015).
10. B. I. Cook, J. S. Mankin, K. J. Anchukaitis, *Curr. Clim. Change Rep.* **4**, 164–179 (2018).
11. A. C. Thomas, J. T. Reager, J. S. Famiglietti, M. Rodell, *Geophys. Res. Lett.* **41**, 1537–1545 (2014).
12. J.-S. Kim, K.-W. Seo, T. Jeon, J. Chen, C. R. Wilson, *Geophys. Res. Lett.* **46**, 12049–12055 (2019).
13. M. Jung *et al*., *Nature* **467**, 951–954 (2010).
14. W. Yuan *et al*., *Sci. Adv.* **5**, eaax1396 (2019).
15. T. J. Peterson, M. Saft, M. C. Peel, A. John, *Science* **372**, 745–749 (2021).
16. H. A. Chandanpurkar *et al*., *Geophys. Res. Lett.* **48**, e2020GL091248 (2021).

17. K.-W. Seo *et al.*, *Geophys. Res. Lett.* **50**, e2023GL103509 (2023).
18. H. Hersbach *et al.*, *Q. J. R. Meteorol. Soc.* **146**, 1999–2049 (2020).
19. J. Muñoz-Sabater *et al.*, *Earth Syst. Sci. Data* **13**, 4349–4383 (2021).
20. Y. Wada *et al.*, *Geophys. Res. Lett.* **37**, L20402 (2010).
21. Y. Wada *et al.*, *Water Resour. Res.* **47**, 2010WR009792 (2011).
22. I. N. Otosaka *et al.*, *Earth Syst. Sci. Data* **15**, 1597–1616 (2023).
23. M. Zemp *et al.*, *Nature* **568**, 382–386 (2019).
24. B. Lehner *et al.*, *Front. Ecol. Environ.* **9**, 494–502 (2011).
25. WCRP Global Sea Level Budget Group, *Earth Syst. Sci. Data* **10**, 1551–1590 (2018).
26. J. Blunden, T. Boyer, *Bull. Am. Meteorol. Soc.* **103**, S1–S465 (2022).
27. F. Li *et al.*, *Science* **381**, 672–677 (2023).
28. M. Rolle, S. Tamea, P. Claps, *Environ. Res. Lett.* **17**, 044017 (2022).
29. L. Zhang, Y. Xie, X. Zhu, Q. Ma, L. Brocca, *Earth System Science Data* **16**, 5207–5226 (2024).
30. G. Forzieri, R. Alkama, D. G. Miralles, A. Cescatti, *Science* **356**, 1180–1184 (2017).
31. Z. Zhu *et al.*, *Nat. Clim. Chang.* **6**, 791–795 (2016).
32. M. Ionita, M. Dima, V. Nagavciuc, P. Scholz, G. Lohmann, *Commun. Earth Environ.* **2**, 61 (2021).
33. V. Blauhut *et al.*, *Nat. Hazards Earth Syst. Sci.* **22**, 2201–2217 (2022).
34. A. Dai, *Nat. Clim. Chang.* **3**, 52–58 (2013).
35. B. I. Cook, J. E. Smerdon, R. Seager, S. Coats, *Clim. Dyn.* **43**, 2607–2627 (2014).
36. S. M. Vicente-Serrano *et al.*, *Philos. Trans. R. Soc. Ser. A* **380**, 20210285 (2022).
37. P. Lal, A. Shekhar, M. Gharun, N. N. Das, *Sci. Total Environ.* **867**, 161470 (2023).
38. A. Berg, J. Sheffield, *Curr. Clim. Change Rep.* **4**, 180–191 (2018).
39. J. P. Eekhout, J. E. Hunink, W. Terink, J. de Vente, *Hydrol. Earth Syst. Sci.* **22**, 5935–5946 (2018).
40. S. Hettiarachchi, C. Wasko, A. Sharma, *Hydrol. Earth Syst. Sci.* **22**, 2041–2056 (2018).
41. C. Wasko, R. Nathan, *J. Hydrol. (Amst.)* **575**, 432–441 (2019).
42. W. Brutsaert, M. Parlange, *Nature* **396**, 30 (1998).
43. T. C. Peterson, V. S. Golubev, P. Y. Groisman, *Nature* **377**, 687–688 (1995).
44. T. R. McVicar *et al.*, *J. Hydrol.* **416–417**, 182–205 (2012).
45. T. Wang, J. Zhang, F. Sun, W. Liu, *WIREs Water* **4**, e1207 (2017).
46. C. M. Stephens, T. R. McVicar, F. M. Johnson, L. A. Marshall, *Geophys. Res. Lett.* **45**, 11164–11172 (2018).
47. P. C. Milly, K. A. Dunne, *Nat. Clim. Chang.* **6**, 946–949 (2016).

ACKNOWLEDGMENTS

Funding: This research was supported by National Research Foundation of Korea (NRF) grants (2022R1C1C2006586, 2023R1A2C100489912, RS-2024-00346384) and a Korea Institute of Marine Science & Technology Promotion grant funded by the Ministry of Ocean Fisheries (RS-2023-00256677; PM24020). C.R.W. was supported by NASA grants (80NSSC20K0820, 80NSSC22K0906). J.C. was supported by the Hong Kong RGC Collaborative Research Fund (C5013-23G) and NSFC Major Programme (42394132). **Author contributions:** Conceptualization: K.-W.S., D.R.; Data processing: K.-W.S., D.R., T.J., K.Y., J.-S.K., E.H.O.; Data analysis: K.-W.S., D.R., T.J., J.C., J.F., C.R.W.; Visualization: E.H.O.; Writing – original draft: K.-W.S., D.R.; Writing – review & editing: J.C., J.F., C.R.W. **Data and materials availability:** All data used in this work are provided in table S1.

SUPPLEMENTARY MATERIALS

science.org/doi/10.1126/science.adq6529
Methods
Figs. S1 to S11
Table S1
References (*48*–*55*)

Submitted 29 May 2024; accepted 3 February 2025
10.1126/science.adq6529

METALLURGY

A high-temperature nanostructured Cu-Ta-Li alloy with complexion-stabilized precipitates

B. C. Hornbuckle[1], J. A. Smeltzer[2], S. Sharma[3], S. Nagar[3], C. J. Marvel[4], P. R. Cantwell[2], M. P. Harmer[2]*, K. Solanki[3]*, K. A. Darling[1]*

We present a bulk nanocrystalline copper alloy that can operate at near-melting temperatures with minimal coarsening and creep deformation. The thermal stability of the Cu-3Ta-0.5Li atomic % (at %) alloy is attributed to coherent, ordered $L1_2$ Cu_3Li precipitates surrounded by a tantalum-rich atomic bilayer phase boundary complexion. Adding 0.5 at % lithium to the immiscible Cu-Ta system changes the morphology of the nanoscale precipitates from spherical to cuboidal while simultaneously tailoring the phase boundary. The resultant complexion-stabilized nanoscale precipitates provide excellent thermal stability, strength, and creep resistance. The underlying alloy design principles may guide the development of next-generation copper alloys for high-temperature applications such as heat exchangers.

The discovery of the gamma prime (γ′) phase and its role in Ni-based superalloys is regarded as one of the most important breakthroughs in the development of advanced structural alloys (*1*, *2*). The γ′ precipitates in superalloys increase strength and decrease creep deformation at elevated temperatures, making these alloys essential materials in power generation and transportation applications. Careful control of coherency between the γ′ precipitates, which have the ordered cubic $L1_2$ crystal structure, and the matrix leads to strengthening by mechanisms of coherency strains that impede dislocation motion (*3*, *4*). This coherency results in low interfacial energies between the precipitates and matrix, thus also increasing the thermal stability by reducing the rate of coarsening at elevated temperatures (*5*). We recreate the superalloy approach of exploiting coherency strains with the additional introduction of electronic contributions from phase boundary complexions (*6*–*9*) to develop a nanostructured Cu-Ta-Li alloy with high-temperature strength and creep performance. Complexions behave in a phase-like manner (*10*), affect the behavior of dislocations and other crystalline defects (*11*, *12*), and substantially influence bulk material properties, such as liquid metal embrittlement (*13*, *14*). In the present work on the Cu-Ta-Li system, a Ta-rich bilayer complexion at the phase boundary between Cu_3Li precipitates and the nanocrystalline Cu matrix enables the formation of nanoscale Cu_3Li precipitates as well as stabilizing them against coarsening at high homologous temperatures.

[1]Army Research Directorate, DEVCOM, Army Research Laboratory, Aberdeen Proving Ground, MD, USA. [2]Department of Materials Science and Engineering, Lehigh University, Bethlehem, PA, USA. [3]School for the Engineering of Matter, Transport, and Energy, Arizona State University, Tempe, AZ, USA. [4]Department of Mechanical and Industrial Engineering, Louisiana State University, Baton Rouge, LA, USA.
***Corresponding author. Email: mph2@lehigh.edu (M.P.H.); kristopher.a.darling.civ@army.mil (K.A.D.); kiran.solanki@asu.edu (K.S.)**

Alloy design

Our alloy is based on the nanocrystalline Cu-Ta model alloy system (*15*), a phase-separating alloy with a positive miscibility gap (*16*), which has exhibited divergent properties under conditions of quasi-static (*17*), dynamic, and shock loading (*18*, *19*) as well as intense radiation (*20*). These properties can be attributed to the nanosized Ta-based precipitates in the Cu-Ta alloy, which exhibit spherical morphology and, depending on their size, either a coherent or semicoherent relationship with the matrix phase (*21*). These findings prompted a focused effort on tailoring the formation, structure, morphology, coherency relationship, and spatial distribution of related Ta-based nanoclusters through alloying with additional dopant elements, specifically elements that are immiscible with Ta, soluble in Cu, and highly reducing. Lithium meets these requirements. The addition of 0.5 atomic % (at %) Li to Cu-3Ta at % results in the formation of a Cu_3Li nanoprecipitate phase in the Cu-3Ta-0.5Li alloy.

Structural evaluation

Our atomic-resolution images from high-angle annular dark-field scanning transmission electron microscopy (HAADF-STEM) (Fig. 1) reveal the structural differences between the spherical precipitates in a Cu-Ta alloy and the faceted Cu_3Li precipitates in the Cu-Ta-Li alloy. Round precipitates are the predominant feature of the binary Cu-Ta alloy (fig. S1, A and C), whereas faceted precipitates are the predominant feature of our ternary Cu-Ta-Li alloy (fig. S1, B and D). The coherency of the Cu_3Li precipitates in the Cu-Ta-Li alloy is visually evident in Fig. 1B, as is the lack of coherency of the precipitates in the Cu-3Ta alloy in Fig. 1A. Inverse Fourier-filtered color images (Fig. 1, C and D) emphasize the enhanced

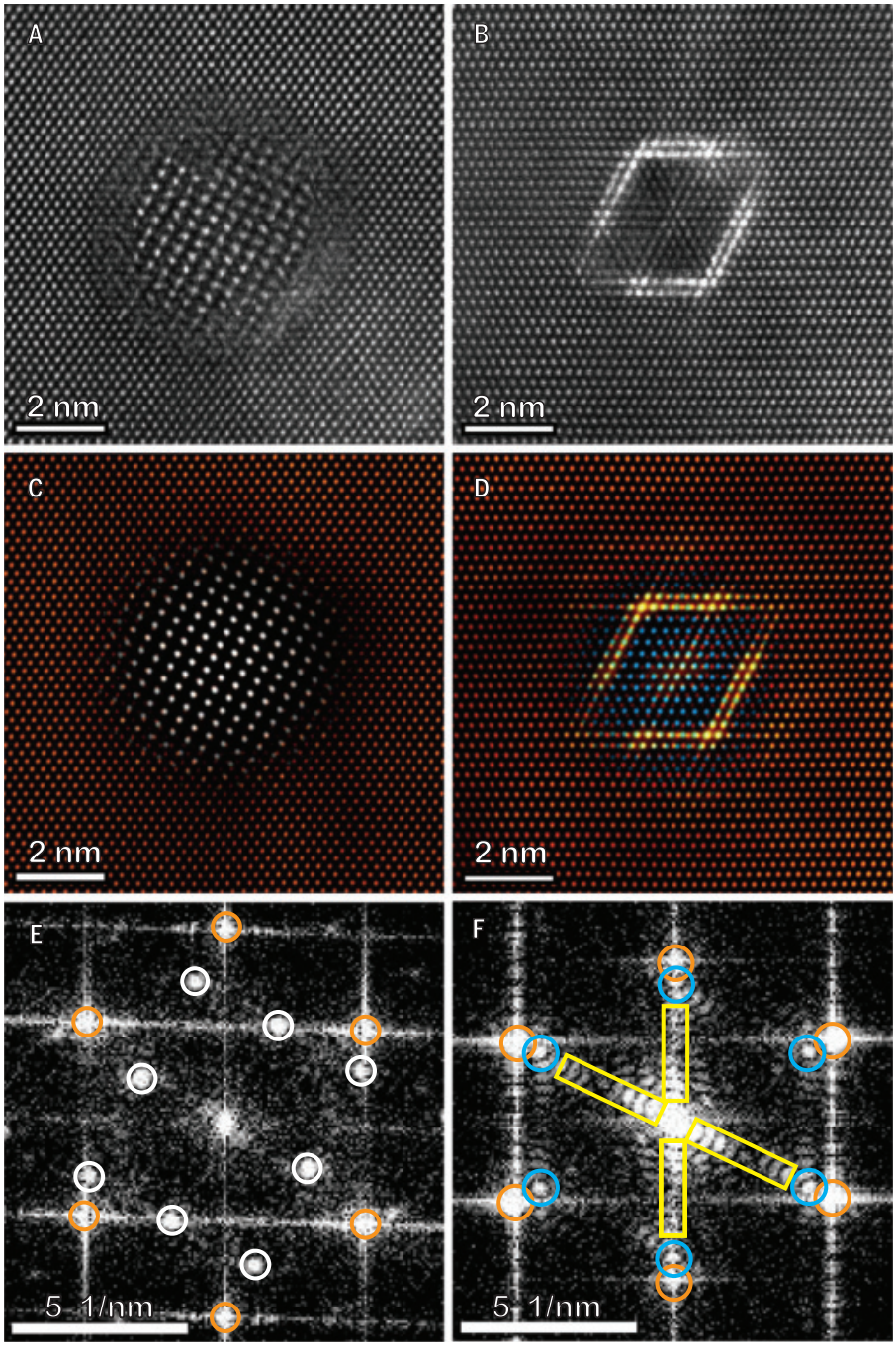

Fig. 1. Cuboidal precipitates in Cu-3Ta-0.5Li with a Ta-rich bilayer complexion compared with spherical precipitates in Cu-3Ta. (**A** to **F**) Atomic-resolution HAADF-STEM images [(A) and (B)], filtered HAADF-STEM images [(C) and (D)], and FFTs [(E) and (F)] comparing the typical spherical morphology of Ta-rich precipitates in Cu-3Ta with the faceted, cuboidal morphology of Cu-3Ta precipitates in Cu-3Ta-0.5Li. The original images for binary Cu-3Ta (A) and ternary Cu-3Ta-0.5Li (B), respectively. Color-filtered images via Fourier filtering [(C) and (D)] and the respective FFTs [(E) and (F)]. In (C), the orange-colored features represent the Cu matrix atoms, whereas the white features represent the O atoms within the precipitates. In (D), the orange-colored features represent Cu matrix atoms, the yellow-colored features represent Ta atoms, and the blue features represent Li atoms. In (E) and (F), the colored features represent the reflections used to generate the inverse FFT-filtered images in (C) and (D).

coherency in the Cu-Ta-Li precipitates as compared with the precipitates in Cu-Ta, as a periodic overlap of the matrix and particle lattices can be seen in the Cu_3Li precipitates in Cu-Ta-Li.

Fast Fourier transforms (FFTs) of the HAADF-STEM images (Fig. 1, E and F) illustrate that the lattice parameters of both precipitates are larger than the matrix phase. The measured lattice misfit between the Cu_3Li precipitates and the matrix phase was 14.3%, whereas in the binary Cu-Ta system, the mismatch was 22.7% (table S1). The lattice parameter of the Cu_3Li precipitates we measured was ~4.16 Å. Despite the relatively large 14.3% misfit, the faceted Cu_3Li precipitates remain coherent with the matrix phase, and we did not observe misfit dislocations around the faceted Cu_3Li precipitates (fig. S2). We believe that the atomic Ta bilayer surrounding the Cu_3Li precipitates, visible as bright atomic columns along the facets of the precipitates in Fig. 1B, plays a key role in maintaining coherency across this 14.3% misfit. This can be most clearly seen in the color-filtered HAADF-STEM image in Fig. 1D. Moreover, because of the high melting point of Ta (3020°C), this bilayer of Ta serves to thermally stabilize the precipitates against coarsening, given the limited mobility of Ta in the Cu matrix.

We collected additional HAADF-STEM images of the Cu_3Li precipitate from the [110] and [100] crystallographic directions of a face-centered cubic (fcc) matrix grain (fig. S3). We observed a coherent cube-on-cube crystallographic orientation relationship between the fcc matrix grains and the faceted, cuboidal Cu_3Li precipitates (fig. S3, A and E). This relationship demonstrates that the Cu_3Li precipitates are cubic and coherent with the matrix.

Atom probe tomography (APT) results of the Cu-Ta-Li confirm that Li atoms exist mainly within Cu-rich precipitates, having a composition of ~25 at % Li and ~75 at % Cu (Fig. 2). Furthermore, the concentrations of Li and Cu within these precipitates vary periodically and inversely on the atomic scale (Fig. 2D), with a period on the order of 0.3 to 0.4 nm, suggesting that the Cu_3Li precipitates have an ordered crystal structure with alternating Li-rich atomic planes along the [001] crystallographic direction consisting of either nearly 100 at % Cu or ~50 at % Li and ~50 at % Cu. This compositional variation is consistent with, although not specific to, the $Pm\bar{3}m$ space group, to which the ordered, cubic $L1_2$ crystal structure belongs. APT results also show that the addition of Li to Cu-Ta reduces the average precipitate size, as seen in the cumulative distribution plot (fig. S4), in which the fraction of precipitate with a size of <5 nm is greatly increased. This reduction in precipitate size is accompanied by an increase in the number density of precipitates, from $5.3 \times 10^{23}/m^3$ in

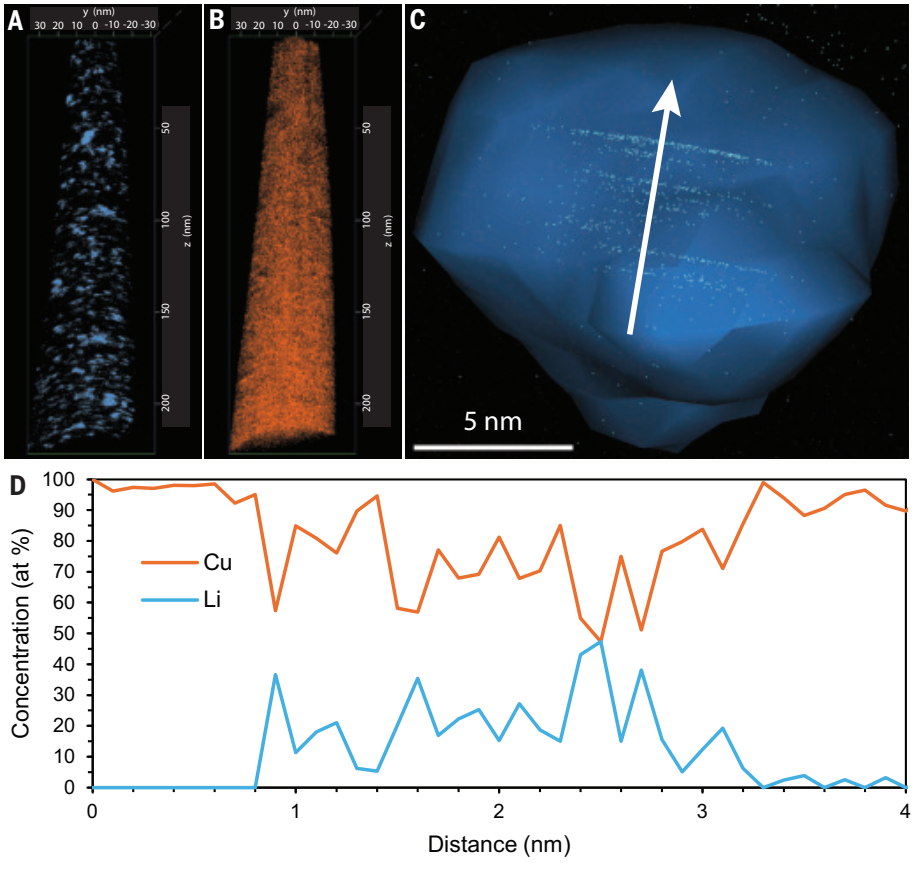

Fig. 2. APT results from Cu-3Ta-0.5Li. (**A**) Atom map for Cu-3Ta-0.5Li displaying only the Li atoms over the entire tip. (**B**) Atom map for Cu-3Ta-0.5Li displaying only the Cu atoms over the entire tip. (**C**) Higher-magnification map highlighting the periodicity of the locus of Li atoms within an $L1_2$ precipitate (delineated by a 1 at % Li isoconcentration surface); the white arrow denotes the direction of the one-dimensional concentration profile. (**D**) One-dimensional concentration profile, taken by placing the region of interest vertically through the interface between the $L1_2$ precipitate and the Cu matrix interface, showing the periodic spacing of the Li and Cu planes.

Cu-3Ta to $6.3 \times 10^{23}/m^3$ in Cu-3Ta-0.5Li. Moreover, APT results demonstrate that chemical order exists within the Cu_3Li precipitates, with Cu and Li concentrations varying periodically on the atomic scale. Taken together, the HAADF-STEM images and APT results suggest that the Cu_3Li precipitates have an ordered, cubic crystal structure. This structure is likely the $L1_2$ crystal structure, although we cannot entirely rule out the possibility of a different ordered, cubic structure.

Atomistic origin of the precipitate formation

To investigate the atomistic origin of Cu_3Li precipitate formation and stability, we applied density functional theory (DFT) (*22*, *23*), using the Vienna ab initio simulation package (*24*). In accordance with the experimental observations, we modeled Cu_3Li with the $L1_2$ crystal structure in these simulations. We performed the interface energy and electronic charge transfer calculations to assess the stability of Cu_3Li and the role of the atomic bilayer of Ta at the phase boundary. First, we obtained elastic constants, with C_{11} of 107.2 GPa, C_{12} of 85.6 GPa, C_{44} of 62.3 GPa, and bulk modulus of 92.8 GPa. These constants satisfy the stability criterion for the cubic systems; hence, we found the structure to be stable. Next, we found the ideal work of separation (W_{sep}) to be 3.33 and 1.11 J/m^2 for a Cu_3Li precipitate with and without the Ta atomic bilayer, respectively. These results suggest that Cu_3Li precipitates with the Ta bilayer are more mechanically stable, as the W_{sep} is a direct measure of the interface bond strength. Similarly, we computed the interface energy to be 1.11 and 4.76 J/m^2 for a Cu_3Li precipitate with and without the Ta bilayer, respectively. The markedly lower interface energy in the presence of the Ta bilayer is consistent with the stability of the Cu_3Li precipitates, as we observed experimentally.

To further elucidate the role of the Ta bilayer on the structural stability of Cu_3Li, the local density of states (LDOS) shows the electronic distribution of each orbital on a particular atom (Fig. 3, A to D). After analyzing the LDOS for Ta atoms (Fig. 3, A and C), we conclude that in the case of Ta next to Li, a larger contribution originates from the 6s orbital in Ta bonding with Li (i.e., the red line in Fig. 3B). Moreover, in the case of Ta next to Cu, the bond formation occurs at a deeper level as compared with Fig. 3A, which shows more bonding in the $5d_{xy}$ and the $5d_{z2}$ orbitals (i.e., the deep blue and cyan lines in Fig. 3A). Similarly, Li atoms present in the Cu_3Li cluster surrounded by an atomic bilayer of Ta also show more states per electron volt (Fig. 3B) than Li atoms in bulk Cu_3Li in the absence of Ta (Fig. 3D). Overall, these calculations reveal that the electronic configuration of the Ta atomic bilayer plays a critical role in the formation and stability of Cu_3Li. Furthermore, the charge transfer plot (Fig. 3, H and J) reveals that charge is being lost from the Ta bilayer and moving toward the Cu_3Li phase, and from the top layer of Cu_3Li to the Cu substrate, as shown from the top in Fig. 3, E and F, and at the interface in Fig. 2, G to J. A total of 8.14 electrons moved from the top Cu_3Li with Ta to the lower Cu substrate, indicating a strong electron transfer. This DFT analysis indicates that Cu_3Li precipitates with the $L1_2$ crystal structure are energetically favorable and that the atomic bilayer of Ta acts as a buffer to absorb electrons from the Cu_3Li precipitates. The analysis further suggests that the Ta bilayer acts to prevent the dissolution of Cu_3Li at high temperatures, increasing the thermal stability of the alloy and preventing the overaging typically seen in Cu alloys at elevated temperatures.

Long-term annealing

The yield strength of Cu-3Ta-0.5Li after isothermal annealing at 800°C [0.8 melting temperature (T_M)] remains almost constant regardless of aging time, experiencing only a 4% decrease in its yield strength from 983 to 947 MPa after 10,000 hours, in contrast to Cu-3Ta, whose yield strength rises initially but ultimately drops by 20% to ~800 MPa (fig. S5). STEM imaging of the two alloys reveals that the Cu-3Ta alloy (fig. S6A) suffers from abnormal grain growth and an approximate doubling in average grain size compared with Cu-3Ta-0.5Li (figs., S6B, S7D, and S8C). The average grain size of the Cu-Ta-Li alloy increased from 35 to 91 nm (refer to histogram in fig. S7), a growth rate equivalent to 0.035 Å/hour, or ~100 hours to grow the distance of one lattice parameter in Cu (i.e., 3.62 Å). This growth rate is one-third that of the binary Cu-3Ta alloy. The ability of the ternary Cu-Ta-Li alloy to maintain a uniform grain size and to resist coarsening is attributable to the coherence of the Cu_3Li precipitates with the matrix, the electronic contributions from the Ta bilayer, and the tendency of the Cu_3Li precipitates to adopt discrete diameters in a manner that inhibits coarsening.

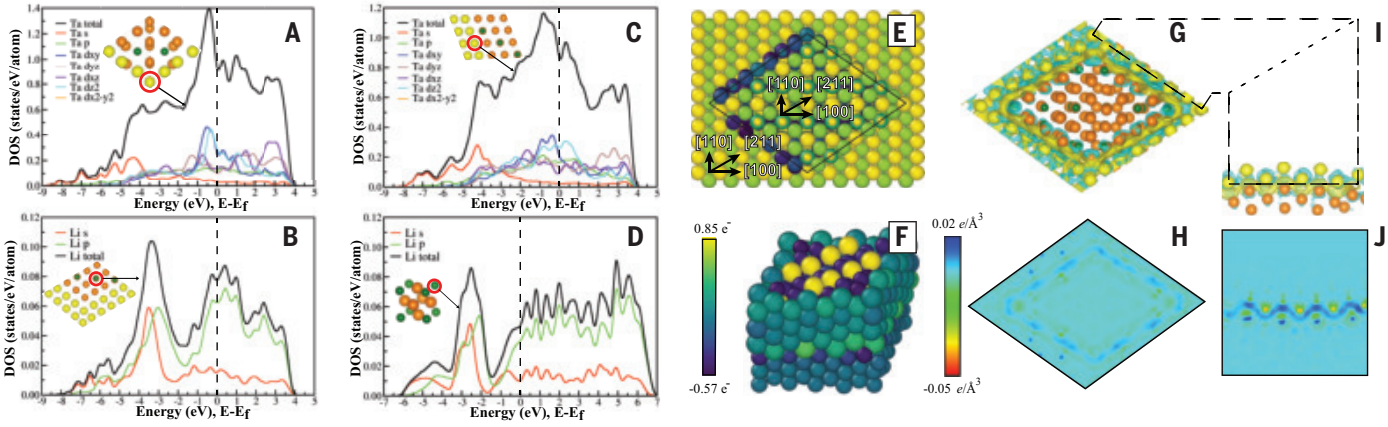

Fig. 3. DFT simulations of electronic and structural properties. (**A**) LDOS of Ta at interface having Cu atoms as nearest neighbors (orange spheres are of Cu, green spheres are Li, and yellow spheres are Ta atoms). (**B**) LDOS of Li atoms present in Cu_3Li with a Ta bilayer at the phase boundaries. (**C**) LDOS of Ta atoms at the interface with the nearest neighbor Li atom; comparison of (A) with (C) reveals participation from the 6s, $5d_{xy}$, and $5d_{z2}$ orbitals [i.e., red, deep blue, and cyan lines in (A) and (C), respectively] in Ta. (**D**) LDOS of Li in case of pure Cu_3Li bulk crystal; comparison of (B) with (D) reveals deeper electron occupation in (B) and hence is electronically stable. (**E**) Cu_3Li precipitate embedded in the Cu matrix atoms, color-coded by depth into the plane; directions for matrix and precipitate follow cube-on-cube relationship as observed in STEM imaging. (**F**) Structure of the interface with color-coding applied to each atom according to the Bader net atomic charge. (**G**) Valence charge transfer between the Cu_3Li precipitate and Ta bilayer phase boundary is shown with an isosurface value of 0.0025 $e/Å^3$; positive and negative isosurface are shown in yellow and cyan, respectively. (**H**) Two-dimensional slice of the interface as that in (G); a darker blue shade implies more charge is present at the boundary with Ta. (**I**) Valence charge transfer at the cross section of the Ta boundary around the Cu_3Li precipitate and Cu matrix, isosurface value of 0.0025 $e/Å^3$. (**J**) Two-dimensional slice of the plane in (I) shows Ta atoms in the bright red spots and Cu in the blue spots.

As shown in Fig. 1D, the atomic columns of the relatively Li-rich lattice of the Cu_3Li precipitate (blue atoms) and the Cu matrix (orange atoms) overlap and become coincident once every eight matrix atoms. This periodicity suggests that the Cu_3Li precipitates may nucleate and grow in a stepwise fashion, resulting in a set of discrete, preferred precipitate dimensions. On the basis of STEM analysis of Cu_3Li precipitate dimensions, the Cu_3Li precipitates have a multimodal size distribution with peaks centering on 1.6, 3.2, 4.8, and 6.4 nm (fig. S9). The gaps between these preferred precipitate dimensions imply that a discontinuous energetic barrier to coarsening exists that must be overcome for coarsening to occur, consistent with the notable thermal stability of the Cu-Ta-Li alloy.

We compare the yield strength at elevated temperatures of Cu-Ta-Li, Cu-Ta, commercial Cu alloys (*25*, *26*), and pure Cu (*27*) (Fig. 4A). Representative values of yield strength from the commercial alloys Glidcop AL-15, GRCop-42, GRCop-84, and NARloy-Z were taken from the literature (*25*, *26*), as well as values for pure Cu (*27*). These commercial alloys were chosen for comparison because they are among the best high-temperature copper alloys available in terms of retaining mechanical strength at elevated temperature. Although these commercial alloys have other desirable properties as well, such as high thermal conductivity and oxidation resistance, we focus here on their mechanical properties. Although their room-temperature yield strength is lower than that of high-strength copper alloys such as Cu-Be, their high-temperature yield strength is superior. Compared with these high-temperature commercial copper alloys, our Cu-Ta-Li alloy has the highest yield strength of 1120 MPa at room temperature, which is several times higher than those of the commercial Cu alloys and somewhat higher than those of the Cu-Ta alloys. Although Cu-Ta-Li exhibits a marked drop in yield strength at 673 K when compared with Cu-Ta alloys, the difference becomes smaller at even higher temperatures. The drop in strength of Cu-Ta-Li at intermediate temperatures is probably linked to the highly coherent interface of the Cu_3Li precipitates. These coherent interfaces are more prone to being bypassed by dislocations at elevated temperatures compared with the spherical Ta-rich precipitates in the binary Cu-Ta alloys.

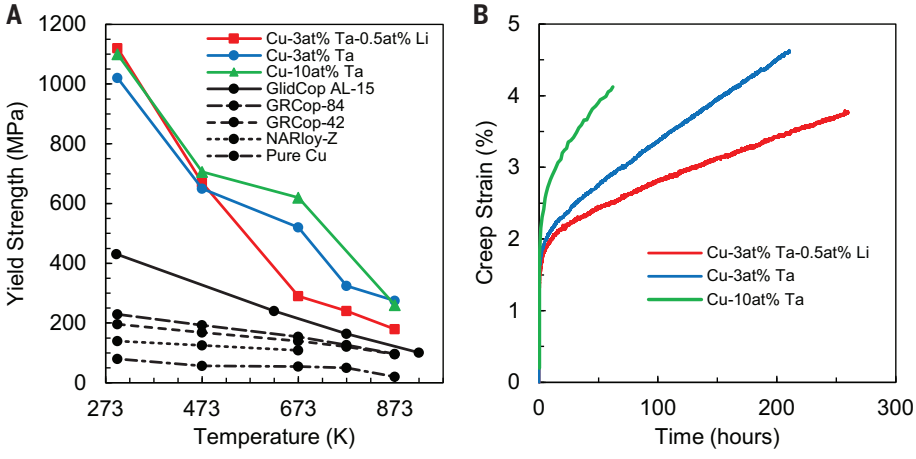

Fig. 4. Mechanical behavior comparison of Cu-Ta-Li, Cu-Ta, and commercial Cu alloys. (**A**) Yield strength at elevated temperatures. (**B**) Compressive creep behavior at 873 K (0.64 T_M) under applied stress of 0.5 YS.

We obtained compressive creep strain as a function of time at a temperature of 873 K (0.64 T_M) at an applied stress of 0.5 of the yield strength (0.5 YS) and compared it with Cu-3Ta and Cu-10Ta (*15*) (Fig. 4B). In general, fcc materials such as Cu do not show tension-compression asymmetry as has been demonstrated in nanocrystalline Cu-Ta (*15*); therefore, the creep behavior in compression is comparable to tension (*28*). Nevertheless, in the case of Cu-3Ta-0.5Li, a prominent primary creep regime can be identified. Similar to the case of Cu-3Ta, the large

primary creep strain was found to follow a cubic-root dependence with respect to time ($t^{1/3}$). This behavior is consistent with the Andrade β-flow theory (*28*). The primary creep is transient in nature and eventually culminates into a steady-state creep behavior. Upon the application of stress, certain regions within the microstructure experience stress concentrations, such as grain boundaries and triple junctions. The local stresses in those regions are higher than the applied global stress but lower than the stress required to cause local yielding (*28*). As such, the microstructure undergoes relaxation to overcome the local stress buildup, which slows down with time. This relaxation can explain the primary creep deformation observed in Cu-Ta-Li. Thus, elevated temperatures and reduced stresses lead to quicker relaxation toward equilibrium, causing the emergence of lower instantaneous strains. When compared with the three Cu-Ta alloys, Cu-Ta-Li demonstrates higher resistance to creep deformation than Cu-3Ta and Cu-10Ta at 0.64 T_M and 0.5 YS.

Processing and microstructure

The microstructure of the Cu-Ta-Li alloy, with its ordered Cu_3Li precipitates and their Ta-rich atomic bilayer phase boundary complexions, was achieved via powder metallurgy and high-energy cryogenic milling. We hypothesize that this processing approach forces the Ta into a metastable solid solution, and subsequent annealing of the green compact enables the Ta to diffuse small distances during the formation of the Cu_3Li precipitates. The Ta migrates far enough to effectively cap the precipitates by forming the Ta-rich bilayer phase boundary complexion. This Ta bilayer then effectively inhibits coarsening by slowing diffusion into and out of the precipitates, making the overall microstructure highly resistant to further changes. The combination of high-energy cryogenic milling and alloying with an element, Ta, that is essentially immiscible in the base Cu-rich phase of the alloy appears to be responsible for the presence of the Ta-rich bilayer complexion that enables the formation of the Cu_3Li precipitates, stabilizes these precipitates against coarsening, and results in the excellent high-temperature properties of the alloy.

Parallels with superalloys

The Cu_3Li precipitates we discovered have many parallels with γ′ precipitates in superalloys; they are chemically ordered, appear to have the same L_{12} crystal structure, are coherent with the matrix, and exhibit cuboidal morphology. Their presence makes the Cu-3Ta-0.5Li alloy structurally similar to γ/γ′ superalloys, in which the γ′ phase is the primary strengthening phase and is largely responsible for high-temperature properties and performance. In addition to forming the Cu_3Li precipitates, alloying Li with Cu-Ta results in the formation of a Ta-rich bilayer complexion that surrounds the Cu_3Li precipitates. This atomic bilayer of Ta protects the Cu_3Li nanoprecipitates from dissolution and overaging. Furthermore, the Ta bilayer plays a key role in maintaining coherency between the Cu_3Li precipitates and the matrix. These physical attributes permit the Cu-Ta-Li alloy to operate in elevated temperatures with minimal creep and loss of strength, in a manner similar to superalloys albeit at somewhat lower temperatures, thereby substantially expanding the current application space of Cu alloys.

Conclusions

By alloying Li with Cu-Ta, we discovered a nanocrystalline copper alloy with exceptional thermal stability and high-temperature mechanical properties. The basis of its thermal stability and performance is the formation of precipitates of Cu_3Li, which have an ordered cubic crystal structure and are capped by a Ta-rich bilayer phase boundary complexion that forms at the interface between the precipitates and the matrix.

The cuboidal Cu_3Li precipitates exhibit a stronger coherent relationship with the Cu matrix than their spherical predecessors in binary Cu-Ta and contribute to the retention of yield strength even after long-term, high-temperature exposure. This retention of yield strength is attributed to the much slower grain growth kinetics of Cu-3Ta-0.5Li, equivalent to a coarsening rate of one Cu lattice parameter per 100 hours at 800°C (0.8 T_M).

The microstructure of this Cu-Ta-Li alloy parallels the classic γ/γ′ structure of some traditional superalloys, which is fundamental to the stability and performance of those superalloys (*1*, *2*). Furthermore, the Cu-Ta-Li is a true high-temperature alloy, maintaining higher yield strength at elevated temperatures than some of the best available high-temperature commercial copper alloys. Although this Cu-Ta-Li alloy is not a direct substitute for traditional superalloys, given that its potential service temperature range is on the lower end of superalloys, it has the potential for use alongside other superalloys in a complementary role.

The alloy design strategy of alloying Cu-Ta with Li—an element that is immiscible with Ta, soluble in Cu, and highly reducing—could potentially be exploited and perhaps generalized to develop other high-temperature alloys with the γ/γ′-type microstructure and similar microstructures that rely on thermally stable precipitates for high-temperature applications.

REFERENCES AND NOTES

1. R. C. Reed, *The Superalloys: Fundamentals and Applications* (Cambridge Univ. Press, 2008).
2. W. Betteridge, S. W. K. Shaw, *Mater. Sci. Technol.* **3**, 682–694 (1987).
3. M. Sundararaman, P. Mukhopadhyay, S. Banerjee, *Acta Metall.* **36**, 847–864 (1988).
4. I. Adlakha, P. Garg, K. N. Solanki, *J. Alloys Compd.* **797**, 325–333 (2019).
5. J. Tiley *et al.*, *Acta Mater.* **57**, 2538–2549 (2009).
6. S. J. Dillon, M. Tang, W. C. Carter, M. P. Harmer, *Acta Mater.* **55**, 6208–6218 (2007).
7. S. J. Dillon, M. P. Harmer, J. Luo, *J. Miner. Met. Mater. Soc.* **61**, 38–44 (2009).
8. P. R. Cantwell *et al.*, *Acta Mater.* **62**, 1–48 (2014).
9. P. R. Cantwell *et al.*, *Annu. Rev. Mater. Res.* **50**, 465–492 (2020).
10. M. P. Harmer, *Science* **332**, 182–183 (2011).
11. M. Kuzmina, M. Herbig, D. Ponge, S. Sandlöbes, D. Raabe, *Science* **349**, 1080–1083 (2015).
12. S. Pemma, R. Janisch, G. Dehm, T. Brink, *Phys. Rev. Mater.* **8**, 063602 (2024).
13. J. Luo, H. Cheng, K. M. Asl, C. J. Kiely, M. P. Harmer, *Science* **333**, 1730–1733 (2011).
14. Z. Yu *et al.*, *Science* **358**, 97–101 (2017).
15. K. A. Darling *et al.*, *Nature* **537**, 378–381 (2016).
16. P. R. Subramanian, D. E. Laughlin, *Bull. Alloy Phase Diagr.* **10**, 652–655 (1989).
17. M. Rajagopalan *et al.*, *Mater. Today* **31**, 10–20 (2019).
18. B. C. Hornbuckle *et al.*, *Commun. Mater.* **1**, 22 (2020).
19. B. C. Hornbuckle *et al.*, *Appl. Phys. Lett.* **116**, 231901 (2020).
20. S. Srinivasan *et al.*, *Acta Mater.* **195**, 621–630 (2020).
21. M. Rajagopalan *et al.*, *Mater. Des.* **113**, 178–185 (2017).
22. Q. Zhao, R. G. Parr, *J. Chem. Phys.* **98**, 543–548 (1993).
23. Q. Zhao, R. C. Morrison, R. G. Parr, *Phys. Rev. A* **50**, 2138–2142 (1994).
24. G. Kresse, J. Hafner, *Phys. Rev. B Condens. Matter* **47**, 558–561 (1993).
25. H. C. de Groh III, D. L. Ellis, W. S. Loewenthal, *J. Mater. Eng. Perform.* **17**, 594–606 (2008).
26. R. P. Minneci, E. A. Lass, J. R. Bunn, H. Choo, C. J. Rawn, *Int. Mater. Rev.* **66**, 394–425 (2021).
27. K. A. Darling, E. L. Huskins, B. E. Schuster, Q. Wei, L. J. Kecskes, *Mater. Sci. Eng. A* **638**, 322–328 (2015).
28. C. Kale *et al.*, *Acta Mater.* **199**, 141–154 (2020).

ACKNOWLEDGMENTS

The authors acknowledge A. J. Roberts, B. Fullenwider, and A. Ostlind for the synthesis of the Cu-Ta and Cu-Ta-Li powder; J. Priedeman and G. B. Thompson for conducting and monitoring the 10,000-hour annealing experiments; and Y. Mishin for fruitful discussion. **Funding:** US Army Research Laboratory (contract W911NF-15-2-0038 to S.S., S.N., and K.S.); National Science Foundation (grants 1663287 and 1810431 to S.S., S.N., and K.S.); Army Research Laboratory [Cooperative Agreement Number W911NF-22-2-0032, Lightweight High Entropy Alloy Design (LHEAD) Project to M.P.H., C.J.M, J.A.S., and P.R.C.]; and Lehigh University Presidential Nano-Human Interfaces (NHI) Initiative (to M.P.H., C.J.M, J.A.S., and P.R.C.). **Author contributions:** B.C.H., K.S., and K.A.D. equally contributed to developing the idea. B.C.H. and K.A.D. processed the nanocrystalline materials and performed the aging treatments. B.C.H., J.A.S., and C.J.M. performed the microstructural characterization. S.N. and K.S. performed the DFT calculations. S.S. performed thermomechanical experiments. B.C.H., J.A.S., S.S, S.N., C.J.M., M.P.H., K.S., K.A.D., and P.R.C. analyzed the data. K.A.D., B.C.H., J.A.S., C.J.M., K.S., and P.R.C. wrote the paper. K.A.D., B.C.H., J.A.S., C.J.M., P.R.C., S.S., S.N., and K.S. edited the figures. M.P.H. supervised J.A.S., and K.S. supervised S.S. and S.N. **Competing interests:** A US patent (patent no. US 11,975,385 B2) for the Cu-Ta-Li alloy was granted on May 7, 2024. The patent applicant was US Army DEVCOM, Army Research Laboratory, Adelphi, MD (US). The inventors are K. A. Darling, B. C. Hornbuckle, B. P. Fullenwider, A. M. Ostlind, A. J. Roberts, and A. K. Giri. **Data and materials availability:** Data are available in the main text and supplementary materials.

SUPPLEMENTARY MATERIALS

science.org/doi/10.1126/science.adr0299
Materials and Methods
Figs. S1 to S12
Tables S1 and S2

Submitted 25 June 2024; accepted 7 February 2025
10.1126/science.adr0299

PLANT PATHOLOGY

A wheat tandem kinase and NLR pair confers resistance to multiple fungal pathogens

Ping Lu[1]*†, Gaohua Zhang[2,3]†, Jing Li[4]†, Zhen Gong[5]†, Gaojie Wang[1], Lingli Dong[1], Huaizhi Zhang[1], Guanghao Guo[1], Min Su[2], Ke Wang[2], Yueming Wang[2], Keyu Zhu[1], Qiuhong Wu[6], Yongxing Chen[6], Miaomiao Li[1], Baoge Huang[1,3], Beibei Li[1,3], Wenling Li[1,3], Lei Dong[1,3], Yikun Hou[1,3], Xuejia Cui[1,3], Hongkui Fu[1,3], Dan Qiu[1], Chengguo Yuan[7], Hongjie Li[6]*, Jian-Min Zhou[1,8]*, Guan-Zhu Han[5,8]*, Yuhang Chen[2,3]*, Zhiyong Liu[1,3,9]*

Tandem kinase proteins underlie the innate immune systems of cereal plants, but how they initiate plant immune responses remains unclear. This report identifies wheat protein wheat tandem NBD 1 (WTN1), a noncanonical nucleotide-binding leucine-rich repeat (NLR) receptor featuring tandem nucleotide binding adaptor shared by APAF-1, plant R proteins, and CED-4 (NB-ARC) domains, required for WTK3-mediated disease resistance. Both WTK3 and its allelic variant Rwt4—known for conferring resistance to wheat powdery mildew and blast, respectively—are capable of recognizing the blast effector PWT4. They activate WTN1 to form calcium-permeable channels, akin to ZAR1 and Sr35. Thus, tandem kinase proteins and their associated NLRs operate as "sensor-executor" pairs against fungal pathogens. Additionally, evolutionary analyses reveal a coevolutionary trajectory of the tandem kinase-NLR module, highlighting their cooperative role in triggering plant immunity.

To combat pathogens, plants have evolved a highly sophisticated immune system that includes both surface-localized and intracellular receptors. Most cloned resistance genes encode intracellular nucleotide-binding leucine-rich repeat (NLR) receptors (*1*, *2*). Plant NLRs function in various forms—singletons, pairs, or within complex networks—to bolster plant immunity. Singleton NLRs typically trigger hypersensitive immunity by detecting effectors either directly or indirectly (*3*–*6*). NLR pairs consist of a sensor NLR that recognizes effectors and a helper NLR responsible for immune signaling (*3*, *7*). These paired NLR genes usually are arranged in a head-to-head orientation in plant genomes, and their proteins undergo hetero-oligomerization to form "dimers of heterodimers," which initiate immune response and cell death (*7*). Within the NLR network, helper NLRs are members of the NLR required for cell death (NRC) family, exhibiting specificity for various sensor NLRs (*3*, *8*).

[1]State Key Laboratory of Seed Innovation, Institute of Genetics and Developmental Biology, Chinese Academy of Sciences, Beijing, China. [2]State Key Laboratory of Molecular Developmental Biology, Institute of Genetics and Developmental Biology, Chinese Academy of Sciences, Beijing, China. [3]College of Advanced Agricultural Sciences, University of Chinese Academy of Sciences, Beijing, China. [4]College of Bioscience and Resources Environment, Beijing University of Agriculture, Beijing, China. [5]College of Life Sciences, Nanjing Normal University, Nanjing, Jiangsu, China. [6]Institute of Biotechnology, Xianghu Laboratory, Hangzhou, Zhejiang, China. [7]Hebei Gaoyi Stock Seeds Farm, Gaoyi, Hebei, China. [8]Yazhouwan National Laboratory, Sanya, Hainan, China. [9]Hainan Seed Industry Laboratory, Sanya, Hainan, China.
*Corresponding author. Email: plu@genetics.ac.cn (P.L.); lihongjie@xhlab.ac.cn (H.L.); jmzhou@genetics.ac.cn (J.-M.Z.); guanzhu@njnu.edu.cn (G.-Z.H.); yuhang.chen@genetics.ac.cn (Yu.C.); zyliu@genetics.ac.cn (Z.L.)
†Those authors contributed equally to this work.

Upon recognizing pathogen effectors, the NLR proteins are activated and assemble into an oligomeric structure known as the resistosome (*9*, *10*). The wheat stem rust resistance gene *Sr35*, derived from einkorn wheat (*Triticum monococcum*), encodes an NLR receptor that directly interacts with the avirulence (Avr) effector AvrSr35, forming a pentameric complex and conferring resistance against *Puccinia graminis* f. sp. *tritici* (*11*). By contrast, the *Arabidopsis* NLR protein ZAR1 pre-associates with the pseudokinase RKS1 in a complex to detect the uridylyltransferase effector AvrAC from *Xanthomonas campestris*. The PBL2 kinase, modified by AvrAC, is recruited to the ZAR1-RKS1 complex, ultimately forming a resistosome that functions as a calcium channel to trigger immunity (*6*, *9*).

Within the *Triticeae* tribe, tandem kinase proteins are an essential family of intracellular proteins that can contribute to plant immune responses (*12*). This family encompasses a series of wheat genes conferring resistance against stripe rust (*Yr15*/*WTK1*) (*13*), stem rust (*Sr60*/*WTK2* and *Sr62*/*WTK5*) (*14*, *15*), leaf rust (*Lr9*/*WTK6-vWA*) (*16*), powdery mildew (*Pm24*/*WTK3*, *WTK4*, *Pm36*/*WTK7-TM*, *Pm57*/*WTK6b-vWA*) (*17*–*20*), and wheat blast (*Rwt4*) (*21*), as well as the barley stem rust resistance gene *Rpg1* (*22*). The precise mechanisms by which tandem kinase proteins mediate immune responses remain elusive.

A noncanonical NLR is required for *WTK3*-mediated powdery mildew resistance

To identify genes implicated in the *WTK3*-mediated powdery mildew resistance pathway, we analyzed 3860 M_2 descendants of ethyl methanesulfonate (EMS)–mutagenized wheat landrace Hulutou (HLT). M_2 generation plants were inoculated with *Blumeria graminis* f. sp. *tritici* (*Bgt*) isolate E09, avirulent to *Pm24* (*WTK3*). Among the susceptible mutants, 16 that retained an intact *WTK3* gene were chosen for subsequent RNA-sequencing and PCR amplification. Mutations leading to amino acid substitutions were identified in five mutants ($M1048^{L122F}$, $M1116^{G408E}$, $M1037^{T528I}$, $M1136^{G589S}$, and $M189^{D636N}$) of an atypical NLR protein featuring two NB-ARC domains (NBD) (figs. S1 and S2, A and C), hereafter referred to as wheat tandem NBD 1 (WTN1), located 114 kb adjacent to *WTK3* on chromosome 1DS (Fig. 1, A and B). However, overexpression of *WTN1* alone in Fielder wheat does not confer powdery mildew resistance (*17*) (fig. S3, A and B).

Two *WTK3* nonsense mutants, $M410^{W429*}$ and $M1091^{W478*}$ (*17*) (fig. S2B) were crossed with the five *WTN1* mutants (Fig. 1B). All F_1 plants from the ten crosses exhibited resistance to *Bgt* isolate E09 (Fig. 1B). Conversely, F_1 plants from half diallel crosses among the *WTN1* mutants showed high susceptibility (fig. S3C), demonstrating the essential role of *WTN1* in *WTK3*-dependent resistance to the *Bgt* pathogen.

Using *Barley stripe mosaic virus* (BSMV)-induced gene silencing (VIGS), *WTN1* expression was suppressed in the resistant HLT line. Compared with the controls plants, *WTN1* expression in the *WTN1*-knockdown plants was considerably reduced at 14 days post inoculation (dpi) with *Bgt* isolate E09, leading to increased production of powdery mildew spores (Fig. 1, C and D).

We then developed *WTN1* CRISPR-Cas9 knockout mutants in a transgenic Fielder line, WTK3-COM4, which carries a *WTK3* transgene and is resistant to *Bgt* (*17*). Wild-type (WT) Fielder contains a *wtk3*-susceptible allele, a functional *WTN1* allele on 1DS, and a homeolog, *WTN1-1B*, on 1BS, which has 91.66% amino acid sequence identity to *WTN1* (fig. S4). Two specific guide RNAs (gRNA1 and gRNA2, see fig. S4) targeting the 5′-terminus of exon 1 of *WTN1* and *WTN1-1B* were introduced into WTK3-COM4 using Agrobacterium-mediated transformation. This approach yielded eight independent knockout mutants, with KO#1 to KO#4 being double mutants for *WTN1* and *WTN1-1B*, KO#5 and KO#6 only affecting *WTN1*, and KO#7 and KO#8 specifically targeting *WTN1-1B* (fig. S5). When inoculated with *Bgt* isolate E09, KO#1 to KO#6 displayed susceptibility to powdery mildew, in contrast to the resistance observed in KO#7 and KO#8, as well as in the unedited control (Fig. 1E). These findings further confirm that *WTN1* is indispensable for *WTK3*-mediated powdery mildew resistance.

WTK3 interacts with WTN1

We conducted a comprehensive analysis to characterize the interaction between WTN1 and WTK3. A bimolecular fluorescence complementation (BiFC) assay yielded yellow fluorescent protein (YFP) fluorescence upon coexpression of FLAG-WTK3-cYFP with $WTN1^{\Delta 23}$-HA-nYFP,

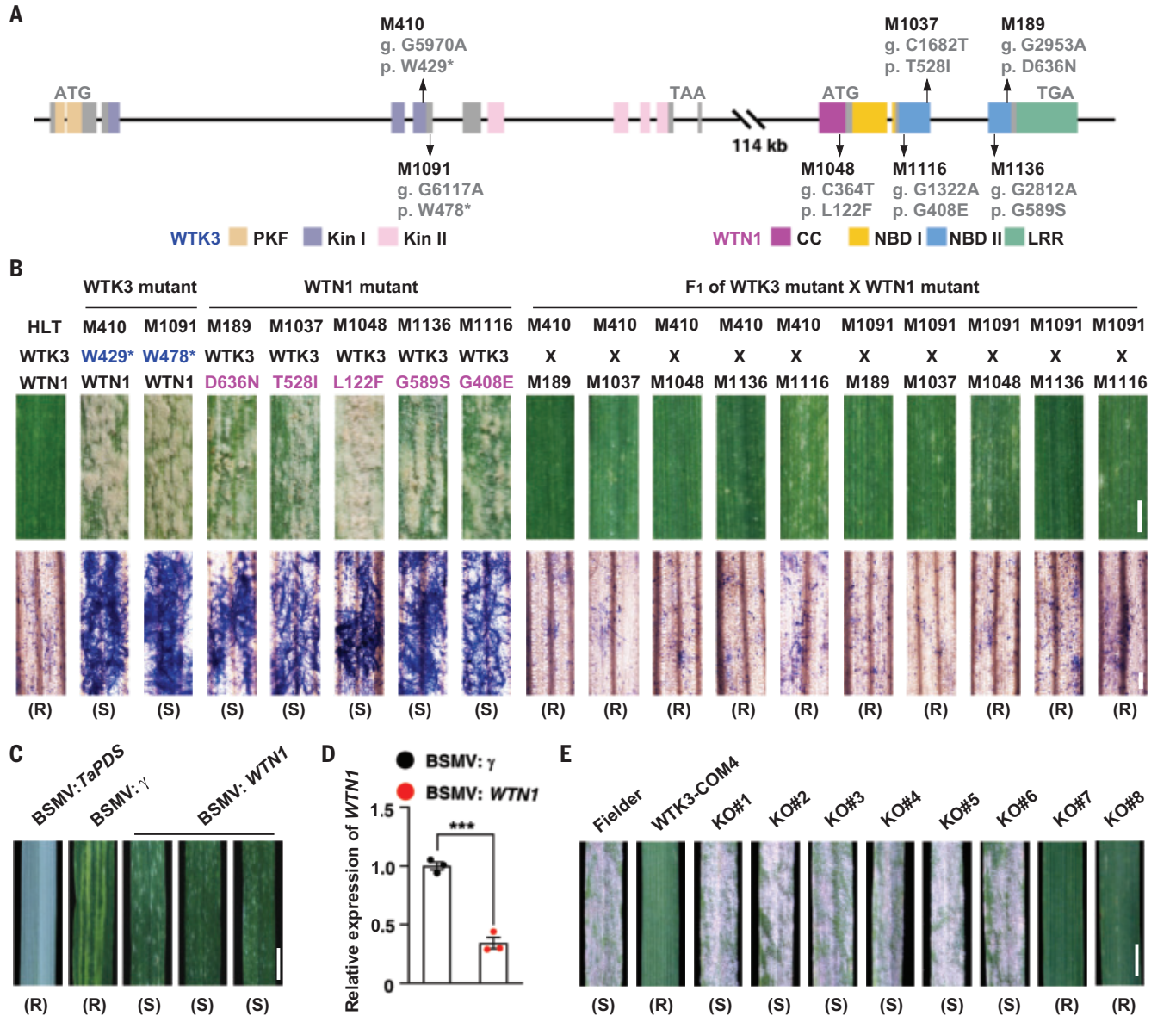

Fig. 1. Functional roles of tandem kinase *WTK3* and NLR *WTN1* in powdery mildew resistance at the *Pm24* locus. (**A**) Chromosome location and gene structures of tandem kinase *WTK3* and NLR *WTN1* on chromosome 1DS, including mutations (marked in black) and their impacts on the translated proteins in susceptible mutant lines. (**B**) Comparison of powdery mildew infection on leaves of WT HLT, susceptible mutants of *WTK3* and *WTN1*, and their F_1 hybrids. Images show representative leaves (scale bar, 0.3 cm) and Trypan blue staining to highlight fungal structures (scale bar, 200 μm). R and S indicate plant resistance and susceptibility, respectively, to powdery mildew. (**C**) Disease symptoms on the third leaves of HLT plants, following pre-inoculation with BSMV:*TaPDS* or BSMV:γ or BSMV:*WTN1* (scale bar, 0.5 cm). (**D**) Expression levels of *WTN1* in BSMV:γ and BSMV:*WTN1* plants. Data are means ± SEM (n = 3 biologically independent samples). The wheat *ACTIN1* served as an internal control. Data were analyzed by two-tailed Student's t-test (***$P < 0.001$). (**E**) Infection phenotypes of Fielder, *WTK3* transgenic line WTK3-COM4, and eight different *WTN1* CRISPR-Cas9 knockout mutants (KO#1 - KO#8) (scale bar, 0.5 cm). Reactions to powdery mildew were photographed at 14 dpi of *Blumeria graminis* f. sp. *tritici* (*Bgt*) isolate E09. In (B), (C), (D), and (E), experiments were repeated three times with similar results.

indicating an in vivo interaction between WTN1-WTK3 (Fig. 2A). This interaction was further confirmed by co-immunoprecipitation (Co-IP) and split firefly luciferase complementation (SFLC) assays in *Nicotiana benthamiana* leaves (Fig. 2, B and C). Additionally, SFLC and Co-IP assays implicated the C-terminal half of WTK3, WTK3-C (residues 521 to 893, Kin II domain), as the specific region mediating interaction with WTN1 (Fig. 2, C and D). In control experiments, WTK3 did not interact with stem rust resistance NLR protein Sr35 (*11*) and tandem kinase protein WTK2 encoded by stem rust resistance gene *Sr60* (*14*) did not interact with WTN1 (Fig. 2, B and C). These results demonstrate an interaction between WTK3 and WTN1, suggesting their cooperative role in plant immune regulation.

Rwt4/WTK3 detect avirulent protein and induce WTN1 oligomerization

Next, we sought to unravel the functional role and activation mechanism of WTN1. Wheat blast resistance gene *Rwt4* is an allelic variant of

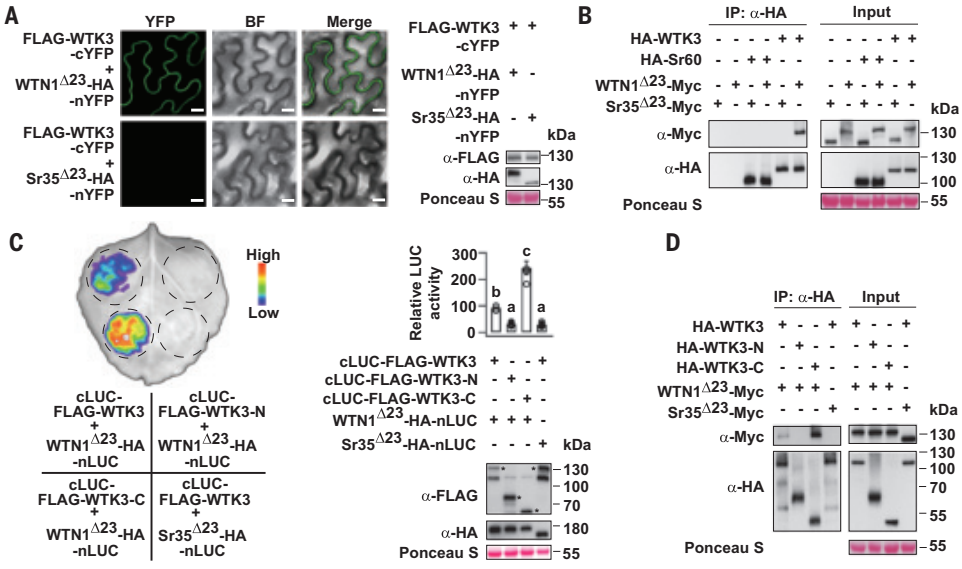

Fig. 2. WTN1 interacts with WTK3. (**A**) BiFC assay showing in vivo interaction between WTK3 and WTN1$^{\Delta 23}$ (WTN1$^{24\text{-}1038}$) in *Nicotiana benthamiana* leaves. Sr35$^{\Delta 23}$ (Sr35$^{24\text{-}919}$) served as a negative control. Scale bar, 20 μm. Target proteins were probed with indicated antibodies. Ponceau staining of ribulose-1,5-bisphosphate carboxylase/oxygenase (Rubisco) was used as a loading control. (**B**) Co-IP assay. WTK3 and Sr60 fused to 3xHA tag at the N-terminus; WTN1$^{\Delta 23}$ and Sr35$^{\Delta 23}$ fused to 6xMyc tag at the C-terminus. Sr60 and Sr35$^{\Delta 23}$ served as negative controls. (**C**) SFLC assays between WTK3, WTK3-N$^{1\text{-}500}$, WTK3-C$^{521\text{-}893}$, WTN1$^{\Delta 23}$ and Sr35$^{\Delta 23}$ in *N. benthamiana*. Data are means ± SEM (n = 5 biologically independent samples). Different letters denote the significance tested by one-way analysis of variance (ANOVA) and Tukey's post-hoc test at $P < 0.05$. Asterisks indicate the target proteins. (**D**) Co-IP assay confirming the interaction between WTK3, WTK3-N, WTK3-C, and WTN1$^{\Delta 23}$ in *N. benthamiana*. Sr35$^{\Delta 23}$ served as a negative control. The experiment was repeated three times in (A), (C), and (D) and two times in (B), with similar results.

WTK3 and recognizes the *Magnaporthe oryzae* pathotype *Triticum* effector PWT4 (*21*, *23*). Compared with WTK3, Rwt4 contains a two-residue (K400/G401) insertion in a loop within the Kin I domain, caused by a 6-bp InDel (AAAGGA/-) in the fifth exon of the two alleles (Fig. 3, A and B, and fig. S6, A and B). Thus, we took advantage of Rwt4 together with its cognate effector PWT4 to elucidate how the tandem kinase detects pathogen effectors and activates NLR to trigger immune responses.

To mimic pathogen attack, we expressed PWT4 in wheat protoplasts containing endogenous WTN1 along with either Rwt4 or WTK3, then performed luminescence-based cell viability assays. Relative luminescence activity measurements revealed that expression of PWT4 induced >90% cell death in protoplasts carrying Rwt4/WTN1 from Jagger and Cadenza, as well as in those carrying WTK3/WTN1 from WTK3-COM4, Chiyacao, and HLT lines. By contrast, protoplasts harboring only WTN1 (WTK3^{W429*}) or only WTK3 (WTN1-KO) did not undergo cell death (Fig. 3C). Control treatment with the AvrPm3bc/c2, specific for powdery mildew resistance NLR protein Pm3b (*24*), did not induce cell death, confirming the specificity of the PWT4-induced hypersensitive response. Additionally, coexpression of PWT4 with either Rwt4 and WTK3 or WTN1 alone did not induce hypersensitive response, but coexpression of Rwt4/WTN1/PWT4 or WTK3/WTN1/PWT4 together resulted in cell death in *N. benthamiana* (Fig. 3D and fig. S7). These results demonstrate that both a tandem kinase protein and an NLR are required to trigger hypersensitive responses, supporting their cooperative role in disease resistance.

When PWT4 was coexpressed with Rwt4, WTK3, or WTN1 in *N. benthamiana* leaves, both SFLC and Co-IP assays confirmed protein-protein interactions between PWT4 and Rwt4, as well as between PWT4 and WTK3 (Fig. 3, E and F). These interactions were further validated by an in vitro glutathione S-transferase (GST) pulldown assay (Fig. 3G), but no interaction was observed between PWT4 and WTN1 (fig. S8). These results consistently demonstrate that PWT4 can recognize and bind to both Rwt4 and WTK3. This is not surprising, given that WTK3 and Rwt4 differ by only two residues in Kin I domain. This finding raises the possibility that the WTK3 allele may also confer resistance to wheat blast.

To determine whether the Avr protein PWT4 can induce WTN1 oligomerization in a manner similar to that of ZAR1 and Sr35, we employed blue native–polyacrylamide gel electrophoresis to assess WTN1 oligomerization in leaves from *N. benthamiana* (fig. S9A), protoplasts from wheat cultivar Jagger (Rwt4/WTN1) (fig. S9B), and HLT (WTK3/WTN1) (fig. S9C). Coexpression of tandem kinase (WTK3 or Rwt4), WTN1, and PWT4 resulted in considerable formation and accumulation of high-molecular-weight oligomeric complexes (>880 kDa) (fig. S9, A to C), comparable to those observed in ZAR1 and SR35 resistosome (*9*, *11*). By contrast, in the control group where the tandem kinase and WTN1 were expressed alone, in pairs, or coexpressed with the irrelevant AvrPm3bc/c2, the oligomeric complexes predominantly accumulated at approximately 300 kDa (fig S9, B and C). Similar results were observed in protoplasts from FLAG-WTK3 transgenic wheat plants (FLAG-WTK3/wtk3/WTN1) (fig. S9D). Western blotting analyses confirmed the presence of the tandem kinase (WTK3 or Rwt4), WTN1 and PWT4 proteins within the high-molecular-weight bands (>880 kDa). These results indicate that PWT4 induces WTN1 oligomerization when co-expressed with tandem kinase (WTK3 or Rwt4). Additionally, SFLC and Co-IP assays revealed that PWT4 promotes the association between Rwt4 and WTN1 (fig. S10, A and B).

WTN1 activation forms calcium-permeable channels

To investigate the functional role of activated WTN1, we coexpressed WTN1 with PWT4, and either Rwt4 or WTK3 in *Xenopus laevis* oocytes, and performed two-electrode voltage clamp (TEVC) measurements (Fig. 4, A and B). No detectable currents were observed when WTN1, PWT4, Rwt4, and WTK3 cRNAs were injected individually or in pairs. However, substantial currents emerged when WTN1 was coexpressed with both PWT4 and Rwt4 (or WTK3), suggesting the formation of resistosome channels reminiscent of those formed by ZAR1 and Sr35 (*9*, *11*). Previous studies have shown that ZAR1- and Sr35-dependent currents recorded from *Xenopus* oocytes were confounded by Cl^- currents mediated through the endogenous calcium-activated chloride channel (CaCC) following Ca^{2+} influx (*6*, *9*, *11*). We hypothesized that WTN1-dependent currents might involve a similar mechanism. Supporting this, these currents were partially diminished upon application of a CaCC inhibitor (CaCCinh-A01) and completely counteracted by the calcium channel blocker $LaCl_3$ (Fig. 4C). Additionally, the hypersensitive response induced by coexpression of PWT4/Rwt4/WTN1 in *N. benthamiana* leaves was also suppressed by $LaCl_3$ (fig. S11A). These results indicate the activated

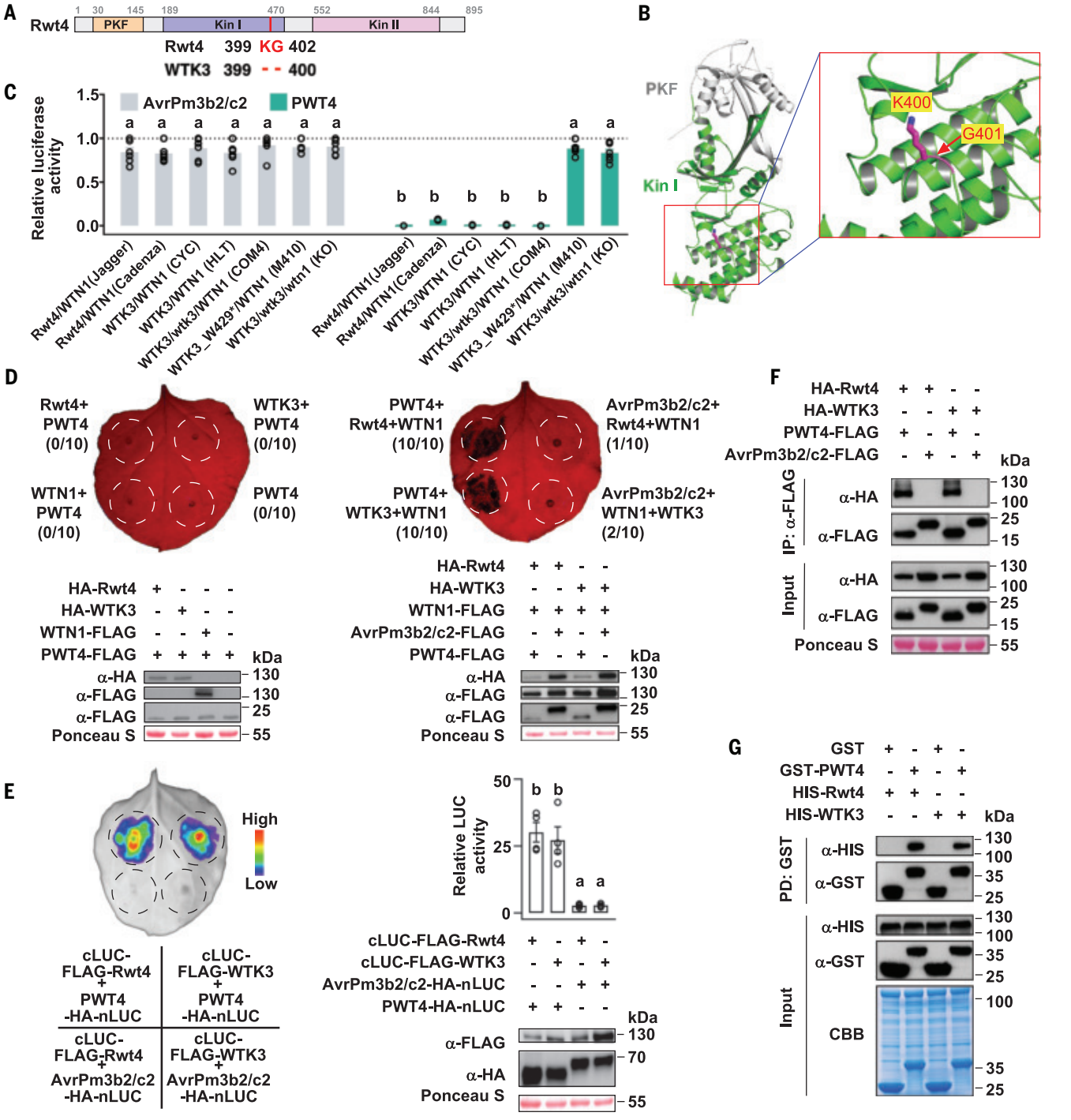

Fig. 3. Rwt4 and WTK3 interact with PWT4. (**A**) Comparison of amino acid sequences of Rwt4 and WTK3. (**B**) The N-terminus of Rwt4 protein structures was predicted using AlphaFold2. The positions of K400G401 in Kin I were shown. (**C**) Protoplast cell death assays in various wheat genotypes transfected with PWT4 and AvrPm3b2/c2, comparing genotypes with different combinations of *Rwt4/WTN1* and *WTK3/WTN1* alleles. Cell death was quantified using relative luminescence. (**D**) *N. benthamiana* leaves were co-infiltrated with Agrobacterial strains containing different pairs of constructs. Autofluorescence under UV light is shown. White dotted circles represent infected areas. Numbers indicate necrotic/total infiltrated spots. The expression of proteins was detected by immunoblot and Ponceau staining of Rubisco served as a loading control. (**E**) SFLC assay demonstrating the interaction between Rwt4/WTK3 and PWT4 in *N. benthamiana* leaves. AvrPm3b2/c2 served as a negative control. Data are means ± SEM (n = 4 biologically independent samples). Different letters denote the significance tested by ANOVA and Tukey's post-hoc test at $P < 0.05$. The expression of proteins was detected by immunoblot and Ponceau staining of Rubisco served as a loading control. (**F**) Co-IP assay confirming the interaction between Rwt4/WTK3 and PWT4 in *N. benthamiana*. AvrPm3b2/c2 served as a negative control. (**G**) PWT4 interacts with Rwt4 and WTK3 in vitro. GST-tagged PWT4 and HIS-tagged Rwt4 and WTK3 were purified from *Escherichia coli*, and protein-protein interaction was examined by a GST pull-down assay. GST was used as a control. CBB, Coomassie brilliant blue staining. The experiment was repeated for three times in (C), (D), (E), (F), and (G) with similar results.

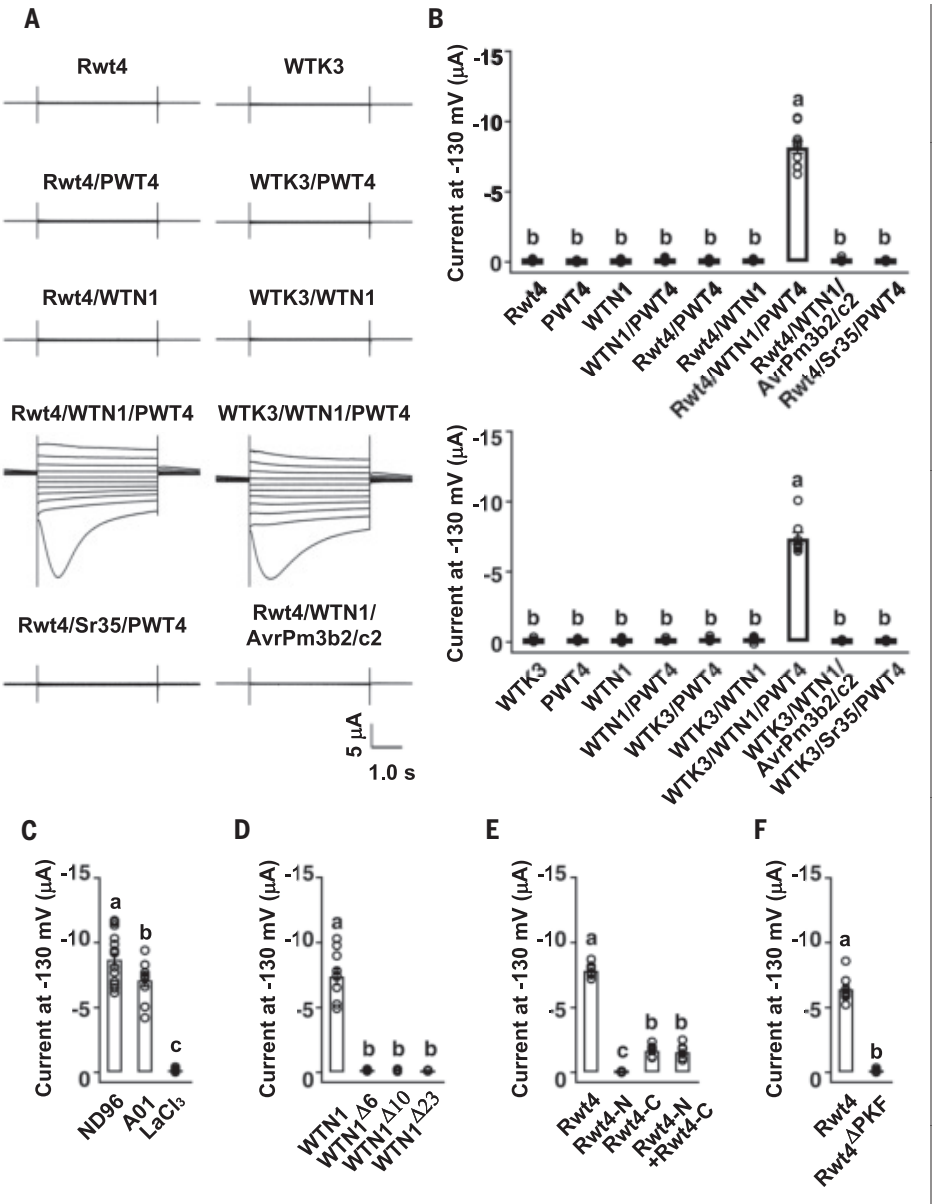

Fig. 4. Rwt4/WTK3 sense PWT4 to activate WTN1 for forming calcium-permeable channels. (**A** and **B**) TEVC measurements in *Xenopus* oocytes expressing Rwt4/WTN1/PWT4 and WTK3/WTN1/PWT4, with control oocytes injected with Rwt4/Sr35/PWT4 and Rwt4/WTN1/AvrPm3b2/c2. TEVC recordings were performed in ND96 solution. Representative current traces over arrange of voltages (from −130 mV to +70 mV in 20-mV increments) are shown in (A), and current amplitudes measured at −130 mV are shown in (B). (**C**) Electrophysiological effects of inhibitors: The impact of CaCCinh-A01 (Ca^{2+}-activated chloride channel inhibitor) and $LaCl_3$ (Ca^{2+} channel blocker) on the WTN1-dependant currents in ND96 solution, showing preincubation effects on WTK3/WTN1/PWT4–injected oocytes. (**D**) Truncational analysis of the α1-helix at the N-terminus of WTN1. Coexpressing Rwt4/PWT4 with WTN1, $WTN1^{\Delta6}$, $WTN1^{\Delta10}$, and $WTN1^{\Delta23}$ in *Xenopus*, respectively. (**E**) Truncational analysis of the N-terminus (Rwt4-N, $Rwt4^{1\text{-}480}$) and C-terminus (Rwt4-C, $Rwt4^{481\text{-}895}$) of Rwt4. Coexpressing WTN1/PWT4 with Rwt4, Rwt4-N, Rwt4-C, and Rwt4-N/Rwt4-C in *Xenopus* oocytes, respectively. (**F**) Truncational analysis of the PKF of Rwt4. Coexpressing WTN1/PWT4 with Rwt4 and $Rwt4^{\Delta PKF}$ ($Rwt4^{146\text{-}895}$) in *Xenopus* oocytes, respectively. Data are presented as means ± SEM, n ≥ 8. Different letters denote the significance tested by one-way ANOVA and Tukey's post-hoc test at $P < 0.01$. The experiment was repeated for three times in (A), (B), (C), (D), (E), and (F) with similar results.

WTN1 functions as a proxy for Ca^{2+} channels, mediating calcium-dependent immune response.

N-terminal deletions (Δ6, Δ10, and Δ23) suppressed the WTN1-dependent currents (Fig. 4D) and prevented cell death in *N. benthamiana* leaves (fig. S11B), highlighting the crucial role of the N-terminal α1 helix in forming a membrane-penetrating channel. Among the five EMS-induced WTN1 mutations, D636N markedly impaired channel activity whereas the other four mutations (L122F, G408E, T528I, and G589S) resulted in nearly undetectable currents (fig. S12A). The functional impact of these mutations was further confirmed by their inability to induce cell death in *N. benthamiana* leaves (fig. S12B). Predictive modeling using Alphafold2 elucidated that the amino acid substitutions in mutants $WTN1^{G408E}$, $WTN1^{T528I}$, $WTN1^{G589S}$, and $WTN1^{D636N}$ are located either within or proximate to the ATP binding site (fig. S12C), a region crucial for assembling the resistosome complex that mediates immune responses (*10*). These findings support the conclusion that activated WTN1 mediates plant immunity through its channel activity and that loss-of-function mutations disrupt this mechanism, thereby impairing immune function.

While the C-terminal segment of the tandem kinase protein binds the NLR, its N-terminal portion is primarily responsible for Avr detection. In vivo Y2H (fig. S13, A and B), SFLC (fig. S13C), and in vitro GST-pull down (fig. S13D) assays demonstrated that the N-terminal regions of both Rwt4 (Rwt4-N) and WTK3 (WTK3-N) interact with PWT4. Electrophysiological studies revealed that, when coexpressed with WTN1/PWT4, the N-terminal portion (Rwt4-N) could not stimulate currents, unlike the full-length Rwt4. By contrast, the C-terminal portion (Rwt4-C) elicited weak currents, but adding Rwt4-N neither enhanced nor suppressed its activity (Fig. 4E). Furthermore, this weak activity was independent of the presence or absence of Avr (fig. S13E and S13F), highlighting a direct role of the C-terminal fragment in activating WTN1. Similar results were observed in hypersensitive response triggered in *N. benthamiana* leaves (fig. S13G). Five previously identified loss-of-function mutations in WTK3, two at the N terminus (E372K and G389S) and three at the C terminus (A600T, G718R, and P835S), reduced channel activity and eliminated hypersensitive response to varying degrees, from moderate to negligible (fig. S14, A and B). These findings suggest that both kinase domains and their structural integrity are required for Avr detection, NLR activation, and resistosome channel assembly.

Further in vivo Y2H (fig. S15A), SFLC (fig. S15, B and C), in vitro GST-pull down (fig. S15D), and in vivo Co-IP (fig. S15E) assays revealed that the pseudo-kinase fragment (PKF) (residues 1 to 145) in Rwt4 can bind to PWT4, suggesting its crucial role in Avr detection. Electrophysiological studies showed that Rwt4 mutants lacking

the PKF region exhibit virtually no current, indicating an inability to recognize Avr (Fig. 4F). Additionally, deletion of the PKF region from Rwt4 lost the ability to induce cell death in *N. benthamiana* (fig. S15F). This deficiency likely prevents NLR activation, which is required to form ion channels that confer disease resistance.

Rwt4/WTK3 and WTN1 coevolved during Pooideae evolution

Rwt4/WTK3 contain a degenerated PKF and two intact kinase domains, Kin I and Kin II (fig. S16A). Kin I and Kin II were found broadly across the Pooideae subfamily, whereas the PKF is specific to the Triticeae tribe and *Lolium perenne* (fig. S17). Phylogenetic analysis delineated PKF/Kin I and Kin II into two distinct clades, with PKF sequences clustering within the diversity of Kin I sequences (fig. S16, B to D). This suggest that Rwt4/WTK3 likely originated from the fusion of two distinct kinase domains prior to the last common ancestor of Pooideae, with the PKF emerging from a recent duplication of Kin I in the early evolution of Triticeae. Crucial kinase catalytic motifs, including the ATP-binding, His-Arg-Asp (HRD), and Asp-Phe-Gly (DFG) motifs, are well-conserved in Kin I but absent or poorly conserved in the degenerated PKF and Kin II (fig. S16A), indicating the pseudo-kinase nature of PKF and Kin II. The ratio of nonsynonymous to synonymous nucleotide substitution rates (dN/dS) for PKF (0.964) and Kin I (0.896) was markedly higher than that for Kin II (0.487), suggesting that PKF and Kin I have undergone a stronger positive selection, potentially driven by host-pathogen interactions (fig. S16E). Moreover, several residues critical for immune function (such as G389, W429, A600, G679, G718, R834, and P835) (*17*) were found to be under negative selection, further emphasizing their functional relevance (fig. S16F).

The NBD domains of WTN1 segregated into two distinct clades, with orthologs of NBD I and NBD II dispersed among species within the Pooideae subfamily (figs. S17 and S18, A to C), suggesting that WTN1 orthologs originated before the last common ancestor of the Pooideae. The NBD domains from WTN1-related proteins clustered into two monophyletic groups, with each NBD group identified throughout the Poaceae, indicating that an ancestral duplication event of the NBD domain probably occurred prior to the last common ancestor of the Poaceae (fig. S19). Analysis of the distribution of Rwt4/WTK3 and WTN1 proteins across plant species revealed a pattern: The absence of Rwt4/WTK3 in certain species often coincided with the loss of the WTN1 ortholog (figs. S17 and S20). At least five instances of simultaneous losses of both Rwt4/WTK3 and WTN1 were observed (fig. S17), suggesting that the Rwt4/WTK3-WTN1 pair functioned as a cohesive module that was lost entirely during the evolution of Pooideae. Such findings further substantiate the hypothesis that Rwt4/WTK3 and WTN1 coevolved and acted in concert prior to the last common ancestor of the Pooideae.

Discussion

The "sensor-helper" relationship of NLR pairs in plant immunity has been well- characterized (*3*, *7*, *8*). In this study, we identified WTN1 as a genomic component essential for tandem kinase-mediated disease resistance in wheat. This tandem kinase-NLR protein pair functions as a disease-resistance module, capable of recognizing pathogen Avr and activating plant immunity by forming calcium-permeable channels. Our findings, together with the discovery of $Sr62^{TK}$-$Sr62^{NLR}$ (*25*), uncovers a plant defense mechanism in which tandem kinase proteins and their cognate NLRs act as "sensor-executor" duos to counteract fungal pathogens in cereal crops. Furthermore, evolutionary analyses revealed a coevolutionary trajectory of the tandem kinase-NLR module, highlighting their cooperative role in triggering plant immunity.

Compared with the ZAR1 and Sr35 resistosomes (*6*, *9*, *11*), the activation mechanism of WTN1 differs: Sr35 directly recognizes AvrSr35 to form a resistosome and trigger immune response, whereas WTN1—similar to ZAR1—relies on auxiliary Rwt4/WTK3 for indirect Avr recognition and activation. Nonetheless, they share similar yet distinct strategies for Avr detection, "decoy" versus "guard." ZAR1 teams up with a pseudokinase RKS1 (adaptor) and a PBL2 (sensor) to detect AvrAC-mediated uridylylation on PBL2, while WTN1 cooperates with Rwt4/WTK3 protein harboring two tandem kinase domains with distinct roles: The N-terminal PKF/Kin I binds Avr as a sensor, and the C-terminal Kin II interacts with NLRs, transmitting pathogen signals to activate NLRs. Our bioinformatic analysis also revealed highly conserved kinase motifs presented in Kin I, supporting the finding that Rwt4 interacts with and transphosphorylates Avr PWT4 (*26*). Thus, further investigation is needed to clarify the kinase activity of the Kin I and how it cooperates with Kin II to regulate resistosome formation. Unlike ZAR1 and Sr35, the noncanonical NLR WTN1 possesses two NB-ARC domains, with NBD I being a degenerated NB-ARC domain lacking the WHD. Further research, especially structural studies, is needed to elucidate how NBD I and NBD II, in coordination with tandem kinase, perceive Avr and assemble into the resistosome.

Wheat diseases pose major challenges to agriculture, resulting in substantial yield reductions worldwide (*27*–*29*). Identifying disease resistance genes and elucidating their mechanisms are crucial for breeding and deploying resistant wheat cultivars. The tandem kinase protein family, as a class of intracellular immune receptors, has evolved new functions through the duplication of kinase domains or the fusion with additional domains, playing a central role in mediating pathogen Avr detection and immune signaling activation. For example, the wheat blast resistance genes *Rmg7* and *Rmg8* are homeologs of the powdery mildew resistance gene *Pm4*, encoding a serine/threonine kinase and multiple C2 domains and transmembrane regions (*30*, *31*). Allelic variations in tandem kinase proteins significantly influence resistance to different pathogens in wheat (*16*, *17*, *20*, *21*). *Rwt4* was identified as a resistance gene against *M. oryzae* pathotype *Triticum* (*21*) through its Avr PWT4, whereas its allele *Pm24* (*WTK3*) gained resistance to powdery mildew through a two–amino acid (^{399}KG^{400}) deletion (*17*). Our work demonstrated that *Pm24* (*WTK3*), like *Rwt4*, can sense PWT4 and activate WTN1 to form calcium channel for triggering immunity. Further validation of whether *Pm24* (*WTK3*) confers resistance to wheat blast will provide valuable insights for developing wheat cultivars with broad-spectrum disease resistance.

In plant defense, pathogen-specific recognition and immune signal activation are central to disease resistance. The wheat tandem kinase-NLR module exhibits potentially distinct structural and functional mechanisms, making it a focus of plant immunity research. Moreover, the broad-spectrum disease resistance of these modules makes them promising targets for breeding. In the future, in-depth research into the mechanisms of tandem kinase-NLR, particularly the underlying mechanisms mediated by WTK3 against wheat powdery mildew and blast, will provide new strategies for molecular breeding and contribute to sustainable agricultural development.

REFERENCES AND NOTES

1. B. P. M. Ngou, P. Ding, J. D. G. Jones, *Plant Cell* **34**, 1447–1478 (2022).
2. S. Cesari, *New Phytol.* **219**, 17–24 (2018).
3. H. Adachi, L. Derevnina, S. Kamoun, *Curr. Opin. Plant Biol.* **50**, 121–131 (2019).
4. S. Ma *et al.*, *Science* **370**, eabe3069 (2020).
5. R. Martin *et al.*, *Science* **370**, eabe9993 (2020).
6. G. Bi *et al.*, *Cell* **184**, 3528–3541.e12 (2021).
7. Y. Yang *et al.*, *Science* **383**, eadk3468 (2024).
8. C. H. Wu *et al.*, *Proc. Natl. Acad. Sci. U.S.A.* **114**, 8113–8118 (2017).
9. J. Wang *et al.*, *Science* **364**, eaav5870 (2019).
10. J. Wang *et al.*, *Science* **364**, eaav5868 (2019).
11. A. Förderer *et al.*, *Nature* **610**, 532–539 (2022).
12. T. Reveguk *et al.*, *Nat. Genet.* **57**, 254–262 (2025).
13. V. Klymiuk *et al.*, *Nat. Commun.* **9**, 3735 (2018).
14. S. Chen *et al.*, *New Phytol.* **225**, 948–959 (2020).
15. G. Yu *et al.*, *Nat. Commun.* **13**, 1607 (2022).
16. Y. Wang *et al.*, *Nat. Genet.* **55**, 914–920 (2023).
17. P. Lu *et al.*, *Nat. Commun.* **11**, 680 (2020).
18. K. Gaurav *et al.*, *Nat. Biotechnol.* **40**, 422–431 (2022).
19. M. Li *et al.*, *Nat. Commun.* **15**, 3124 (2024).
20. Y. Zhao *et al.*, *Nat. Commun.* **15**, 4796 (2024).
21. S. Arora *et al.*, *Nat. Plants* **9**, 385–392 (2023).
22. R. Brueggeman *et al.*, *Proc. Natl. Acad. Sci. U.S.A.* **99**, 9328–9333 (2002).
23. Y. Inoue *et al.*, *Science* **357**, 80–83 (2017).
24. S. Bourras *et al.*, *Nat. Commun.* **10**, 2292 (2019).
25. R. J. Chen *et al.*, *Science* **387**, eadp5034 (2025).
26. Y-C. Sung *et al.*, Direct binding of a fungal effector by the wheat RWT4 tandem kinase activates defense. BioRxiv [preprint] 2024.04.30.591956; https://doi.org/10.1101/2024.04.30.591956.

27. R. P. Singh *et al*., *Annu. Rev. Phytopathol.* **54**, 303–322 (2016).
28. B. K. Singh *et al*., *Nat. Rev. Microbiol.* **21**, 640–656 (2023).
29. D. N. L. Pequeno *et al*., *Nat. Clim. Chang.* **14**, 178–183 (2024).
30. J. Sánchez-Martín *et al*., *Nat. Plants* **7**, 327–341 (2021).
31. S. Asuke *et al*., *Nat. Plants* **10**, 971–983 (2024).
32. Z. Gong, G. Z. Han, WTK3/WTN1 pair confer multiple disease resistance in wheat. Version 1, Mendeley Data (2025); https://data.mendeley.com/datasets/9tdwzgh8v7/1.

ACKNOWLEDGMENTS

We are grateful to R. McIntosh (University of Sydney) and E. Lagudah (CSIRO, Australia) for critical improvement of the manuscript. We thank C. Lan of Huazhong Agricultural University for providing the Jagger and Cadenza seeds and B. Wulff (King Abdullah University of Science and Technology, Saudi Arabia) and P. Dodds (CSIRO, Australia) for valuable discussions. Z. Liu is applying a WTN1-related patent with application number 2024116811289 of China National Intellectual Property Administration. **Funding:** This study was supported by the National Key Research and Development Program of China (2021YFA1300700 to Z.L. and J.-M.Z., 2023YFD1200402 to Z.L., 2022YFF1001503 to P.L.), Strategic Priority Research Program of the Chinese Academy of Sciences (XDA24010305 to Z.L.), the National Natural Science Foundation of China (31801345 to P.L., 32172001 to H.L., and U21A20224 to Z.L.), Biological Breeding-National Science and Technology Major Project (2023ZD04073 to M.L.), and Youth Innovation Promotion Association CAS (2021093 to P.L.). This project was also supported by grants from the Hainan Seed Industry Laboratory (B21HJ0111 to Z.L.), Key Research and Development Program of Zhejiang (2024SSYS0099 to Z.L.), and Key Research and Development Program of Hebei (22326305D to C.Y.). **Author contributions:** P.L., G.Z., J.L., and Z.G. performed experimental procedures and analyzed results. G.W., Li.D., H.Z., K.Z., Q.W., G.G., M.L., B.H., B.L., W.L., Le.D., Y.H., X.C., H.F., and D.Q. contributed to gene expression, protein identification, and greenhouse experiments. Yo.C. and C.Y. contributed to field trials and phenotypic analyses. G.Z., M.S., K.W., and Y.W. contributed to the electrophysiology experiments. Z.G. and G.-Z.H. contributed to the evolutionary analyses. P.L., Yu.C, G.-Z.H., and Z.L. conceived of the idea, designed experiments, analyzed genotypic and phenotypic data, and interpreted results. P.L., H.L., J.-M.Z, G.-Z.H., Yu.C., and Z.L. wrote the manuscript. **Competing interests:** The authors declare no competing interests. **Data and materials availability:** All data are available in the main text or the supplementary materials. Alignments and phylogenetic trees generated in this study have been deposited to Mendeley Data (*32*).

SUPPLEMENTARY MATERIALS

science.org/doi/10.1126/science.adp5469
Materials and Methods
Figs. S1 to S20
Tables S1 to S11
MDAR Reproducibility Checklist
References (*33*–*62*)

Submitted 2 April 2024; resubmitted 26 November 2024
Accepted 14 February 2025
10.1126/science.adp5469

QUANTUM OPTICS

Selective filtering of photonic quantum entanglement via anti–parity-time symmetry

Mahmoud A. Selim[1]*, Max Ehrhardt[2], Yuqiang Ding[3], Hediyeh M. Dinani[1], Qi Zhong[3,4,5], Armando Perez-Leija[3], Şahin K. Özdemir[4,5], Matthias Heinrich[2], Alexander Szameit[2], Demetrios N. Christodoulides[1,6], Mercedeh Khajavikhan[1,6]*

Entanglement is a key resource for quantum computing, sensing, and communication, but it is susceptible to decoherence. To address this, research in quantum optics has explored filtering techniques such as photon ancillas and Rydberg atom blockade to restore entangled states. We introduce an approach to entanglement retrieval that exploits the features of non-Hermitian systems. By designing an anti–parity-time two-state guiding configuration, we demonstrate efficient extraction of entanglement from any input state. This filter is implemented on a lossless waveguide network and achieves near-unity fidelity under single- and two-photon excitation and is scalable to higher photon levels, remaining robust against decoherence during propagation. Our results offer an approach to using non-Hermitian symmetries to address central challenges in quantum technologies.

Entanglement is a fundamental aspect of quantum mechanics, representing a distinctive and powerful form of nonclassical correlations between particles, and has far-reaching implications for quantum technologies. In quantum communications, for instance, the ability to manipulate entangled photon states underpins secure quantum key distribution (*1*, *2*), and in quantum computing, entanglement serves as the basis for the inherent parallelism that exponentially enhances computational capabilities (*3*–*6*). Similarly, in quantum sensing, entangled photons provide increased sensitivity and noise resilience that exceed the classical limit (*7*). Yet the intrinsic fragility associated with entanglement poses a challenge, whereby minimal environmental interactions can destroy the delicate quantum superposition, leading to a collapse into mixed or classical states (*8*). Although such deterioration is almost universally anticipated in the presence of loss, it remains unclear to what extent non-Hermiticity can preserve or even restore this resource in a manner that is both scalable and ultimately efficient.

To retrieve an entangled state that has decomposed into a mixed state, a targeted approach can be used to selectively eliminate its classical components. This strategy closely resembles those associated with classical optical filters designed to isolate specific degrees of freedom of light, such as wavelength or polarization (*9*). In quantum optics, various methodologies for entanglement filtering have been explored, including schemes that use photon ancillas (*10*, *11*) or the nonlinear response of Rydberg atoms (*12*). Given that filters are inherently non-Hermitian entities, an intriguing question arises: Can dissipation be engineered within specific nonconservative configurations to effectively restore entanglement from a mixed input state (*13*, *14*)?

Non-Hermitian systems have been extensively investigated in classical optical contexts, revealing a host of counterintuitive phenomena (*15*), including phase transitions (*16*), topological chirality (*17*–*20*), unidirectional invisibility (*21*), laser mode management (*22*, *23*), loss-induced transparency (*24*, *25*), and enhanced sensitivity (*26*–*28*), among others. In this work, we leveraged the distinctive properties of photonic non-Hermitian anti–parity-time (APT) symmetric configurations (*29*, *30*) to realize a class of structures with functionalities in the quantum regime. Our approach isolated a desired entangled state within a bosonic subspace, thereby providing a highly versatile linear mechanism for state selection through photon-photon interference. Importantly, this configuration functions as a decoherence-free subspace (*31*), preserving quantum states against dephasing while enhancing the robustness of quantum information processing.

Photonic entanglement filter system—theory

APT symmetry, a subclass of non-Hermitian systems, is associated with Hamiltonians $\mathcal{H}$ that anticommute with the parity-time ($\hat{\mathcal{P}}\hat{\mathcal{T}}$) operator, that is, $\{\hat{\mathcal{P}}\hat{\mathcal{T}}, \mathcal{H}\} = \hat{\mathcal{P}}\hat{\mathcal{T}}\mathcal{H} + \mathcal{H}\hat{\mathcal{P}}\hat{\mathcal{T}} = 0$. In optics, APT symmetry can be established in scenarios where two elements (e.g., waveguides or cavities), labeled L and R, are dissipatively coupled (upper left panel of Fig. 1A) with a Hamiltonian given by

$$\mathcal{H}_{\text{eff}} = -i\Gamma(\sigma_x + I) \tag{1}$$

where σ_x denotes the x Pauli operator, I is the identity matrix, and Γ represents the coupling coefficient. Realizing an APT-symmetric system is challenging, as it requires the dissipative coupling $i\Gamma$ to precisely match the local dissipations at sites L and R. Serendipitously, this symmetry emerges naturally in a mirrored Wigner-Weisskopf configuration (*32*) (upper

[1]Ming Hsieh Department of Electrical and Computer Engineering, University of Southern California, CA, USA. [2]Institut für Physik, Universität Rostock, Albert-Einstein-Straße 23, Rostock, Germany. [3]CREOL, College of Optics and Photonics, University of Central Florida, Orlando, FL, USA. [4]Department of Engineering Science and Mechanics, The Pennsylvania State University, University Park, PA, USA. [5]Department of Electrical and Computer Engineering, Saint Louis University, St. Louis, MO, USA. [6]Department of Physics and Astronomy, University of Southern California, Los Angeles, CA, USA.
***Corresponding author. Email: maabdelr@usc.edu (M.A.S.); khajavik@usc.edu (M.K.)**

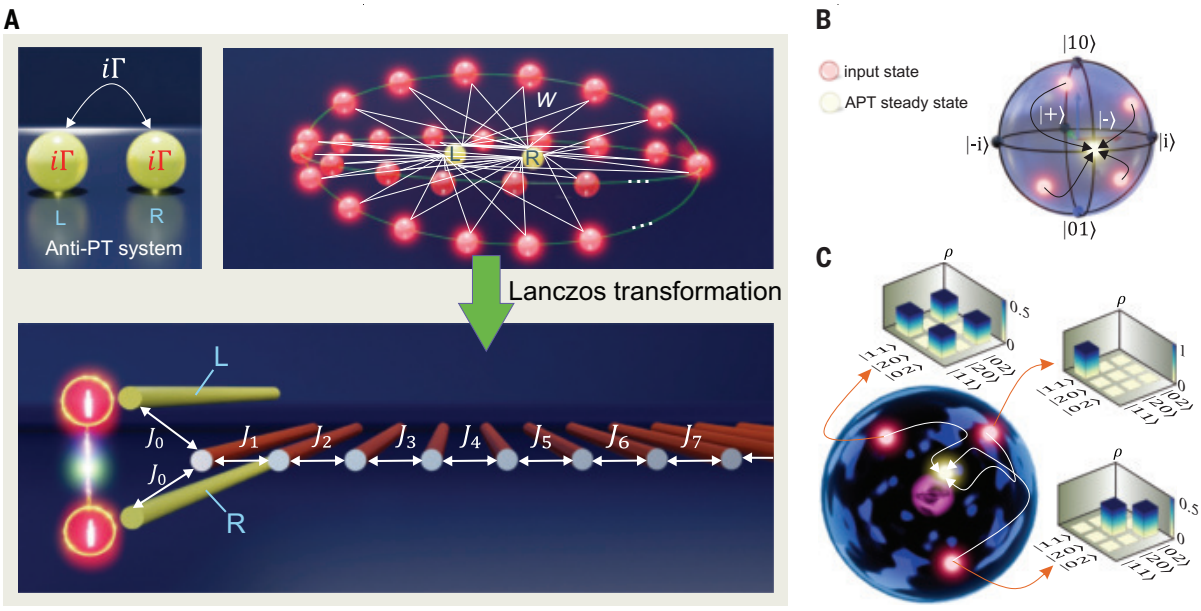

Fig. 1. All-photonic scalable entanglement APT filter. (**A**) Schematic of an APT symmetric configuration, representing two lossy cavities or waveguides with an imaginary coupling coefficient (top left). Through Wigner-Weisskopf theory, dissipation is modeled through coupling to a continuum of elements with uniformly increasing detuning (top right). By using the Lanczos transformations, the system is reformulated into an array of coupled waveguides that selectively transmits the desired entangled state (bottom). (**B**) APT dynamics on the single-photon Bloch sphere. Regardless of the input single-photon state, the output irreversibly yields $|\psi^{(1)}\rangle = (|10\rangle - |01\rangle)/\sqrt{2}$. (**C**) Bloch ball for two-photon states. In this case, the output state consistently evolves into the two-photon entangled state $|\psi^{(2)}\rangle = (|20\rangle + |02\rangle)/2 - |11\rangle/\sqrt{2}$.

right panel of Fig. 1A), where two isoenergetic states happens to exhibit APT symmetry, provided both elements are coupled with equal strength w to a Hermitian bath consisting of a continuum of equidistantly spaced energy levels [supplementary text I (*33*)]. In this case, the effective Hamiltonian governing the dynamics at sites L and R is precisely given by the non-Hermitian Hamiltonian of Eq. 1—a rather surprising result given that the infinite chain in between the two waveguides is itself conservative. Yet even at this stage, achieving an optical realization of the configuration in Fig. 1A remains a formidable challenge. Geometrically, it is not feasible to surround a cavity or waveguide site with large number of elements whose local eigenvalues continuously increase or decrease at a uniform rate. To circumvent this physical constraint, we used isospectral Lanczos transformations [supplementary text II (*33*)], which enable mapping the intermediate infinite chain onto a tridiagonal matrix with elements that share identical local eigenvalues (*34*, *35*). This mapping holds as long as the exchange strength between nearest-neighbor elements is appropriately engineered (bottom panel of Fig. 1A) [supplementary text III (*33*)]. It should be emphasized that the collective quantum mechanics of a subsystem, together with its environment, is inherently Hermitian, and any presence of non-Hermiticity only emerges when projecting onto the subsystem through postselection.

To benchmark our experimental and theoretical studies, we numerically modeled the Markovian dynamics of the reduced density matrix $\hat{\rho} = \sum_j p_j |\psi_j\rangle\langle\psi_j|$, where p_j denotes the probability of the state $|\psi_j\rangle$, by using the standard Lindblad master equation (*36*)

$$\partial_z \rho(z) = -i\left(\mathcal{H}_{\text{eff}}\,\hat{\rho} - \hat{\rho}\mathcal{H}_{\text{eff}}^{\dagger}\right) + 2\Gamma \hat{a}_{\text{L}}\hat{\rho}\hat{a}_{\text{L}}^{\dagger} + 2\Gamma \hat{a}_{\text{R}}\hat{\rho}\hat{a}_{\text{R}}^{\dagger} = \mathcal{L}\,\rho \quad (2)$$

In general, the solution of the master equation [$\hat{\rho} = e^{\mathcal{L}z}\hat{\rho}(0)$] can be obtained from the system's eigenmodes after diagonalizing the Liouvillian operator $\mathcal{L}$ (*37*). For instance, under one- and two-photon excitation conditions, one can show that the APT effective Hamiltonian of Eq. 1 allows a lossless eigenstate: (i) $|\psi^{(1)}\rangle = 1/\sqrt{2}(|10\rangle - |01\rangle)$ (also known as the W-state), which exists within the single-photon subspace, and (ii) $|\psi^{(2)}\rangle = 1/2(|20\rangle + |02\rangle) - |11\rangle/\sqrt{2}$, which arises when the subspace engages two photons [supplementary text IV to VI (*33*)]. By contrast, the rest of the modes undergo loss, decaying over a propagation distance $z \gg 1/\Gamma$, as their corresponding eigenvalues exhibit a finite imaginary component. Note that these two lossless states $|\psi^{(1)}\rangle$ and $|\psi^{(2)}\rangle$ are path entangled. More broadly, any arbitrary N-photon excitation, whether on the Bloch sphere (for pure states) or within the Bloch ball (for mixed states), irreversibly evolves toward a single point, corresponding to a specific entangled mode. This process is schematically illustrated in Fig. 1B for $N = 1$, where all states on the one-photon Bloch sphere converge after propagation to the W-state (*38*). Conversely, for $N = 2$, all possible excitations eventually yield $|\psi^{(2)}\rangle = 1/2(|20\rangle + |02\rangle) - |11\rangle/\sqrt{2}$ (Fig. 1C). Evidently, this behavior is consistent with that expected from an entanglement filter. In principle, the quantum dynamics in this altogether Hermitian setting (APT subsystem and Lanczos array) can be theoretically described by treating this waveguide array arrangement as a multiport Hong-Ou-Mandel (HOM) system [supplementary text IV (*33*)]. Moreover, this approach and that of Lindblad (Eq. 2) yield identical results. We also note that, in principle, postselecting the anticoincidence events projects the $|\psi^{(2)}\rangle$ state onto the two-photon NOON state, which is a resource for quantum metrology [supplementary text V (*33*)].

Experimental results

To experimentally verify the filtering behavior of the APT system, we designed a set of multi-element waveguide structures using Lanczos transformations. These arrangements are then fabricated through femtosecond direct laser writing in fused silica glass (*39*) [supplementary text VI (*33*)]. Samples with different lengths are prepared to enable the observation of the dynamics of the quantum system. In our experiments, the imaginary coupling factor was set to be $\Gamma = 0.25\ \text{cm}^{-1}$, and a Lanczos's array of 52 nonuniformly coupled waveguides was deployed. In all cases, the loss factor was experimentally characterized using a modified variable stripe technique [supplementary text

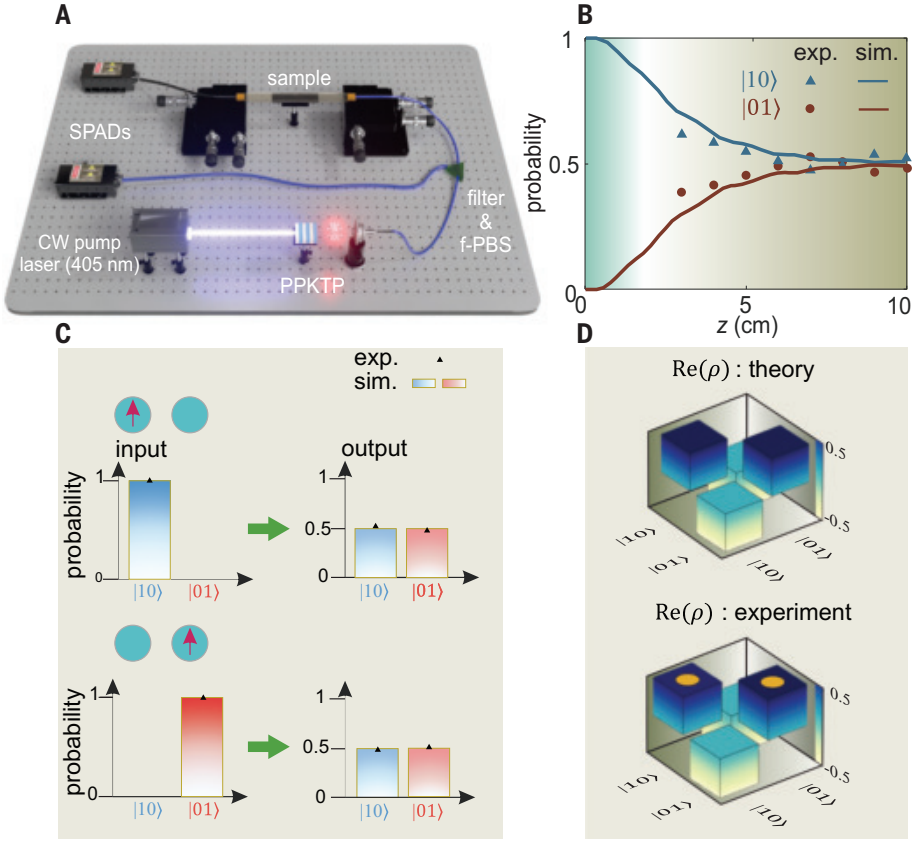

Fig. 2. Single-photon response of the APT filter. (**A**) Schematic of the experimental setup for single-photon measurements. CW, continuous wave; f-PBS, fiber polarizing beam splitter; SPAD, single-photon avalanche diode. (**B**) Measured probability of finding a photon in each waveguide after varying propagation lengths. Solid lines represent theoretical predictions for the design parameter $\Gamma = 0.25\ \mathrm{cm}^{-1}$. Measurement errors are within the symbol size. (**C**) Performance evaluation of the APT entanglement filter at $z = 10$ cm, where single photons are injected via $|10\rangle$ and $|01\rangle$ states. (**D**) Comparison of the theoretical (top) and experimentally measured (bottom) density matrix $\rho = |\psi\rangle\langle\psi|$ at the APT filter output at $z = 10$ cm. Experimental errors (orange cylinders) denote Poisson standard deviations, typically less than 2% in all cases.

III (*33*)]. As a first step, we monitored the classical evolution by measuring the intensity ratios at the output of the two waveguides using laser light at a wavelength of $\lambda = 810$ nm.

We then investigated the APT entanglement filter's response under single-photon excitation by means of heralded detection. Entangled photon pairs were generated through type II spontaneous parametric down-conversion (SPDC) in a periodically poled potassium titanyl phosphate (PPKTP) crystal, which converted a 405-nm pump photon into a pair of polarization-entangled signal and idler photons at 810 nm. These two photons were subsequently split using a fiber-coupled polarization beam splitter, after which one photon was used for heralding and the other was coupled to one of the sites of the APT arrangement (Fig. 2A). The single-photon evolution dynamics were monitored within the basis states $|10\rangle$ or $|01\rangle$, as depicted in Fig. 2B, using structures of varying lengths (3 to 10 cm in 1 cm increments). Figure 2C shows the photon detection probability at the output of each waveguide element after a propagation of $z = 10$ cm, confirming that, irrespective of the input photon state $|10\rangle$ or $|01\rangle$, the system reaches an equilibrium with equal photon probabilities at both outputs ($P_{10} = P_{01} = 0.5$). However, the probability measurement by itself does not uniquely specify the quantum state. In general, this measurement only indicates that the output state is of the form $\left(|10\rangle + e^{i\phi}|01\rangle\right)/\sqrt{2}$, where ϕ can be an arbitrary phase. To characterize this state, we performed quantum state tomography using additional measurement configurations where we interfered the output of the two channels using a 3dB coupler after adding a $\pi/4$ phase shift in one of the arms. By considering these measurements, one can determine ϕ [supplementary text VII and VIII (*33*)], which, as indicated by the density matrix in Fig. 2D, is equal to π in this case. This observation corroborates that the output state was indeed $\left|\psi^{(1)}\right\rangle = \left(|10\rangle - |01\rangle\right)/\sqrt{2}$. Note that the orange cylinders in Fig. 2D highlight the experimental error.

We next considered the APT filtering action when two photons are injected using the experimental setup depicted in Fig. 3A. In this case, timing of the photon pairs was achieved by leveraging the HOM interference effect (*40*) [supplementary text IX (*33*)]. After that, one arm of the HOM interferometer was directed toward the sample while the other port was blocked. This arrangement and its variants allowed us to excite the sample with basis vectors $|20\rangle$, $|02\rangle$, or $|11\rangle$. At the output, the sample was aligned with a two-element multimode fiber array that had a pitch of 127 μm, to match the fan-out of the APT filter's waveguides. The multimode fibers were then routed to single-photon detectors, interfaced with a time tagger for time-correlated single-photon counting. As before, to characterize the evolution dynamics of the two-photon quantum state, we performed a series of measurements on samples with a constant imaginary coupling factor but varying lengths (3 to 10 cm). As anticipated, after sufficient propagation distance ($z \gg 1/\Gamma$), the output consistently converged to the system's attractor state, as shown in Fig. 3B for the $|20\rangle$ input state. Next, we tested the APT filter by launching the other aforementioned two-photon input states and monitoring their dynamics after propagation over a distance of 3 to 10 cm. In all cases, the output state consistently exhibited the expected detection probabilities (Figs. 3C). These initial measurements suggested that the observed state is of the form $\left(|20\rangle + e^{i\phi_1}|02\rangle\right)/2 + e^{i\phi_2}|11\rangle/\sqrt{2}$. To identify the relative phases ϕ_1 and ϕ_2, we next performed interferometric measurements to reconstruct the density matrix using quantum tomography techniques. By further examining the output state using a balanced and quarter-wave-shifted 3dB coupler, we determined $\phi_1 \approx 0$ and $\phi_2 \approx \pi$ (see Fig. 3D). The observed entangled state was consistent with our theoretical predictions, as shown in Fig. 3E.

The experiments above highlight the universality of the APT filter across different photon subspaces. This is attributed to the presence of a solitary attractor in each subspace, facilitated by the interplay of non-Hermiticity and photon-photon interference. Although our current setup limits us to $N = 2$ photons, the APT filter can function under N-photon excitation conditions, where the zero-loss quantum state attractor assumes the form [supplementary text X (*33*)]

$$|\psi\rangle = \sum_{k=0}^{N} (-1)^k \sqrt{\frac{1}{2^N}\binom{N}{k}}\,|N-k,k\rangle \quad (3)$$

Furthermore, these states are resilient to phase or structural perturbations manifested in the Lanczos array. Indeed, when the eigenvector is perturbed after reaching a steady state, it automatically returns to equilibrium after propagating over a distance on the order of $z \gg 1/\Gamma$. This

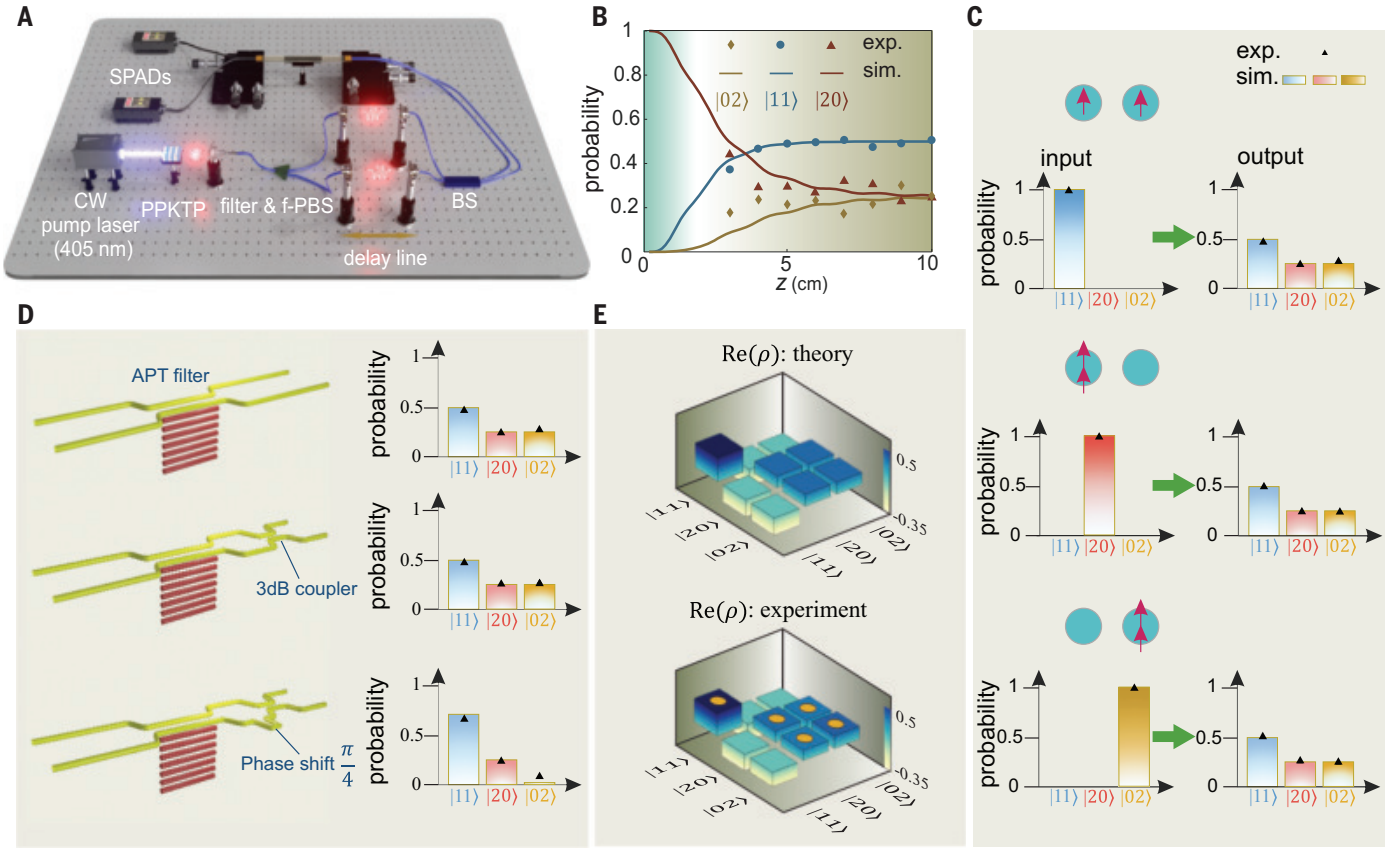

Fig. 3. Two-photon dynamics of the APT filter. (**A**) Experimental setup for examining the APT entanglement filter under two-photon excitation. BS, beam splitter. (**B**) The response of the APT filter for two-photon excitations, characterized by measuring samples with the same APT coupling parameter Γ for different propagation distances. (**C**) Probabilities of detecting photons at the output of the APT filter under various two-photon excitation conditions. (**D**) Quantum state tomography measurements. Additional configurations based on a 50/50 coupler with phase shifts of 0 and π/4 in one of the arms are used to uniquely identify the phases. (**E**) Theoretically calculated (top) and experimentally measured (bottom) two-photon density matrix $\rho = |\psi\rangle\langle\psi|$ at z = 10 cm. Experimental errors, indicated by orange cylinders, typically ranged between 1 and 4%.

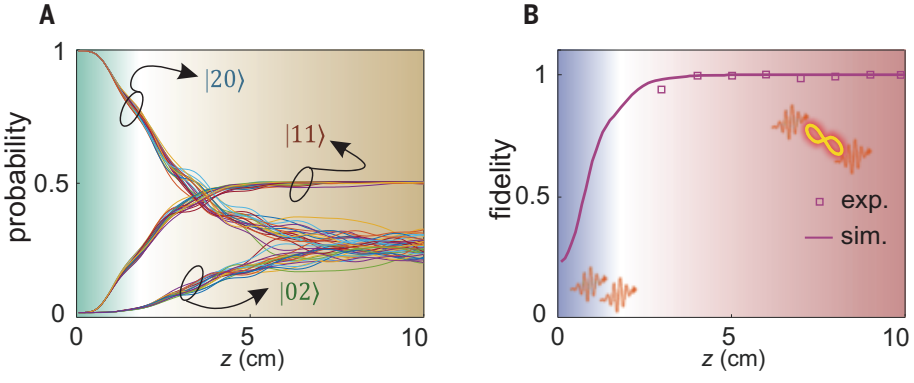

Fig. 4. Resilience of the APT entanglement filter. (**A**) Ensemble response of the system's evolution with approximately 10% variation in the coupling coefficients. Even in the presence of this perturbation, the output still settles into the entangled state. (**B**) The evolution of the fidelity of the APT state.

behavior is analogous to that of a decoherence-free subspace, where states propagate without being substantially affected by environmental noise (Fig. 4A) [supplementary text XI (*33*)]. In addition to its reduced implementation complexity, an advantage of the APT filter lies in its capacity to achieve the target state with high fidelity, circumventing the constraints associated with other filtering techniques. For example, measurement-based protocols typically exhibit lower fidelities, whereas double Rydberg excitation filters face intrinsic challenges in suppressing unwanted interactions. To quantify this aspect, we defined the fidelity $\mathcal{F}$ through the diagonal elements of the density matrix using Bhattacharyya centroids (*41*), as $\mathcal{F} = \sum P_{\text{exp}} P_{\text{meas}}$, where, P_{exp} represents the expected probability of the entangled wave function [e.g., $|\psi\rangle = (|20\rangle + |02\rangle)/2 - |11\rangle/\sqrt{2}$ for two-photon excitation], and P_{meas} denotes the measured probability from the APT system. In this context, the measured fidelity of the APT entanglement filter exceeds 99% for $z > 1/\Gamma$, as shown in Fig. 4B. Finally, it should be noted that the filter introduced in this work has the capability to purify mixed states [supplementary text XII (*33*)].

Concluding remarks

We have demonstrated that non-Hermiticity in the form of APT symmetry can be harnessed to realize a class of entanglement filters. We designed the APT structure using a methodology based on isospectral Lanczos transformations and experimentally validated it under both single- and two-photon excitation conditions. The filtering response was achieved in a

linear manner through the interplay of photon-photon interference and dissipation engineering. Furthermore, implementing APT systems within a completely Hermitian environment presents a promising path forward in non-Hermitian quantum mechanics, eliminating the need for absorbing or amplifying materials. Ultimately, by enabling the on-demand generation of entangled photons and nondestructive entanglement purification on-chip, this work sets the stage for advanced quantum technologies to be developed on integrated and compact platforms.

REFERENCES AND NOTES

1. C. H. Bennett, G. Brassard, in *Proceedings of IEEE International Conference on Computers, Systems and Signal Processing* (Steering Committee, 1984), pp. 175–179.
2. A. K. Ekert, *Phys. Rev. Lett.* **67**, 661–663 (1991).
3. Y. I. Manin, *Computable and Non-Computable* (Sovetskoe Radio, 1980), pp. 13–15.
4. R. Feynman, *Int. J. Theor. Phys.* **21**, 467–488 (1982).
5. D. P. DiVincenzo, *Science* **270**, 255–261 (1995).
6. J. L. O'Brien, *Science* **318**, 1567–1570 (2007).
7. V. Giovannetti, S. Lloyd, L. Maccone, *Science* **306**, 1330–1336 (2004).
8. W. H. Zurek, *Rev. Mod. Phys.* **75**, 715–775 (2003).
9. B. E. A. Saleh, M. C. Teich, *Fundamentals of Photonics* (Wiley, ed. 3, 2019)
10. T. B. Pittman, B. C. Jacobs, J. D. Franson, *Phys. Rev. A* **64**, 062311 (2001).
11. R. Okamoto *et al*., *Science* **323**, 483–485 (2009).
12. G. S. Ye *et al*., *Nat. Photonics* **17**, 538–543 (2023).
13. P. M. Harrington, E. J. Mueller, K. W. Murch, *Nat. Rev. Phys.* **4**, 660–671 (2022).
14. Z. Z. Li, W. Chen, M. Abbasi, K. W. Murch, K. B. Whaley, *Phys. Rev. Lett.* **131**, 100202 (2023).
15. R. El-Ganainy *et al*., *Nat. Phys.* **14**, 11–19 (2018).
16. C. E. Rüter *et al*., *Nat. Phys.* **6**, 192–195 (2010).
17. H. Xu, D. Mason, L. Jiang, J. G. E. Harris, *Nature* **537**, 80–83 (2016).
18. J. Doppler *et al*., *Nature* **537**, 76–79 (2016).
19. H. Nasari *et al*., *Nature* **605**, 256–261 (2022).
20. A. Schumer *et al*., *Science* **375**, 884–888 (2022).
21. A. Regensburger *et al*., *Nature* **488**, 167–171 (2012).
22. H. Hodaei, M. A. Miri, M. Heinrich, D. N. Christodoulides, M. Khajavikhan, *Science* **346**, 975–978 (2014).
23. L. Feng, Z. J. Wong, R. M. Ma, Y. Wang, X. Zhang, *Science* **346**, 972–975 (2014).
24. A. Guo *et al*., *Phys. Rev. Lett.* **103**, 093902 (2009).
25. B. Peng *et al*., *Science* **346**, 328–332 (2014).
26. J. Wiersig, *Phys. Rev. Lett.* **112**, 203901 (2014).
27. W. Chen, Ş. Kaya Özdemir, G. Zhao, J. Wiersig, L. Yang, *Nature* **548**, 192–196 (2017).
28. H. Hodaei *et al*., *Nature* **548**, 187–191 (2017).
29. C. M. Gentry, M. A. Popović, *Opt. Lett.* **39**, 4136–4139 (2014).
30. Y. Li *et al*., *Science* **364**, 170–173 (2019).
31. D. A. Lidar, I. L. Chuang, K. B. Whaley, *Phys. Rev. Lett.* **81**, 2594–2597 (1998).
32. V. F. Weisskopf, E. P. Wigner, *Eur. Phys. J. A* **63**, 54–73 (1930).
33. See supplementary materials.
34. C. Lanczos, *J. Res. Natl. Bur. Stand.* **45**, 255–282 (1950).
35. L. J. Maczewsky *et al*., *Nat. Photonics* **14**, 76–81 (2020).
36. I. Arkhipov, F. Minganti, A. Miranowicz, F. Nori, *Phys. Rev. A* **104**, 012205 (2021).
37. F. Klauck *et al*., *Nat. Photonics* **13**, 883–887 (2019).
38. M. Gräfe *et al*., *Nat. Photonics* **8**, 791–795 (2014).
39. T. Meany *et al*., *Laser Photonics Rev.* **9**, 363–384 (2015).
40. C. K. Hong, Z. Y. Ou, L. Mandel, *Phys. Rev. Lett.* **59**, 2044–2046 (1987).
41. F. Nielsen, S. Boltz, *IEEE Trans. Inf. Theory* **57**, 5455–5466 (2011).
42. M. A. Selim *et al*., Dataset—Selective filtering of photonic quantum entanglement via anti-parity-time symmetry, Dryad (2024); https://doi.org/10.5061/dryad.2ngf1vhzw.

ACKNOWLEDGMENTS

We thank C. Otto for preparing the high-quality fused silica samples used for the inscription of all photonic structures utilized in this work. We thank Y. Joglekar for fruitful discussions. **Funding:** This work was supported by Air Force Office of Scientific Research (AFOSR) grants MURI FA9550-21-1-0202 (M.A.S., Y.D., H.M.D., Q.Z., A.P.-L., Ş.K.Ö., D.N.C., M.K.) and FA9550-20-1-0322 (M.A.S., H.M.D., D.N.C., M.K.); Office of Naval Research (ONR) grant MURI N00014-20-1-2789 (M.A.S., H.M.D., D.N.C., M.K.); the W.M. Keck Foundation (D.N.C.); the MPS Simons collaboration (Simons grant 733682) (D.N.C.); US Air Force Research Laboratory grant FA86511820019 (D.N.C.); and Department of Energy grant DESC0022282 (D.N.C., M.K., M.A.S.). A.S. acknowledges funding from the Deutsche Forschungsgemeinschaft (grants SZ 276/9-2, SZ 276/19-1, SZ 276/20-1, SZ 276/21-1, SZ 276/27-1, and GRK 2676/1-2023 "Imaging of Quantum Systems," project no. 437567992). A.S. also acknowledges funding from the Krupp von Bohlen and Halbach Foundation and from the FET Open Grant EPIQUS (grant no. 899368) within the framework of the European H2020 program for Excellent Science. A.S. and M.H. acknowledge funding from the Deutsche Forschungsgemeinschaft via SFB 1477 "Light–Matter Interactions at Interfaces" (project no. 441234705). **Author contributions:** M.A.S., A.P.-L., D.N.C., and M.K. conceived the idea for this work. M.A.S., M.E., A.P.-L., Q.Z., Y.D., and M.H. designed the structures and fabricated the samples. M.A.S. and M.E. performed the experiments. M.A.S., M.E., H.M.D., A.P.-L., Ş.K.Ö., A.S., D.N.C., and M.K. interpreted the results. All authors discussed the results and co-wrote the manuscript. **Competing interests:** The authors declare no competing interests. **Data and materials availability:** All data are available in the manuscript, in the supplementary materials, or through Dryad (*42*).

SUPPLEMENTARY MATERIALS

science.org/doi/10.1126/science.adu3777
Supplementary Text
Figs. S1 to S10
Table S1
References (*43*–*45*)

Submitted 5 November 2024; accepted 22 January 2025
10.1126/science.adu3777

Who's the top employer for 2024?

Science 2024 TOP EMPLOYER

Science Careers' annual survey reveals the top companies in biotech & pharma voted on by *Science* readers.

Explore these highly-rated employers in our new interactive experience:
sciencecareers.org/topemployers

By **Nina Ockendon-Powell**

ADHD, at 42

Sitting in the seminar I realized I was holding myself still. Upright, contained. I needed to move, even just a little bit. In the past I would have resisted the urge, but now I was empowered with some life-changing knowledge: At the age of 42, I had just been diagnosed with attention-deficit/hyperactivity disorder (ADHD). Keeping still in settings where that's the social norm was one of many masks I'd worn for years—and as I shifted in my seat, it felt good to remove it.

I didn't know much about ADHD until a few years ago. I'd held the common misconception that ADHD was about fidgety, naughty children who didn't do very well at school. But I loved learning and had never really struggled to apply myself. Nor had I been badly behaved or hyperactive.

I had, however, always had an overactive brain. I experienced a constant and rapid stream of thoughts, exasperating my mother, who was often telling me to "switch that brain off." I was also a chronic daydreamer and very emotionally sensitive. This internalized energy had nowhere to go, so it manifested as anxiety. I didn't know it then, but these symptoms are hallmarks of ADHD in women and girls.

"My diagnosis was transformative—but it brought bitter regrets."

It wasn't until an ill-fated attempt at a Ph.D., where I was bullied by a colleague, that the anxiety became problematic. I was unable to finish the work, so wrote it up as a master's. Emotionally devastated, I ran as far away from academia as I could, spending years in various roles in the civil service. I was also misdiagnosed with generalized anxiety disorder.

Yet my love of science didn't go away. I eventually went back to complete my Ph.D. in a topic I felt passionate about, in a highly supportive group, and then pursued a research career. It wasn't a smooth path: On some days I'd be focused and confident, whereas on others adrenaline and emotion derailed my productivity. This roller coaster ride of anxiety left me struggling to believe I would make it as an independent academic. By my early 40s, I was feeling more overwhelmed than ever: Not only did I have a career to worry about, but I was now also the primary caregiver for two small children.

One day, my mother told me about a friend's child who was an adult with ADHD. They sounded a lot like me, she said. Within the year, I received an official diagnosis.

My diagnosis was transformative—but it brought bitter regrets. I grieved for the life and career that could have been had my ADHD been detected earlier. I might have coped better with the negative first Ph.D. experience, for instance, and continued my studies in a related field rather than leaving academia—a decision that still affects how I am assessed in grant and job applications. And if I had understood the cause of my anxiety, I could have started the right treatment to manage it.

But I also came to understand how ADHD has given me unique strengths. I used to criticize myself for not being great at any one thing, but I've since realized my diverse abilities and creativity make me an innovative interdisciplinary thinker, which is a huge benefit in academia. I also realized that my emotional intelligence, intuition, and infectious energy make me a good leader, while my tendency to become intensely absorbed in interesting activities means I work well to grant deadlines. And I saw how I'd had to work harder than neurotypical peers to get to the same level, giving me a resilience that now keeps me committed to achieving my goals.

I was initially worried about divulging my diagnosis to my colleagues—but I've found that most people have been supportive and understanding. I'm lucky my peers talk openly about neurodiversity. That's not always the case: Academia can be very traditional and dogmatic, and it's important we create a culture where everyone feels they belong.

A year into my ADHD diagnosis, I've established daily well-being habits including exercise, mindfulness, and a good diet, and I'm taking medication. Thanks to these, combined with my ADHD superpowers of hyperfocus and creatively connecting ideas, I'm now making strides in my career—and finally beginning to believe I have what it takes to succeed in science. ■

Nina Ockendon-Powell is a molecular and computational ecologist/pathologist at the University of Bristol.

ILLUSTRATION: ROBERT NEUBECKER